Probing galaxy evolution through numerical simulations:
mergers, gas, and star formation

by

Maan H. Hani
B.Sc., Saint Mary's University, 2013
M.Sc., Saint Mary's University, 2015

A Dissertation Submitted in Partial Fulfillment of the
Requirements for the Degree of

DOCTOR OF PHILOSOPHY

in the Department of Physics and Astronomy

Probing galaxy evolution through numerical simulations:
mergers, gas, and star formation

by

Maan H. Hani
B.Sc., Saint Mary's University, 2013
M.Sc., Saint Mary's University, 2015

Supervisory Committee

Dr. Sara L. Ellison, Supervisor
(Department of Physics & Astronomy)

Dr. Julio F. Navarro, Departmental Member
(Department of Physics & Astronomy)

Dr. Ian Putnam, Outside Member
(Department of Mathematics & Statistics)

ABSTRACT

Large observational surveys have compiled substantial galaxy samples with an array of different properties across cosmic time. While we have a broad understanding of how galaxies grow and build their observable properties, the details of galaxy growth and evolution pose a fundamental challenge to galaxy evolution theories. Nonetheless, galaxy evolution is ultimately regulated by the properties of the gas reservoir. In this thesis I use numerical simulations to answer key questions related to the galactic gas reservoir, and galaxy mergers: a major transformational process.

In Chapter 2 I present an analysis of 28 simulated $L^{\star}$ galaxies to understand the physical processes that shape the massive gas reservoir surrounding galaxies (i.e. the circum-galactic medium; CGM). I show that (1) the gas and metal content of the CGM is driven by galaxy growth and the strength/presence of feedback processes, and (2) the ionisation and internal structures of the CGM are shaped by galactic outflows, and active galactic nucleus luminosity. Albeit dependent on internal galactic properties and the physical processes that shape them, the CGM remains greatly diverse, thus posing a challenge for observational surveys.

As a follow-up to my study of normal $L^{\star}$ galaxy gas halos, in Chapter 3 I present a theoretical study of the effect of galaxy mergers on the CGM. I demonstrate that galaxy mergers can leave a strong imprint on the CGM's gas and metal content, metallicity, and size. The merger can increase (1) the CGM's metallicity by $0.2-0.3$ dex within 0.5 Gyr post-merge, and (2) the metal covering fractions by factors of 2-3. In spite of the increase in the CGM's metal content, the hard ionising field during the merger can drive a decline in the covering fractions of commonly observed ions.

In Chapter 4 I shift focus to star formation, particularly the effects of galaxy mergers on star formation. While the effects of galaxy mergers have been proven observationally, theoretical predictions are limited to small binary merger suites and cosmological zoom-in studies. I present a statistical study of 27,691 post-merger galaxies from IllustrisTNG to quantify the effect of galaxy mergers on galactic star formation. I report a dependence in the merger-induced star formation rate (SFR) on mass ratio, stellar mass, gas fraction, and galaxy SFR. I also track the evolution of the effects of galaxy mergers demonstrating their decay over ~ 500 Myr.

In Chapter 6, I leverage galactic scaling relations to extend my work on the effects of galaxy mergers to resolved scales. However, before using the simulated resolved scaling relations, I first examine their existence and robustness. In Chapter 5, I

demonstrate the emergence of the kpc-scale star forming main sequence (rSFMS) in the FIRE-2 simulations. Nonetheless, the slope of the rSFMS is dependent on the (1) star formation tracer's timescale, and (2) observed resolution, which I propose is caused by the clumpiness of star formation. I develop a toy model that quantitatively captures the effects of clumpy star formation. I then illustrate how the model can be used to characterise the mass of star-forming clumps.

Having demonstrated the existence and robustness of known scaling relations in numerical simulations, I explore the effects of galaxy mergers on resolved scales in Chapter 6. I generate synthetic observations for 1,927 post-mergers in IllustrisTNG and examine the radially-dependent merger-driven SFR enhancement, and metallicity suppression in post-mergers. Galaxy mergers preferentially boost star formation in the centres and suppress metallicities globally. The effects of the merger depends on galaxy properties such as stellar mass, SFR, mass ratio, and gas fraction.

Contents

List of Tables

List of Figures

Acknowledgements

First and foremost, I am indebted to S. Ellison for her invaluable mentorship, enthusiastic support, guidance, and advice. Sara made my graduate studies truly enjoyable, challenging, and fulfilling. I would also like to thank my committee members for their time, and interesting discussions.

I have been blessed with a wonderful academic family. I couldn't have hoped for a more supportive, dynamic, witty, and memorable group. Also, thank you to the Physics & Astronomy grads for making UVic an enjoyable workplace.

Beyond astrophysics, tip of the hat to my friends in Victoria! You made Victoria feel like home. I will always treasure our amazing memories. *Al Wehda*, thank you for sharing your music with me. To my teammates on *the noodles* (and variations thereof), and *SK FC*, I will always cherish your camaraderie, and the memorable moments we shared on, and off the field.

I am grateful for my family; their endless patience, encouragement, and unconditional support keeps me going. Hani, tu es mon super-héros. Karim, you're my space hero. Sarah, you're not born yet, but I know I'm going to love you. Hani, Karim, and Sarah, and [insert new nephews or nieces]: It is my unequivocal conviction that I'm your favourite uncle; probably your favourite person. I get it. Lama and Rima, you're wonderful! Mak and Nouh: you, sirs, still owe me for dart ball. Mom and Dad, yet again, I find myself speechless; there isn't a parenting book in the world that could've prepared you for me.

Dedication

إلى والديّ حكمت وأليسار
لن استطيع أن افي ولو بالبسيط من تضحياتكم

Chapter 1

Introduction

1.1 The life and death of galaxies

Theoretical models trace the observed structure in today's Universe back to slight inhomogeneities in the early Universe (e.g., Springel et al., 2005b) dating back to the era of recombination. At recombination, the rapidly expanding early Universe cooled sufficiently to become optically thin to radiation less energetic than 1Ryd. The escaping radiation is observed today as the Cosmic Microwave Background (CMB). As the Universe continued to expand, the inhomogeneities grew, acting as seeds for the observed structure in today's Universe (e.g., Edwards & Heath, 1976). Under the current paradigm for structure formation, observations favour a scenario where structures form in a hierarchical, bottom-up fashion (e.g., Lacey & Cole, 1993): small structures form first and then combine (merge) to form larger structures such as groups, clusters, and super clusters. This is known as "bottom-up" structure formation.

With the Universe's expansion, dark matter halos began forming before any baryonic matter structures. Hence, dark matter forms the backbone for the cosmological filamentary structures which gravitationally accrete baryonic matter, forming galaxies at the centres of dark matter halos (e.g., Springel et al., 2005b). Within dark matter halos, gas can cool and form stars. The formation of a significant stellar component marks the birth of an observable galaxy. The galaxies can then grow by accreting more gas and forming stars, or, as mentioned above, by merging with other galaxies.

The diverse galaxy population

Following their formation, galaxies evolve on a variety of evolutionary tracks that in turn give rise to the diverse galaxy populations observed today. Galaxies show a wide

variety of intrinsic properties such as colour (e.g., Baldry et al., 2004), morphology and size (e.g., Simard et al., 2011), metallicity (e.g., Tremonti et al., 2004), stellar mass (e.g., Baldry et al., 2008; Li & White, 2009), halo mass (e.g., Behroozi et al., 2010), and central supermassive black hole (BH) mass (e.g., Kormendy & Ho, 2013; McConnell & Ma, 2013). Moreover, galaxies live in an array of environments (e.g., Moffett et al., 2015), and exhibit a range of star formation rates (SFRs; e.g., Brinchmann et al., 2004), and active galactic nucleus (AGN) activity (e.g., Hickox et al., 2014).

While galaxies show strong diversity, galaxy properties are often correlated. For example, a galaxy's stellar mass correlates with its colour (e.g., Blanton et al., 2003; Baldry et al., 2006), morphology (e.g., Conselice, 2003), metallicity (e.g., Tremonti et al., 2004; Kewley & Ellison, 2008), dark matter halo mass (e.g., Behroozi et al., 2010, and references therein), probability of hosting an AGN (e.g., Kauffmann et al., 2003; Schawinski et al., 2007), probability of being star forming (e.g., Peng et al., 2010; Woo et al., 2013), and, in the case of a star forming galaxy, its SFR (e.g., Brinchmann et al., 2004; Daddi et al., 2007; Noeske et al., 2007; Salim et al., 2007). The prevalent correlations amongst galaxy properties are suggestive of underlying physical processes linking, and possibly giving rise to, the observed galaxy properties.

Many inter-dependencies[1] between galaxy properties are an imprint of the complex physical mechanisms that influence (or are influenced by) the galactic gaseous component. For instance, the correlations between a galaxy's environment and its colour and SFR (Gerke et al., 2007; Wetzel et al., 2012) are borne of a variety of environmental processes (e.g., ram-pressure stripping, tidal stripping) that deplete the gas reservoir, thus accelerating the galaxy's transition into quiescence (environmental quenching; e.g., Woo et al., 2013, 2015; Bluck et al., 2016). Understanding the galactic gas reservoir, and the physical mechanisms that shape it, are key to our understanding of galaxy evolution.

Two physical processes that are tightly tied to the gas reservoir and can strongly impact galaxy evolution are star formation and AGN activity. Theoretical studies show that stellar feedback can induce significant outflows, launching low angular momentum gas into the galactic halo (Oppenheimer & Davé, 2006; Agertz & Kravtsov, 2016) and/or driving shocks and turbulence in the gas reservoir up to kpc scales (e.g.,

[1]Note that the gas reservoir is not the sole driver of the inter-dependencies between galaxy properties. Some known galaxy correlations (e.g., the FaberJackson relation) are driven by other galaxy properties (e.g., dark matter content).

Grisdale et al., 2017). The theoretical picture where stellar feedback can launch massive, large-scale winds is complemented by observational studies that report ubiquitous star formation-driven winds (e.g., Martin, 2005; Rupke et al., 2005a; Strickland & Heckman, 2009). The observed outflows are often massive (e.g., Strickland & Heckman, 2009) and metal enriched (e.g., Chisholm et al., 2018). In addition to driving outflows, stellar evolution is a leading channel of galactic chemical evolution. As stars age they return significant amounts of metals[2] to the surrounding gas. The effects of metal enrichment are evident across cosmic time with a monotonic increase in metallicity since $z \sim 4$ (e.g. Timmes et al., 1995; Prochaska et al., 2003; Ly et al., 2016).

Besides star formation and stellar feedback, AGN represent an additional energetic process that can significantly impact galaxy properties. Observational studies infer that AGN feedback drives the correlations between BH and galactic properties (e.g., McLure & Dunlop, 2002; Aller & Richstone, 2007; Hopkins et al., 2007a,b; Snyder et al., 2011; Kormendy & Ho, 2013), inflates void bubbles in the intra-cluster medium (Fabian, 2012), and controls the high tail of the stellar mass-halo mass distribution (e.g., Behroozi et al., 2013). Theoretical studies further support the effects of AGN feedback on the gas reservoir; AGN feedback can drive strong outflows (Silk & Rees, 1998), halt gas accretion (e.g. Zubovas & Nayakshin, 2012; Bower et al., 2006), and regulate star formation (Taylor & Kobayashi, 2014).

Many mechanisms have been put forward to explain the physics governing the coupling of the energy produced by AGN to the environment (e.g. Buff & McCray, 1974; Castor et al., 1975; Cowie et al., 1978; Ciotti & Ostriker, 2001; Murray et al., 2005). However, the detailed physics governing the coupling of the energy to the environment remains poorly understood. AGN feedback has been categorised into two major forms: (1) radiative (thermal) feedback and (2) kinetic (mechanical) feedback. The radiative mode of feedback, also known as the wind mode or quasar mode, requires high accretion rates (e.g. Narayan & Yi, 1994; Trump et al., 2011). The energy is released in the form of a sub-relativistic wind. This mode is likely responsible for correlations with the spheroidal component of the galaxy (i.e., the correlation between the black hole mass, M_{BH}, and the velocity dispersion of the spheroidal stellar component, $\sigma_{\rm bulge}$). The other mode of feedback is the kinetic feedback (radio mode). The energy is released in the form of jets launched from the optically thin,

[2]Note that, unlike the chemical definition, in astronomy all elements with atomic numbers larger than that of He (Z = 2) are considered metals.

geometrically thick accretion disc surrounding the BH during radiatively inefficient accretion. This mode drives gas away in the form of relativistic jets, keeping it too hot to be accreted (Fabian, 2012).

1.2 Galactic gas reservoir

The gas reservoir *within* a given galaxy can be loosely separated into two components: the interstellar medium (ISM), and the circumgalactic medium (CGM). In this section, I introduce both of these components, and discuss the roles they play in galaxy evolution.

1.2.1 The interstellar medium

The ISM is the gas reservoir within which most of the galactic stellar component resides. The ISM is a multiphase gas reservoir that consists of molecular gas ($T \simeq 20$ K, $n > 10^3$ cm^{-3}), cold neutral warm gas ($T \simeq 100$ K, $n \simeq 20$ cm^{-3}), warm neutral gas ($T \geq 6000$ K, $n \simeq 0.3$ cm^{-3}), warm ionised gas ($T \simeq 8000$ K, $n \simeq 0.3$ cm^{-3}), and hot ionised gas ($T \simeq 10^6$ K, $n \simeq 10^{-3}$ cm^{-3}).

The various phases of the ISM enable us to probe the gas reservoir using a wide range of observations. For example, molecular gas is most commonly observed using molecular transitions in the millimetre/sub-millimetre (vibration and rotation modes) and the infrared. Alternatively, the neutral gas reservoir can be traced in emission/absorption (e.g., Ly$-\alpha$) in the rest frame ultra-violet (UV), and 21-cm emission/absorption at radio wavelengths. The cool and warm ionised gas components are observed in emission (e.g., Hα, metal lines), while the hot ionised gas is observed in X-rays or absorption lines of high ionisation species in the UV. Note that while metals contribute a small fraction of the ISM's mass, they are key to observing and tracing the ISM (e.g., Stark et al., 2015; Berg et al., 2016; Feltre et al., 2018).

1.2.2 The circum-galactic medium

Beyond the ISM, the presence of an extended, yet bound, gas reservoir around galaxies is a fundamental prediction of the current paradigm of structure formation (White & Rees, 1978). This gas reservoir is commonly referred to as the circum-galactic medium (CGM). Extending well beyond the observed galactic stellar component and ISM, the CGM acts as a mediator between the galaxy and the extra galactic gas:

Gas accreted into the halo surrounding the galaxy mixes in the CGM before it settles onto the galaxy, while gas launched from the galaxy may either (1) diffuse and mix into the CGM, (2) cool and settle back onto the galaxy, or (3) leave the halo. Figure 1.1 shows a schematic representing the complex fate of gas within the CGM.

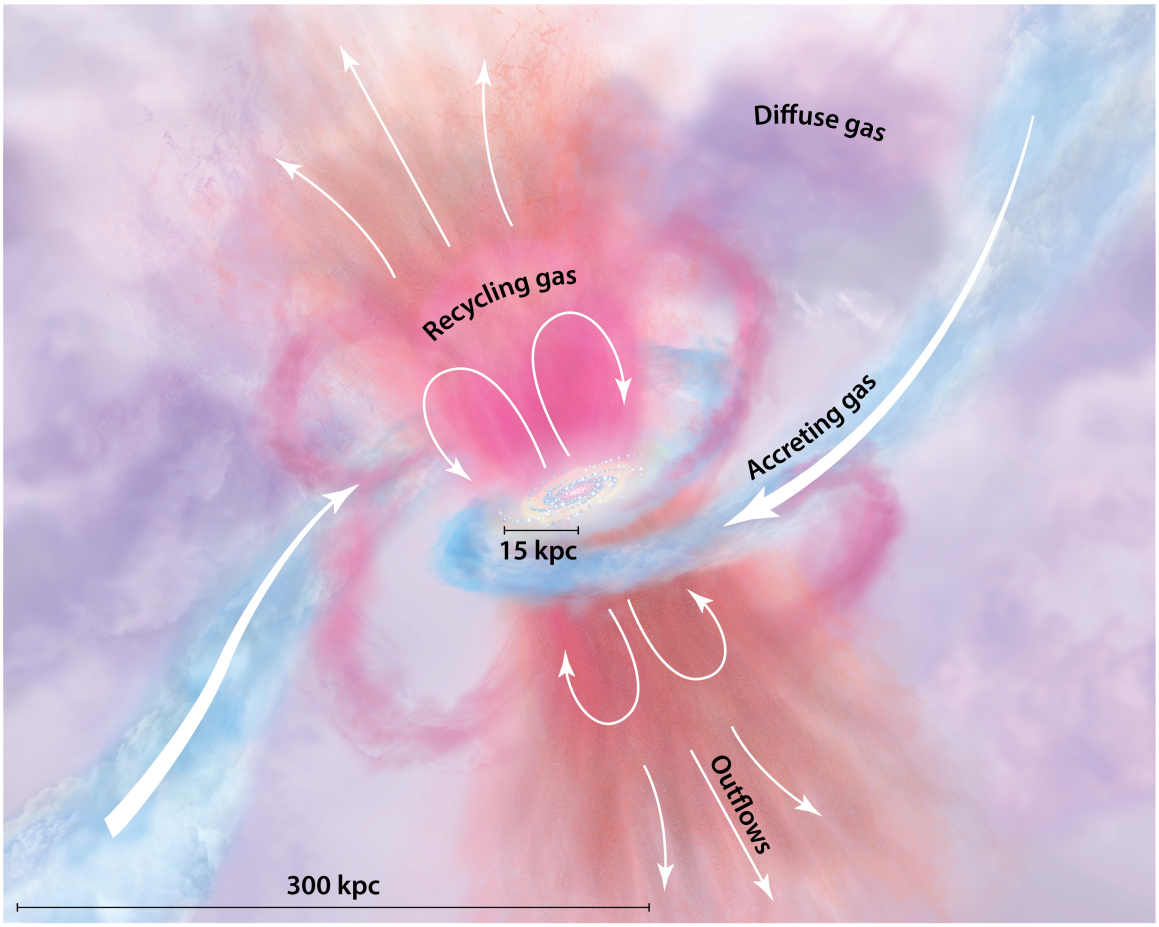

Figure 1.1: A schematic of the CGM courtesy of Tumlinson et al. (2017). The diagram highlights the complexity of processes feeding and affecting the massive gas reservoir. Cold filaments (blue) can feed the galactic ISM from the intergalactic medium. Outflows (pink and orange), previously ejected from the ISM via feedback processes, can mix, recycle, or pass through the CGM thus escaping the galaxy. The purple colours represent the diffuse gas component of the CGM (and its internal structure) which is the fate of gas that remains in the CGM after being introduced through one of the many channels (e.g., accretion, outflows).

Historical consideration

The topic of the CGM has been subject to several re-incarnations in literature discussions. The first proposal of a CGM, formerly known as the *Galactic Corona*, dates to 1956 when Spitzer (1956) proposed a possible diffuse, hot, galactic corona that keeps cooler clumps in pressure confinement. In the late 1960s, Bahcall & Spitzer (1969) proposed that "most of the absorption lines observed in quasi-stellar sources with multiple absorption redshifts are caused by gas in extended halos of normal galaxies". Since the early proposals of Spitzer and Bahcall & Spitzer, the existence of extended galactic gas halos (i.e., Galactic Coronae, CGM) has been borne out by a plethora of observations.

Early studies of the CGM relied on serendipitous absorption in quasar spectra, which was ascribed to foreground galaxies and their respective extended halos (e.g., Bergeron, 1986; Bergeron & Boissé, 1991; Lanzetta et al., 1995; Tripp et al., 2000; Chen et al., 2001). In the past decade, owing to large spectroscopic surveys of galaxies with well-determined physical properties (e.g., Sloan Digital Sky Survey – SDSS), all sky UV surveys (e.g., Galaxy Evolution Explorer – *GALEX*), and the improved sensitivity of UV spectrographs (e.g., Cosmic Origins Spectrograph – COS), CGM studies began to systematically connect gas absorption properties to galaxy properties in statistically meaningful samples (e.g., Cooksey et al., 2010; Prochaska et al., 2011; Tumlinson et al., 2013; Liang & Chen, 2014; Lehner et al., 2015). Contemporary CGM studies have thus demonstrated the ubiquitous nature of the CGM (e.g., Thom et al., 2012; Werk et al., 2013; Bordoloi et al., 2014b; Prochaska et al., 2017). Nonetheless, the observed CGM properties show a strong dependence on some galaxy properties such as stellar mass (Tumlinson et al., 2011; Bordoloi et al., 2014b), colour (Borthakur et al., 2016), black hole activity (Berg et al., 2018), star formation activity (Tumlinson et al., 2011; Borthakur et al., 2013; Heckman et al., 2017; Prochaska et al., 2017), and environment (Pointon et al., 2017; Nielsen et al., 2018).

Physical Picture

Observational surveys imply that the CGM consists of a massive, metal-enriched, and clumpy multi-phase gas reservoir with a declining density profile extending well beyond the virial radius of the host galaxy (e.g., Werk et al., 2013, 2014; Liang & Chen, 2014; Lehner et al., 2014, 2015; Prochaska et al., 2017). The current picture of the CGM invokes a clumpy multi-phase medium where cool/warm ($T \sim 10^{4-5}$K)

and dense gas clumps are embedded within a hot ($T \sim 10^6$K) and diffuse medium (e.g., Heitsch & Putman, 2009; Bordoloi et al., 2017; Armillotta et al., 2017). The clumpy multi-phase nature of the CGM is evident through the distinct observable ionisation states: The cool dense clumps provide a suitable environment where the low ionisation species can survive (e.g., H I, Mg II, Si II, Si III, Si IV, C IV) while the hot diffuse medium hosts the highly ionised species (e.g., O VI, O VII). Additional evidence for a clumpy multi-phase CGM arises from the analysis of quasar absorption line profiles (e.g., Stern et al., 2016; Werk et al., 2016), where gas clumps in the CGM contribute to the total absorption along a given line-of-sight whilst leaving a strong kinematic imprint on the absorption line profiles. The clumpy nature of the CGM gives rise to a complex ionisation structure which is often sensitive to internal galaxy properties; for example, Tumlinson et al. (2011) reports a bimodality in the O VI column densities and covering fractions around star forming and passive galaxies.

Observational surveys targeting the CGM of $L^\star$ galaxies infer a CGM gas mass comparable to the mass of the ISM (e.g., Chen et al., 2010; Tumlinson et al., 2011; Werk et al., 2014; Prochaska et al., 2017), and report a correlation between CGM gas properties and properties of the ISM (Borthakur et al., 2015), suggesting a common evolution for both the ISM and the CGM. Additionally, studies focusing on the metal content of the CGM report a significant metal content (e.g., Werk et al., 2013; Peeples et al., 2014). For example, Peeples et al. (2014) showed that, for $L^\star$ galaxies, a significant fraction of the metal budget resides in the CGM. The CGM's sizeable metal content is evident when examining CGM metallicities, which may extend to super-solar metallicities (Prochaska et al., 2017): $\sim 25\%$ of the sight lines in the COS-Halos survey exhibit metallicities that exceed the solar value.

The Milky Way provides a complementary approach to the large observational surveys that target the CGMs of galaxy populations in a statistical fashion. Surveys of the Milky Way's CGM are often equipped with multi-wavelength observations and a large number of lines of sight (e.g., Putman et al., 2012; Fox et al., 2015; Richter et al., 2017). Similar to other $L^\star$ galaxies, the Milky Way hosts a massive, extended, multi-phase, and structurally/kinematically complex CGM (e.g., Gupta et al., 2012; Putman et al., 2012; Moss et al., 2017; Richter et al., 2017; Werk et al., 2019; Zheng et al., 2019). Observations of the Galactic CGM infer a large covering fraction of gas, thus indicating an extended and massive gas reservoir (Gupta et al., 2012; Richter et al., 2017; Zheng et al., 2019). The Galactic CGM also shows kinematically distinct features in H I (e.g., Moss et al., 2017) and low ionisation species (e.g., Richter et al.,

2017; Werk et al., 2019) along different lines-of-sight, which is indicative of a clumpy, multi-phase medium. Whereas, the high ionisation (i.e. O VI) gas is more uniform on larger scales (Werk et al., 2019).

Numerical simulations of galaxy formation and evolution provide a complementary view to the results from observations. A particular strength of numerical simulations is that they provide an environment to study the evolution of the CGM and the feedback processes shaping its structure, ionisation, and metallicity (e.g., Hummels et al., 2013; Bird et al., 2016; Christensen et al., 2016; Oppenheimer et al., 2016; Nelson et al., 2018b). Simulated CGM properties show many remarkable similarities to those observed. For example, recent cosmological hydrodynamical simulations reproduce the observed extended galactic gas halos with a sizeable, metal-enriched, and multi-phase gas reservoir (e.g., Shen et al., 2013; Stinson et al., 2012; Ford et al., 2013; Nelson et al., 2016; Suresh et al., 2017; Machado et al., 2018; Hani et al., 2019). Additionally, numerical simulations demonstrate the redshift evolution of the CGM and its structure (e.g., Shen et al., 2012; Corlies & Schiminovich, 2016; Ford et al., 2014; Muratov et al., 2015; Christensen et al., 2016; van de Voort et al., 2012). The observed bimodality in the O VI column densities and covering fractions between star forming and quenched galaxies has also been addressed by different numerical simulations (e.g., Suresh et al., 2015; Oppenheimer et al., 2016; Nelson et al., 2018b).

Moulding the CGM

Various numerical works have emphasized the importance of galactic outflows for populating the CGM with metals out to large radii and driving some of the commonly observed CGM properties (e.g., Oppenheimer & Davé, 2006; Hummels et al., 2013; Suresh et al., 2015; Bird et al., 2016; Hani et al., 2018). For example, numerical simulations have demonstrated the vital role of outflows driven by supernova feedback at populating the CGM with metals: Metal-rich winds launched by SNe deposit metals in the CGM, thus giving rise to the high metallicities reported by observations (e.g., Oppenheimer & Davé, 2006; Ford et al., 2014; Hummels et al., 2013; Bird et al., 2016). In addition to being a strong driver of outflows (e.g., Suresh et al., 2015; Nelson et al., 2018b), AGN feedback has a profound effect on the ionisation structure of the CGM (e.g., Hani et al., 2019) through an aggressive radiation field that keeps the CGM out of ionisation equilibrium (e.g. Oppenheimer & Schaye, 2013; Segers et al., 2017; Oppenheimer et al., 2018b,a). Additionally, the CGM is

shaped by small-scale physical processes (e.g., turbulent and conductive mixing) that have significant effects on the CGM's large scale structure; simulations modelling the CGM or clouds of gas at high resolution particularly underline the effects of resolution on the CGM and its neutral gas content in cosmological (e.g., Corlies et al., 2018; Peeples et al., 2019; van de Voort et al., 2019; Suresh et al., 2019) as well as idealised settings (e.g., Scannapieco & Brüggen, 2015; Armillotta et al., 2017; Forbes & Lin, 2018; McCourt et al., 2018; Schneider et al., 2018; Sparre et al., 2019). Furthermore, simulated galaxy interactions stress the long lasting effects an interaction can have on the CGM metal content and temperature/ionisation (e.g., Cox et al., 2006b; Hani et al., 2018).

The framework in which the CGM is driven by feedback processes on a galactic scale (i.e. AGN and SN feedback) is reflected by the ubiquitous observations of outflows and their effects on the CGM kinematics, densities, and ionisation. Observational studies show that vigorous outflows arising from enhanced star formation (e.g., Martin, 2005; Rupke et al., 2005a; Strickland & Heckman, 2009) or AGN activity (e.g., Rupke et al., 2005b; Zschaechner et al., 2016; Woo et al., 2017) can populate the CGM with metals and alter its density structure, thus giving rise to the observed multi-phase absorbers (e.g., Borthakur et al., 2013; Bird et al., 2015; Heckman & Borthakur, 2016; Heckman et al., 2017; Bordoloi et al., 2017). Consequently, starburst galaxies and AGN hosts show different CGM properties when compared to their non-active counterparts (Heckman et al., 2017; Berg et al., 2018). The effects of outflows have also been demonstrated by studies focusing on the CGM where low ionisation species exhibit an azimuthal dependence in disc-dominated galaxies (e.g., Bordoloi et al., 2011; Nielsen et al., 2017). The Milky Way's CGM provides a local illustration of outflows and their influence on the CGM. For example, Fermi Bubbles are the $\gamma-$ray (Su et al., 2010) signature of a biconical outflow originating at the centre of the Galaxy where hot gas sweeps the cool gas into the flow (i.e., Keeney et al., 2006; Zech et al., 2008; Fox et al., 2015). In addition to the effects of galactic feedback, a galaxy's environment drives changes in the CGM structure, for example the CGM of galaxies in group environments exhibits distinct kinematics (Pointon et al., 2017; Nielsen et al., 2018) and covering fractions (e.g., Johnson et al., 2015a; Burchett et al., 2016).

Observing the CGM

Most CGM studies resort to quasar absorption line (QAL) spectroscopy, a method that is sensitive to gas column densities many orders of magnitude lower than what is observable in emission (e.g., Bergeron, 1986; Lanzetta et al., 1995; Peeples et al., 2014; Werk et al., 2014). Figure 1.2 shows a schematic explanation of how QAL surveys study the CGM of foreground galaxies using background quasars. QAL studies of the CGM use multi-phase ions (e.g., H I, Si II, Si III, Si IV, C II, C IV, O II, O VI) that probe gas with a range of temperatures, densities, and origins. A plethora of information can be gained from QAL studies such as the gas density, metallicity, ionisation state, and kinematics.

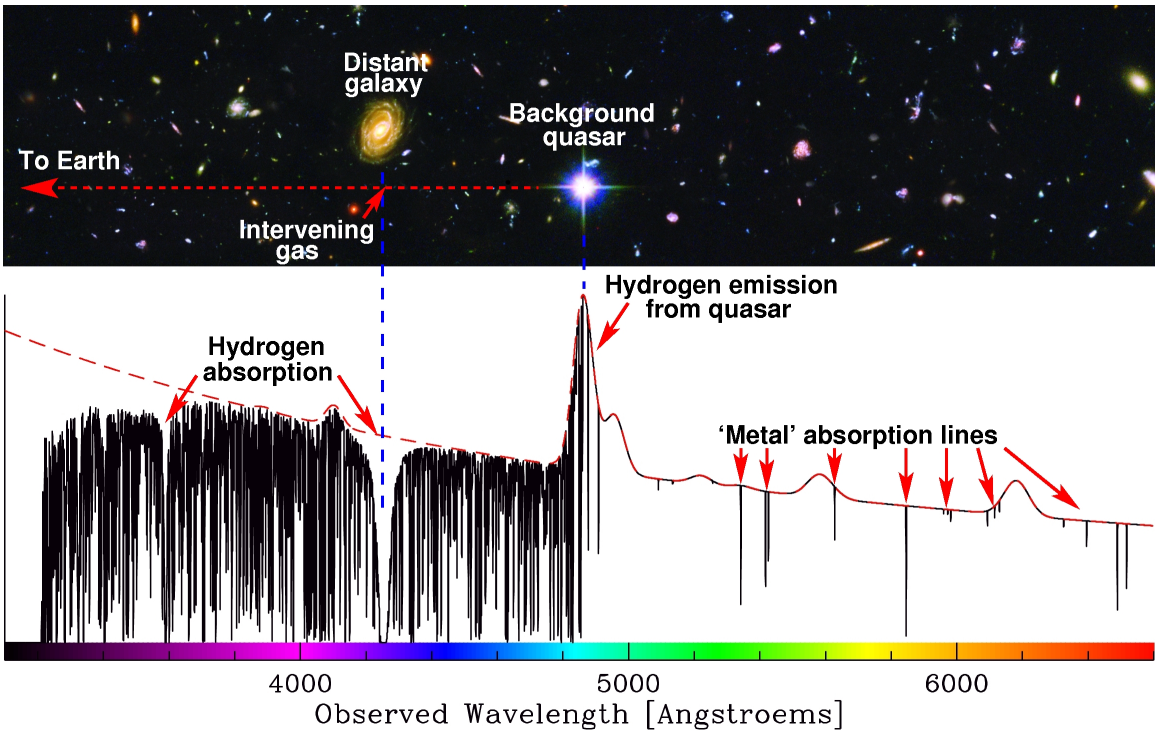

Figure 1.2: A diagram depicting a quasar absorption line system. The light from the quasar is absorbed by gas along the line of site. If the quasar passes through the CGM of a galaxy, the available ions will leave their imprint on the spectrum. This information can then be used to study the CGM composition and kinematics. Figure courtesy of Joe Liske.

The techniques used in QAL studies have been developed over decades by studies targeting gas within a few 10s of kpc from distant galaxies along quasar lines of sight. (e.g. Wolfe, 1986; Wolfe et al., 1995; Lanzetta & Bowen, 1990; Sargent et al.,

1988). For example, Lanzetta & Bowen (1990) studied Mg II absorbers in galaxies at $z < 0.8$ and reported a declining radial metallicity profile. In addition, Sargent et al. (1988) used Mg II absorbers to study the density of absorbers as a function of redshift. These authors report an increase in absorber density up to $z \sim 1$; the absorber density decreases for $z > 2.5$.

Building on previous methodology of QALs, CGM studies started by targeting quasars and looking for serendipitous absorbers in the spectra. The absorbers were then associated with nearby galactic hosts (e.g. Lanzetta et al., 1995; Prochaska et al., 2011). Nonetheless, the CGM field has been revolutionised by contemporary surveys (e.g., Tumlinson et al., 2011; Bordoloi et al., 2014b; Borthakur et al., 2015; Heckman et al., 2017; Berg et al., 2018) using COS on the Hubble Space Telescope (HST). Modern surveys target low redshift galaxy-quasar pairs and study the CGM of the foreground galaxies by searching for absorption at the galaxy's redshift.

Despite their advantages, QAL studies of the CGM suffer from two major limitations. The surveys are often limited to small galaxy-quasar pairs and are therefore subject to small number statistics. Moreover, they often use a single line of sight through each galaxy's CGM. Therefore, QAL studies of the CGM can not properly capture the substructure within a galaxy's CGM.

QAL studies are not the only observational technique used to study the CGM. Other popular techniques to observe the CGM include:

i. **Down the barrel:** Similar to QAL studies, this method relies on a background light-source. The light from the host galaxy (usually a star-forming galaxy) is used as a background source instead of a background quasar (e.g., Martin, 2005; Bordoloi et al., 2011). A major disadvantage of the down-the-barrel approach is the unconstrained distance of absorbers from the host.

ii. **Spectral stacking:** Although this is not a different technique, spectral stacking is a supplementary approach to QAL studies. Thousands of spectra of background objects are stacked to extract faint absorption signatures (e.g., Steidel et al., 2010). This technique heavily utilises reliable/complete redshift catalogues of foreground galaxies. A major disadvantage is the loss of any kinematic or ionisation signatures which are key when studying the CGM.

iii. **Gravitational lensing:** Building on the methodology of QAL spectroscopy, gravitationally lensed quasars (e.g., Chen et al., 2014; Koyamada et al., 2017;

Rudie et al., 2019), or lensed galaxy arcs (e.g., Lopez et al., 2018), are used to study the CGM. This technique is well-suited for studying the internal structure of the CGM. However, the physical CGM properties infered from gravitationally lensed background sources rely heavily on the lensed model which poses a limitation to this technique.

iv. **Imaging:** The CGM exhibits low surface densities, which severely hinder imaging. However, with the advancements in ground-based integral field spectroscopy, observations of the CGM are now possible in emission (Wisotzki et al., 2016; Vanzella et al., 2017; Cantalupo et al., 2019; Martin et al., 2019; Rupke et al., 2019). For example, Rupke et al. (2019) imaged extended bipolar, hourglass-shaped outflows (analogous to the Milky-Way's Fermi Bubbles) in a highly star-forming galaxy using the Keck Cosmic Web Imager (KCWI). The authors infer complex sub-structure from the ionisation of the outflow. Similarly, Martin et al. (2019) reported multiple filaments of inflowing gas feeding star formation at $z \sim 2.2 - 2.7$. Complementary work by Wisotzki et al. (2016), using the Multi-Unit Spectroscopic Explorer (MUSE), demonstrates that Lyα halos at high redshift are ~ 5 times more extended than their low redshift counterparts. Systematic CGM imaging surveys may become possible in the near future, thus unveiling the mysteries surrounding the CGM's structure.On the other hand, the advancement in integral field spectroscopy also facilitated absorption line studies using extended background sources. Using extended galaxies as background light sources, enables direct mapping of the CGM's structure (i.e., distribution and sizes of absorbers; e.g., Cooke & O'Meara, 2015; Péroux et al., 2018).

1.3 Galaxy mergers

In previous sections I made passing references to the effects of galaxy mergers on galaxy growth and the CGM. However, galaxy mergers represent a significant path of transformation for galaxies during which they grow their stellar, gas, and dark matter content, and alter their morphologies (Hernquist, 1989; Barnes & Hernquist, 1996; Cox et al., 2006a, 2008; Di Matteo et al., 2008; Scott et al., 2014). In this section, I will discuss our current understanding of the role that galaxy mergers play in galaxy evolution.

The current paradigm for structure formation (bottom-up scenario) implies that galaxy mergers play a key role in the formation and evolution of observed structure

(e.g. Lacey & Cole, 1993). However, the role of galaxy mergers transcends beyond hierarchical growth of structure. There exists a rich body of theoretical predictions and observational evidence linking mergers to triggering and accelerating gas evolution (i.e., depletion, ejection, accretion, enrichment, cooling/heating), which renders them the ideal laboratories to study galaxy evolution.

Observationally, a profusion of studies report several well accepted observational signatures of galaxy mergers. A dilution in the central metallicity has been reported by observational studies of galaxy pairs (e.g., Kewley et al., 2006; Ellison et al., 2008a; Scudder et al., 2012; Ellison et al., 2018b), and post-mergers (Ellison et al., 2013b; Thorp et al., 2019). Additionally, merging galaxies exhibit enhanced morphological disturbances (Hernquist & Quinn, 1987; Hernández-Toledo et al., 2005; Casteels et al., 2014; Patton et al., 2016), increased atomic and molecular gas fractions (e.g., Ellison et al., 2015, 2018b; Pan et al., 2018; Violino et al., 2018; Dutta et al., 2018, 2019), elevated AGN fractions (e.g., Ellison et al., 2011; Satyapal et al., 2014; Ellison et al., 2019), and enhanced SFRs (e.g., Ellison et al., 2008a, 2013b; Patton et al., 2013; Knapen et al., 2015; Thorp et al., 2019) when compared to their non-interacting counterparts. The effects of galaxy interactions can persist for galaxy pairs with separations as wide as 150 kpc (Scudder et al., 2012; Patton et al., 2013). Coupled with enhanced star formation and AGN activity, feedback processes (e.g., stellar & AGN feedback) play a vital role in the evolution of mergers. Galactic outflows have been linked to enhanced star formation (e.g., Martin, 2005; Rupke et al., 2005a; Strickland & Heckman, 2009) and AGN activity (e.g., Rupke et al., 2005b; Veilleux et al., 2013; Woo et al., 2017).

The observational signatures of galaxy interactions and mergers are complemented by a well-posed theoretical framework. Galaxy interactions trigger strong non-axisymmetric features that create tidal torques capable of driving instabilities in the dynamically cool inter-stellar medium (ISM), thus causing strong inflows of gas into the galactic centre (e.g., Hernquist, 1989; Barnes & Hernquist, 1991; Mihos & Hernquist, 1996; Blumenthal & Barnes, 2018). The gravitational instability-driven gas inflow manifests in simulations as a dilution in central metallicities (e.g., Montuori et al., 2010; Torrey et al., 2012; Moreno et al., 2015; Bustamante et al., 2018), an enhancement in central star formation rates (SFRs; e.g., Cox et al., 2008; Di Matteo et al., 2008; Moreno et al., 2015; Sparre & Springel, 2016), and an increase in accretion onto the central super-massive black hole, thus giving rise to an active galactic nucleus (AGN; e.g., Di Matteo et al., 2005; Hopkins & Quataert, 2010). The associated feedback

processes often manifest (or are implemented) as outflows (e.g., Hayward & Hopkins, 2017; Moreno et al., 2019), which can shape the ISM and even the circum-galactic medium (e.g., Cox et al., 2004; Hani et al., 2018). Additionally, mergers' descendants possess unique morphological disturbances such as shells, ripples, tidal tails, and tidal plumes (e.g., Di Matteo et al., 2007; Lotz et al., 2008, 2010a,b; Pop et al., 2018).

The early Universe was teeming with galaxy interactions and mergers. Several theoretical and observational studies report an anti-correlation between the galaxy merger rate and cosmic time (e.g., Lin et al., 2008; de Ravel et al., 2009; Lotz et al., 2011; López-Sanjuan et al., 2013; Rodriguez-Gomez et al., 2015). The increasing galaxy merger rate with increasing redshift further stresses that galaxy mergers are a major rite of passage in galaxy evolution.

1.4 Numerical simulations of galaxy evolution

In the previous sections, I introduced the myriad of processes driving galaxy evolution, with a particular focus on the galactic gas reservoir and galaxy mergers, the topics on which my thesis focuses. I will use numerical simulations to investigate galaxy mergers and the CGM in the following chapters. The simulations used in this thesis span a variety of resolution, volumes, and physical models.

Numerical simulations provide a controlled environment to experiment and investigate highly complex systems (e.g., atmospheric, economic, and seismic models). In astrophysics, numerical simulations have been extremely useful, when paired with observational studies, to investigate the physical processes at play in various astrophysical environments (e.g., planet formation, star formation, galaxy evolution). One particular strength of astrophysical numerical simulations is making the time domain immediately accessible. Resorting to simulations is important when exploring astrophysical processes that evolve on long timescales.

In this section, I discuss the two types of simulations used in the thesis: (1) large box cosmological hydrodynamical simulations, and (2) zoom-in cosmological hydrodynamical simulations. Note that the distinction I make is based on the simulations' initial conditions and not the numerical methods, computational techniques, or mathematical formalisms.

Before discussing cosmological hydrodynamical simulations, one must first pay tribute to the ancestor simulations which were introduced in the 1970s and early 1980s (e.g., White, 1978; Farouki & Shapiro, 1982): N-body simulations of galaxy evolu-

tion. Following their debut, N-body simulations of galaxies improved significantly in the latter half of the 1980s with the introduction of Tree codes (e.g., Barnes & Hut, 1986; Hernquist, 1987). In later years, hydrodynamics were incorporated in galaxy simulations thus producing progressively more realistic simulations and paving the way for studies of hydrodynamical processes, feedback processes, and galaxy evolution (e.g., Umemura, 1993; Tissera et al., 1997; Springel, 2000; Davé et al., 2002; Stinson et al., 2006; Keller et al., 2014; Moreno et al., 2019). With the introduction of hydrodynamics (and magneto-hydrodynamics) the numerical methods diversified. Currently, many complementary approaches are used to model hydrodynamical processes (e.g., Monaghan, 1992; Stone et al., 2008; Springel, 2011; Bryan et al., 2014; Hopkins, 2014).

The earliest self-consistent N-body hydrodynamical simulations of galaxies and halos were evolved in isolation (e.g., Barnes & Hernquist, 1996). In isolated galaxy simulations, galaxies are initialised following analytical, yet observationally motivated, profiles for stellar, gaseous, and dark matter components. Albeit simplistic, isolated simulations have provided, and continue to provide, a wealth of valuable insight into the importance and impact of galaxy-scale physics (e.g., Stinson et al., 2006; Keller et al., 2014; Marinacci et al., 2019; Shimizu et al., 2019). While isolated simulations offer a controlled environment to study the details of galaxy evolution (feedback processes, secular evolution, mergers and interactions) at substantially high resolution, they are limited in their level of realism. Namely, isolated galaxy simulations are evolved in a non-cosmological environment and therefore lack any interactions with the local environment such as gas accretion. Additionally, galaxies evolved in isolation are typically initialised without a CGM. Even when a gaseous halo is included, the implementation is ad hoc and lacks substructure. Moreover, isolated simulations explore a limited set of galaxy morphologies, and properties such as gas fraction, and orbital geometries in the case of galaxy mergers. Although such limitations allow for a simple deconstruction of the role of various physical processes in galaxy evolution, isolated simulations do not capture the diversity in observed galaxies (e.g., morphology, gas fraction, stellar mass).

Cosmological hydrodynamical simulations provide a more realistic approach to studying galaxy evolution where galaxies are evolved from cosmological initial conditions and include a realistic cosmological environment. Large box cosmological hydrodynamical simulations (e.g., Vogelsberger et al., 2013; Schaye et al., 2015; Davé et al., 2016; Springel et al., 2018; Davé et al., 2019) offer large, diverse, and repre-

sentative galaxy samples, which render them ideal for statistical studies of galaxy formation. However, large-box hydrodynamical simulation sacrifice temporal, spatial, and mass resolution. On the other hand, cosmological zoom-in simulations (e.g., Christensen et al., 2016; Anglés-Alcázar et al., 2014; Ceverino et al., 2014; Hopkins et al., 2014; Wang et al., 2015; Fattahi et al., 2016; Sparre & Springel, 2016; Grand et al., 2017) remedy the lower resolution in their large-box counterpart by (1) focusing on a smaller cosmological volume (while still accounting for the cosmological environment), and (2) implementing stratified resolutions. However, the limited spatial extent of cosmological zoom-in simulation implies a limited galaxy sample (e.g., stellar mass, morphology, gas fraction, interaction orbital geometry). With the advancement of computational technologies and numerical techniques, cosmological simulations of modestly sized boxes are now possible at a resolution comparable to zoom-in simulations (e.g., Illustris–TNG50; Nelson et al., 2019b; Pillepich et al., 2019).

Capitalising on the strength of cosmological zoom-in simulations, a new class of simulations arose with altered resolution criteria targeted at enhancing the resolution in the CGM (e.g., Hummels et al., 2019; Peeples et al., 2019; Suresh et al., 2019; van de Voort et al., 2019). Although these simulations are still considered cosmological zoom-in hydrodynamical simulations, they provide unprecedented resolution in the CGM, which is necessary for studying the multi-phase gas reservoir and its complex structure. These simulations provide a fully cosmological model of the CGM while resolving the interaction boundaries between the different gas phases.

A combination of large-box cosmological simulations and cosmological zoom-in simulations are used in this thesis. The complementary approaches provide valuable high-resolution insight while maintaining a diverse galaxy sample which allows for a statistical investigation of galaxy evolution.

Challenges for simulations of galaxy formation

A major challenge that numerical simulations of galaxy evolution face is the diversity of relevant scales (e.g., spatial, temporal): i.e., the scale problem. Properly modelling galaxy evolution requires simulations to resolve ~ 13 dex in spatial scales, ~ 10 dex in temporal scales, and ~ 4 dex in density. For example, star formation occurs on sub-pc scales while stellar feedback affects the host giant molecular cloud ($\sim 1 - 100$ pc), the interstellar medium ($\sim 1 - 10$ kpc), and the circumgalactic medium ($\sim 10 - 100$ kpc). On the other hand, BHs feed on the gas reservoir in their neighbourhood

($\sim 10^{-5} - 10^{-3}$ pc), yet AGN feedback can impact gas on galactic ($\sim 1 - 100$ kpc) and inter-galactic scales ($\sim$ Mpc). The gas reservoir fuelling star formation and BH accretion includes ISM gas (10^{2-6} cm^{-3}), while the medium impacted by the feedback includes the circumgalactic medium and intracluster medium ($\sim 10^{-3}$ cm^{-3}) in addition to the ISM.

Simultaneously resolving the diversity of scales remains unthinkable with current computational resources. Consequently, the physical processes that affect galaxy evolution often occur on scales smaller than the simulations' resolution. Therefore, one must resort to sub-resolution models. Sub-resolution models represent how small scale physics manifests on the scales resolved by the simulation. For example, star formation, BH accretion, and their corresponding feedback are often modelled using sub-resolution models in most simulations.

Understanding the challenges numerical simulations face is key to understanding numerical simulations: their power, and limitations. One should consider the aforementioned challenges when comparing different simulations, and when comparing the results of numerical simulations to observational results. Moreover, the balance between the strengths, and limitations of various types of numerical simulations, is ultimately what makes them best-suited to investigate different problems. Striking such a balance is one of the motivations behind using a diverse set of simulations in this thesis.

1.5 Thesis Overview

This thesis investigates the massive gas reservoirs surrounding galaxies, galactic star formation, and galaxy mergers. I use numerical simulations paired with observationally motivated analysis methodologies to constrain the properties of the CGM, and quantify the effects of galaxy mergers on star formation, and the gas reservoir.

In Chapter 2, I use a suite of cosmological zoom-in magneto-hydrodynamical simulations to study the CGM of Milky-Way mass galaxies. I demonstrate the remarkable diversity within the CGM of a given galaxy and amongst a mass-controlled sample. I also tie the CGM properties to galactic properties, thus identifying some of the major physical processes that shape the CGM.

Galaxy mergers are considered one of the most influential evolutionary processes in galaxy evolution. They are associated with enhancements in star formation, AGN activity, molecular and neutral gas fractions, and morphological asymmetries. There-

fore, one would expect galaxy mergers to have a strong effect on the CGM. In Chapter 3, I demonstrate the effects of galaxy mergers on the CGM. I showcase a cosmological zoom-in hydrodynamical simulation of a major merger and highlight the effects of merger-induced outflows on the CGM's (1) gas and metal content, (2) size, (3) metallicity, and (4) ionisation.

In the latter part of my thesis, I switch focus to galactic star formation and how it responds to galaxy interactions. Having shown the critical effects galaxy mergers have on the extended CGM in Chapter 3, I then quantify the effects of galaxy mergers on galactic star formation in Chapter 4. I employ a large sample of post-merger galaxies selected from IllustrisTNG (a large-box cosmological magneto-hydrodynamical simulation) to explore the effects of galaxy mergers on galactic star formation, and identify the dependence of SFR enhancement on merger properties.

In the final part of the thesis, I extend my analysis of star formation in post-mergers to resolved scales. First, I demonstrate the existence and robustness of the resolved star forming main sequence (rSFMS) using the FIRE cosmological zoom-in simulations in Chapter 5. I then leverage the existence of resolved galaxy scaling relations in simulations to quantify the effects of galaxy mergers on star formation, and gas metallicities on kpc-scales in Chapter 6.

Chapter 7 concludes the thesis with a summary of the main highlights of my research. I use my results as a stepping-stone to reflect on current challenges in the field, and future prospects for both observational surveys and theoretical studies.

Chapter 2

The diversity of the circum-galactic medium around $z = 0$ Milky Way-mass galaxies

This chapter is published as Hani et al. (2019) .

Abstract

Galaxies are surrounded by massive gas reservoirs (i.e. the circumgalactic medium; CGM) which play a key role in their evolution. The properties of the CGM, which are dependent on a variety of internal and environmental factors, are often inferred from absorption line surveys which rely on a limited number of single lines-of-sight. In this chapter, I present an analysis of 28 galaxy haloes selected from the Auriga project, a cosmological magneto-hydrodynamical zoom-in simulation suite of isolated Milky Way-mass galaxies, to understand the impact of CGM diversity on observational studies. Although the Auriga haloes are selected to populate a narrow range in halo mass, my work demonstrates that the CGM of L* galaxies is extremely diverse: column densities of commonly observed species span $\sim 3-4$ dex and their covering fractions range from ~ 5 to 90 per cent. Despite this diversity, I identify the following correlations: 1) the covering fractions (CF) of hydrogen and metals of the Auriga haloes positively correlate with stellar mass, 2) the CF of H I, C IV, and Si II anticorrelate with active galactic nucleus luminosity due to ionization effects, and 3) the CF of H I, C IV, and Si II positively correlate with galaxy disc fraction due to outflows populating the CGM with cool and dense gas. The Auriga sample demonstrates striking diversity within the CGM of L* galaxies, which poses a challenge for observations reconstructing CGM characteristics from limited samples, and also indicates that long-term merger assembly history and recent star formation are not the dominant sculptors of the CGM.

2.1 Introduction

Whilst the *presence* of a CGM is ubiquitous in galaxies (e.g., Thom et al., 2012; Werk et al., 2013; Bordoloi et al., 2014b; Prochaska et al., 2017), in its details, these galactic gas reservoirs are both complex and sensitive to a number of structural (e.g., total stellar or halo mass, and morphology; Tumlinson et al., 2011; Bordoloi et al., 2014b), internal (e.g., star formation and nuclear activity; Tumlinson et al., 2011; Borthakur et al., 2013; Heckman et al., 2017; Prochaska et al., 2017; Berg et al., 2018) and environmental (e.g., clustering and merging; Pointon et al., 2017; Nielsen et al., 2018) properties. However, many of these properties are inter-related. For example, high mass galaxies tend to have more bulge-dominated morphologies (e.g., Bernardi et al., 2010; Huertas-Company et al., 2013), more massive central super-massive black holes (e.g., Kormendy & Ho, 2013), more frequent AGN activity (e.g., Best et al., 2005; Pimbblet et al., 2013), higher star formation rates for star-forming galaxies (e.g., Brinchmann et al., 2004), and a higher fraction of passive galaxies (e.g., Peng et al., 2010). Empirical studies of the CGM are usually reliant on single lines of sight that can not capture the diversity of the CGM within a given galaxy (see Section 1.2.2). Therefore, numerical simulations can provide a valuable tool to quantify the impact of this diversity and the effects of limited observational samples.

In this chapter, I study the properties of the CGM in a set of simulations designed to yield $z = 0$ Milky Way-mass galaxies (hereafter referred to as L* galaxies). These simulated galaxies therefore all have a consistent end-product – galaxies similar to the Milky Way – but they show significant variation in the rest of their properties, such as morphology (i.e., Grand et al., 2016; Marinacci et al., 2017), SFR and AGN luminosity. The goal of this analysis is therefore two-fold: first to quantify the diversity of line of sight column densities through a given L*-like halo, and second, to study how CGM properties correlate with the host properties and therefore identify the mechanisms responsible for shaping the CGM.

This chapter is structured as follows: In Section 2.2 I describe the numerical model, the halo selection method, and the ionisation analysis. I then present the results of the simulations in Section 2.3 highlighting the major correlations between the host properties and the CGM ionisation and metal content. In Section 2.4 I discuss the implications of the diversity in the CGM on observational survey results. Lastly, Section 2.5 summarises the conclusions of this chapter.

2.2 Methods

The work presented in this chapter aims to understand the processes responsible for shaping the CGM of $z = 0$, L* galaxies. I use cosmological zoom-in simulations which provide a self-consistent cosmological framework to study the CGM while allowing for superior spatial and mass resolutions when compared to large-box cosmological simulations. The simulations are part of the Auriga simulation suite (Grand et al., 2017). The simulated galaxies reproduce several observable properties – such as disc galaxies with appropriate stellar masses, stellar disc sizes, rotation curves, star formation rates, and metallicities (see Grand et al., 2017) – which makes the Auriga suite ideal to study the CGM of L* galaxies in the local universe.

2.2.1 The Auriga simulation suite and halo selection

The Auriga simulation suite consists of 40[1] magneto-hydrodynamical, cosmological zoom-in simulations of L* halos (Milky Way-like in halo mass) in isolated environments. The galaxies are simulated using the quasi-Lagrangian moving-mesh code Arepo (Springel, 2010; Pakmor et al., 2016) with dark matter resolution elements of mass $M_{\rm dm} \sim 3 \times 10^5\,{\rm M}_\odot$, and a gas mass resolution of $M_{\rm gas} \sim 5 \times 10^4\,{\rm M}_\odot$ (i.e. resolution level 4 as defined by Grand et al. (2017)). The Auriga project adopts a ΛCDM cosmology where $\Omega_{\rm m} = 0.307$, $\Omega_{\rm b} = 0.048$, $\Omega_\Lambda = 0.693$, and $H_0 = 67.77\,{\rm km\,s^{-1}\,Mpc^{-1}}$.

The Auriga simulation suite employs a comprehensive galaxy formation model (Grand et al., 2017) which is based on the physical model of the Illustris project (Vogelsberger et al., 2013) and the modifications of Marinacci et al. (2014a). The model is described in detail in Grand et al. (2017). Here, I present a summary of the galaxy formation model which includes:

1. an effective equation of state describing a multi-phase ISM in pressure equilibrium (Springel & Hernquist, 2003),

2. a star formation model and associated stellar feedback in the form of a phenomenological wind model, as well as metal enrichment from asymptotic giant branch (AGB) stars, supernovae (SN) type Ia, and SN II (Vogelsberger et al., 2013; Marinacci et al., 2014a; Grand et al., 2017),

[1] Ten halos have been added to the original 30 since the suite was introduced in Grand et al. (2017)

3. a model accounting for BH seeding, growth, and associated feedback from AGN in radio and quasar modes (Springel et al., 2005a; Vogelsberger et al., 2013; Marinacci et al., 2014a; Grand et al., 2017) using the scaling of Nulsen & Fabian (2000),

4. gas cooling via primordial channels alongside metal-line cooling (Vogelsberger et al., 2013),

5. gas heating from a spatially-uniform, redshift-dependent ultra-violet background (UVB; Faucher-Giguère et al., 2009) and radiation from nearby AGN (Vogelsberger et al., 2013; Grand et al., 2017), and

6. a prescription for magnetic fields (Pakmor & Springel, 2013; Pakmor et al., 2014).

The Auriga model deviates from the Illustris model (Vogelsberger et al., 2013) in two major ways: (1) the Auriga model implements a gentler radio-mode AGN feedback (Marinacci et al., 2014a) where several hot buoyant bubbles are inflated stochastically, and isotropically in the halo (following an inverse square distance profile) each with a fraction of the feedback energy prescribed in Vogelsberger et al. (2013) thus yielding much gentler halo heating, and (2) *isotropic* stellar winds (Grand et al., 2017) are also endowed by a thermal energy budget thus reducing the mass loading (Marinacci et al., 2014a).

In the work presented in this chapter, I follow stringent selection criteria to ensure that the sample only includes galaxies that have had quiet recent merging histories (no mergers with mass ratios greater than 1 : 3 in the past 2 Gyr) and is therefore free of systems in transient stages (i.e. ongoing interactions and post-merger galaxies) that may skew the results. Knowing that recent galaxy interactions can have a noticeable impact on the CGM (Hani et al., 2018), I exclude[2] some of the Auriga halos from my analysis based on:

1. the existence of a neighbouring galaxy more massive than $1/3 \times M_\star$ of the central halo and at a distance $R < 0.4 \times R_{200}$ from the central halo, or

2. the presence of a recent (within the past 2 Gyr) major merger (more major than 1 : 3) based on the merger trees, or

[2]I exclude Auriga halos Au8, Au11, Au21, Au25, Au30, Au$^{\rm x}$2, Au$^{\rm x}$3, Au$^{\rm x}$4, Au$^{\rm x}$5, Au$^{\rm x}$6, Au$^{\rm x}$9, and Au$^{\rm x}$10

3. the existence of prominent signatures (visually inspected) of a recent or ongoing interaction in the stellar or gas profiles (i.e. tidal tails, caustic structures, streams).

My selection criteria yield a sample of 28 Auriga galaxies with quiet recent merger histories. The halos studied in this chapter are all at $z = 0$, and they span a limited range in halo mass[3], $0.5 \leq M_{200}\,[10^{12}\,\mathrm{M}_\odot] \leq 2.0$, and stellar mass, $2.1 \leq M_\star\,[10^{10}\,\mathrm{M}_\odot] \leq 11.7$. The selected halos are actively star forming with star formation rates $1.9 \leq \mathrm{SFR}\,[\mathrm{M}_\odot \cdot \mathrm{yr}^{-1}] \leq 12.4$, and AGN bolometric luminosities $10^{42.1} \leq L_{\mathrm{bol}}\,[\mathrm{erg} \cdot \mathrm{s}^{-1}] \leq 10^{45.5}$. Figure 2.1 provides a summary of the galactic properties of the sample.

Although the complete Auriga suite reproduces a wide range of present-day observables including star formation rates, my selection criteria inadvertently leads to a sub-sample with higher star formation rates. Additionally, the full Auriga suite includes AGN with bolometric luminosities $\geq 41.7\,\mathrm{erg} \cdot \mathrm{s}^{-1}$ consequently causing the sub-sample I selected to have bolometric luminosities $\geq 42.1\,\mathrm{erg} \cdot \mathrm{s}^{-1}$. I note that the star formation rates and AGN luminosities in my sample are higher than comparable observational studies focusing on Milky Way-mass galaxies (e.g., Werk et al., 2012). Other studies with comparably high SFRs or L_{bol} explicitly select their sample to control for the effects of star formation (e.g., Tumlinson et al., 2011), starbursts (i.e., COS-BURST; Heckman et al., 2017) or AGN (i.e., COS-AGN; Berg et al., 2018). One should proceed with caution when quantitatively comparing the results reported here to observational studies of the CGM. The results presented in this chapter investigate the physical processes responsible for shaping the CGM within the Auriga model. Hence, the qualitative correlations are not affected by the high SFR and L_{bol} values.

[3] M_{200} is defined to be the mass inside a sphere in which the mean matter density is 200 times the critical density, $\rho_{\mathrm{crit}} = 3H^2(z)/(8\pi G)$.

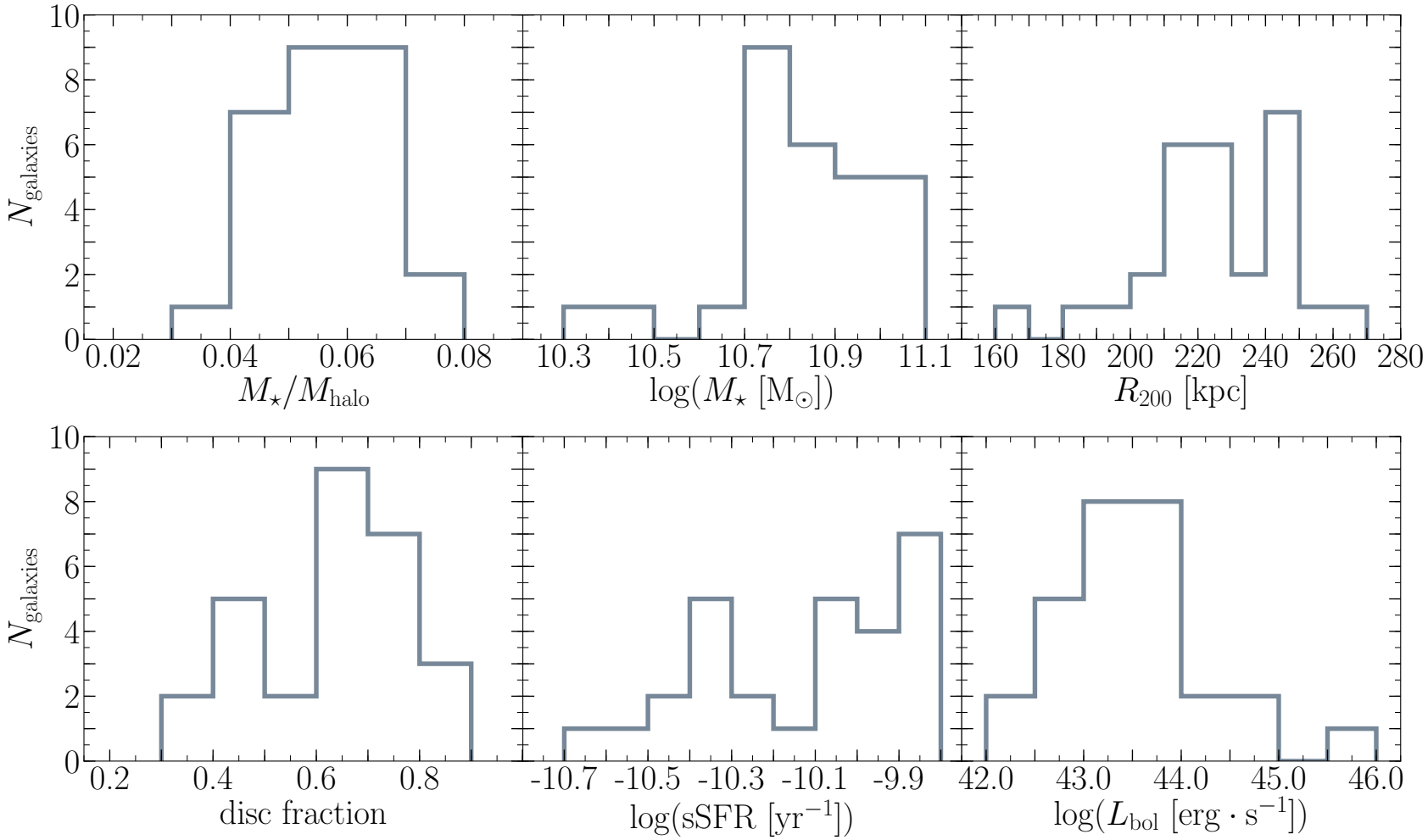

Figure 2.1: A summary of the galaxy properties for the 28 Auriga halos studied in this chapter: Stellar mass to halo mass ratio ($M_\star/M_{\rm halo}$), stellar mass ($M_\star$), virial radius (R_{200}), disc fraction, specific star formation rate (sSFR), and bolometric AGN luminosity ($L_{\rm bol}$).

2.2.2 CGM ionisation

It is particularly interesting to study the ionisation of the CGM as this includes valuable information about the observed temperature and density structure of the gas within. Moreover, predictions of the column densities of particular species facilitate a comparison with observations. In this section, I discuss the details of the ionisation calculations.

I use CLOUDY v13.03 (Ferland et al., 2013a) to calculate the ionisation fractions of metal species under the assumption of ionisation equilibrium for a gas exposed to an external radiation field. Both photoionization and collisional ionisation processes are included in my calculations. I run a grid of CLOUDY simulations which I then interpolate, using multilinear interpolation, to calculate the ionisation fractions of every gas cell. The grid of CLOUDY simulations spans a five-dimensional space of metallicities, temperatures, densities, redshifts, and bolometric AGN intensities summarised in Table 2.1.

Table 2.1: The grid of CLOUDY simulations used to calculate gas ionisation fractions.

	Grid range	Grid increments
$\log(Z\,[Z_\odot])$	$[-4,\,1]$	1.0 dex
$\log(T\,[\mathrm{K}])$	$[1,\,9]$	0.1 dex
$\log(n_\mathrm{H}\,[\mathrm{cm}^{-3}])$	$[-8,\,2]$	0.25 dex
z	$[0,\,1.05]$	0.05
$\log(J_\mathrm{AGN}\,[\mathrm{erg\ s^{-1}\ cm^{-2}}])$	$\{0,\,[-5,\,5]\}$	1.0 dex

I include two radiation fields in the CLOUDY simulations which are consistent with the radiation fields included in the simulations. I employ the publicly available spatially-uniform redshift-dependent UVB of Faucher-Giguère et al. (2009) which accounts for radiation from quasars and star-forming galaxies, although the radiation from quasars dominates the UVB at the redshift of the merger ($z \leq 1$). AGN radiation is also included assuming a universal, time-independent AGN spectral energy distribution (SED) which is scaled with the bolometric AGN intensity (J_AGN) at the position of each gas cell. I adopt the same parametrization used in the simulations (Vogelsberger et al., 2013), such that the AGN SED is given as

$$f^\mathrm{AGN}(\nu) = \nu^{\alpha_\mathrm{UV}} \exp\left(-\frac{h\nu}{kT_\mathrm{BB}} - \frac{0.01\mathrm{Ryd}}{h\nu}\right) + a\nu^{\alpha_\mathrm{X}}, \tag{2.1}$$

where $T_\mathrm{BB} = 10^6$ K, $\alpha_\mathrm{UV} = -0.5$, $\alpha_\mathrm{X} = -1$, and a is defined by the ratio of the X-ray

to the UV component as follows:

$$\frac{f^{\rm AGN}(2\,{\rm keV})}{f^{\rm AGN}(2500\,\text{Å})} = 403.3^{\alpha_{\rm 0X}} \tag{2.2}$$

with $\alpha_{\rm 0X} = -1.4$.

At high densities ($n \geq 10^{-3}$ cm^{-3}), gas can no longer be assumed to be optically thin to ionising radiation and it becomes self-shielding to radiation more energetic than 1 Ryd: At high densities hydrogen absorbs notable fractions of the incident radiation for photon energies ≥ 1 Ryd, therefore attenuating the radiation field. This, in turn, affects the heating and cooling rates of the gas, hence affecting its ionisation. To account for self-shielding I suppress the intensity of the incident radiation field, at energies > 1 Ryd, by the factor given in equation A1 of Rahmati et al. (2013). The values of the parameters in the self-shielding equation are computed by linearly interpolating table A1 of Rahmati et al. (2013). Although self-shielding is not expected to play a significant role in the CGM where the densities are lower than the star formation threshold, it is included in my calculations for completeness especially considering that (i) we expect dense clumps to appear in the CGM due to the tidal effects of the merger and outflows, and (ii) I also calculate the ionisation of the ISM where self-shielding effects become dominant.

I stress some caveats of the ionisation calculations described above. First, CLOUDY is run in single cell mode which assumes that the temperature and densities of the gas are constant. Therefore, I do not resolve any density or thermal substructure in the gas. This is a reasonable assumption given that the CLOUDY calculations are applied below the resolution scale. I also assume a molecule and dust free gas in the CLOUDY simulations because molecules and dust form in molecular clouds at scales well below the resolution limit of my simulations. Moreover, the ionisation balance is calculated for a gas with relative solar abundances. Relative abundance deviations from solar have insignificant effects on the cooling rates of the gas, especially given the large uncertainties associated with metal enrichment (e.g., Wiersma et al., 2009). Therefore, calculating the ionisation balance on an element-by-element basis would introduce an unreasonable computational overhead with limited enhancement in the accuracy of the ionisation calculations. Additionally, the galaxy formation model I use does not include an on-the-fly treatment of non-equilibrium ionisation (e.g., Oppenheimer et al., 2016, 2018a,b); consequently, I assume ionisation equilibrium (collisional and photoionization equilibrium) in all the CLOUDY simulations, which

poses a limitation to the ionisation modelling presented in this dissertation. We revisit the assumption of ionization equilibrium in Section 3.3.3; non-equilibrium effects appear to be negligible in the simulations I present. On the other hand, knowing that star-forming gas is treated with a sub-grid model where the vast majority of the gas is in the form of cold/dense clouds embedded in an ambient hot medium (see Figure 1 of Springel & Hernquist, 2003), I consider star-forming gas to be fully neutral in my post-processing. This does not have any effect on the results of my work as I focus on the CGM, however, one should proceed with caution when extending my analysis to regions where star formation is dominant (i.e. ISM; galactic disc). Lastly, I do not include the stellar radiation component of the host galaxy's SED. This is solely due to the radiation from the stellar component not being included in the galaxy formation model used in the simulations. Therefore, including a stellar radiation component in post-processing would result in an inconsistent treatment of the state of the gas (i.e. underestimating the effect of the radiation field on gas heating). Moreover, Werk et al. (2016) showed that a stellar radiation field is only effective at altering the ionisation of the CGM for extreme SFRs and low impact parameters (see Section 4.3 of Werk et al., 2016).

2.2.3 Tracking CGM properties

In order to analyse the CGM properties of the Auriga halos I measure the covering fractions of four ionic species –i.e., H I, Si II, C IV, O VI– and their parent elements –i.e, H, Si, C, and O– in the CGM. In this work, I am primarily interested in the absorption properties of the CGM (within the virial radius) rather than in the properties of the galactic disc's ISM. In order to avoid the need to explicitly "mask out" the galactic disk, lines-of-sight are drawn parallel to the galactic disc plane, along the disc's minor axis. When viewed edge-on, the galactic disc has a negligible contribution to the CGM properties as measured by the metrics used in this chapter (i.e. covering fraction). For example, only $\sim 0.9\%$ of the lines of sight probe the disc plane assuming the median disc optical radius (23 kpc; see Grand et al. (2017), a conservative disc height of 5 kpc, and the median halo virial radius, 225 kpc. Additionally, viewing the galaxies edge-on highlights the effect of galactic outflows, which form fountain-like features extending out of the disc plane. In order to remove any biases due to recent outflow properties, I ignore lines-of-sight with impact parameters $\leq 0.2R_{200}$. I note that viewing the galaxies edge-on does not have any effect on the correlations presented

in this chapter.

The CGM is examined within a square field of view (FOV) extending out to the virial radius of the central galaxy (R_{200}). Namely, the FOV has a size of $2R_{200} \times 2R_{200}$. See Figure 2.1 for the distribution of virial radii; the median virial radius of the sample $R_{200} = 225\,\mathrm{kpc}$ yields a FOV of $450 \times 450\,\mathrm{kpc}^2$. The normalisation of the FOV to the galaxy's virial radius ensures a consistent comparison between galaxies regardless of galaxy or halo mass. Each FOV is then sampled using 1024^2 uniformly sampled lines-of-sight with a depth of $6R_{200}$ along the line-of-sight. I compute the column densities of hydrogen, metals (i.e. Si, C, O), and ionic species (i.e. H I, Si II, C IV, O VI) along each line-of-sight. Subsequently, covering fractions of each ion/element above a limiting column density threshold are calculated. The over-sampling of the CGM allows me to compute the 'true' covering fraction; see Section 2.4 for a discussion of the effects of under-sampling the CGM.

Knowing that the focus of this chapter is to understand the effects of galaxy evolution on the $z = 0$ CGM, I focus my analysis on the $z = 0$ snapshots. The evolutionary histories are only used when selecting the sample.

2.3 Results

Our current understanding of galaxy evolution draws strong connections between evolutionary processes and their effect on observable galaxy properties. This work aims at understanding the processes which shape the CGM of L* galaxies. Therefore, I focus my analysis on understanding the physical processes driving correlations between the CGM and 'observed' galactic properties of the simulated Auriga galaxies.

2.3.1 The diverse CGM

The Auriga halos studied here are selected to have similar halo mass and recently quiet histories (see Section 2.2.1). However, they nonetheless have a range of SFRs, disc fractions and AGN activity (see Figure 2.1). In this section, I explore the inter-halo and intra-halo diversity of the CGM in the Auriga sample.

Figure 2.2 shows projections of two sample Auriga halos, Au 23 (left panels) and Au 26 (right panels), in hydrogen (top panels), carbon (middle panels) and C IV (bottom panels). The two halos depicted in Figure 2.2 show significant diversity in their CGM structure, column density distributions, and covering fractions of carbon

and C IV. While Au 23 exhibits strong CGM structures (i.e. filaments, clumps), the CGM of Au 26 is smoothly varying which is evident in the C IV projection.

Figures 2.3, 2.5, 2.4, and 2.6 show grouped split violin plots representing the column density distributions of hydrogen/H I, silicon/Si II, carbon/C IV, and oxygen/O VI along lines-of-sight passing through the Auriga halos, respectively. Each split violin represents the line-of-sight column density distribution for an element (left) and its corresponding ion (right). The median of the distribution is marked by a dashed horizontal line, while the dotted lines show the inter-quartile range. Note that the distributions are not commonly normalised and hence should only be used for visual inspection. It is immediately evident that the Auriga halos display stark differences and variations in their CGM column density distributions. The distributions of each halo span several dex in column densities of metals and hydrogen. The differences in the line-of-sight column density distributions are even more pronounced for the ionic species studied in this chapter; the column density distributions of H I, Si II, C IV, and O VI span ~ 5 dex. The wide variation for a given halo is indicative of the complex structure (density, metallicity, temperature) within the CGM. Furthermore, the CGMs of the Auriga halos present striking differences: the distributions differ significantly in their shapes and medians, indicating significant diversity in the CGM properties of the simulated sample. Similar diversity in CGM gas properties along different lines-of-sight is reported in other numerical simulations (e.g., Nelson et al., 2018b; Oppenheimer et al., 2018b; Peeples et al., 2019), and observations of Galactic (e.g., Richter et al., 2017; Werk et al., 2019) and extra-galactic halos (e.g., Ellison et al., 2004; Lopez et al., 2007; Tumlinson et al., 2011; Prochaska et al., 2017).

Figure 2.7 shows the distributions of covering fractions of commonly observed ionic species (bottom panels) and their parent elements (top panels) at representative column densities. The column density thresholds are chosen such that the median cumulative density profile of all the Auriga halos has a covering fraction of 50%. Note that the choice of column density threshold does not affect the qualitative conclusions presented in this chapter. The covering fractions of all elements and ions vary by about an order of magnitude revealing vast differences in the CGM structure and content. While some CGMs are rich in dense absorbers –reflected by the high covering fractions of H I, Si II, C IV, and O VI, and their parent species– other CGMs are dominated by comparatively diffuse gas –therefore, exhibiting low covering fractions: $< 10\%$ for H I, Si II, C IV, and O VI, and $< 20\%$ their parent species. The aforementioned diversity in the covering fractions of elements and ions is driven by

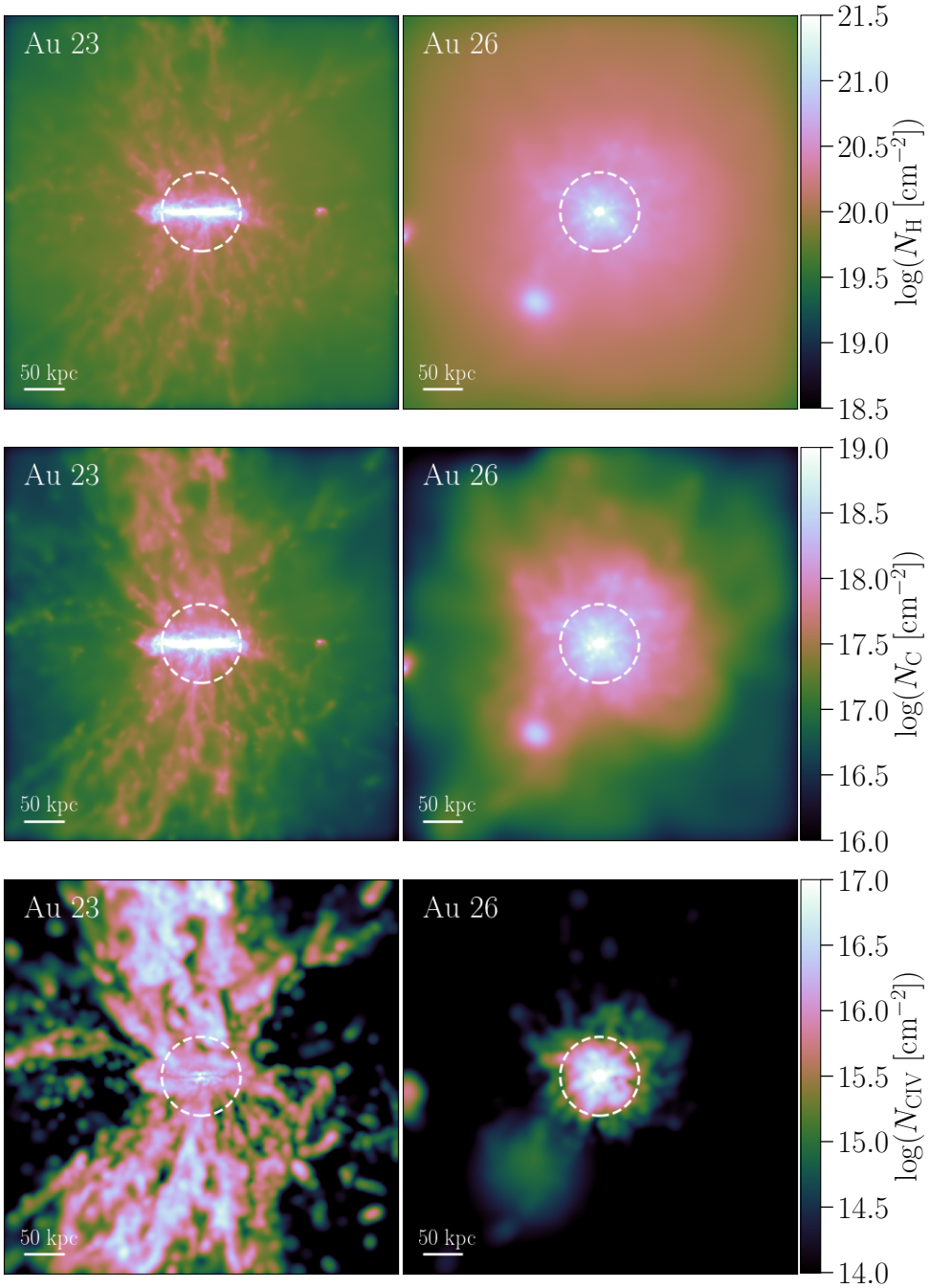

Figure 2.2: Projections ($2R_{200} \times 2R_{200}$) of hydrogen (top), carbon (middle) and C IV (bottom) for Au 23 (left) and Au 26 (right). The two halos show significant differences in their covering fractions of C IV as well as their CGM structure. While Au 26 shows a smooth CGM, the CGM of Au 23 is rich in filaments and clumps. Additionally, the signature of conical outflows is evident in Au 23.

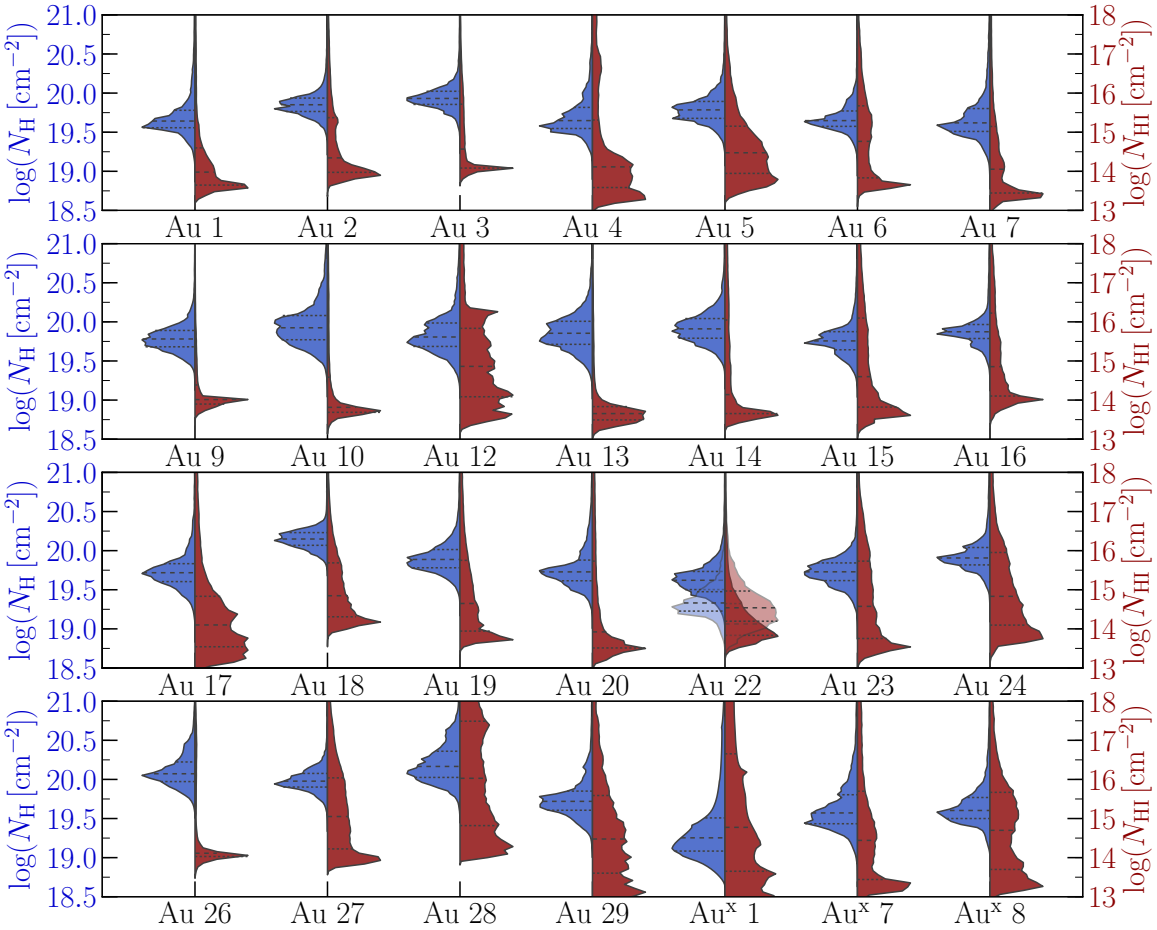

Figure 2.3: A grouped split violin plot representing the column density distributions of hydrogen (blue, left) and H I (red, right) along lines-of-sight through the 28 Auriga halos. The dashed lines indicate the median column density of each distribution while the inter-quartile range is indicated by the dotted lines. The transparent violin plot represents the re-run of Au 22 with no AGN feedback (i.e. Au 22-NOAGN). The diversity in the CGM of each halo is evident by the column density distributions which extend over several decades in column density. Additionally, the diversity in CGM properties within the Auriga sample is evident by the vast differences between the halos in the shapes and medians of the distributions.

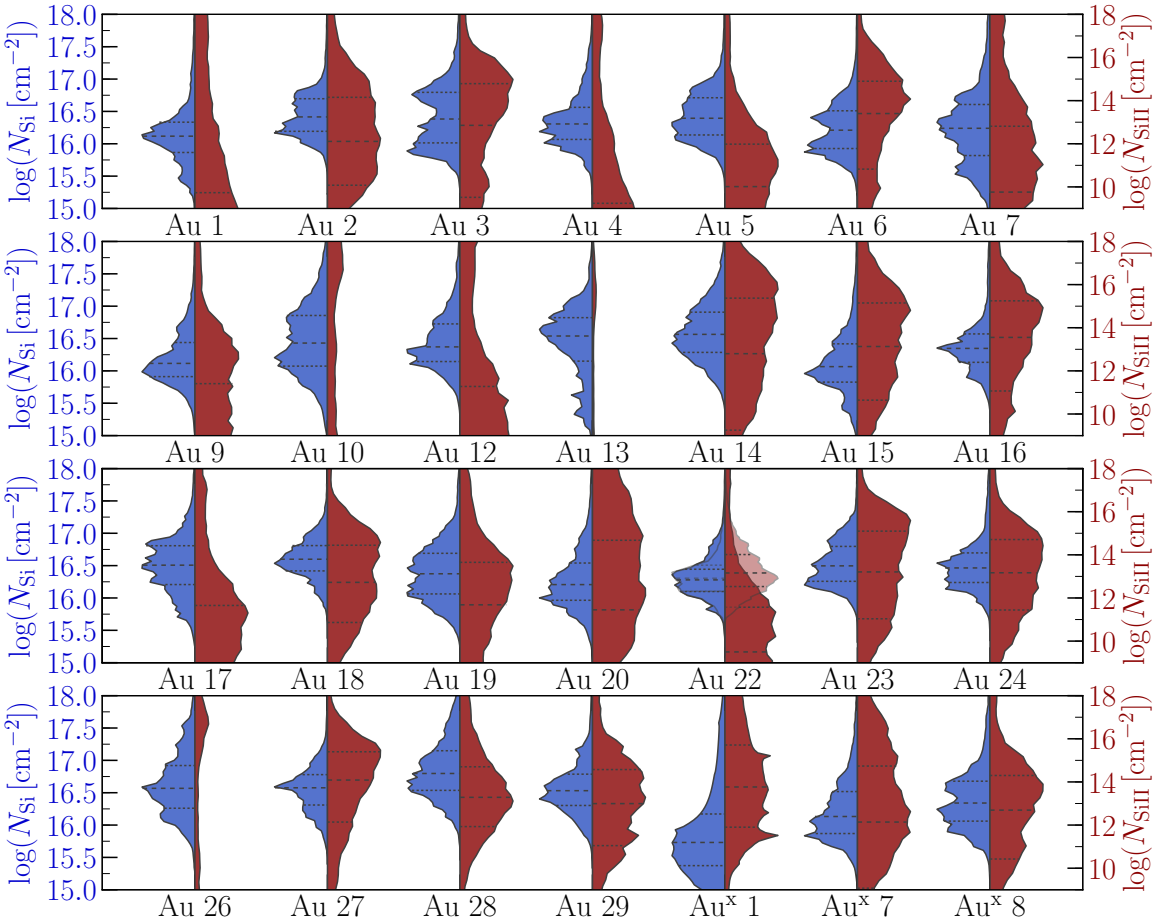

Figure 2.4: A grouped split violin plot representing the column density distributions of silicon (blue, left) and Si II (red, right) along lines-of-sight through the 28 Auriga halos.

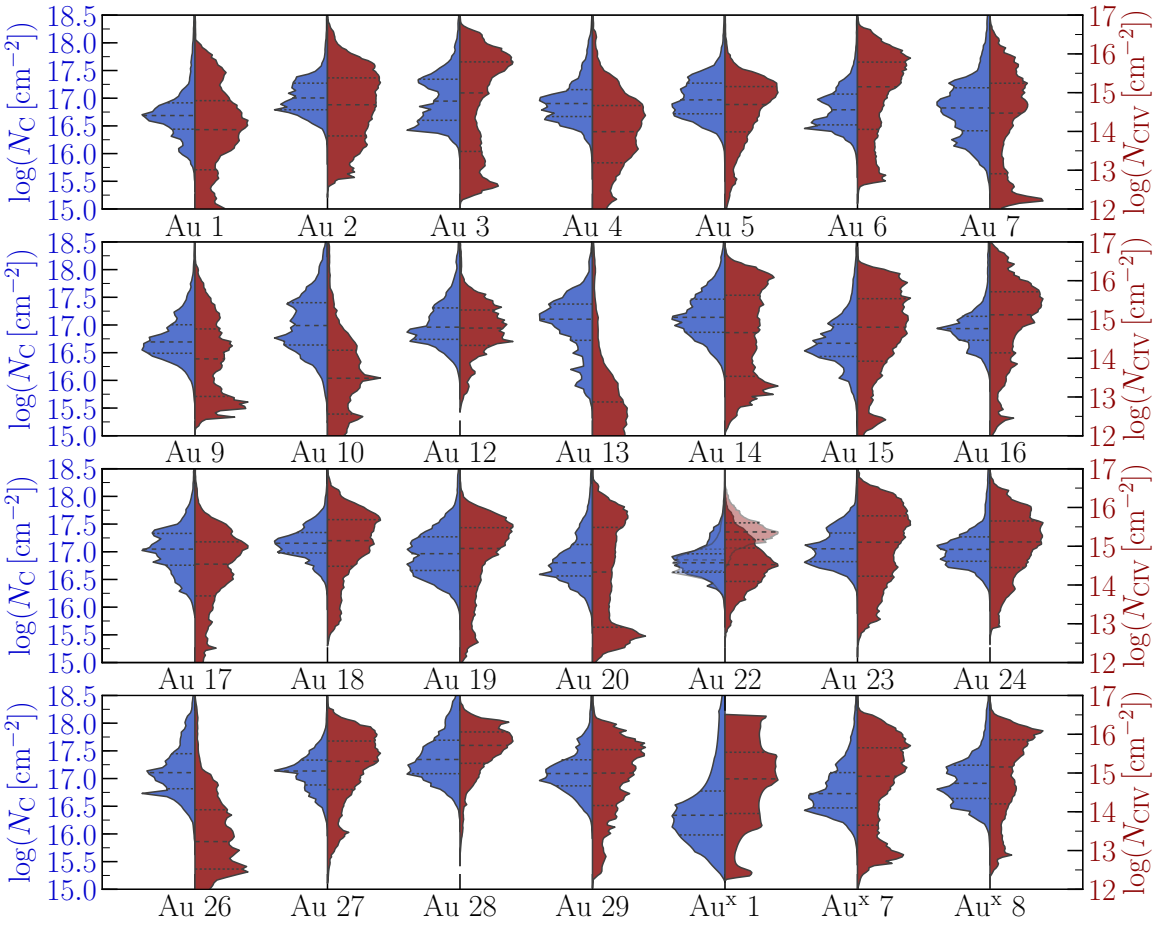

Figure 2.5: A grouped split violin plot representing the column density distributions of carbon (blue, left) and C IV (red, right) along lines-of-sight through the 28 Auriga halos.

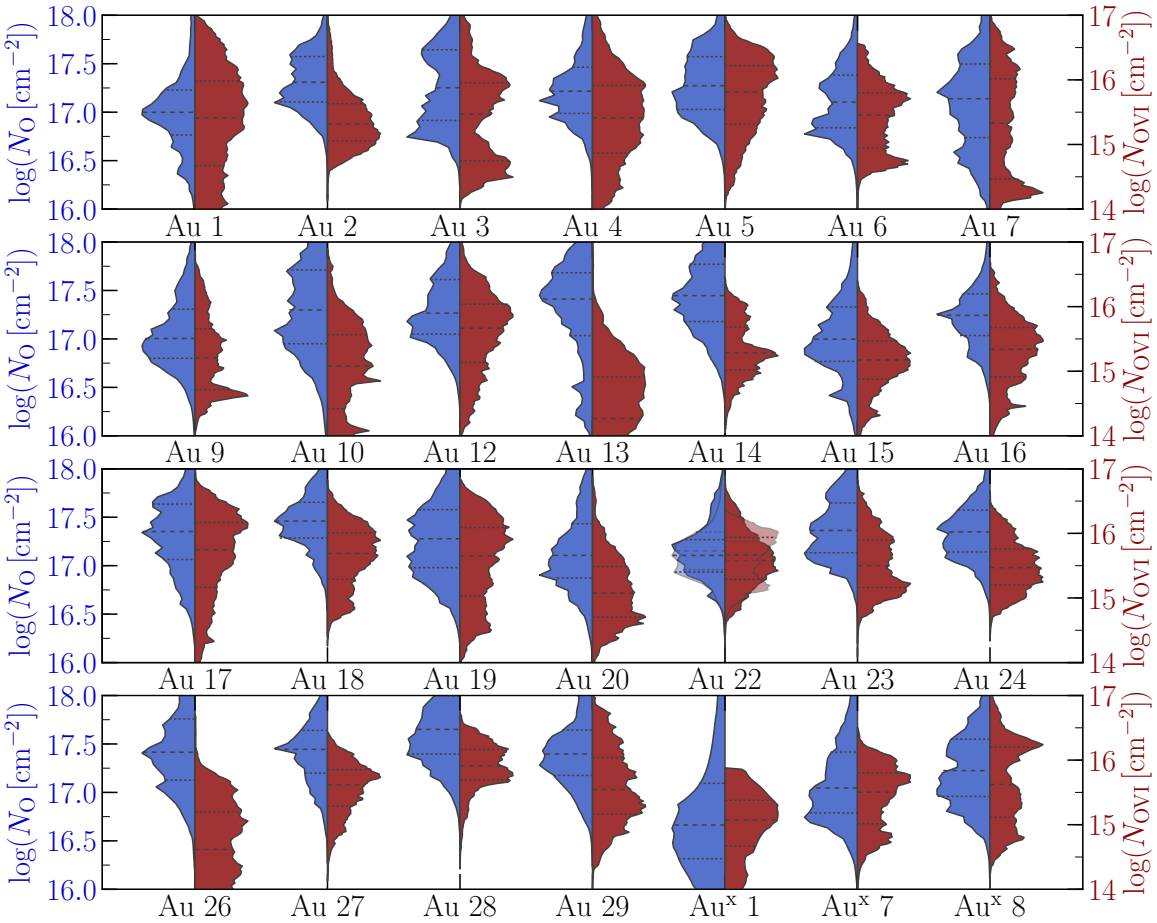

Figure 2.6: A grouped split violin plot representing the column density distributions of oxygen (blue, left) and O VI (red, right) along lines-of-sight through the 28 Auriga halos.

fundamental differences in the CGM structure and column densities.

I note that the column densities of O VI are higher than those inferred from observations (e.g., COS-Halos; Tumlinson et al., 2011; Werk et al., 2016) and even from other simulations with remarkably similar physics models (i.e., Illustris-TNG; Nelson et al., 2018b). The Auriga halos studied in this chapter have active AGN (see Figure 2.1), which is not the case in most observational studies. The local AGN radiation field (which is ignored in Nelson et al. (2018b)) drives the high O VI column densities in my model (equivalently the Si II column densities are slightly lower than the observed column densities in L* CGMs). As shown in Section 3.3.3, AGN radiation (modelled in a similar fashion) can be a significant contributor to the ionisation in the CGM.

Figures 2.3, 2.4, 2.5, 2.6, and 2.7 therefore show that although the sub-sample of the Auriga halos used in this study was selected to span a limited range in halo mass, similar isolated environments (see Section 2.2.1), and quiet recent merger histories, their CGM reveals significant differences in densities and structure. The CGM of the Auriga halos bears evidence of their distinct evolution. In the following sections I will highlight some of the major culprits in shaping the CGM of L* galaxies.

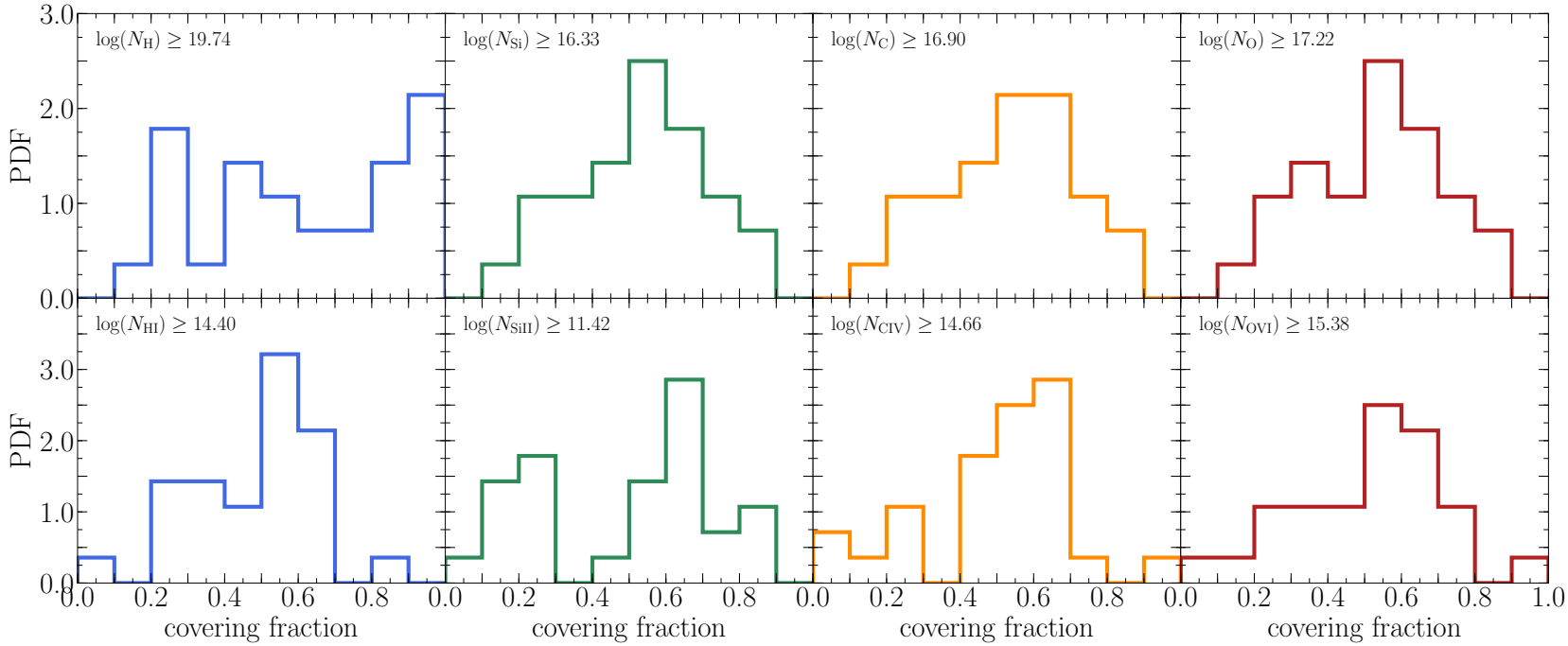

Figure 2.7: The covering fractions of absorbers in the CGM of Auriga galaxies. The top panels show the distributions of hydrogen, silicon, carbon, and oxygen absorbers (left to right) with column densities higher than $10^{19.74}\,\mathrm{cm}^{-2}$, $10^{16.33}\,\mathrm{cm}^{-2}$, $10^{16.9}\,\mathrm{cm}^{-2}$, and $10^{17.22}\,\mathrm{cm}^{-2}$, respectively. The bottom panels show the distributions of H I, S II, C IV, and O VI absorbers (left to right) with column densities higher than $10^{14.40}\,\mathrm{cm}^{-2}$, $10^{11.42}\,\mathrm{cm}^{-2}$, $10^{14.66}\,\mathrm{cm}^{-2}$, and $10^{15.38}\,\mathrm{cm}^{-2}$, respectively. Despite the Auriga halos exhibiting remarkable similarities in their galactic (i.e. halo mass) and environmental properties (i.e. isolated at $z = 0$, quiet recent merger histories) their CGM gas shows significant differences.

2.3.2 The effect of the host galaxy's stellar mass

The galaxy mass metallicity relation (MZR) is considered to be one of the most fundamental observed galaxy characteristics: a galaxy's stellar mass correlates (with little intrinsic scatter) with the gas-phase metallicity (Tremonti et al., 2004), and the relationship is even tighter when additional variables are considered, such as SFR, size and gas content (e.g. Ellison et al., 2008b; Bothwell et al., 2016). The MZR (modulo normalisation and temporal evolution) holds for a range of galaxy masses (extending from dwarf to $L^{\star}$ galaxies; e.g., Lee et al., 2006; Zahid et al., 2012), over a range of redshifts (extending from the local universe up to $z \sim 2$; e.g., Zahid et al., 2011; Steidel et al., 2014; Sanders et al., 2015), and at a multitude of scales where recent integral field unit surveys demonstrate the existence of the MZR on kpc scales (i.e. Sánchez et al., 2013; Barrera-Ballesteros et al., 2017; Sánchez et al., 2017; Ellison et al., 2018a). The presence and robustness of the MZR highlights the influence of stellar feedback and self-regulation on the galactic gas reservoir, and particularly the importance of the associated star formation and metallicity variation timescales in defining the MZR (e.g., Torrey et al., 2018).

The presence of a MZR on the galactic scale motivates investigating if such a correlation exists at larger scale viz. the CGM. Stellar feedback is responsible for enriching the ISM via AGB stars, SNe Ia, and SNe II. The enriched gas can then be launched out of the ISM by SN-driven stellar winds or BH-driven winds (see Veilleux et al., 2005; Oppenheimer & Davé, 2006; Muratov et al., 2017). Therefore, given that the processes responsible for the MZR on galactic scale also enrich the CGM, one may expect the CGM metal content to increase with stellar mass. Note that there need not be a MZR in the CGM; unlike the ISM there is no local process regulating the gas content and metal injection in the CGM. Knowing that metal injection in the CGM is driven by feedback processes which depend on ISM properties (i.e. SFR, AGN activity) one may infer that the integrated metal injection into the CGM (i.e. metal mass, or metal covering fraction) scales with galaxy stellar mass which does not necessarily imply an increase in metallicity. Scannapieco et al. (2006) demonstrated that a positive scaling between the CGM metal mass and the galaxy stellar mass is a natural outcome of SN feedback.

Figure 2.8 shows the dependence of covering fraction for ionic species (bottom panels) and their parent elements (top panels) in the CGM on the host galaxy's stellar mass. The positive correlation of the covering fractions of hydrogen, carbon, and

oxygen with stellar mass is suggestive of the effect of stellar feedback and galactic outflows on enriching the CGM with metals which correspond to galaxy growth. As the galaxy's mass increases, the CGM is increasingly enriched with metals (due to outflows, accretion) which manifests in the increase in the column densities and covering fractions of metals with stellar mass shown in Figure 2.8. Unlike the elements, the corresponding ionic species do not show a dependence on stellar mass. The abundance of a given ionic species is driven by the density and temperature structure of the gas as well as the ionising field. The density and temperature of CGM gas do not immediately scale with stellar mass. Additionally, the incident radiation field (UVB and AGN) is independent of stellar mass in the limited mass range studied in this chapter. Note that the only ion that shows a possible shallow correlation with stellar mass is O VI which is thought to be driven by the halo's virial temperature (e.g. Suresh et al., 2017). To properly demonstrate the dependence of ionic species on stellar/halo mass one would require a wider range of halo mass than I have achieved in this analysis (e.g., see Bordoloi et al., 2018; Oppenheimer et al., 2016). I stress that the normalisation and slope of the trends depend on the column density threshold used when calculating the covering fraction; nonetheless, the correlation of the element covering fraction with stellar mass holds for all column densities.

The positive correlation of oxygen covering fraction with stellar mass is broadly consistent with other theoretical work. For example, Machado et al. (2018) demonstrated a positive correlation between the mass of oxygen in the CGM and stellar mass over ~ 2 decades in stellar mass. A similar dependence of the column densities of oxygen and O VI on halo mass were also reported by Oppenheimer et al. (2016). Additionally, the results presented in this chapter agree with the predictions of SN feedback in Scannapieco et al. (2006). Although the correlation of the CGM's oxygen content with the galaxy's stellar mass may seem at odds with current observations (i.e. Tumlinson et al., 2011), computing oxygen mass in observations suffers from various assumptions involved in the ionisation corrections.

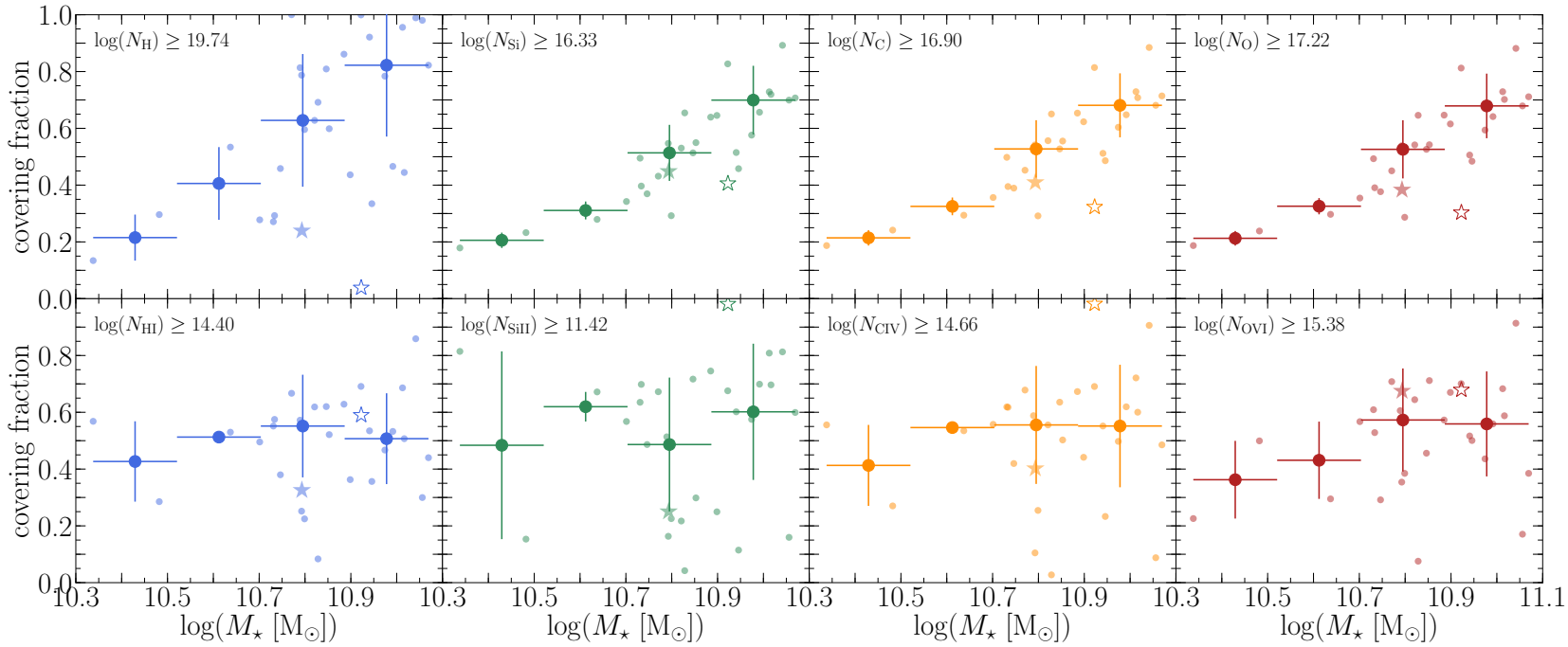

Figure 2.8: The effect of the host galaxy's stellar mass on the CGM gas. The small circles and diamonds show the covering fractions for individual halos. The large circles represent the median covering fractions in stellar mass bins while the error bars show the bin width and 1σ variations in covering fraction. The filled and empty stars represent Au 22 and the re-run of Au 22 with no AGN feedback (i.e. Au 22-NOAGN), respectively. The covering fractions of hydrogen, silicon, carbon, and oxygen (top panels) correlate positively with the host galaxy's stellar mass. As the galaxy's mass increases (via star formation or mergers) the CGM is enriched with more metals leading to an enhanced covering fraction. It is worth noting that such an enhancement does not necessarily imply an enhancement in the covering fractions of commonly observed ions as the CGM ionisation is dependent on gas density, temperature, and the radiation field. In fact, the covering fractions of H I, Si II, C IV, and O VI (bottom panels) show no correlation with stellar mass.

2.3.3 The effects of galaxy morphology

Section 2.3.2 demonstrates the effect of galaxy growth (i.e. mergers, accretion, star formation) on the CGM metal content where the metals created by stellar feedback are transported into the CGM by galactic outflows driven by SNe II or AGN. The physical properties of the outflow depend on the environments from which they are launched and the medium through which they propagate. For example, a wind launched in a dense medium will shock and halt its flow well before reaching the CGM. On the other hand, a wind launched in a thin disc will likely escape the disc vertically into a low density environment, where it can retain the clumpy nature that may sustain low ionisation species. Although the decoupling of winds in the simulation reduces the aforementioned effect (Vogelsberger et al., 2013, and references therein), the density profile of the medium through which the wind propagates in a disc-like galaxy exhibits a sharper gradient than its counterpart in bulge-dominated galaxies. Therefore, one may still expect to see an effect of galaxy morphology on the ionisation of the CGM.

Figure 2.9 shows the covering fractions of hydrogen, silicon, carbon, oxygen, H I, Si II, C IV, and O VI for different galaxy disc fractions. The disc fraction (i.e. D/T) is calculated following the assumption of Abadi et al. (2003) that the bulge component has zero net rotation hence the bulge mass is twice the mass of the counter rotating component while the disc accounts for everything else[4]. The covering fractions of H I, Si II and C IV positively correlate with the disc fraction whilst O VI (typically tracing hot diffuse gas) shows no correlation with the disc fraction. On the other hand, there appears to be no correlation between the covering fractions of hydrogen, silicon, carbon, or oxygen and the disc fraction which suggests that outflows originating in galaxies with higher disc fraction are more likely to sustain a dense nature (e.g. filamentary, clumpy) where low ionisation species can survive. Moreover, examining the gas phase in edge-on projections of the galaxies reveals a visual correlation between the filamentary and clumpy structure of the CGM (above the disc plane) and the disc fraction. Figure 2.2 highlights the vivid filamentary/clumpy structure in the CGM of Au 23 (D/T = 0.63) while the structure in the CGM of Au 26 ($D/T = 0.46$) is less pronounced. Succinctly, outflows originating in disc-dominated galaxies remain filamentary (see left panels in Figure 2.2) and can host low ionisation species after they reach the CGM. Therefore, the CGM of disc-dominated galaxies shows a higher

[4]Note that the results presented in this chapter are independent of the formalism by which the disc fraction is calculated: i.e. using disc fractions inferred from Gaussian mixture models of dynamical variables shows similar results.

covering fraction of low ionisation species when compared to bulge-dominated galaxies (all else being similar). Additionally, the enhanced structure in the CGM along the disc angular momentum axis is consistent with observations (e.g. Bordoloi et al., 2011; Kacprzak et al., 2012). For example, the observed strong azimuthal dependence of Mg II absorption in inclined disc-dominated galaxies (i.e. Bordoloi et al., 2011; Kacprzak et al., 2012) is often attributed to galactic outflows (e.g. Bordoloi et al., 2014a). The filamentary outflow structures in disc-dominated galaxies sustain higher densities and can therefore preferentially host low ionisation species. However, the results presented in this chapter are in tension with the observational results of Kacprzak et al. (2015). The Auriga galaxies show no significant azimuthal dependence of O VI absorption. O VI probes the diffuse ionised gas in the CGM which, broadly speaking, shows a smooth profile. It is worth noting that this tension could be artificially induced by the simulation's resolution in the CGM, or the lack of shielding of AGN radiation by intervening gas. The AGN radiation field intensity is computed at the location of a gas cell only considering its distance from the source ($J_{\rm AGN} \propto r^{-2}$) which could possibly over ionise the gas in the disc plane which would normally experience the highest levels of shielding.

I note that although I draw lines-of-sight along the disc's minor axis the results presented here (i.e. dependence of covering fractions on morphology) hold for any viewing angle (even face-on projections of the galaxies).

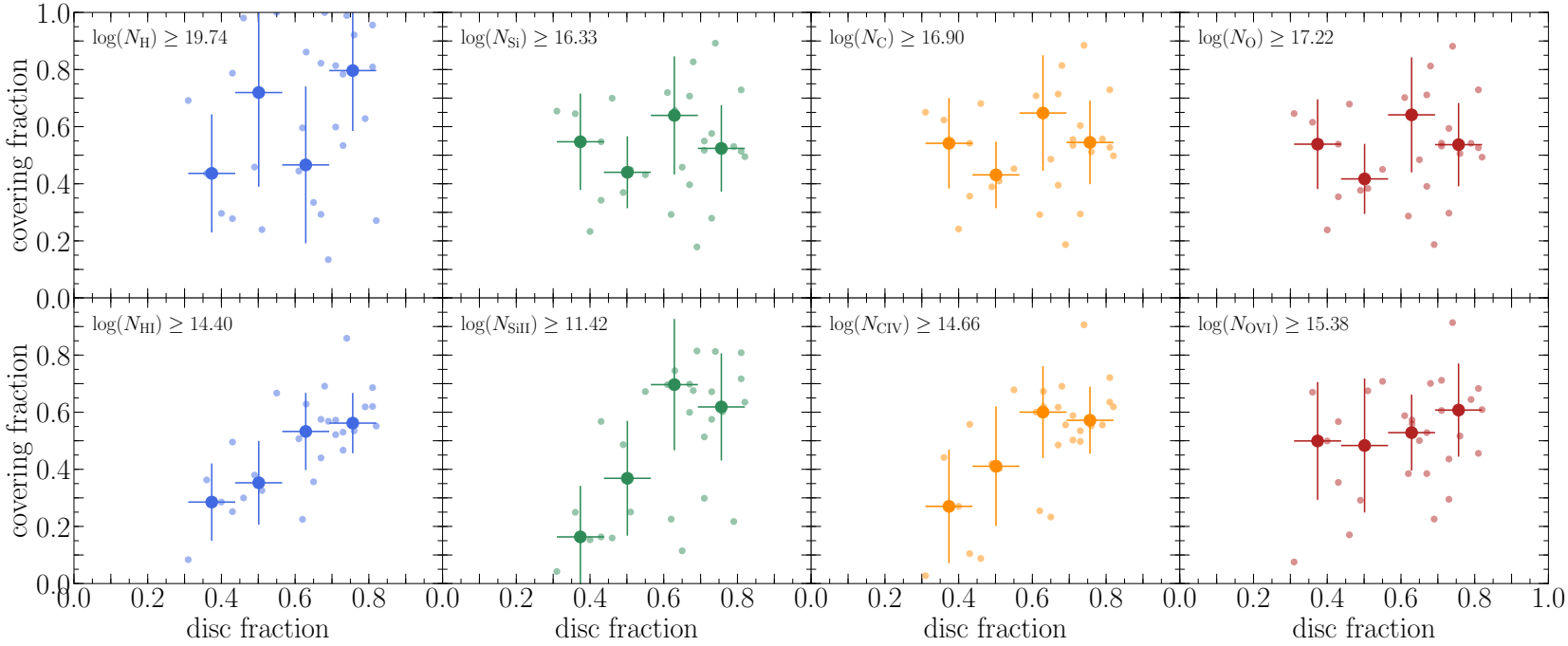

Figure 2.9: The covering fractions of commonly observed ions, H I, Si II, C IV, and O VI (bottom panels), and their parent species (top panels) along lines of sight parallel to the galaxy's disc correlate positively with the disc fraction. The small circles show the covering fractions in individual halos while the large solid circles show the median covering fraction in D/T bins. Outflows driven by stellar feedback and AGN transport gas into the CGM with densities which can sustain low ionisation species. A disc-dominated morphology facilitates the ability for clumpy outflows to travel into the CGM without being destroyed near the galaxy. This yields a higher abundance of clumpy clouds in the CGM outside the disc plane therefore increasing the covering fractions shown here.

2.3.4 The effects of recent star formation

Sections 2.3.2 stresses the effect of galaxy growth on the covering fraction of hydrogen and metals in the CGM. A galaxy's stellar mass reflects its integrated history of star formation, accretion, and mergers. In this section I investigate the effect of recent star formation on the extended CGM.

Star formation and the associated stellar feedback (i.e. SN feedback) are major drivers of strong galactic outflows (e.g., Martin, 2005; Rupke et al., 2005a; Strickland & Heckman, 2009) which are often thought to contribute to the observed multi-phase, metal rich CGM. In fact, a correlation between CGM properties and star formation have been reported by various studies (e.g., Tumlinson et al., 2011; Prochaska et al., 2017). Additionally, studies investigating the CGM of starburst galaxies (e.g., Borthakur et al., 2013; Heckman et al., 2017) suggest that the effect of starburst-driven winds (within $\sim$ 200 Myr) can be observed out to $\sim$ 200 kpc. Although none of the Auriga galaxies studied here are considered starburst galaxies, I explore the effect of recent star formation of the CGM. Figure 2.10 shows the dependence of the covering fractions of H I, Si II, C IV, and O VI, and their parent species on the 10 Myr averaged specific star formation rate ($sSFR$). I use the $sSFR$ to account for the correlations shown in Section 2.3.2. The covering fractions of the elements and ions examined in this chapter show no dependence on the recent star formation history of the galaxies. The lack of correlation between the covering fractions and $sSFR$ also holds when using the 500 Myr averaged $sSFR$.

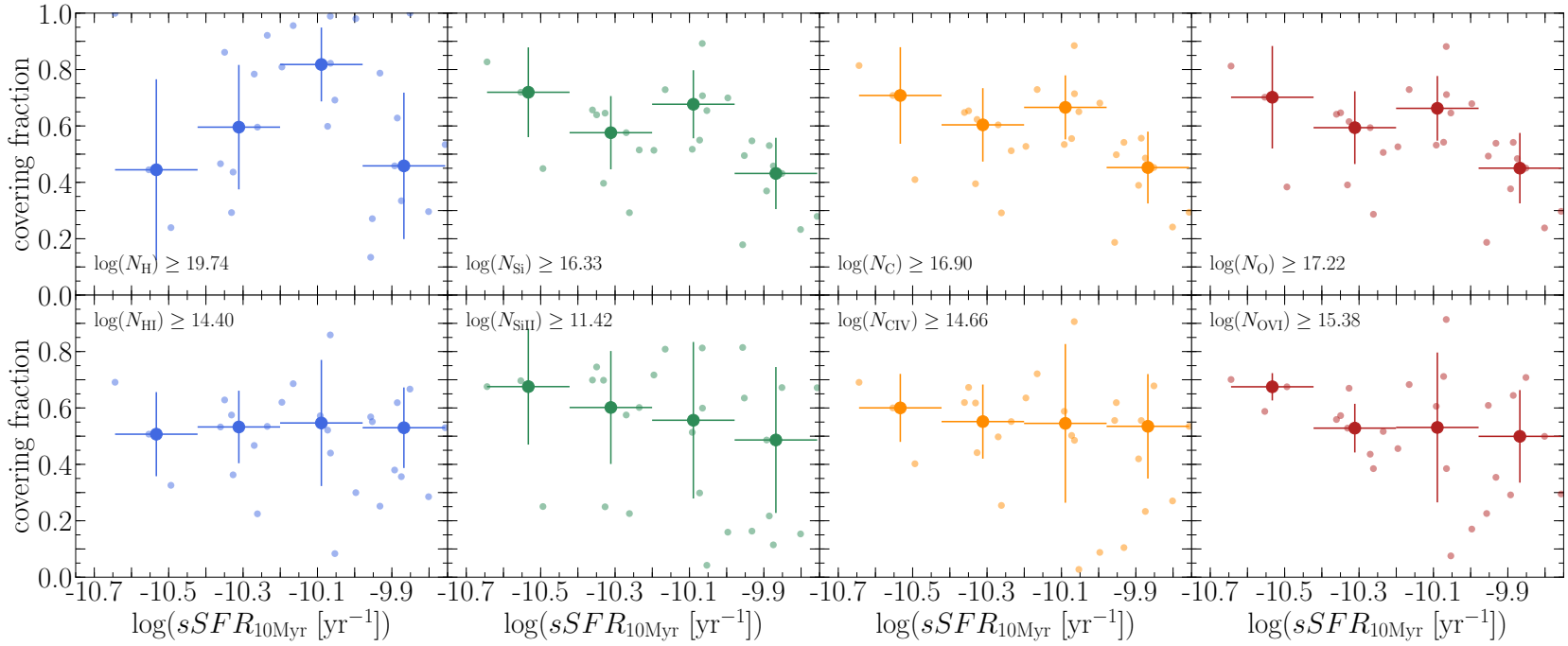

Figure 2.10: The covering fractions of commonly observed ions, H I, Si II, C IV, and O VI (bottom panels), and their parent species (top panels) along lines of sight parallel to the galaxy's disc show no correlation the 10 Myr averaged specific star formation rate. The small circles show the covering fractions in individual halos while the large solid circles show the median covering fraction in SFR bins.

2.3.5 The effect of the central engine

Super-massive BHs residing at the centres of galaxies are thought to play a major role in galaxy evolution. Variations in galaxy and halo properties are often attributed to feedback from AGN in the form of radio jets (Fabian, 2012), AGN driven winds (e.g., Rupke et al., 2005b; Vogelsberger et al., 2013; Woo et al., 2017), or a strong radiation field originating from accretion discs surrounding central super-massive BHs (e.g., Segers et al., 2017; Oppenheimer et al., 2018a,b). Berg et al. (2018) show that AGN hosts show an enhancement in low ionisation species (e.g. H I, Si II, Si III) in their CGM at large radii, hence suggesting that the enhancement might be caused by accretion or the remnants of a previous activity (e.g. AGN episode, starburst). In this section I investigate the effects of AGN feedback on the CGM of L* galaxies.

The AGN radiation field

The accretion disc surrounding central BHs provides a strong radiation field which can have a significant effect on gas ionisation. Oppenheimer et al. (2018a) demonstrate that an AGN can keep the CGM ionised for timescales that significantly exceed the AGN lifetime, leading to proximity fossil zones. Additionally, Oppenheimer et al. (2018a,b) used hydrodynamical simulations with non-equilibrium ionisation to demonstrate the importance of AGN radiation when reproducing the observed O VI covering fractions. Moreover, using an AGN model identical to the one implemented in this chapter, I show the strong effect of the AGN on the ionisation state of the CGM in Section 3.3.3.

Figure 2.11 shows the covering fractions of hydrogen, carbon, oxygen, H I, C IV, and O VI as a function of the AGN bolometric luminosity in the Auriga halos. As the AGN luminosity increases the ionisation of the CGM increases due to the aggressive AGN radiation field. The increase in CGM ionisation manifests as a decrease in the covering fractions of the ionic species studied in this chapter. For AGN luminosities $L_{\rm bol} \gtrsim 10^{44.75}$erg/s, the CGM densities become insufficient for any of the ionisation species studied here (i.e., H I, Si II, C IV, and even O VI) to survive in significant quantities. This effect is even more drastic for the low ionic metal species (i.e., ionSiii where the covering fractions decline drastically at lower AGN luminosities ($L_{\rm bol} \gtrsim 10^{43.7}$erg/s).

I caution the reader that the ionisation calculations were performed in post-processing assuming ionisation equilibrium which poses a limitation for the analysis

presented here. Various works have highlighted the importance of considering non-equilibrium effects in the CGM especially in the presence of a stochastically varying AGN (i.e. Oppenheimer & Schaye, 2013; Oppenheimer et al., 2018a,b). Segers et al. (2017) stress that metals in the CGM may be out of ionisation equilibrium in the presence of a fluctuating radiation field (i.e. AGN) even at large radii (i.e. $2 \times R_{200}$). Non-equilibrium ionisation effects are particularly important when the timescales on which the AGN varies are comparable to the recombination time-scales of the ions of interest $\sim$ 20 Myr (i.e. H I, Si II, C IV, O VI). In the simulations I present, the AGN variability timescales are of order 45 Myr (calculated using the power spectral density) which well exceeds the recombination timescales. Moreover, there is no evidence for a proximity zone fossil in the simulations I present which is expected with the long AGN variation timescales (i.e. Oppenheimer et al., 2018a). Therefore, although the assumption of ionisation equilibrium is a potential limitation of this analysis non-equilibrium effects appear to be negligible in the simulations I present.

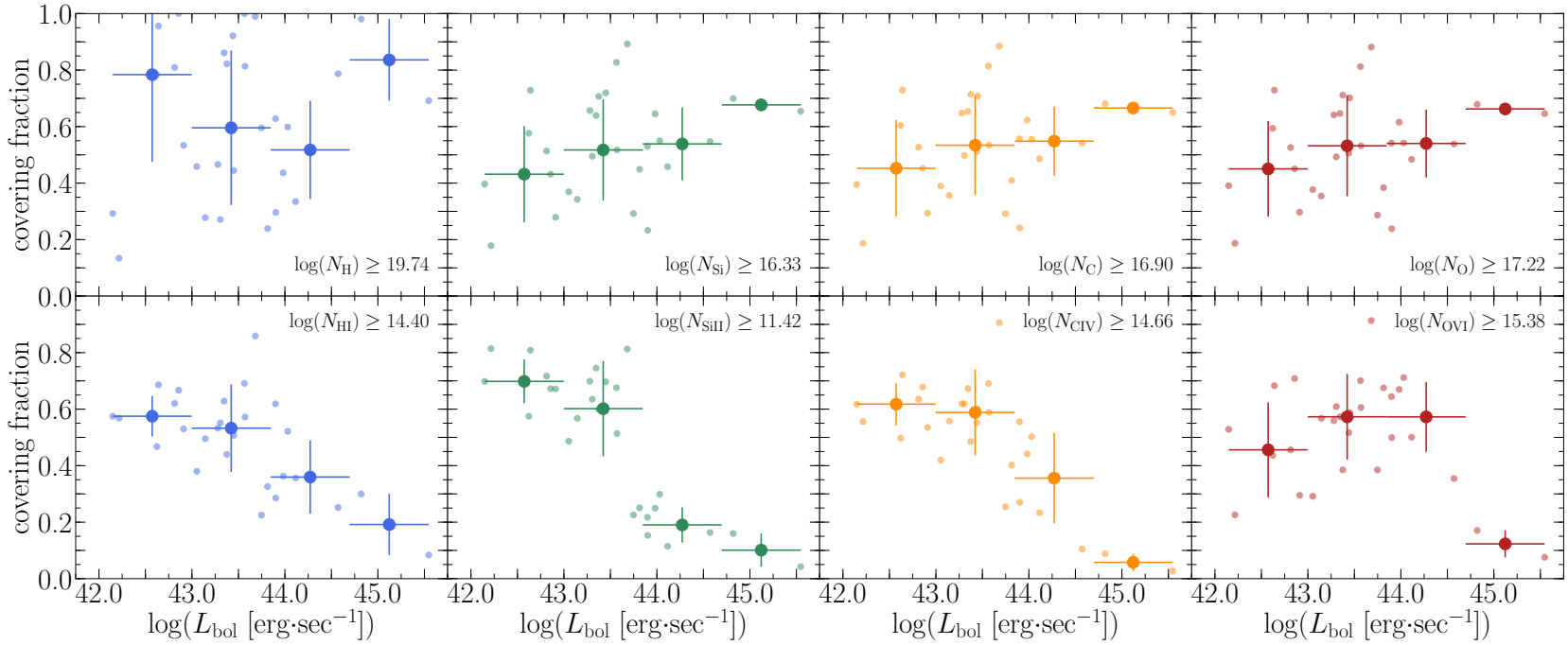

Figure 2.11: The effect of the AGN on the CGM ionisation is evident in the Auriga model. The covering fractions of H I, Si II, C IV, and O VI (bottom panels) and their parent species (top panels) are shown as a function of the AGN bolometric luminosity. The small circles show the covering fractions of individual Auriga halos while the large circles show the median covering fractions in bins of $L_{\rm bol}$ and the error bars show bin sizes and 1σ variations in binned covering fractions. The AGN's radiation field is a significant source of ionisation which drives a decrease in the covering fractions of commonly observed ions.

AGN driven feedback

AGN feedback is often introduced in simulations of galaxy evolution to regulate star formation, quench massive galaxies, and reproduce the high-mass tail of the galaxy mass function and the cosmic star formation history (e.g., Bower et al., 2006; Puchwein & Springel, 2013; Taylor & Kobayashi, 2014). However, AGN feedback has also been shown to have a noticeable impact on the CGM by effectively launching gas into and outside of the CGM (Grand et al., 2017) and creating a hot galactic halo by thermally heating the CGM (Bogdán et al., 2015).

The physical model used in this chapter includes AGN feedback in both quasar and radio mode. The quasar mode isotropically deposits thermal energy into the BH's neighbouring gas cells, while the radio mode exerts mechanical feedback by isotropically and gently inflating hot buoyant bubbles in the halo. For further description of the AGN feedback model see Section 2.2, Vogelsberger et al. (2013), Marinacci et al. (2014a), and Grand et al. (2017). In order to better understand the effect of AGN feedback on the CGM I use a re-run of Au 22 which excludes feedback from the AGN (hereafter Au 22-NOAGN; Grand et al., 2017). The re-run simulates Au 22 with no changes until redshift $z = 1$, after which AGN feedback is eliminated while accretion on to the BH continues. Therefore, differences between Au 22 and Au 22-NOAGN can be attributed to AGN feedback.

AGN feedback reduces the central star formation and therefore produces a smaller bulge component. In the absence of AGN feedback, the galaxy grows a more prominent bulge component, thus decreasing the disc fraction (i.e., Grand et al., 2017). Globally, the galaxy increases its stellar mass from $10^{10.79}\,\mathrm{M}_\odot$ to $10^{10.93}\,\mathrm{M}_\odot$. The increased star formation is driven by gas condensation from the CGM onto the central galaxy. In the presence of AGN feedback, the halo gas is too hot and unable to cool and form stars. As a result, the halo is hotter and more populated with gas. At $z = 0$, the bolometric AGN luminosities are $10^{43.81}\,\mathrm{erg}\cdot\mathrm{s}^{-1}$ and $10^{40.05}\,\mathrm{erg}\cdot\mathrm{s}^{-1}$ for Au 22 and Au 22-NOAGN[5] respectively. For a comprehensive discussion of the effect of the AGN on the galactic properties (briefly discussed above) see Section 4.3 and Figure 17 in Grand et al. (2017).

Returning to Figures 2.3, 2.5, and 2.6, which show the column density distributions of lines-of-sight through the Auriga halos, the column density distributions of lines-of-sight through Au 22-NOAGN are shown as the transparent distributions. The

[5]Note that although AGN feedback is eliminated, accretion onto the black hole is permitted.

halo with no AGN feedback (Au 22-NOAGN) shows significant differences in its hydrogen column density distribution compared to its AGN counterpart (Au 22) where Au 22 shows a shift towards higher hydrogen column densities. AGN feedback stifles accretion and condensation from the CGM onto the galaxy therefore yielding a richer and hotter gas halo and lower galaxy stellar masses. Regardless of the lower hydrogen column densities in Au 22-NOAGN, the halo exhibits higher H I column densities owing to the lower halo AGN luminosity. Unlike hydrogen, the metal column density distributions of Au 22 and Au 22-NOAGN are remarkably similar. Nonetheless, the two halos differ strongly in their ionisation: Au 22-NOAGN has its C IV distribution shifted to significantly higher column densities while the O VI column density distributions remain unchanged. The increased abundance of C IV in Au 22-NOAGN is driven by the lower AGN luminosity (note that the radiation field powered by the AGN aggressively ionises the CGM beyond C IV). However, the presence of O VI in the halo is primarily driven by the halo virial temperature at low AGN bolometric luminosities, where ionisation is independent of the AGN. Knowing that Au 22 and Au 22-NOAGN reside in halos with similar halo mass, their O VI column density distributions are similar.

Comparing Au 22 and Au 22-AGN provides a constraint on the effect of AGN feedback on the properties of a halo. While understanding the effects of AGN feedback through direct comparison of Au 22 and Au 22-NOAGN is key, a further comparison is warranted in the framework of the analysis presented here. Figure 2.8 highlights Au 22 and Au 22-NOAGN by the filled and clear star symbols. Although Au 22-NOAGN's CGM displays similar metal column density distributions to its AGN counterpart, it remains severely under-populated with metals compared to halos with similar stellar mass. Au 22-NOAGN is displaced by $\sim 3\sigma$ from the correlation between metal covering fraction and stellar mass. Moreover, the CGM of Au 22-NOAGN is severely under-populated with hydrogen. The stark differences between the CGM of Au 22-NOAGN and the CGMs of halos with similar stellar mass (i.e. stellar mass matched control) emphasise the key role AGN feedback plays in controlling accretion onto the galaxy, ionizing the CGM, and populating the CGM with metals.

2.3.6 The effects of galaxy assembly

Galaxy mergers are thought to play a key role in galaxy assembly and evolution. In Section 1.3, I introduce some of the observational and theoretical works that paint a

solid picture of the importance of galaxy mergers. Understanding the extent of the effects of galaxy mergers on the CGM requires a comprehensive study: for example, one must first understand the impact of basic merger properties such as the merger mass ratio, merger geometry, and galaxy gas fractions before properly comprehending the effect of complex integrated merger histories. Nonetheless, one can still evaluate the relative importance of mergers (compared to other processes) in building and shaping the CGM of galaxies in the local universe by investigating the strength of the correlation between a galaxy's CGM properties and merger history. Note that although I explicitly remove interacting systems and recent post-mergers from my analysis (Section 2.2.1), I can still investigate the effect of the integrated merger history (*not recent mergers*) on the CGM properties. The most recent major merger (mass ratio $> 1:3$) in my sample happened at $t_{\rm lookback} \sim 2.3\,{\rm Gyr}$, and the most recent minor merger (mass ratio $> 1:10$) happened at $t_{\rm lookback} \sim 2.1\,{\rm Gyr}$. In this chapter I quantify the merger history by computing the stellar mass fraction accreted since $z = 2$ (ex-situ stellar mass fraction) as described by Gómez et al. (2017) and Monachesi et al. (2019). Although this metric has no way of distinguishing between the details of the merger histories it gives a broad brush understanding of the importance of mergers in shaping the CGM of galaxies.

Figure 2.12 shows the dependence of the covering fraction of hydrogen, silicon, carbon, oxygen, H I, Si II, C IV, and O VI on the galaxies' merger history (ex-situ stellar mass fraction). The lack of correlation between CGM properties (covering fraction) and the merger history (ex-situ stellar mass fraction) hints to other processes being at least as dominant as a galaxy's merger history (in the absence of a recent merger) in shaping the CGM. It is, however, worth noting that the galaxies which show the lowest covering fractions have not had a merger more major than $1:10$ since $z = 2$. Nonetheless, not all galaxies with quiet merger histories exhibit low metal covering fractions in their CGM. In Chapter 3, I will revisit the effects of galaxy assembly on the CGM by analysing the properties of the CGM during a major merger.

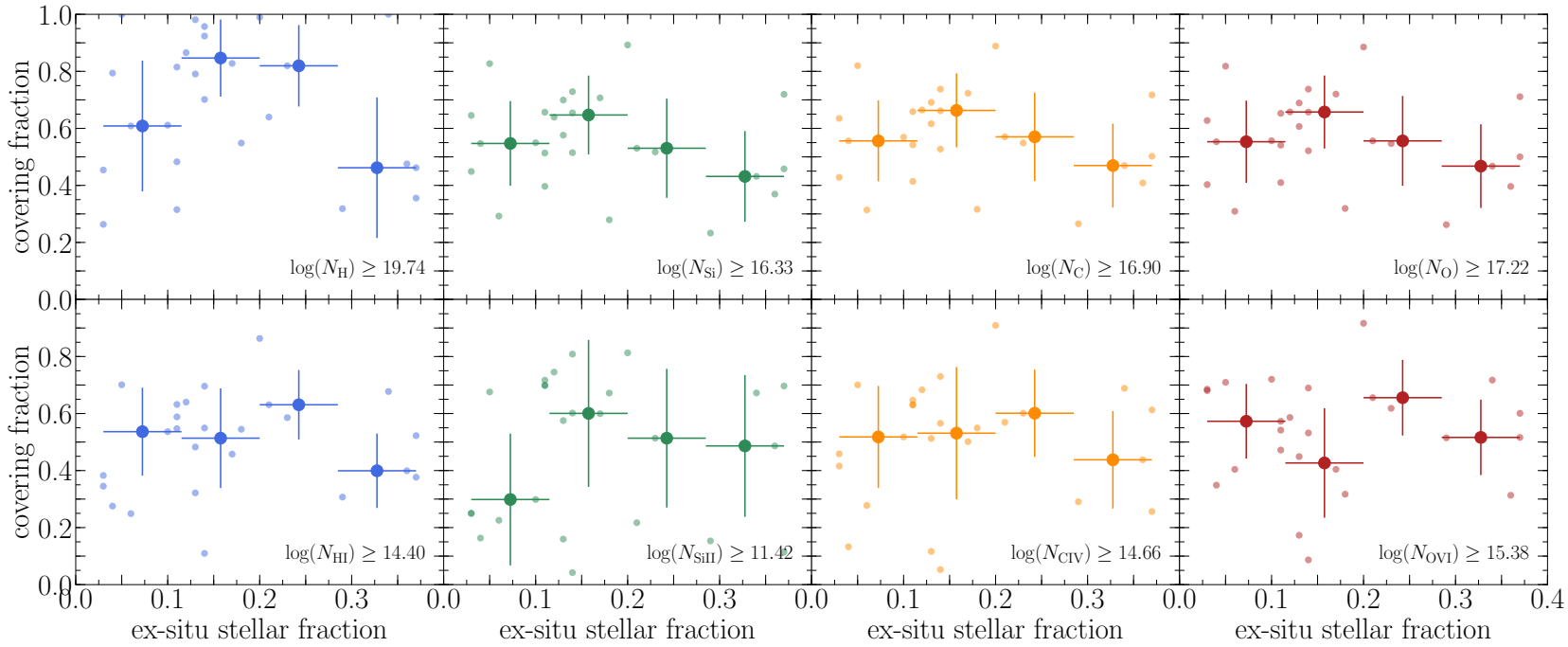

Figure 2.12: The effect of the merger history on the CGM properties. The covering fractions of H I, Si II, C IV, and O VI (bottom panels) and their parent species (top panels) are shown as a function of the ex-situ stellar mass fraction. The small circles represent the covering fractions of individual halos, while the large solid circles show the median covering fractions in bins of ex-situ stellar mass fraction. The error bars show the bin size and 1σ variations in the binned covering fractions. The absence of correlation between the CGM metal content or ionisation and the merger histories suggests that the galaxy merger history is not a major determinant of CGM properties in the absence of recent mergers. Other processes are at least as impactful as galaxy mergers in shaping the CGM of $z = 0$ L* galaxies.

2.4 Discussion

As discussed in Section 1.2.2, observational surveys targeting the CGM are often dependent on the fortuitous coincidence of bright UV quasars and foreground galaxies (e.g. Tumlinson et al., 2013; Bordoloi et al., 2014b; Borthakur et al., 2016; Heckman et al., 2017; Prochaska et al., 2017; Berg et al., 2018). Inferring CGM properties through absorption features provides a sensitive and powerful tool for CGM studies. Current observational surveys have laid a solid foundation to our understanding of the CGM and its relation to galaxy properties in a statistically meaningful way (e.g., Cooksey et al., 2010; Prochaska et al., 2011; Tumlinson et al., 2013; Liang & Chen, 2014; Lehner et al., 2015). Nonetheless, these observational studies suffer from two major limitations: (1) small samples of galaxy-quasar pairs, and (2) a small (often one) number of sight-lines through each galaxy. Therefore, studying the CGM of single galaxies in absorption and understanding its diversity and structure is not currently possible. Consequently, observational surveys often resort to two fundamental assumptions: (1) the CGM of a halo has small azimuthal variations and therefore a single sight-line at a given impact parameter is representative of the CGM at the observed impact parameter, and (2) a well-controlled (often controlled for stellar mass) sample of galaxies has little variations between their CGMs and therefore the observed sight-lines can be used to reproduce a representative median CGM profile defined by the control parameters.

Characterising the diversity in the CGM within a controlled sample requires an unfeasible number of lines-of-sight and galaxies. However, various observational studies tackled the variations within the CGM of single halos. Studies using lensed quasars demonstrate a large dispersion in observed absorption properties (line strength, and equivalent widths) of low and intermediate ionisation species (unlike high ions) over kpc scales (e.g., Ellison et al., 2004; Lopez et al., 2007; Koyamada et al., 2017). The lensed quasar findings are consistent with those of studies using multi-quasar systems which report strong variations in column densities and kinematics within the CGM of single halos (e.g., Bowen et al., 2016). Studies using extended background sources (i.e., galaxies, lensed galaxy arcs) further stress the existence of clumpy absorbers with strong variations in the absorption strength, and distribution within the CGM of single halos (e.g., Lopez et al., 2018; Péroux et al., 2018). Additionally, the Galactic CGM has been studied with a plethora of lines-of-sight stressing the diversity in the CGM (e.g., Moss et al., 2017; Richter et al., 2017; Werk et al., 2019).

Such variations within observed CGMs highlight the complexity of these reservoirs' structure.

Section 2.3.1 demonstrates the diversity within a given halo's CGM and within the Auriga sample, which poses a major challenge to understanding the CGM with limited sampling. Assuming that the diversity in the Auriga CGMs is representative of the observed universe, I investigate the effects that the limited sampling of the *diverse* CGM in observational studies has on reproducing CGM properties. I create mock observational surveys of the CGM of Auriga galaxies whilst controlling for either stellar mass (within $\pm\delta\log(M_\star)$ centred at $\log(M_\star) = 10.8$), or AGN luminosity (within $\pm\delta\log(L_{\rm bol})$ centred at $\log(L_{\rm bol}) = 43.0$), hereafter referred to as the controlled sample. For each controlled sample I pool all the lines-of-sight passing through the CGM of the member galaxies. Then I sample, without replacement, $N_{\rm los}$ lines-of-sight to produce a mock survey for which I compute covering fractions for the elements and ionic species used in this chapter. The lines of sight are then returned to the controlled sample pool and the sampling process is repeated 10^6 times. The inferred covering fractions are then compared to the *true* covering fraction which is computed for a hypothetical halo including all the lines-of-sight in the controlled sample pool.

Figure 2.13 shows the fraction of mock surveys that reproduce a covering fraction within $\pm5\%$ and $\pm10\%$ of the *true* covering fraction as a function of $N_{\rm los}$ for hydrogen, silicon, carbon, and oxygen (top panels), and H I, Si II, C IV, and O VI (middle and bottom panels). The top two rows show the results for a stellar mass matched sample ($\delta\log(M_\star) = 0.05$), whilst the bottom row uses a sample which has been matched for $L_{\rm bol}$ ($\delta\log(L_{\rm bol}) = 0.5$). As the number of lines-of-sight increases, the inferred covering fraction distribution becomes tighter. Consequently, the probability of recovering the *true* covering fraction of the sampled CGM increases. For example, I find that a survey typically needs at least 250 lines-of-sight in order to constrain the covering fraction to within 5%. I note, however, that when deriving the scaling relations shown in this chapter a tolerance of $\sim 10\%$ is sufficient. Therefore, one may be able to reproduce the results presented above using a lower number of lines-of-sight.

The open grey triangles in Figure 2.13 represent a sample that has been matched with less stringent matching criteria: $\delta\log(M_\star) = 0.25$, and $\delta\log(L_{\rm bol}) = 1.5$ (i.e. including all the Auriga galaxies studied in this chapter). The matching criteria has a negligible effect on the probability of a mock survey reproducing the *true* covering fraction. The negligible effect of the matching criteria suggests that the diversity

within a single CGM overshadows the diversity within a controlled sample.

The results of this analysis hint that while matching the galaxy sample by stellar mass and AGN luminosity has a negligible effect on reproducing the *true* covering fraction of the sample, an impractically large number of lines-of-sight is needed to reproduce the *true* covering fraction with high confidence. However, owing to the narrow range of matching investigated in this analysis and the narrow range of galaxy properties spanned by the Auriga halos studied here, one must proceed with caution when considering the importance of controlled galaxy samples: viz. the independence of the success of mock surveys on the matching criteria may not necessarily imply the unimportance of sample matching.

One must be cautious when extrapolating the diversity in the Auriga sample into the observed universe. Although the Auriga physical model reproduces many galactic properties (see Grand et al., 2017) and some observed CGM properties (i.e. azimuthal dependence of low ionisation species, dependence of the CGM gas properties on AGN luminosity and stellar mass), the achieved resolution in the CGM may pose a limitation to the analysis I present. Recent studies targeting the CGM introduce refinement schemes to better resolve the underlying structure that contributes to most of the absorption, and demonstrate the importance of high resolution in CGM studies (i.e. Suresh et al., 2019; Peeples et al., 2019; van de Voort et al., 2019). Suresh et al. (2019) and Peeples et al. (2019) show that although the structure of the CGM changes drastically with increasing resolution, the integrated quantities show smaller changes; harmoniously, van de Voort et al. (2019) and Rhodin et al. (2019) independently demonstrate the strong dependence of column densities and covering fractions of H I on resolution. Additionally, Suresh et al. (2019) demonstrate the effect of resolved structure at producing and sustaining the cool gas in the CGM. I also stress that the galaxy sample studied in this chapter spans a narrow range in halo and stellar mass, and is selected to be isolated at $z = 0$ and to have a quiet recent merger history, all of which are factors worth exploring when comparing to analogous observational samples.

2.5 Conclusions

The CGM is a major gas and metal reservoir that plays a key role in galaxy evolution. Whilst the CGM is ubiquitous, its detailed properties are complex and dependent on a plethora of galactic and environmental properties. I use 28 simulated galaxies from the

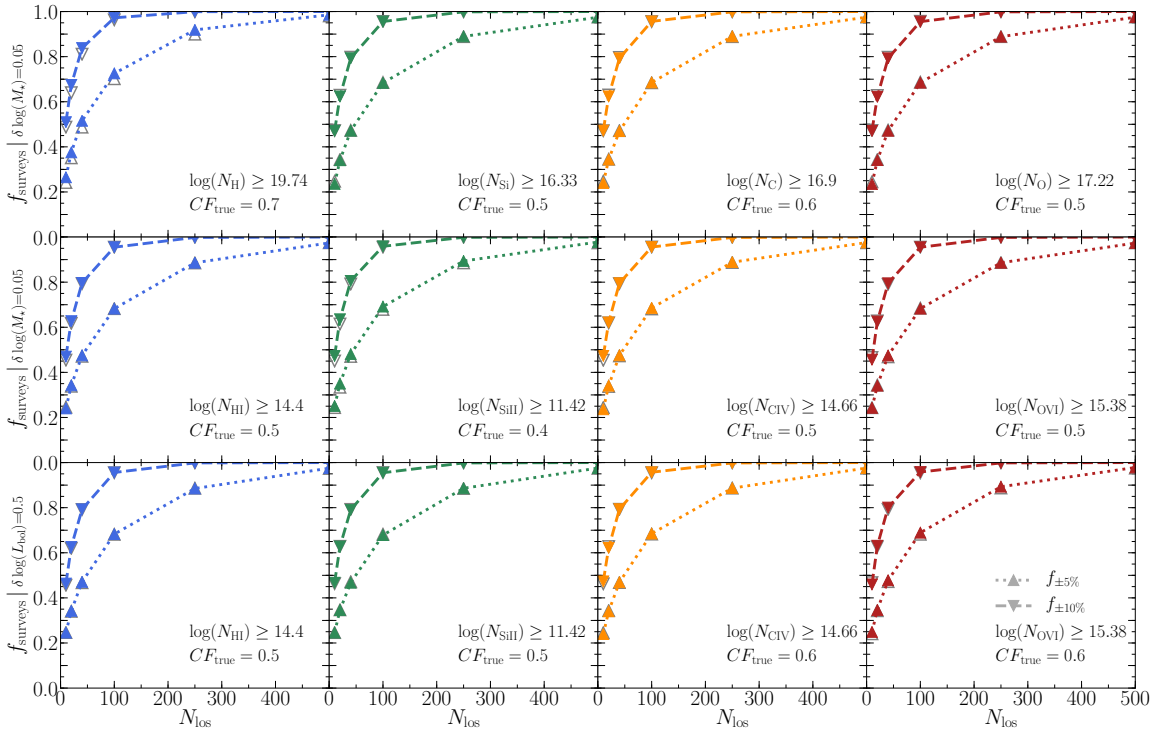

Figure 2.13: Quantifying the effect of limited sampling on measuring the *true* covering fraction of various elements and ionic species. I report the fraction of mock surveys with an inferred covering fraction within ±5% (dotted line/upwards triangles) and 10% (dashed line/downwards triangles) of the *true* covering fraction as a function of the number of lines-of-sight in the survey. The top and middle rows show the results for a stellar mass-matched sample ($\delta\log(M_\star) = 0.05$) while the bottom row shows the effect of $L_{\rm bol}$-matching ($\delta\log(L_{\rm bol}) = 0.5$). The species whose covering fraction is calculated is shown in the bottom right of each panel. Decreasing $N_{\rm los}$ produces a poorer estimate of the *true* covering fraction which is an effect of limited sampling. Consequently, an impractically large number of lines-of-sight is needed to confidently reproduce the underlying CGM properties. The open grey triangles represent a sample which has been matched with $\delta\log(M_\star) = 0.25$ (top and middle rows), or $\delta\log(L_{\rm bol}) = 1.5$ (bottom row). The matching criteria has a negligible effect on the probability of estimating the *true* covering fraction which may suggest that the diversity within a single CGM overshadows the diversity within a controlled sample for the Auriga galaxies studied in this work.

Auriga project, a suite of magneto-hydrodynamical cosmological zoom-in simulations (Grand et al., 2017). The galaxies are chosen to exhibit no signs of current or recent interactions and span a narrow range of halo mass. I examine the diversity within the galaxy sample and individual CGMs, and I investigate correlations with well-understood galaxy properties (e.g. stellar mass, disc fraction, AGN activity, merger history). I have demonstrated that:

1. The CGM of individual halos shows remarkable diversity in the distribution of column densities for hydrogen, metals, and their associated ionic species studied in this chapter. The column density distributions (even within a single halo) span 4-5 decades for the ionic species (H I, Si II, C IV, and O VI), and 2-3 decades for their parent species. Although the Auriga halos studied in this chapter were chosen to occupy a narrow range in halo mass, and have relatively quiet merger histories, they show stark diversity in their CGM properties, covering fractions (a decade in covering fraction), and line-of-sight column density distributions (several decades in column density) for commonly observed ions and their parent species. This is indicative of the sensitivity of the CGM to galaxy evolution.

2. Ionic species (e.g., H I, Si II, C IV, and O VI) do not obey the same scaling relations as the total O, C, Si and H (see Figures 2.8 and 2.11) due to the effects of ionisation. Therefore, when interpreting observations it is important to properly account for ionisation effects.

3. The CGM gas and metal content (i.e. covering fractions) show a tight correlation with the host galaxy's stellar mass. As galaxies grow, the metals produced in the ISM are transported to the CGM via stellar or AGN winds, therefore increasing the CGM's metal content. Conversely, the CGM ionisation is independent of the galaxy's stellar mass as the gas ionisation is sensitive to the density and temperature distributions as well as the ionisation field.

4. While the CGM gas and metal content is independent of current AGN activity (i.e. $L_{\rm bol}$), the CGM ionisation is anti-correlated with $L_{\rm bol}$. The AGN's ionisation field provides a major source of ionisation in the CGM.

5. The CGM gas and metal content is independent (with large scatter) of the recent ($10 - 500$ Myr averaged) specific star formation rate.

6. The CGM ionisation shows a positive correlation with the galaxy's disc fractions. Outflows originating in disc-dominated galaxies can travel unperturbed into the CGM, thus maintaining its filamentary and dense structure which allows the existence of low ionisation species. Nonetheless, the covering fraction of O VI is independent of disc fraction as it traces the hot diffuse medium.

7. No correlation is present between the CGM properties and the long-term galaxy merger history (i.e. ex-situ stellar mass fraction) which indicates that mergers during the early stages of galaxy evolution are not a dominant sculptor of the $z = 0$ CGM in the absence of recent major mergers. I remind the reader that the Auriga galaxies studied in this chapter were selected to have quiet recent merger histories (no mergers more major than $1:3$ within the past 2 Gyr).

8. The diversity of the Auriga CGM stresses the need for impractically large numbers of lines-of-sight when studying the CGM. As a result, with ~ 40 lines-of-sight, only $\sim 50\%$ of mock surveys would infer a covering fraction within 5% of the *true* covering fraction of a controlled galaxy sample.

This chapter presented a sample of $z = 0$ Milky Way-mass ($L^\star$) galaxies simulated in a realistic cosmological environment, and demonstrated the stark diversity within an individual CGM and between the CGMs of the sample. Additionally, I highlight major physical and evolutionary processes which mould the CGM, its gas and metal content, ionisation, and structure. The diversity of the Auriga CGM accentuates a fundamental challenge for observational studies.

Chapter 3

Galaxy mergers moulding the circum-galactic medium: The impact of a major merger

This chapter is published as Hani et al. (2018).

Abstract

Our understanding of how galaxy mergers, a major evolutionary transformation, impact the CGM remains deficient. I present a theoretical study of the effect of galaxy mergers on the CGM. I use a hydrodynamical cosmological zoom-in simulation of a major merger selected from the Illustris project such that the $z = 0$ descendant has a halo mass and stellar mass comparable to the Milky Way. The zoom-in simulation has 40 times better mass resolution than the Illustris project, and my analysis includes detailed post-processing ionization modelling. My work demonstrates the effect that the merger has on the characteristic size of the CGM, its metallicity, and the predicted covering fraction of various commonly observed gas-phase species, such as H I, C IV, and O VI. I show that merger-induced outflows can increase the CGM metallicity by $0.2-0.3$ dex within 0.5 Gyr post-merger. These effects last up to 6 Gyr post-merger. While the merger increases the total metal covering fractions by factors of $2-3$, the covering fractions of commonly observed UV ions decrease due to the hard ionizing radiation from the active galactic nucleus, which I model explicitly. My study of the single simulated major merger demonstrates the significant impact that a galaxy interaction can have on the size, metallicity, and observed column densities of the CGM.

3.1 Introduction

In Chapter 2 I demonstrated the diversity of the CGM of simulated L* galaxies, and highlighted some of the processes that shape this massive gas reservoir. In this chapter, I investigate the possible effects of galaxy mergers on the CGM. Since mergers play a key role in galaxy evolution, they are expected to have a strong effect on the CGM.

Galaxy mergers are often invoked to explain the presence of metals and low ionization species in the CGM at large impact parameters (e.g., Farina et al., 2013, 2014; Johnson et al., 2015b). Indeed, merger-induced tidal torques can give rise to observed stellar tidal features extending to many tens of kpc (e.g., Hernández-Toledo et al., 2006; Patton et al., 2011, 2013; Casteels et al., 2014). Although some gas asymmetries coexist with asymmetries in the stellar profiles of interacting galaxies, tidally induced asymmetries can persist even longer in H I gas (e.g., Lelli et al., 2014a,b; Scott et al., 2014). Such tidal debris can potentially diffuse into the CGM contributing a significant gas and metal mass. In addition to morphological disturbances, galaxy mergers can, in principle, trigger vigorous galactic outflows associated with feedback from enhanced star formation and AGN activity that can populate the CGM with metals and give rise to multiphase absorbers (e.g., Borthakur et al., 2013; Bird et al., 2015; Heckman & Borthakur, 2016; Bordoloi et al., 2017; Heckman et al., 2017). Indeed, galactic outflows have been observationally tied to enhanced SFRs (e.g., Martin, 2005; Rupke et al., 2005a; Strickland & Heckman, 2009; Hayward & Hopkins, 2017) and AGN activity (e.g., Rupke et al., 2005b; Veilleux et al., 2013; Zschaechner et al., 2016; Woo et al., 2017). Besides, merger-induced shocks and feedback can increase the CGM's internal energy; numerical simulations of galaxy mergers show that CGM gas can be significantly heated (to X-ray emitting temperatures) through shocks and feedback processes (e.g., Cox et al., 2004, 2006b; Sinha & Holley-Bockelmann, 2009). Furthermore, studies of galaxies in dense environments (higher merger probability) show different CGM properties when compared to a matched isolated galaxy sample: The CGM of galaxies in groups show distinct kinematics (Pointon et al., 2017) and ionic covering fractions (Johnson et al., 2015a; Burchett et al., 2016).

Despite the possibly significant influence of galaxy mergers on the CGM, the details of the interplay between galaxy mergers and the CGM remain relatively unexplored and we are currently lacking clear and quantitative predictions of how the CGM will be affected during the merger process. Current observations of the impact

of galaxy mergers on the CGM are limited to a few case studies (e.g., Keeney et al., 2011; Johnson et al., 2014). A systematic survey targeting the CGM of kinematic galaxy pairs (i.e. COS-Pairs: Bordoloi et al. in preparation) is needed to place observational constraints on the effect of mergers on the CGM.

In Chapter 2 I used a sample of Milky Way-like galaxies to unravel the physical mechanisms responsible for shaping the CGM of Milky Way-like galaxies. However, the galaxies studied in Chapter 2 were chosen to not have had a recent merger or interactions given the potentially profound impact of galaxy mergers on both the stellar and gas properties (see Section 1.3). In this chapter, I present a study of the effect of galaxy–galaxy major mergers on the CGM. I showcase a zoom-in cosmological hydrodynamical simulation of a major merger from Sparre & Springel (2016) and demonstrate the effects of the merger on the CGM size, metal content, and ionisation. This chapter is structured as follows: In Section 3.2 I describe the halo selection method, the galaxy formation model, and the ionisation modelling implemented in post-processing. I then present the results of the simulations in Section 3.3 focusing on the effect of the merger on the covering fractions of oxygen and hydrogen, the size of the CGM, and the CGM ionisation. In Section 3.4 I discuss the role of merger-induced outflows in populating the CGM with metal rich gas, the thermal state of the CGM, and assess the effect of the simulation resolution on the results. Lastly, Section 3.5 summarises the conclusions of this chapter.

3.2 Methods

The primary goal of this chapter is to study the impact of galaxy–galaxy major mergers on the physical and observable properties of the CGM. I use cosmological zoom-in simulations to study the evolution of the CGM throughout the merger and during the post-merger epoch. The use of cosmological zoom-in simulations allows for self-consistent modelling of the CGM in a cosmological framework while offering superior spatial and mass resolution, which is required when studying the CGM. The initial conditions used in this chapter are the same used in Sparre & Springel (2016), which are drawn from the Illustris project and specifically target galaxy major mergers.

This section briefly describes the simulations; specifically focusing on the physics implementation of the galaxy formation model. Additionally, the post-processing techniques used to analyse the simulations are described here.

3.2.1 Simulation code

Sparre & Springel (2016) use the the moving-mesh magneto-hydrodynamical code Arepo (Springel, 2010; Pakmor et al., 2016) to solve the Euler equations. Arepo handles the hydrodynamical evolution of gas by discretizing the Euler equations over a dynamic Voronoi mesh where the mesh-generating points trace the local fluid flow. The nature of the code reduces advection errors compared to the adaptive static mesh approach as the (de)refinement of the mesh is less frequent due to the adaptive, dynamic mesh.

3.2.2 Simulations and major merger selection

In this study, I showcase one[1] of the four mergers introduced in Sparre & Springel (2016) (merger: 1605-3) to demonstrate the effect of galaxy mergers on the CGM metal budget and ionization. The galaxy merger was selected from the Illustris-1 box of the Illustris project (Genel et al., 2014; Vogelsberger et al., 2014a,b; Sijacki et al., 2015), a large scale hydrodynamical cosmological simulation, and re-simulated at 40 times higher mass resolution[2] (see Table 3.1). The merger was selected such that the remnant at $z = 0$ is Milky Way-sized with stellar mass $M_\star = 10^{10.89}$ $M_\odot$ and a dark matter halo with total mass $M_{200} = 10^{12.00}$ $M_\odot$. The merger occurs at $z = 0.66$, which allows the study of the CGM well beyond the merger event. The progenitors undergoing the merger have stellar masses of $10^{10.27}$ and $10^{10.21}$ $M_\odot$, hence a mass ratio of 1:1.16. The merger chosen for this study is characterized by the presence of a sizeable ($10^{7.14}$ $M_\odot$) very dense star-forming gas reservoir prior to the merger and therefore exhibits a significant starburst during the merger with SFRs of $70 - 100$ $M_\odot$/yr ($3.5 - 5\times$ higher than the pre-merger SFR; see Sparre & Springel, 2016). I note that this merger is gas-rich, and that the merger remnant remains star forming at $z = 0$. Such a behaviour is often seen in simulated mergers in this mass range (Springel & Hernquist, 2005; Governato et al., 2009; Rodriguez-Gomez et al., 2017). Additionally, the progenitors' recent merger histories, as well as the descendant's merger history, are relatively quiet, which makes it possible to highlight the effects of the major merger, i.e. no other major mergers, with mass ratio $>$ 1:3, occur post-merger (only one minor merger with 1:10 $<$ mass ratio $<$ 1:3). For the exact selection

[1] Note that the choice of merger does not affect the results of this study. All three other mergers yield qualitatively similar results.

[2] Note that the lower resolution re-runs of the same merger introduced in Sparre & Springel (2016) (i.e. 1605-1, 1605-2) were only used for a convergence test in Section 3.4.2

Table 3.1: An overview of the three resolution re-runs of the merger simulation showcased in this work (Sparre & Springel, 2016). The results of this chapter use the highest resolution simulation: 1605-3. I follow the same naming convention as Sparre & Springel (2016) where the simulations are named AAAA-B, where AAAA is the z = 0 friends-of-friends group in Illustris, and B is the 'zoom-factor'. $\epsilon_{\rm dm}$ is the maximum softening length for the dark matter resolution elements in physical units. $m_{\rm b}$ and $m_{\rm dm}$ are the masses for the baryon and dark matter resolution elements, respectively.

Sim-name	$\epsilon_{\rm dm}$ [kpc]	$m_{\rm b}$ [$M_\odot$]	$m_{\rm dm}$ [$M_\odot$]
1605-1	0.64	8.90×10^5	4.42×10^6
1605-2	0.32	1.11×10^5	5.53×10^5
1605-3	0.21	3.30×10^4	1.64×10^5

criteria, see Sparre & Springel (2017).

I track the most massive galaxy participating in the merger by identifying the galaxy's stellar population at $z = 0.93$, well before the merger, as a reference population. The associated progenitors and descendants are identified and tracked using the SUBFIND algorithm (Springel et al., 2001).

3.2.3 Galaxy formation model

The galaxy formation model implemented in the simulations was presented in detail in the Auriga simulation paper (Grand et al., 2017). The model is based on the original physical model in the Illustris project (Vogelsberger et al., 2013) and the modifications of Marinacci et al. (2014a).

The ISM is modelled as a multiphase gas governed by an effective equation of state according to the sub-resolution model of Springel & Hernquist (2003). In this model, star formation occurs stochastically in gas cells denser than the star formation threshold, $n_{\rm sfr} = 0.13$ cm^{-3}, with a star formation time-scale, $t_{\rm sfr} = 2.2$ Gyr. Each newly formed star particle is modelled as a simple stellar population. The evolution of star particles and associated mass-loss and chemical enrichment are tracked continuously in the simulation assuming a Chabrier (Chabrier, 2003) initial mass function. Mass lost from AGB stars and SNe is returned to the environment using a top-hat kernel enclosing the 64 nearest neighbouring gas cells. The model follows the abundances of nine elements (H, He, C, N, O, Ne, Mg, Si, Fe) using the yields described in Vogelsberger et al. (2013). AREPO allows metals to advect self-consistently between gas cells therefore creating a smooth metal profile by allowing high metallicity gas to diffuse amongst neighbouring cells. Stellar feedback from SN II is implemented by

probabilistically spawning wind particles from star-forming gas cells. Wind particles are decoupled from the hydrodynamics and travel isotropically at a velocity which scales with the local dark matter velocity dispersion until the surrounding gas density drops slightly below the star formation threshold, or a maximum travel time interval has elapsed. When wind particles re-couple to the hydrodynamics, they deposit their momentum, thermal energy, and metal content into the nearest gas cell.

The simulations also include BHs and consequently feedback from AGNs. When haloes reach a mass of 7.1×10^{10} $M_{\odot}$ they are seeded with a BH of mass 1.4×10^{5} $M_{\odot}$, which grows by Eddington-limited Bondi–Hoyle–Lyttleton accretion. Two modes of AGN feedback are implemented: quasar mode (high accretion rate) and radio mode (low accretion rate) feedback. The quasar mode returns thermal energy to the BH's neighbouring gas cells. On the other hand, the radio mode exerts mechanical feedback where the AGN jets inflate hot bubbles which rise buoyantly in the halo. The radiative loss from the radio mode uses the scaling relations of Nulsen & Fabian (2000). In addition to the two feedback modes, the simulation includes radiative feedback (photoheating) from the AGN which affects the gas heating/cooling rates. The ionization balance is not explicitly calculated within the simulation, instead the cooling/heating rates are interpolated from CLOUDY tables. However, I calculate the ionization balance in post-processing whilst accounting for an AGN radiation field to be consistent with the heating/cooling rate calculations done within the simulation (see Section 3.2.5 for details). Radiative processes and gas heating/cooling are also treated within the simulation as described in Vogelsberger et al. (2013). The associated physics model is discussed in detail in Section 3.2.5. I refer the interested reader to the above references for more details about the galaxy formation model.

The physical model used in this study and close variations thereof have been used in both large-scale cosmological simulations and cosmological zoom-in simulations. The model has been successful at reproducing observable CGM properties, e.g. (i) the bimodality in O VI covering fractions between passive and star forming galaxies (Suresh et al., 2017), (ii) the correlation between the circum-galactic H I content and the galaxy's SFR (Marinacci et al., 2017), (iii) the presence of hot coronae around galaxies (Bogdán et al., 2015), and (iv) the number of damped Ly α and Ly limit systems at high redshift (Suresh et al., 2015). Furthermore, studies employing the same physical model placed constraints on feedback models (stellar and AGN feedback) by comparing simulated CGM properties to observations. AGN feedback has been shown to suppress gas accretion onto the galaxy and launch gas into the CGM and

beyond (Grand et al., 2017). Additionally, thermal AGN feedback heats the CGM giving rise to hot gaseous haloes (Bogdán et al., 2015), and driving the observed O VI bimodality (Suresh et al., 2017). On the other hand, Marinacci et al. (2014b) used cosmological zoom-in simulations to demonstrate the significant effects of stellar feedback (i.e. galactic winds) on the gas morphology and heavy element distribution in the CGM. Studies of C IV in the CGM of simulated galaxies indicate that energetic stellar winds, which are superior at enriching the CGM, are favoured (Bird et al., 2016; Suresh et al., 2015).

3.2.4 Tracking the CGM gas and metals

In order to track the CGM properties of the merging galaxies in an even-handed fashion with CGM observations, viz. calculating the column densities of various ionic species in the CGM, I project a slice of depth 1.35 physical Mpc, centred at the most massive progenitor in the merger, along a random projection axis which is then fixed for all snapshots throughout the analysis. The choice of projection axis does not influence my results. The projections use a static Cartesian grid with 293 pc pixels (comparable to the spatial resolution of the simulation) and a 300×300 physical kpc^2 FOV corresponding to impact parameters ($\lesssim 150$ kpc) which are in accord with current observational surveys targeting the CGM (e.g., Tumlinson et al., 2011, 2013; Werk et al., 2013; Bordoloi et al., 2014b; Peeples et al., 2014; Werk et al., 2014; Borthakur et al., 2015, 2016; Werk et al., 2016; Prochaska et al., 2017). Figure 3.1 shows the gas projections in hydrogen (top two rows) and oxygen (bottom two rows). The projections were performed using the oct-tree projection routines implemented in the `yt` analysis tool-kit version 3.3.2 (Turk et al., 2011).

Unlike observational surveys targeting galaxy mergers, I do not impose a line-of-sight velocity cut since my stringent spatial projection domain implies a velocity distribution well within the 500 km/s cut-off traditionally employed in observations (Tumlinson et al., 2011, 2013; Werk et al., 2013; Bordoloi et al., 2014b; Peeples et al., 2014; Werk et al., 2014; Borthakur et al., 2015, 2016; Werk et al., 2016; Prochaska et al., 2017). Figure 3.2 shows a typical line-of-sight velocity distribution of gas elements in my projection slice which lies well within $v_{\rm los} \sim \pm 300$ km/s. Because element abundances are tracked continuously in the simulation (see Sections 3.2.3), my projections include projected number densities (column densities) of each element included in the simulation. Therefore, I am able to analyse the evolution of the CGM's

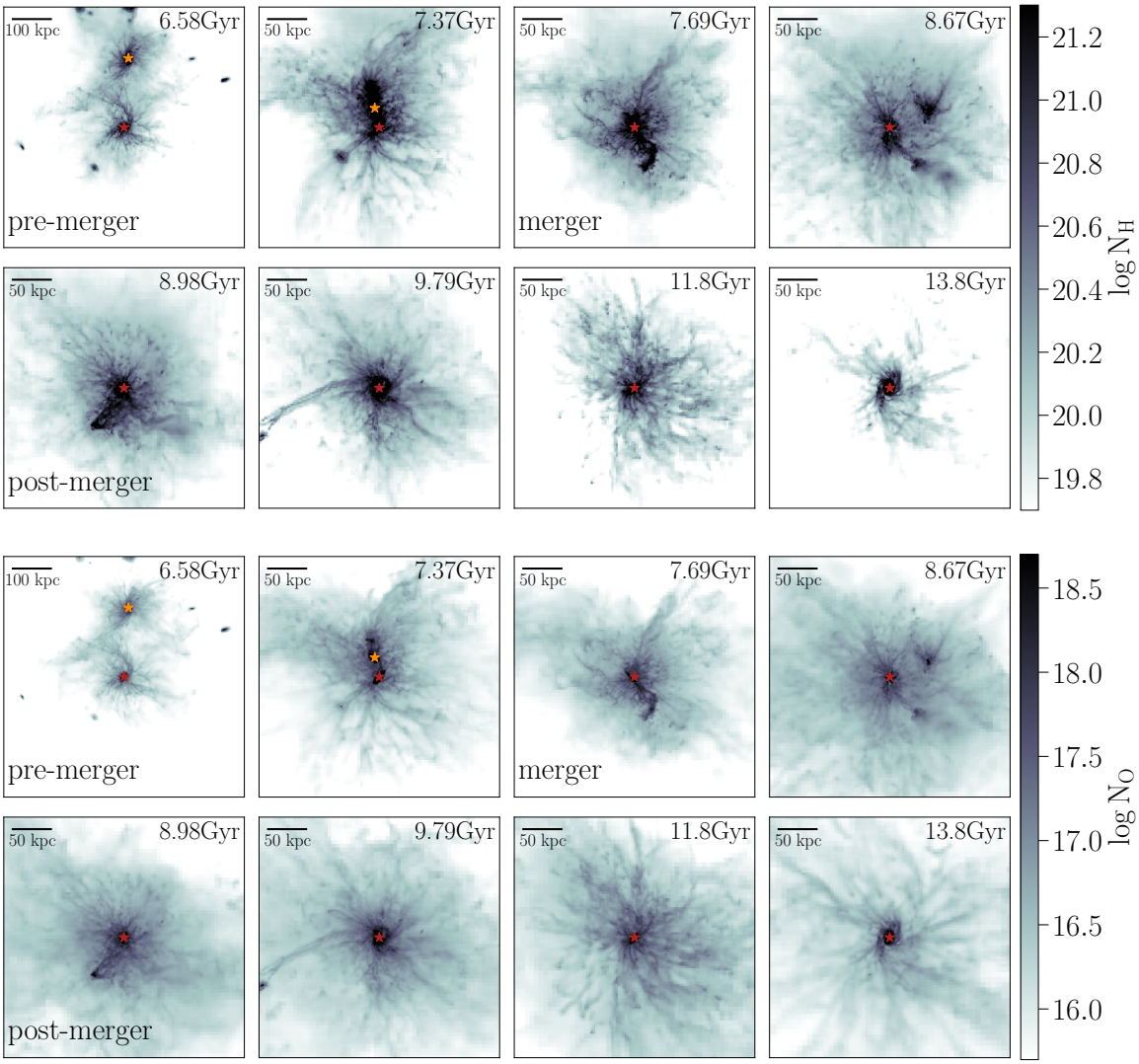

Figure 3.1: 300×300 physical kpc^2 projections (except the left-most projections in the first and third rows for demonstration purposes only: 600×600 physical kpc^2), centred at the most massive progenitor, showing the evolution of the galaxy throughout the stages of the merger. The top two rows depict projections of the hydrogen gas, while the bottom two rows show the projections of the oxygen gas. The bar in the upper-left corner of each frame represents 50 kpc for scale (100 kpc for the left-most projections in the first and third rows), while the cosmic time stamp is annotated in the upper-right corner. The position of the primary (secondary before coalescence) galaxy is marked by a red (orange) star. The frames corresponding to the pre-merger, merger, and post-merger evolutionary stages are annotated in the lower-left corner accordingly. The post-merger CGM contains significantly more oxygen compared to the pre-merger galaxy.

chemical composition on an element-by-element basis.

I will frequently make reference to some key evolutionary stages that mark the evolution of the merger. I define the merger time to correspond to the time of maximum specific BH accretion rate. The pre-merger (post-merger) period is defined to be a $\sim 100 - 200$ Myr window centred at the snapshot 1 Gyr prior to (after) the merger (Figure 3.1).

3.2.5 CGM ionisation

Unlike metals (i.e. C, N, O, Ne, Mg, Si, Fe), which are explicitly tracked in the simulations, ionisation species are not explicitly tracked on-the-fly. Therefore, post-processing of the simulation results is required to calculate the ionisation balance of gas cells. In this chapter, I follow the methodology introduced in Chapter 2 (Section 2.2.2), where a grid of single cell Cloudy (Ferland et al., 2013b) simulations is interpolated to calculate the ionisation balance in each gas cell depending on the cell's temperature, density, metallicity, the bolometric AGN intensity at the cell's location, and the redshift of the galaxy (see Table 2.1). The ionisation calculations account for contributions from two radiation fields: an AGN radiation field, and a spatially-uniform time varying UVB (Faucher-Giguère et al., 2009), and assume ionisation equilibrium. The effects of self shielding are also incorporated following Rahmati et al. (2013).

3.3 Results

In the course of my analysis, I will present the results for oxygen as a representative species for other metals (except when discussing the ionization of the gas); all other elements tracked in the simulation show similar qualitative trends.

In keeping with observational studies of galaxy mergers (e.g., Ellison et al., 2008a, 2011; Patton et al., 2011; Scudder et al., 2012; Ellison et al., 2013a; Patton et al., 2013, 2016) I look at the differential changes in the CGM as a result of the merger. This approach facilitates quantifying the effects of the merger. The aforementioned observational studies compare a 'merger sample' to an 'isolated (control) sample'. Similarly, previous numerical work studying the effects of mergers (e.g., Torrey et al., 2012; Moreno et al., 2015) also evolved the progenitor galaxies in isolation, which allowed a comparison to an isolated 'control sample'. Alas, that option is a sacrifice that one must accept when using cosmological simulations (see Section 3.2). Hence, I

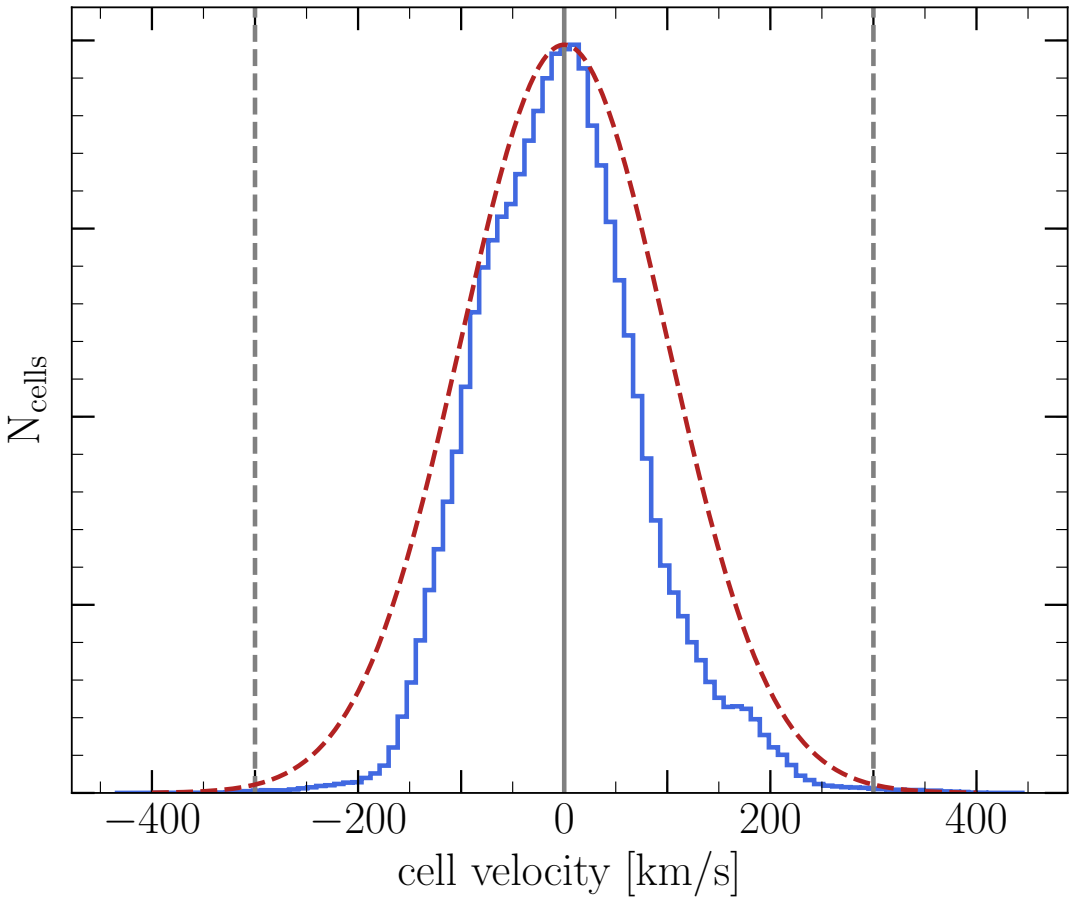

Figure 3.2: The line-of-sight velocity distribution of gas cells within the projection slice relative to the galaxy's systemic velocity (blue histogram). The distribution of gas resolution elements is well within ±300 km/s (grey dashed lines) which is more stringent than that nominally adopted in observational studies of the CGM (±500 km/s), thus motivating the lack of need for further constraints on the velocities. For visual comparison, the dashed brick-red line shows a normal distribution with a characteristic $\sigma = 100$ km/s.

use the pre-merger properties of the CGM as the "control sample" in my comparison. The pre-merger CGM properties are calculated over a $\sim 100 - 200$ Myr range 1 Gyr before the merger (at $t \sim 6.6$ Gyr) where the CGM of the galaxy shows remarkable stability (in the metrics I study).

3.3.1 Gas and metal covering fraction

CGM covering fractions

To quantify the global effects of the merger on the CGM gas and metal content, I first examine the evolution of the covering fraction of gas throughout the merger. The covering fraction is a metric frequently used in observational studies of the CGM (e.g., Tumlinson et al., 2011, 2013; Werk et al., 2013; Bordoloi et al., 2014b; Peeples et al., 2014; Werk et al., 2014; Borthakur et al., 2015, 2016; Werk et al., 2016; Prochaska et al., 2017). The covering fraction is defined as the fraction of lines of sight intersecting an absorber denser than a chosen column density threshold. Equivalently, it can be thought of as the fraction of the FOV ('observed' area) containing absorbers above a given column density threshold. The FOV in the following analysis is defined as a square[3] with a length of 300 kpc centred at the more massive merging galaxy. For comparison, all metrics used in this study are also calculated in an identical FOV centred at the secondary galaxy at the pre-merger time. Note that centring the FOV at the secondary galaxy has no effect on the conclusions of this study as both galaxies show remarkable similarities in their CGM properties.

Figures 3.3 and 3.4 show the evolution of the covering fraction of gas (hydrogen and oxygen respectively) above a given column density threshold. The vertical dashed grey line represents the merger time at $t = 7.6$ Gyr. For a visual projection following the merger's evolution see Figure 3.1.

Before the merger ($t \sim 6.58$ Gyr), the galaxy gas distribution exhibits a disc-like morphology extending to ~ 100 kpc. Figure 3.1 shows the galaxy in a near face-on projection with an extended gas reservoir ($N_{\rm H} > 5 \times 10^{19}$ cm^{-2} out to ~ 100 kpc). As the merger proceeds, the second galaxy enters the FOV causing an increase in the gas covering fractions for all column densities until $t \sim 6.6$ Gyr when the galaxies begin to overlap. This increase is due to an increasing area which is covered by absorbers associated with the merging galaxy. At first passage ($t \sim 7$ Gyr), the superposition

[3]Note that the choice of the FOV's shape does not affect the presented results (square versus circle). I use a square FOV for computational simplicity.

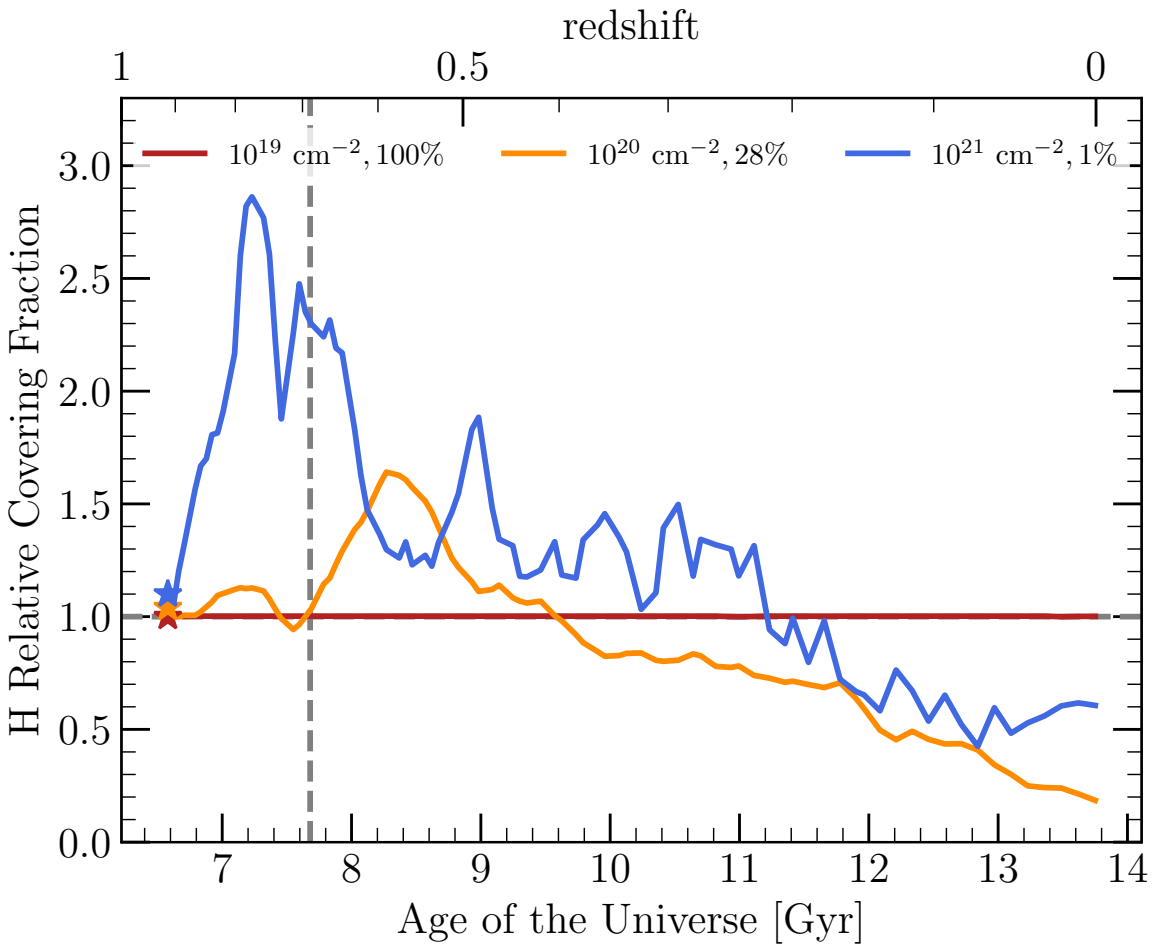

Figure 3.3: The evolution of the covering fraction of hydrogen absorbers (normalized to the pre-merger covering fraction) during the merger. The brick-red, orange, and blue curves represent absorbers with column densities higher than 10^{19}, 10^{20}, and 10^{21} cm^{-2}, respectively. The covering fractions in the CGM of the secondary galaxy are marked by stars; the CGM of both galaxies show remarkable similarity. The legend shows the column density threshold and the associated pre-merger absolute covering fraction. The vertical dashed grey line indicates the time of the merger. The covering fractions are normalized relative to the pre-merger epoch; hence the variation in the CGM covering fractions is a relative variation. As the second galaxy enters the FOV, the covering fraction of all absorbers increases. Shortly after, the covering fractions decrease during the first passage as the galaxies overlap along the line of sight. After the merger, the covering fractions of the highest column density absorbers remain enhanced (compared to the pre-merger stage) yet decrease compared to the merger as tidal torques and feedback processes redistribute the gas. This is evident in the increasing covering fractions of absorbers in the neighbouring column density bin.

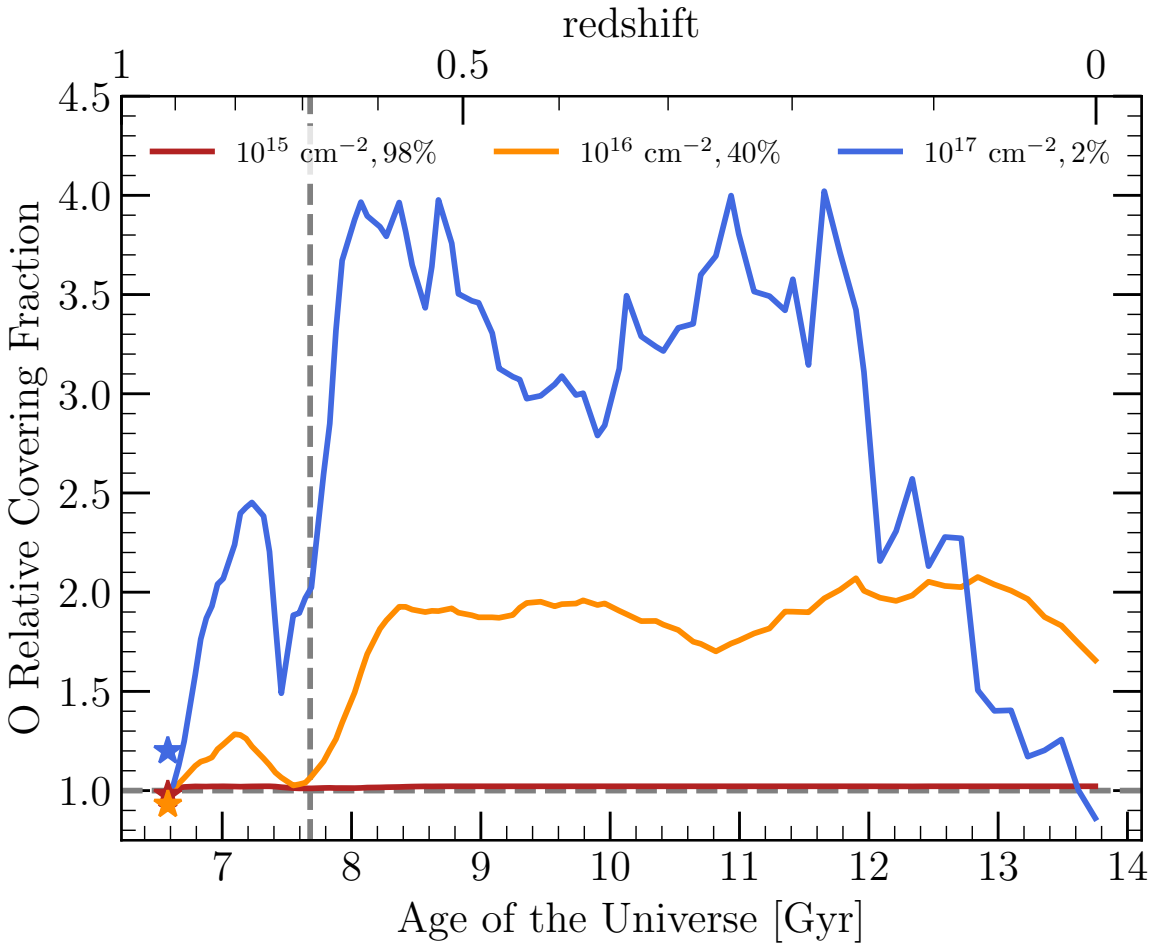

Figure 3.4: Similar to Figure 3.3, this figure represents the evolution of the covering fraction of oxygen during the major merger (normalized relative to the pre-merger epoch). The brick-red, orange, and blue curves represent column densities higher than 10^{15}, 10^{16}, and 10^{17} cm^{-2}, respectively. The covering fractions in an identical FOV centred at the secondary galaxy are marked by stars. The merger populates the CGM with metals which are transported via galactic winds. The enhanced metal covering fractions persist for many Gyrs after the merger has concluded.

of the two galaxies along the line of sight causes a geometrically driven decrease in the gas covering fraction shortly before the merger occurs. The covering fraction of hydrogen and oxygen increases at the time of merger ($t \sim 7.6$ Gyr, indicated by the vertical dashed grey line) by factors of 2 and $2-3$ relative to the pre-merger covering fractions, respectively.

Immediately after the merger ($t \sim 8$ Gyr), the covering fraction of the highest column density hydrogen gas ($\log(N_{\rm H}) > 21$) declines while coinciding with an increase in the covering fraction of absorbers with column densities $\log(N_{\rm H}) > 20$ (see Figure 3.3). During the merger, dense gas is heated by SN and AGN feedback. The combined impact of feedback and tidal fields disrupts and diffuses the gas disc, which drives a decline in the highest hydrogen column densities. On the other hand, outflows primarily contain metal rich gas and the tidally disrupted disc is more metal rich compared to the surrounding medium. Therefore, the covering fraction of oxygen increases after the merger ($t > 7.6$ Gyr) by factors of 2 and 3 for column densities $\log(N_{\rm O}) > 16$ and $\log(N_{\rm O}) > 17$ respectively. I note that the long term enhancements in covering fraction are likely driven by the cosmological evolution of the system as opposed to the merger.

The major merger has a lasting impact on the CGM. The covering fraction of hydrogen gradually decreases for several Gyrs post-merger ($t > 8$ Gyr) but remains above the pre-merger covering fraction until $t \sim 11$ Gyr. The enriched CGM persists well above its pre-merger stage (increase in the covering fraction of oxygen by factors of $2-3$) for several Gyrs post-merger (Figure 3.4). Metals remain present at significant column densities until $z = 0$.

Measuring the extent of the CGM

To further quantify the changes in the extent of the CGM as a result of the merger, I define $R_{50,\,\rm X} = R_{50,\,\rm X}(N_{\rm X},\, t)$ as the radius where the covering fraction of lines of sight with column densities $N > N_{\rm X}$ is at least 50%. The definition of $R_{50,\,\rm X}$ therefore defines a characteristic size for the CGM. Figures 3.5 and 3.6 show the evolution of $R_{50,\,\rm H}$ (hydrogen) and $R_{50,\,\rm O}$ (oxygen), respectively.

Prior to coalescence ($t < 7.6$ Gyr), the area populated with dense hydrogen absorbers increases, therefore increasing $R_{50,\,\rm H}$. After the merger ($t \sim 8$ Gyr), as the tidally disrupted merger remnant settles and the feedback driven outflows push gas outwards, the total hydrogen $R_{50,\,\rm H}(5 \times 10^{20}\,{\rm cm}^{-2},\, 8\,{\rm Gyr})$ decreases back to the

pre-merger state. The highest column density hydrogen is more centrally located (the galactic disc) while the outflowing gas diffuses outwards causing an increase in $R_{50,\,\mathrm{H}}(10^{20}\,\mathrm{cm}^{-2},\,t)$ by a maximum factor of ~ 1.5 which then declines as the gas continues to diffuse below the threshold. The characteristic size of the CGM as observed in hydrogen remains enhanced by a factor of ~ 1.3 for ~ 3 Gyr for $N_{\mathrm{H}} > 5 \times 10^{20}$ cm^{-2}.

$R_{50,\,\mathrm{O}}$ for oxygen absorbers increases after the first passage ($t \sim 7.4$ Gyr) as two processes contribute to the observed increase: (1) the induced starburst enriching the gas, and (2) the geometric superposition of the galaxies increases the column densities. After the merger ($t > 7.6$ Gyr), metal rich outflows cause an increase in $R_{50,\,\mathrm{O}}(10^{16}\,\mathrm{cm}^{-2},\,t > 7.6\,\mathrm{Gyr})$ and $R_{50,\,\mathrm{O}}(3 \times 10^{17}\,\mathrm{cm}^{-2},\,t > 7.6\,\mathrm{Gyr})$ by factors of 2.2 and 1.6, respectively. The increase persists for > 3 Gyr post-merger. I stress that the long term increase in $R_{50,\,\mathrm{X}}$ is likely driven by the cosmological evolution of the system as opposed to the merger.

The effect of mergers on the CGM 'size': In summary, using two different metrics for CGM 'size', the covering fraction and $R_{50,\,\mathrm{X}}$, I have demonstrated that the merger can lead to a long-lasting (> 4 Gyr) increase in the physical extent of halo gas. The CGM growth is evident in both hydrogen and metals. It is worth noting that the aforementioned CGM growth may not translate into an increase in the observed covering fractions of the ionized species which are influenced by the underlying radiation field (see Section 3.3.3).

3.3.2 Gas migration and enrichment

The CGM density profile

In Section 3.3.1 I demonstrated how the merger increases the covering fractions of hydrogen and metal absorbers in the CGM. The effects of the merger populating the CGM with metal enriched gas through feedback processes can also be seen by examining the galaxy's projected density profile. Figure 3.7 shows the projected column density profiles of hydrogen and oxygen at three epochs: pre-merger (solid grey line), merger (dashed black line), and post-merger (dotted black line). During the merger, the column densities of hydrogen and oxygen in the central regions (< 2 kpc) increase by an order of magnitude as the merger tidally induces gas inflows due to the strong tidal torques (e.g., Barnes & Hernquist, 1991, 1996; Kewley et al., 2006; Ellison et al., 2008a; Scudder et al., 2012; Torrey et al., 2012). Consequently, the gas column densi-

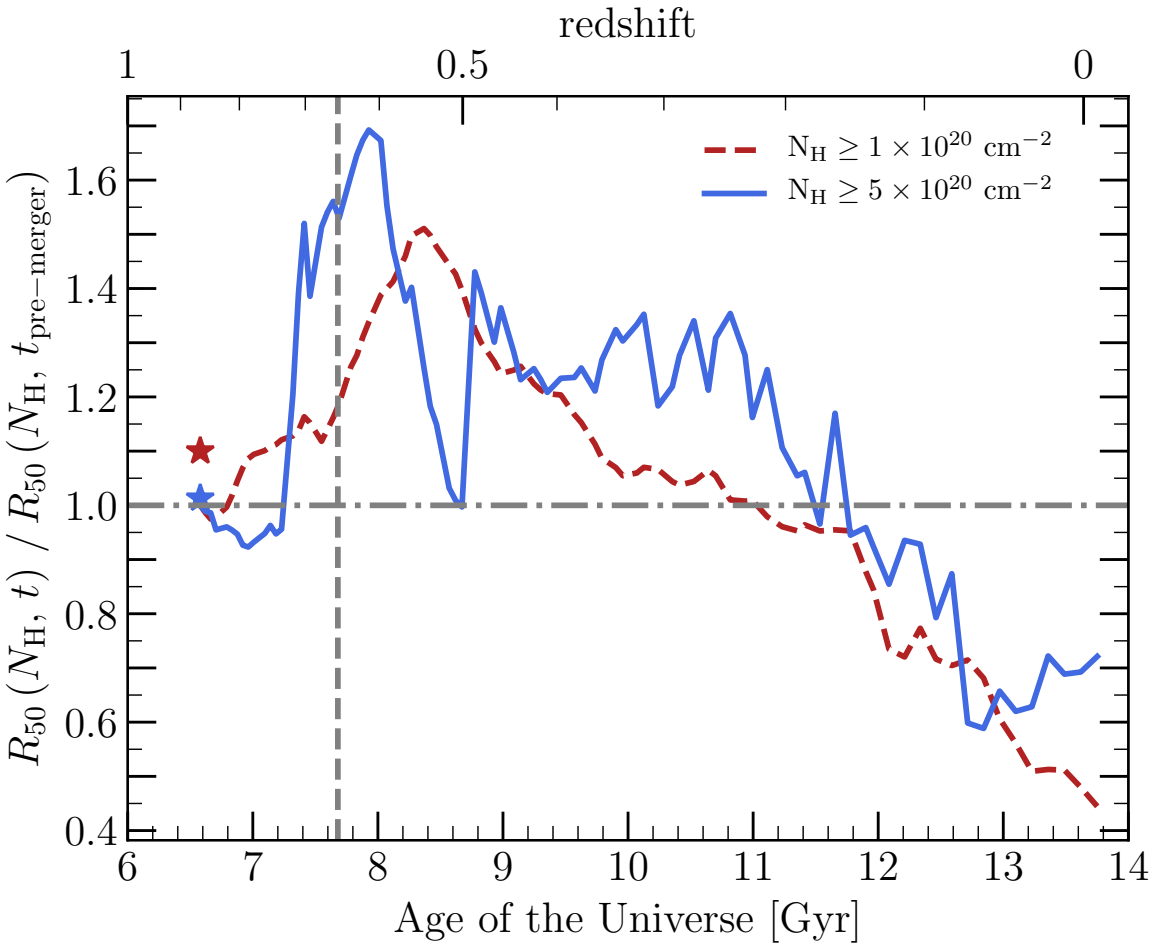

Figure 3.5: The evolution of the $R_{50,\mathrm{H}}(10^{20}\,\mathrm{cm}^{-2}, t)$ (dashed brick-red line) and $R_{50,\mathrm{H}}(5 \times 10^{20}\,\mathrm{cm}^{-2}, t)$ (blue solid line) during the merger. The plot shows $R_{50,\mathrm{H}}$ normalized to the pre-merger epoch ($R_{50,\mathrm{H}}(N_{\mathrm{H}}, 6.58\,\mathrm{Gyr})$). The stars show the corresponding R_{50} of the secondary galaxy relative to the primary galaxy's R_{50}. The merger increases $R_{50,\mathrm{H}}$ as the merger vigorously redistributes the gas. As the merger settles, the $R_{50,\mathrm{H}}$ remains enhanced, albeit to a lesser extent, until the galaxy's activity perishes and the dense CGM gas starts to diffuse without being replenished.

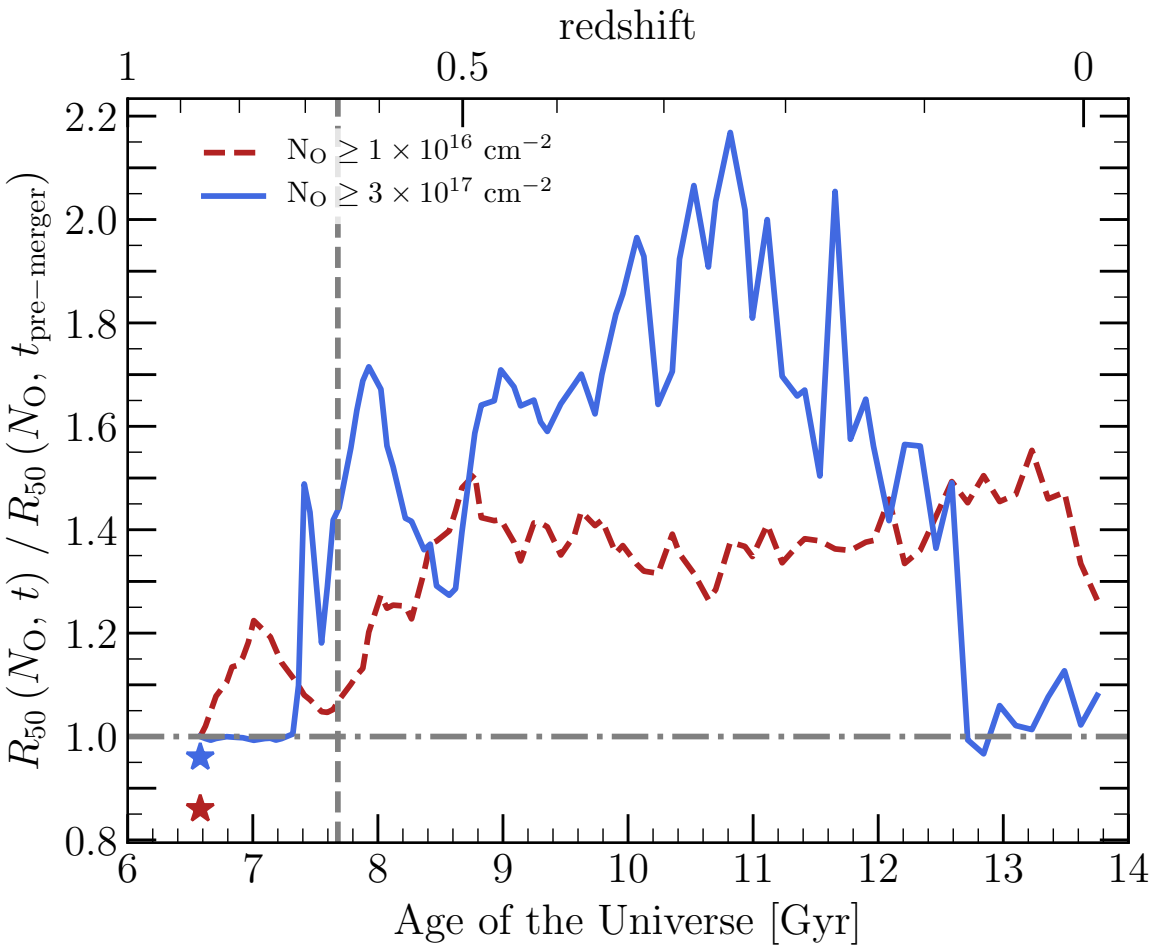

Figure 3.6: Similar to Figure 3.6, showing the evolution of $R_{50,\,O}(10^{16}\,\mathrm{cm}^{-2},\,t)$ (dashed brick-red line) and $R_{50,\,O}(3\times10^{17}\,\mathrm{cm}^{-2},\,t)$ (blue solid line) during the merger. Similar to hydrogen, the merger increases the covering of oxygen absorbers as the CGM is populated with metal enriched gas. The increase in $R_{50,\,O}$ persists long after the merger concludes.

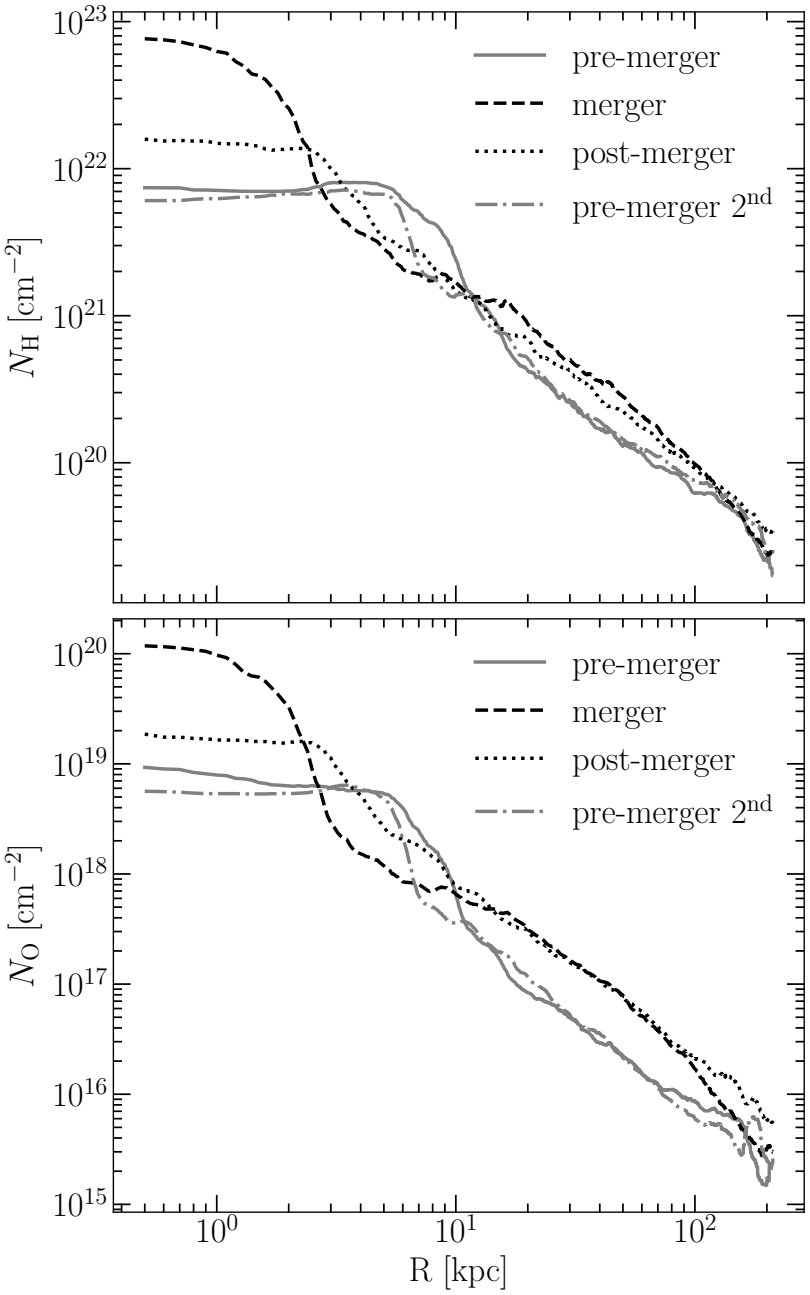

Figure 3.7: The median hydrogen (top) and oxygen (bottom) projected 2D density profile for three selected epochs: pre-merger (grey solid line), merger (black dashed line), and post-merger (black dotted line). The secondary galaxy's profiles are shown by the dot–dashed grey lines at the pre-merger epoch. The two galaxies show remarkable similarity in their density profiles. The merger funnels gas into the central regions of the galaxy while populating the CGM with enriched gas from the galactic disc eventually creating a flatter surface density profile. The enhanced column densities in the CGM persist long after the merger and progressively propagate to larger radii.

ties in the outer disc region ($R \in [2, 10]$ kpc) decline. Additionally, outflows induced by star formation and AGN activity after the first peri-centre passage populate the CGM with gas thus increasing the density profile between 10 and 100 kpc by a factor of ~ 3. After the merger, the central gas reservoir is further depleted being converted to stars, feeding the central BH, or being launched through outflows causing a decline in the central densities. Nonetheless, the post-merger central density profile remains enhanced when compared to its pre-merger counterpart. The outflows responsible for the increased density profile in the CGM continue to propagate outwards causing an increase at radii > 100 kpc post-merger compared to the pre-merger and merger profiles.

The effects of the merger on the CGM density profile: Succinctly, Figure 3.7 shows that the merger produces a shallower projected density profile by increasing the column densities at larger radii (> 10 kpc). After the merger, the central densities decline as the gas is converted into stars or launched in outflows. The CGM remains enriched compared to the pre-merger stage at radii > 10 kpc until $z = 0$; the enrichment progressively propagates outwards consistent with the gas being transported outwards by outflows.

The CGM metallicity

In addition to significant evolution in the gas density profile for merging galaxies, the gas metallicity profile can be impacted through metal enriched outflows that accompany the starburst phase of the merger sequence. To explore changes in the gas metallicity profile, Figure 3.8 shows the evolution of the median log(O/H) in three radial bins. The vertical grey line represents the merger time. The blue line shows evident signs of dilution in the central regions ($R < 10$ kpc) after first passage. The central dilution is caused by low metallicity gas being funnelled towards the centre of the galaxy due to merger-induced tidal torques, an effect that is well documented observationally (e.g., Kewley et al., 2006; Ellison et al., 2008a; Scudder et al., 2012). The central gas metallicity is replenished by stellar enrichment from the merger-induced star formation ~ 700 Myr after the merger. Meanwhile, the metallicity of the CGM, at $R > 75$ kpc, monotonically increases after the merger. The CGM metallicity remains elevated by $\log(\mathrm{O/H}) \sim 0.2 - 0.3$ dex until $z = 0$ (6 Gyr post-merger). I stress that the long term metallicity enrichment is likely driven by the cosmological evolution of the system as opposed to the merger. Comparing the metallicity enhancement

in the outer two radial bins, $R \in [75, 100]$ kpc and $R \in [100, 150]$ kpc, shows a delay in the metallicity enhancement which is indicative of out-flowing metal rich gas propagating to higher radii. The delay of ~ 300 Myr is consistent with the typical velocity of galactic winds (a few 100 km/s); for example, if I assume a wind with constant velocity $v \sim 100$ km/s travelling $\Delta R \sim 25$ kpc, the expected delay would be ~ 244 Myr. In the following section, I address in more detail the mechanisms responsible for enriching the CGM.

The increase in the metallicity in the CGM is also evident as a flattening of the metallicity profile. Figure 3.9 shows the metallicity profile of the galaxy's halo at three epochs: pre-merger (solid grey line), merger (dashed black line), and post-merger (dotted black line). After the merger, the CGM's metallicity increases, thus causing a flatter metallicity profile extending out to the halo. The flattening of the galactic disc's metallicity profile due to merger-driven inflows has been predicted by simulations (e.g., Perez et al., 2006; Rupke et al., 2010a; Perez et al., 2011) and confirmed in observations (e.g., Kewley et al., 2010; Rupke et al., 2010b). Moreover, although a central metallicity dilution is visible when using a large aperture (see $R \in [0, 10]$ kpc in Figure 3.8), the central 2 kpc region exhibits an enhancement in metallicity. The dilution effect is dependent on the initial metallicity profile of the pre-merger galactic discs (e.g., Torrey et al., 2012). A similar dependence of the dilution effect on the aperture has been reported in a spatially resolved analysis of the metallicity profiles of interacting galaxies, e.g., Barrera-Ballesteros et al. (2015) report an enhancement in the central SFRs of interacting galaxies accompanied by no variations in the central metallicity when compared to their isolated counterparts. The authors note that a central dilution in metallicity is seen when the aperture of the observation is large (similar to Figure 3.8).

The effect of the merger on the CGM metallicity: Summarizing, the merger populates the CGM with metal rich gas therefore enhancing the total CGM metallicity by a factor of ~ 3, and reducing the relative difference between the metallicity of the galaxy and its halo.

3.3.3 CGM ionization

I have shown in the previous sub-sections a long-lasting increase in the covering fractions of hydrogen and metals, and an increase in CGM metallicity. In this sub-section, I now compute the quantities that are directly measurable by observational

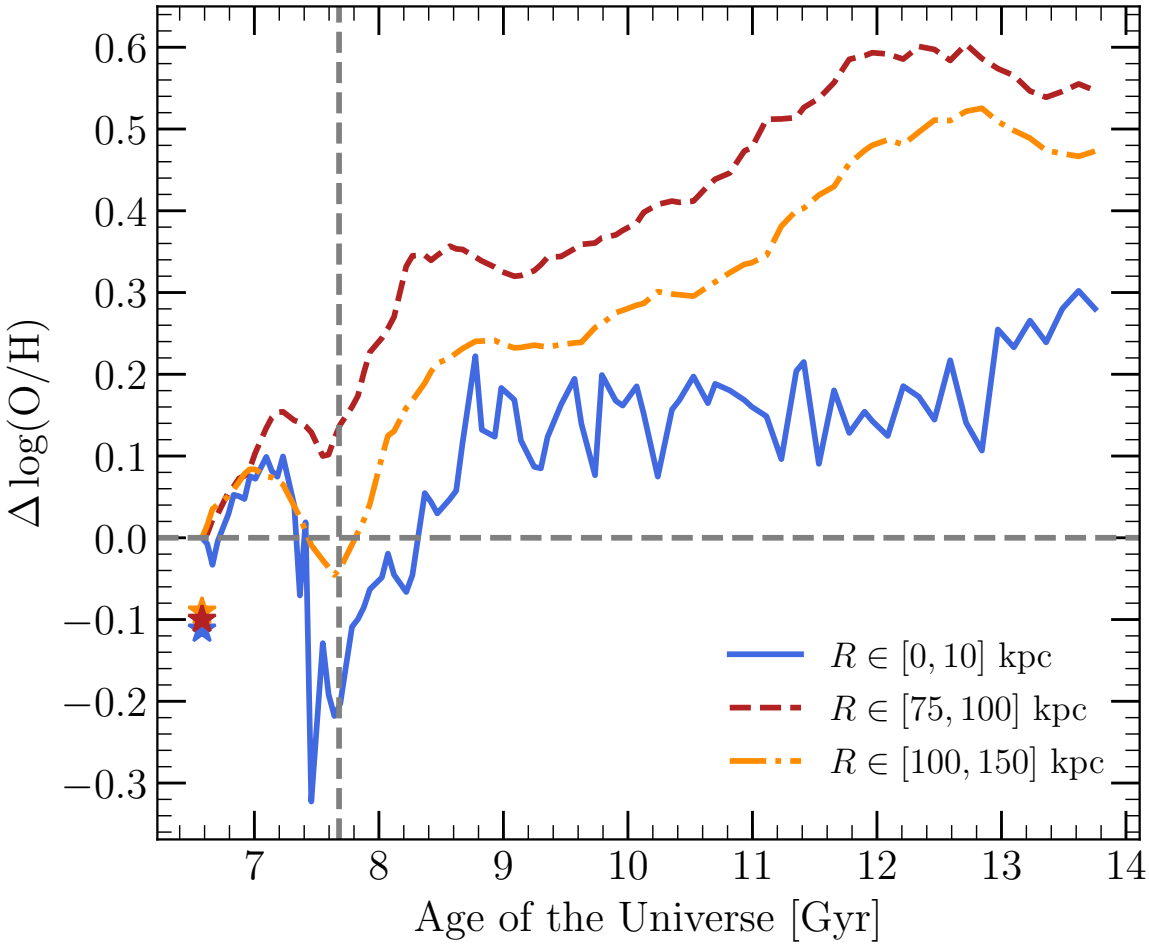

Figure 3.8: The evolution of the median oxygen abundance (normalized to the pre-merger O/H) in different radial bins (coloured lines) during the merger. The metallicity of the secondary galaxy relative to the primary galaxy at the pre-merger epoch is marked by star symbols representing the different radial bins. The secondary galaxy is metal poor compared to the primary galaxy. The vertical grey line marks the merger time. The merger increases the metallicity of the gas in the CGM. The long-lived enhancement propagates outwards; this is illustrated by the delayed response of the orange and brick-red lines. Known effects of mergers are also evident, i.e. the dilution effect in the central region of the galaxy due to metal poor gas being tidally funnelled into the centre during mergers.

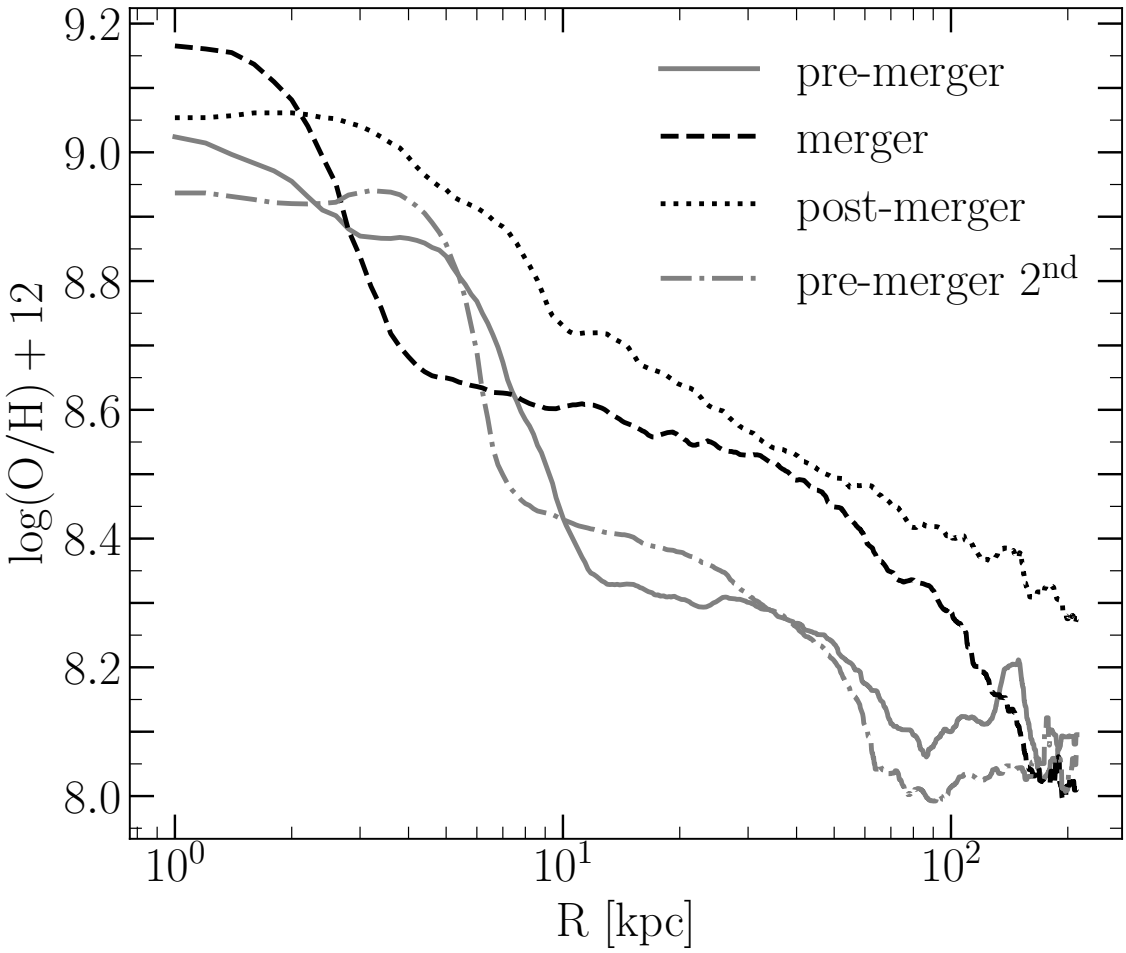

Figure 3.9: The evolution of the radially-averaged, projected metallicity profile for three selected epochs: pre-merger (grey solid line), merger (black dashed line), and post-merger (black dotted line). The secondary galaxy's metallicity profile at the pre-merger epoch is shown by the dot–dashed grey line. The merger produces a flatter metallicity profile by enriching the CGM metallicity.

studies of the CGM in absorption (e.g., Tumlinson et al., 2011, 2013; Werk et al., 2013; Bordoloi et al., 2014b; Peeples et al., 2014; Werk et al., 2014; Borthakur et al., 2015, 2016; Werk et al., 2016; Prochaska et al., 2017). Specifically, I use the ionization calculations from CLOUDY to predict the column densities of commonly observed species in absorption line studies. The ionization calculations in post-processing were done self-consistently with the physics models implemented in the simulation. As described in Section 3.2.5, I include radiation from an AGN and a time-varying UVB.

The presence of a stochastically varying AGN manifests as stochastic variations in the ionization of various species. Figure 3.10 shows the evolution of the covering fractions of absorbers with column densities characteristic of the CGM for three species: O VI, C IV, and H I. The species were chosen for demonstration purposes as their ionization energies span a large range. Consequently, these ions span gas that ranges in temperature from $T \sim 10^4$ K to $T \sim 10^6$ K. Before the merger ($t \sim 6.5$ Gyr), the galactic halo is mostly virialized and dominated by a hot gas traced by O VI; the halo has a smooth profile with little visible substructure. After the merger ($t > 7.6$ Gyr), the covering fractions of H I, C IV, and O VI decline. The hard radiation field from the AGN ionizes even O VI when radiating at a maximum ($\geq 10^{44}$ erg s^{-1}). Additionally, the enhanced activity (AGN and SFR) during the merger is responsible for strong outflows that populate the CGM with cool gas and metals and increase the covering fractions and R_{50}; the peak in SFR coincides with the sharpest increase in R_{50}, covering fractions, and CGM metallicity. When the AGN activity declines ($t > 10$ Gyr) the CGM begins to cool and the covering fractions of the various species increase again. At this epoch, the CGM is populated by outflows from the galactic disc which manifest in a clumpy CGM rather than the halo's mostly smooth hot gas profile prior to the merger. Notice that the variation in the covering fractions coincides with AGN intensity peaks. This is indicative of the effectiveness of the AGN model at altering the ionization of the CGM. Coupled with the expectation from both simulations and observations that mergers can fuel AGNs, Figure 3.10 suggests that even modest enhancements in the AGN luminosity will lead to a dominance of more highly ionized species. This is consistent with Oppenheimer & Schaye (2013) who show that AGN radiation can be an effective ionization source for the CGM.

I caution the reader that the ionization calculations presented in this study may be prone to uncertainties and further corrections owing to the ionization equilibrium assumption. Segers et al. (2017) demonstrate that stochastic AGN behaviour can keep CGM gas (i.e. metals) out of ionization equilibrium even at large radii (i.e. $2\times$

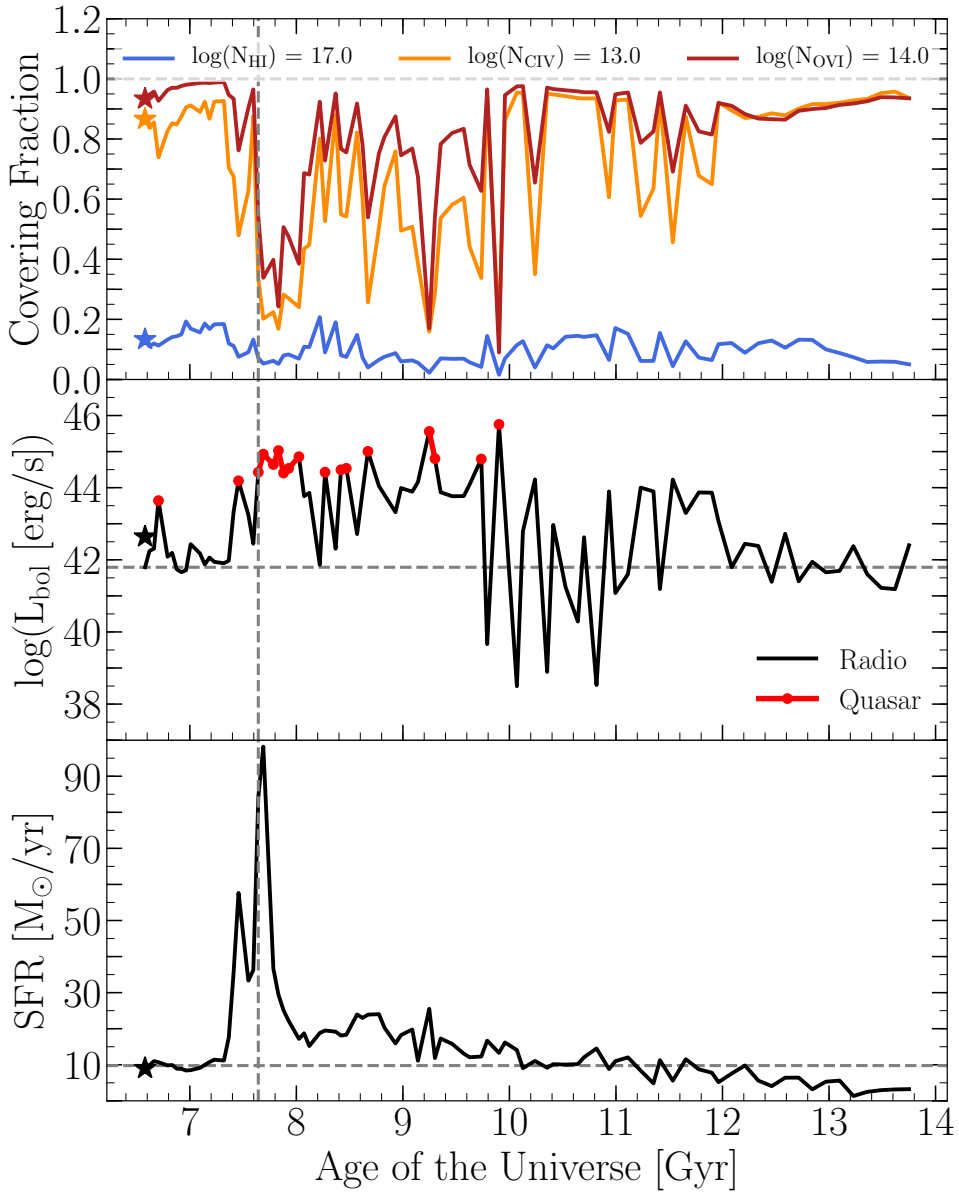

Figure 3.10: The evolution of the covering fractions of O VI, C IV, and H I are shown in blue, orange, and brick-red in the top panel, along with the AGN bolometric luminosity in the middle panel (colours refer to the associated AGN feedback mode – red: quasar mode, black: radio mode), and the SFR in the bottom panel. The stars represent the properties of the secondary galaxy at the pre-merger time. After the merger, the covering fraction of all ionization species decreases due to AGN radiative feedback decreasing the cooling rates of the CGM gas and increasing its internal energy. The stochastic fluctuations in AGN activity are matched by fluctuations in the ionization highlighting the effect of the AGN's hard ionizing radiation field on the ionization of the gas. Low ionization species (e.g., H I) survive in self-shielding regions. Note that the peak SFR (merger-induced) is responsible for the outflows leading to the aforementioned increase in covering fractions and R_{50}.

R_{200}). Additionally, Oppenheimer & Schaye (2013) and Oppenheimer et al. (2018a) illustrate the importance of non-equilibrium effects when modelling the ionization of the CGM. Simulations including non-ionization equilibrium (e.g. Oppenheimer et al., 2018b) predict CGM ionizations consistent with observed CGM properties. Therefore, assuming ionization equilibrium poses a principal limitation on the predictions of the work presented above. In order to understand the extent of the aforementioned limitation, I first examine the AGN variability time-scales. The AGN varies on time-scales $\gtrsim$ 45 Myr, which well exceed the recombination time-scales of the ions of interest, i.e. O VI, C IV, H I, in the simulated CGM ($\lesssim$ 20 Myr). Therefore, the simulated CGM reaches equilibrium on time-scales shorter than the variations in the underlying radiation field. Next, I investigate the presence of a proximity zone fossil (PZF) in the CGM. The simulated CGM shows no signs of a PZF, consistent with studies showing that AGN lifetimes $\lesssim$ 1 Myr are needed to produce a significant PZF (i.e. Oppenheimer et al., 2018a). The absence of a PZF is evident in Figure 3.10 where the covering fractions of ions immediately trace changes in the AGN bolometric luminosity. Therefore, although the assumption of ionization equilibrium is a limitation of this work, non-equilibrium effects appear to be negligible in the simulations I present. Furthermore, I note that the ionization state of the merger remnant's CGM in this study is consistent with the results of the COS-Haloes survey (Werk et al., 2014); both the H I and O VI covering fractions for absorbers with $N_{\rm H} \geq 10^{17}$ cm^{-2} and $N_{\rm O} \geq 10^{14}$ cm^{-2}, respectively, are in agreement with the covering fractions reported in COS-Haloes. The median redshift of the COS-Haloes sample corresponds to $t \sim 11$ Gyr ($\sim$ 3.5 Gyr post-merger) where the simulated merger remnant is an isolated disc galaxy showing no visible signatures of the merger (e.g. asymmetries in the stellar or H I profile) and the median AGN luminosity is $L_{\rm AGN} \lesssim 10^{41}$ erg/s. The agreement with the COS-Haloes results may be suggestive of the insignificance of the non-equilibrium ionization effects in the CGM of the simulated galaxy in this study.

Figure 3.10 demonstrates that the presence of the AGN provides a hard radiation field such that even the O VI covering fraction decreases. The ionized O VI populates higher ionization states. Therefore, I use the (rarely observed) O VII to trace the highly ionized gas by examining the gas ionization profile. Figure 3.11 shows the ionization profile, O VII / O I, at three evolutionary epochs during the merger. After the merger, the ionization of the gas increases at all radii, most notably in the CGM (R $\in [60, 150]$ kpc). This further supports the picture of AGN radiation increasing the

ionization of the CGM gas (i.e. declining covering fraction of all species). I remind the reader that my ionization model does not account for contributions from the host galaxy's stars to the ionizing radiation field.

In addition to the AGN's hard ionizing radiation field, during galaxy mergers gas in the colliding galactic discs may be shock heated up to X-ray emitting temperatures (i.e. Cox et al., 2006b). Cox et al. (2006b) demonstrated that the hot X-ray metal enriched gas can then be launched into the galactic halo to populate the CGM especially in the presence of an AGN [see figures 1 and 3 from Cox et al. (2006b)].

The effects of the merger on the CGM's ionization: In summary, my simulations show that, in agreement with previous works, AGN fuelling can be enhanced during a merger. As a result, the CGM gas around merger systems experiences competing effects between (i) increases in CGM metallicity driven by metal rich outflows and (ii) decreases in the observable ionization fractions as AGN activity significantly increases photoionization. Therefore, despite the increase in CGM metallicity by a factor of $2-3$, the covering fraction of the majority of ions observed in rest-frame UV spectra may actually decrease during a merger, as a result of the dominance of the AGN's hard ionization field. To recover the increase covering fraction and $R_{50,\,\mathrm{X}}$ reported in Section 3.3.1, one would need to apply proper ionization corrections.

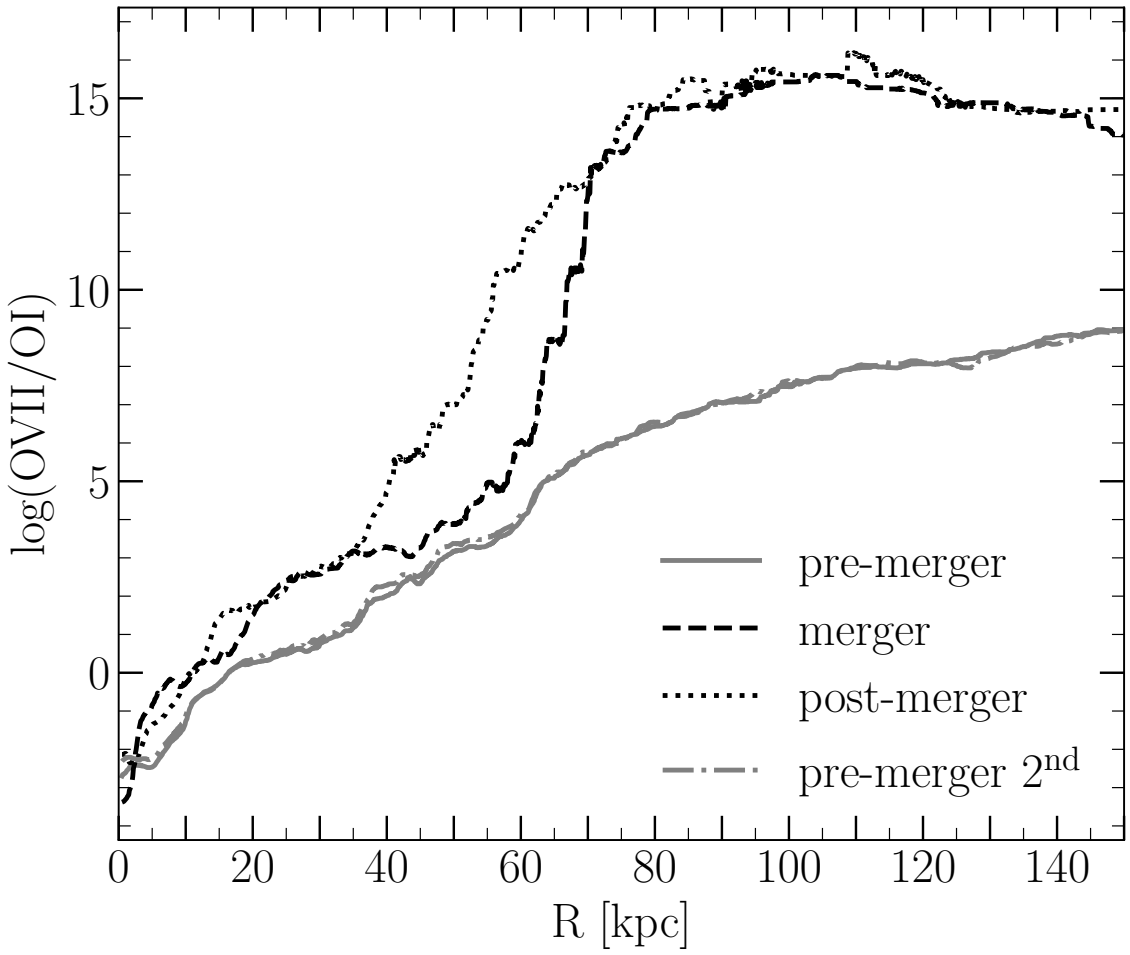

Figure 3.11: The ionization profile of oxygen at three stages of the merger: pre-merger, merger, and post-merger. The secondary galaxy's ionization profile at the pre-merger time is shown by the dot–dashed grey line. The ionization states of the CGM of both merging galaxies show remarkable similarity. After the merger the increase in the ionizing radiation field manifests as an increase in the gas ionization ratio. Low ionization species (i.e. O I) only survive in regions where the gas is self-shielding (i.e. galactic disc). 1 Gyr after the merger, O VII dominates the ionization profile as the CGM becomes more ionized.

3.4 Discussion

3.4.1 Merger-induced outflows populating the CGM

Galactic winds are observed to be ubiquitous in galaxies (e.g., Pettini et al., 2002; Adelberger et al., 2003, 2005; Martin, 2005; Rupke et al., 2005a,b; Veilleux et al., 2005, 2013; McElroy et al., 2015; Zschaechner et al., 2016; Maiolino et al., 2017; Woo et al., 2017). Moreover, galactic winds are a common feature in simulations of galaxy evolution where stellar and AGN feedback prescriptions produce large scale outflows of metal-enriched gas (e.g., Vogelsberger et al., 2013; Hopkins et al., 2014; Schaye et al., 2015; Grand et al., 2017). While such feedback mechanisms are primarily introduced to regulate star formation in galaxies (e.g., Oppenheimer & Davé, 2006; Puchwein & Springel, 2013), they are also responsible for recycling the galactic metal content and enriching the CGM (as shown in this study). Simulations of galaxy evolution illustrate that galaxies with no/low feedback lack a sufficient amount of metals in their haloes (e.g., Cox et al., 2006b; Zahid et al., 2014; Stinson et al., 2012), where a significant fraction of CGM metals are carried by galactic outflows (e.g., Fumagalli et al., 2011; Muratov et al., 2017).

In previous sections I have demonstrated that the merger increases the covering fractions of gas and metals in the CGM, the CGM metallicity, and CGM 'size' (i.e. as explored with the $R_{50,\,\mathrm{X}}$ parameter introduced in this work). The enhanced metallicity in the CGM propagates outwards with time (see Figure 3.8). There are two plausible mechanisms for transporting the gas into the CGM during a merger: tidal stripping and galactic winds/outflows. Whereas feedback driven outflows only directly impact the gas, tidal effects impact the stellar and gaseous components at a comparable level. Therefore, examining the spatial re-distribution of the stellar profile, one can better constrain the role of tidal torques in enriching the CGM gas. However, while inspecting the evolution of the stellar distribution throughout the merger, no significant transport of star particles is observed out to large radii which I attribute with the CGM ($R > 50$ kpc). The absence of a tidally stripped stellar component propagating outwards disfavours the tidal stripping mechanism to be the leading mechanism in populating the CGM at radii $R > 50$ kpc.

On the other hand, a wind-enrichment scenario is supported by an examination of the gas velocity field within the simulation, shown in Figure 3.12. The panels show mass-weighted projections (300×300 kpc^2) of the gas radial velocity in the

galaxy's reference frame at three stages of the merger (left to right). The direction and magnitude of the underlying gas velocity field is indicated by the colour map. Red colours indicate out-flowing gas, while blue colours show inflows. The galaxy's projected density profile is shown by the black contours. It is evident from Figure 3.12 that, post-merger, the velocity field becomes divergent (i.e., $\hat{r} \cdot \hat{v} > 0$) consistent with merger-driven outflows. More evidence of powerful outflows can be seen in the strong decline in the covering fractions, $R_{50,\,\mathrm{H}}$, and $R_{50,\,\mathrm{O}}$ at $t > 11$ Gyr which coincide with a strong AGN episode where the associated AGN feedback is returned in a series of radio bubbles (see Figure 3.10; i.e. 11.6 Gyr $\leq t \leq$ 11.9 Gyr). The radio-mode feedback is injected into the halo (at $R = 50$ kpc) in the form of rising buoyant hot bubbles. This form of feedback can efficiently remove gas from the halo causing a decline in the covering fractions of denser clumps ($N_{\mathrm{O}} > 10^{17}$ cm^{-2} and $N_{\mathrm{H}} > 10^{21}$ cm^{-2}). Meanwhile, the ambient hot dense medium probed by absorbers with $N_{\mathrm{O}} > 10^{16}$ cm^{-2} is sustained. Note that the metallicity of the gas is not affected, however the covering fraction is.

The outflows induced during the merger are responsible for increasing the CGM (50 kpc $\leq R \leq$ 150 kpc) metal mass by factors $3 - 4$ for up to 6 Gyr post-merger. This picture of outflows is consistent with current observational studies of the CGM which find a metal-enriched gas population out to impact parameters $\sim$ 150 kpc (e.g., Werk et al., 2014; Prochaska et al., 2017). Other studies report enhanced low-ionization column densities (stronger Lyα, Si II, and C IV), and different dynamics (Lyα equivalent width and velocity offset from the host's systemic velocity) in the CGM of starburst/post-starburst galaxies (i.e. Heckman & Borthakur, 2016; Heckman et al., 2017) when compared to normal star-forming galaxies; such differences can be explained by invoking galactic outflows from starburst regions within the hosts. Similar results are seen at high impact parameters in a sample of AGN hosts: The column densities of low-ionization species (e.g., H I, Si II, Si III) are enhanced in the CGM of AGN hosts when compared to normal star-forming galaxies or passive galaxies matched in stellar mass (Berg et al., 2018). Galactic outflows have also been shown to be the source of metals in the CGM in hydrodynamical simulations where the CGM gas of galaxies simulated without outflows remains relatively un-enriched (e.g., Oppenheimer & Davé, 2006; Ford et al., 2013; Hummels et al., 2013; Suresh et al., 2015).

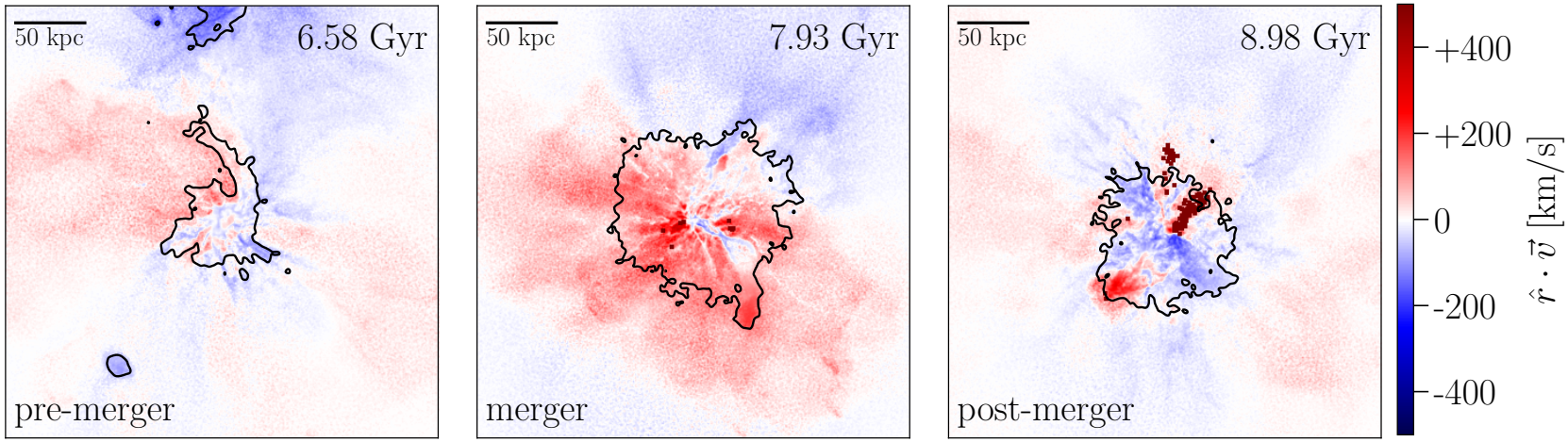

Figure 3.12: Mass-weighted gas radial velocity projections ($\hat{r} \cdot \vec{v}$) in the galaxy's reference frame at three epochs: pre-merger, merger, and post-merger (left to right). The red colours indicate outflowing gas while the blue colours represent inflows. The black density contour shows the galaxy's gas distribution as shown in figure 3.1. After the merger, the velocity field becomes divergent as it is dominated by merger-driven outflows. These outflows are responsible for increasing the CGM metal content and therefore metal covering fractions.

3.4.2 Analysis limitations and the effects of resolution

The presented analysis focuses on studying the CGM of galaxies undergoing a major merger to understand the interplay between mergers, a major evolutionary path, and the CGM. I use cosmological zoom-in simulations which enable us to study the CGM in a self-consistent evolutionary context. It is, however, worth noting that the physical models and simulation resolution may potentially have a significant impact on the simulated CGM properties.

The physical models implemented in the simulations (i.e. feedback processes, chemical enrichment) may have remarkable impact on the predicted CGM metal and energy budget (i.e. abundances and ionization) especially in cases where the physical model does not convergence at varying resolutions. The convergence of the model has been demonstrated at resolutions comparable to the ones used in this study (see Sparre & Springel, 2016; Grand et al., 2017). Moreover, the galaxy formation model used in this study has been calibrated to reproduce physical properties of $z = 0$ L* galaxies in cosmological zoom-in hydrodynamical simulations (Marinacci et al., 2014a; Vogelsberger et al., 2013; Grand et al., 2017). Grand et al. (2017) simulated a sample of 30 L* galaxies and demonstrated that the galaxy formation model reproduces appropriate stellar masses, stellar disc sizes, rotation curves, SFRs, and metallicities as in the local Universe. I leave a detailed discussion of the effects of varying the physical models on the CGM to future work.

The simulation resolution may strongly limit the resolved CGM structure and gas properties (i.e. density, metallicity, temperature; e.g., Nelson et al., 2016). Nonetheless, resolution is a necessary sacrifice bearing in mind the computational expense involved in cosmological simulations. Simulating gas clouds on observationally motivated scales ($\sim$ pc scales) is not currently possible in cosmological simulations. For example, in order to achieve ~ 1 pc scale resolution in the CGM, with typical CGM densities $n_{\rm H} \lesssim 10^{-2}$ cm^{-3}, a baryonic mass resolution limit of $m_{\rm b} \lesssim 2.5 \times 10^{-4}$ M$_\odot$ is required. Such an exorbitant mass resolution is well beyond the resolution limit of the current generation of galaxy evolution (even isolated simulations). However, small-scale, high-resolution simulations studying the evolution of single clouds in the CGM (e.g., Heitsch & Putman, 2009; Armillotta et al., 2017) complement my approach by providing a sub-resolution understanding of cloud survival in the CGM.

To test test the effect that the simulation resolution (mass and spatial resolution) can have on the results, and demonstrate the convergence of the CGM properties,

I use the re-runs of Sparre & Springel (2016) of the same halo (1605) at different resolutions (1605-1 and 1605-3). The halo 1605-1 is simulated $\sim 1.4\times$ the resolution of the Illustris project, while 1605-3 is the fiducial simulation with a $\sim 40\times$ better mass resolution than Illustris. Figure 3.13 shows the evolution of the covering fractions (normalized to the pre-merger state) of hydrogen and oxygen throughout the merger. The colours represent column density absorption thresholds while the different line styles represent the two resolution runs (1605-1: dashed lines; 1605-3: dotted lines). Increasing the resolution has no qualitative effect on the relative change in the covering fraction induced by the merger except for the highest $N_{\rm H}$ absorbers. The global enhancement (and the strengths of the enhancement) in the covering fractions of metals in the CGM reported in previous sections are reproduced at low-resolution. At high column densities (i.e. $N_{\rm H} > 10^{21}$ cm^{-2}), the contributing gas is dominated by high density gas cells. In the low resolution simulation, the high densities are not resolved as the dense substructure is dissolved into larger gas cells, therefore reducing the associated covering fractions. Similarly, increasing the resolution has little (qualitative) effect on the relative changes in the ionization of the CGM. The differences in the evolution of the CGM ionization (the strength and length of ionization) are dominated by the variations in the AGN accretion. At all resolutions the CGM's ionization directly follows the fluctuations in the BH's accretion rate.

3.4.3 An accounting of the CGM metal budget

Galactic feedback can have a significant impact on the CGM gas: In addition to launching gas into the CGM, galactic feedback enriches the gas reservoir with metals (stellar feedback) and increases the internal energy of the gas (stellar and AGN feedback; e.g., Cox et al., 2004, 2006b; Sinha & Holley-Bockelmann, 2009). It has been observationally inferred that sizeable amounts of gas and metals (equivalent to the gas within the ISM) reside in the extended gaseous halo surrounding galaxies (e.g., Bordoloi et al., 2014b; Peeples et al., 2014; Werk et al., 2014; Prochaska et al., 2017). Therefore, tracking the CGM metal budget and accounting for the different gas phases constrains the effect of merger-induced feedback processes on the CGM. Figure 3.14 shows a metal census in the CGM of the merging galaxy: 50 kpc $\leq$ R $\leq$ 150 kpc. After the merger, the metal mass fraction in hot (T $\geq 10^6$ K) and warm (10^5 K $<$ T $< 10^6$ K) gas increases by a factor of ~ 4. The hot gas cools within < 1 Gyr post-merger, while the warm gas continues to host $\gtrsim 50\%$ of the CGM's metals by

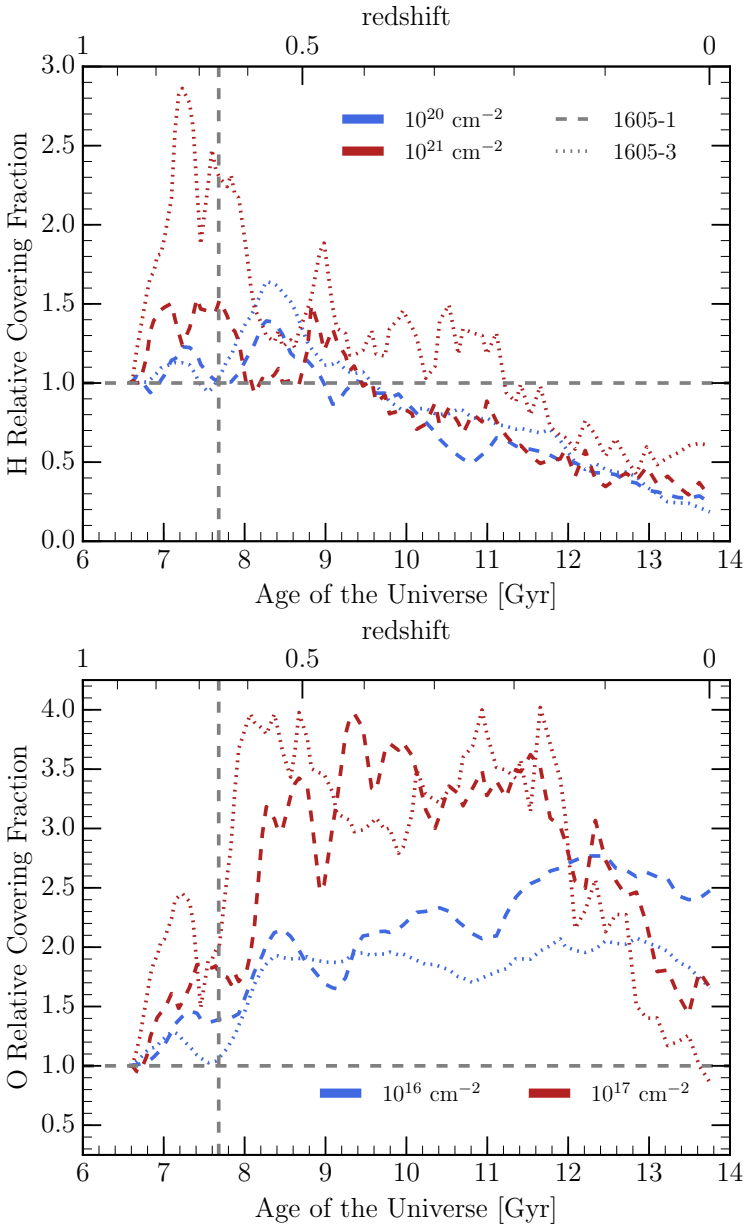

Figure 3.13: The evolution of the column density of hydrogen (left) and oxygen (right) absorbers throughout the merger. The different colours indicate absorption thresholds, while the line styles represent the different resolutions – 1605-1 ($\sim 1.4\times$ higher than the original resolution of the Illustris simulation): dashed lines; 1605-3 (the fiducial resolution simulation used for analysis in this chapter, $\sim 40\times$ higher than Illustris): dotted lines. The vertical grey dashed line indicates the merger time in the high-resolution simulation. Changing the resolution by a factor of ~ 40 has a negligible quantitative effect on the relative change in CGM properties except at the highest gas column densities. Qualitatively, the simulated CGM covering fractions remain unchanged for different resolutions.

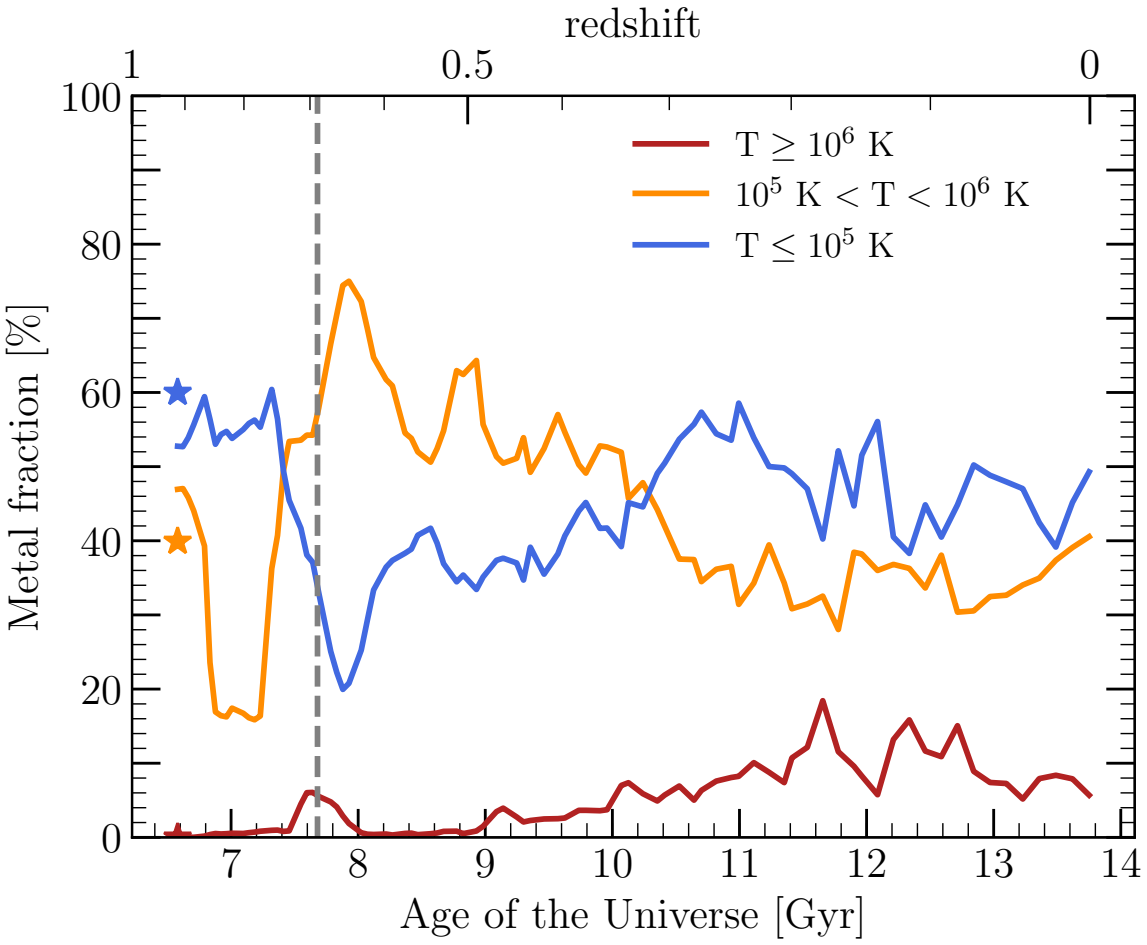

Figure 3.14: An accounting of the CGM metal budget for the various physical phases (coloured lines show the evolution of the metal fraction by mass: $M_{Z,\mathrm{phase}}/M_{Z,\mathrm{total}}$) around the merging halo (50 kpc $\leq$ R $\leq$ 150 kpc). The vertical dashed grey line indicates the time of the merger. The stars mark the metal fractions, by mass, in the CGM of the secondary galaxy. Although the secondary galaxy and its CGM are metal poor when compared to the primary galaxy, both parent galaxies' CGM show remarkable similarity in their fractional distribution of metals. After the merger, the induced stellar feedback enriches the gas while both stellar and AGN feedback increase the gas's internal energy. This is evident as an increase in the mass fraction of metals in the hot (T $\geq 10^6$ K; brick-red) and warm (10^5 K < T < 10^6 K; orange) gas phases by a factor of ~ 4. While the hot metal-enriched gas cools within ~ 1 Gyr post-merger, the warm gas continues to account for $\gtrsim 50\%$ of the halo's metal budget (by mass) for ~ 2.3 Gyr post-merger.

mass. The hot gas metal mass fraction starts to increase again at $t > 9$ Gyr potentially due to: (1) metal-rich, fast outflows (see the right-hand panel of Figure 3.12) populating the CGM, and (2) shock heating in the more massive merger remnant halo. The metal fraction hosted by the cool gas phase ($T \leq 10^5$ K) increases after the merger ($t \sim 8$ Gyr) as more cool metal-enriched outflows are deposited at $R > 50$ kpc. At $t \sim 10$ Gyr, the warm gas experiences significant cooling which coincides with a decrease in the mean AGN bolometric luminosity (see the lower panel of Figure 3.10). This suggests that AGN feedback (and radiative contributions) plays a key role in maintaining a warm CGM component. My result is consistent with the work of Oppenheimer et al. (2016) who showed that the covering fraction of O VI (which probes temperatures characteristic of the warm gas shown in Figure 3.14) in simulations which do not include AGN feedback is well below the observed O VI covering fraction. Therefore, the merger increases the metal mass fraction in the warm/hot CGM gas for > 3 Gyr post-merger.

The increase in the metal mass fractions in the gas phases may be driven by two factors: (1) changes in the gas-mass in each phase, and/or (2) changes in the metallicity of the respective phases. Figure 3.15 shows the probability density function of the gas-phase metallicity at three key epochs: pre-merger (top panel), merger (middle panel), and post-merger (lower panel). The coloured histograms represent the gas phases shown in Figure 3.14: $T \leq 10^5$ K (blue), 10^5 K $< T < 10^6$ K (orange), and $T \geq 10^6$ K (brick-red). The number of gas cells contributing to the individual gas phases is indicated in the top-right corner of each panel. It is evident that the merger drives an increase in the gas metallicity of all phases (notice the shift in the distributions' median to higher metallicities). Moreover, the merger induces the presence of a prominent super-solar metallicity gas component in all phases, although it is most evident in the cool gas phase ($T \leq 10^5$ K). The presence of high metallicity gas in the CGM is consistent with observations of the CGM (e.g. Tumlinson et al., 2011; Prochaska et al., 2017). For example, Prochaska et al. (2017) showed that $\sim 25\%$ of the COS-Haloes sightlines show super-solar metallicities. Although the merger drives an increase in the global CGM gas metallicity, a warm/hot metal poor ($\log(Z/Z_\odot) < -0.25$) gas component persists after the merger. Moreover, feedback processes excited during the merger increase the gas internal energy causing an enhancement in the amount of hot and warm gas during the merger. The heated gas then cools driving a decline in the amount of hot and warm gas in the post-merger epoch.

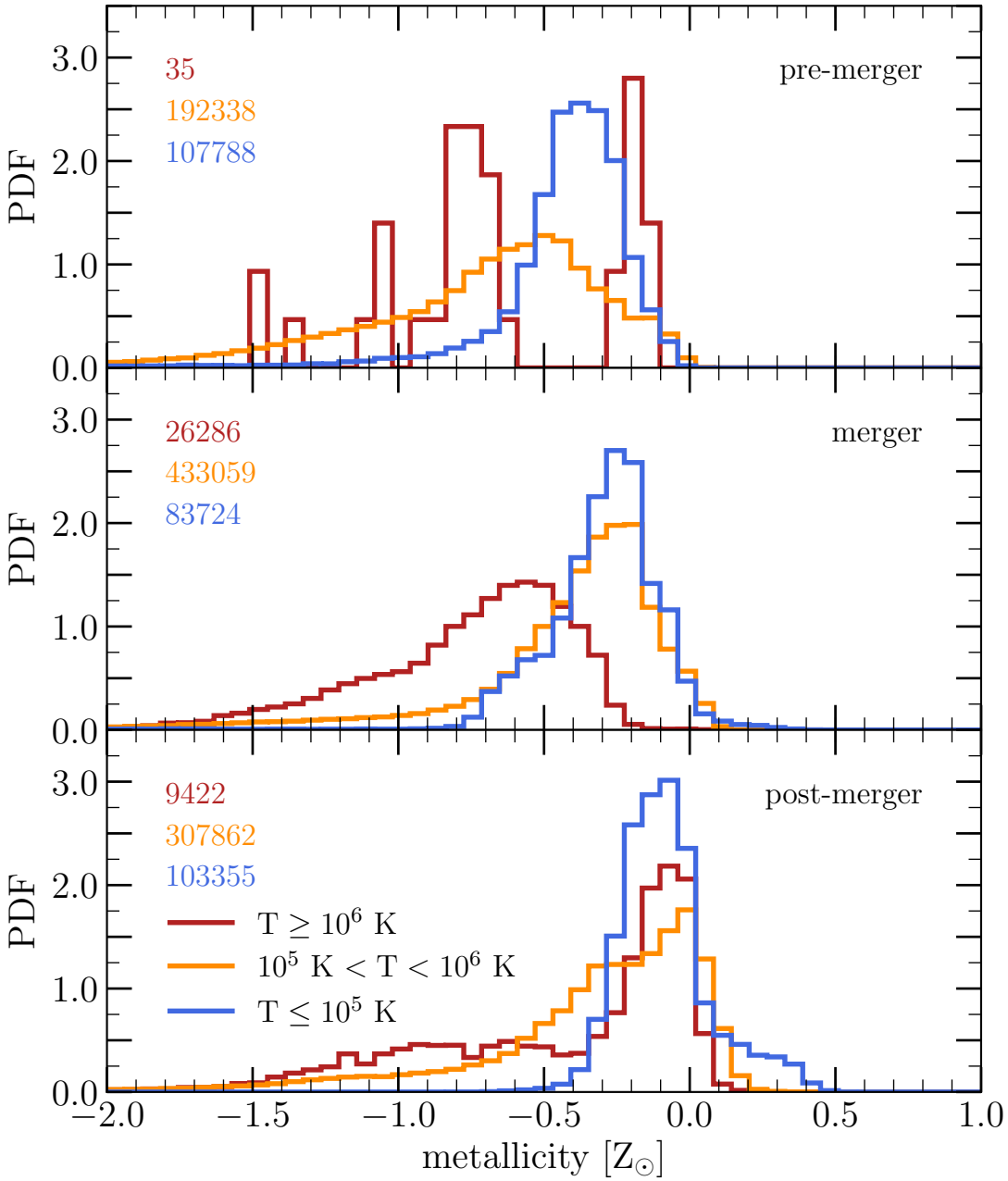

Figure 3.15: A census of gas phase metallicities in the CGM of the merging halo (50 kpc $\leq$ R $\leq$ 150 kpc). The coloured histograms represent different gas phases defined by their temperature. The number of gas cells contributing to each gas phase ($\propto M_{\text{gas phase}}$) is shown in the top right corner of each panel. After the merger, the median metallicity of all phases increases leading to a prominent super-solar metallicity gas component in all phases as the merger enriches the CGM with metals. Additionally, the budget of hot and warm gas (T $>$ 10^5 K) increases after the merger while a large fraction ($>$ 50%) of that gas remains at low metallicities ($\log(Z/\text{Z}_\odot) < -0.23$) extending to $\log(Z/\text{Z}_\odot) < -1.5$.

3.5 Conclusions

This chapter's primary focus is to demonstrate the effect that a major merger can have on the CGM of a galaxy. I use cosmological zoom-in hydrodynamical simulations (Sparre & Springel, 2016) to model the evolution of the CGM of a galaxy undergoing a major merger. I selected a merging galaxy from the Illustris project, where the merger occurs at $z = 0.66$ with a merger ratio of 1:1.16. The $z = 0$ descendant is a Milky Way-sized galaxy with stellar mass $M_\star = 10^{10.89}$ $M_\odot$ residing in a dark matter halo with total mass $M_{200} = 10^{12.00}$ $M_\odot$. I model gas ionization in post-processing using an ionization source which accounts for contributions from the host galaxy's AGN and a UVB consistent with the physics model adopted in the simulations (Marinacci et al., 2014a; Vogelsberger et al., 2013; Grand et al., 2017).

To quantify the effect of the major merger on the CGM chemical and ionization properties, I assess the change in the covering fractions of commonly observed ionic species, as well as total hydrogen and metals. Additionally, I define a characteristic CGM size ($R_{50,\,\mathrm{X}}$) to follow the spatial effect of the merger on the CGM gas/ionization profile.

I have demonstrated that:

1. The major merger can increase the covering fractions of oxygen ($N_\mathrm{O} > 10^{16-17}$ cm^{-2}) by factors of $2-4$ for > 4 Gyr post-merger. The total hydrogen covering fractions ($N_\mathrm{H} > 10^{20-21}$ cm^{-2}) can increase by factors of $1-1.25$ for ~ 3 Gyr post-merger. The increase in covering fraction is more evident for metals (e.g., oxygen) as the CGM gets enriched.

2. The newly populated CGM shows significant enhancement in its metal and baryonic budget, and its characteristic size ($R_{50,\,\mathrm{X}}$). The increasing size is more evident when probed using metal absorption which is consistent with metal rich outflows preferentially populating the CGM with metals. A factor of 1.3 increase in $R_{50,\,\mathrm{H}}(5 \times 10^{17}\,\mathrm{cm}^{-2},\, t)$ persists for a ~ 3 Gyr post-merger. $R_{50,\,\mathrm{H}}(10^{20}\,\mathrm{cm}^{-2},\, t > 11\,\mathrm{Gyr})$ declines as the gas in the CGM diffuses below the density threshold. The presence of oxygen in the CGM extends to larger radii with a factoral increase in $R_{50,\,\mathrm{O}}(10^{16}\,\mathrm{cm}^{-2},\, t)$ as high as $1.4\times$ persisting for ~ 6 Gyr.

3. The simulation predicts a $0.2-0.3$ dex increase in the CGM metallicity ($\log(\mathrm{O/H})$) that lasts for ~ 6 Gyr.

4. Merger-induced outflows populate the CGM with metals preferentially increasing the metal covering fraction and CGM metallicity.

5. The major merger triggers an AGN episode which, in addition to inducing outflows, returns significant amounts of energy to the surrounding halo causing an increase in the CGM ionization. Therefore, although the simulations predict an increase in the metallicity of the CGM, observationally one might expect a drop in the covering fraction or typical column densities of metal species in the rest-frame UV.

I stress that the long term ($> 2 - 3$ Gyr) enhancements in the CGM are likely driven by the cosmological evolution of the system as opposed to the merger.

Chapter 4

The effect of galaxy mergers on galactic star formation

This chapter is published as Hani et al. (2020b).

Abstract

Galaxy mergers are a major evolutionary transformation whose effects are borne out by a plethora of observations and numerical simulations. However, most previous simulations of galaxy mergers have used idealised, isolated, binary mergers and there has not been significant progress on studying statistical samples of galaxy mergers in large cosmological simulations. I present a sample of 27,691 post-merger (PM) galaxies ($0 \leq z \leq 1$) identified from IllustrisTNG: a cosmological, large box, magneto-hydrodynamical simulation suite. The PM sample spans a wide range of merger and galaxy properties (stellar mass, mass ratio, gas fraction). I demonstrate that star forming (SF) PMs exhibit enhanced SFRs on average by a factor of ~ 2, while the passive PMs show no statistical enhancement. I find that the SFR enhancements: (1) show no dependence on redshift, (2) anti-correlate with the PM's stellar mass, and (3) correlate with the gas fraction of the PM's progenitors. However, SF PMs show stronger enhancements which may indicate that other processes are at play (e.g., feedback efficiency). Although the SFR enhancement correlates mildly with the merger mass ratio, the more abundant minor mergers ($0.1 \leq \mu < 0.3$) still contribute $\sim 50\%$ of the total SFR enhancement. By tracing the PM sample forward in time, I find that galaxy mergers can drive significant SFR enhancements which decay over ~ 0.5 Gyr independent of the merger mass ratio, although the decay timescale is dependent on the simulation resolution. The strongest merger-driven starburst galaxies evolve to be passive/quenched on faster timescales than their controls.

4.1 Introduction

Chapters 2 and 3 focus on the CGM: a key component of the gas reservoir around galaxies. In Chapter 3, I demonstrated the critical effects that galaxy mergers can have on the galactic gas reservoir. Therefore, in the latter part of the thesis, I will shift focus to the effects of galaxy mergers on star formation by investigating how galactic star formation responds to galaxy interactions.

Galaxy mergers have been both theoretically predicted and observationally proven to play a key role in galaxy evolution (see Section 1.3). Merging galaxies have been observationally shown to have higher atomic and molecular gas fractions (e.g., Ellison et al., 2015, 2018b; Violino et al., 2018; Dutta et al., 2018), along with diluted central metallicities (e.g., Kewley et al., 2006; Scudder et al., 2012; Ellison et al., 2013b; Thorp et al., 2019). Observational studies also report that merging galaxies exhibit enhanced SFRs (e.g., Ellison et al., 2013b; Patton et al., 2013; Knapen et al., 2015; Cortijo-Ferrero et al., 2017a), and AGN activity (e.g., Ellison et al., 2011; Bessiere et al., 2012; Satyapal et al., 2014; Goulding et al., 2018; Ellison et al., 2019). The observed effects of galaxy mergers have been explained by numerical simulations as the outcome of non-axisymmetric gravitational torques which can lead to angular momentum losses in the galaxies ISM (e.g., Hernquist, 1989; Barnes & Hernquist, 1991; Mihos & Hernquist, 1996; Blumenthal & Barnes, 2018) and give rise to disturbed morphologies (e.g., Di Matteo et al., 2007; Lotz et al., 2008, 2010a,b; Pop et al., 2018). The loss of angular momentum leads the gas to being funnelled into the central regions, where it may cause a suppression in the central metallicity (e.g., Montuori et al., 2010; Torrey et al., 2012; Moreno et al., 2015; Bustamante et al., 2018), increase the central SFRs (e.g., Cox et al., 2008; Di Matteo et al., 2008; Moreno et al., 2015; Sparre & Springel, 2016), and feed an AGN (e.g., Di Matteo et al., 2005; Hopkins & Quataert, 2010).

Theoretical studies of galaxy mergers are often carried out in simulations of binary mergers where the same galaxies that partake in the merger are evolved in isolation (e.g., Barnes & Hernquist, 1996; Lotz et al., 2008; Torrey et al., 2012; Patton et al., 2013; Moreno et al., 2015, 2019). Recent efforts use cosmological zoom-in simulations (e.g., Sparre & Springel, 2016; Bustamante et al., 2018, Chapter 3), although identifying a control galaxy for comparison is a major challenge for zoom-in studies. While both binary merger simulations and cosmological zoom-in simulations provide powerful tools to study galaxy mergers at high resolution (spatial and temporal), they

both lack the large and diverse galaxy samples of large-box cosmological simulations. Recent studies have begun to investigate the effect of galaxy mergers in large cosmological boxes (e.g., Blumenthal et al., 2019; Patton et al., 2020; Rodríguez Montero et al., 2019). For an overview and comparison of isolated simulations, cosmological zoom-in simulations, and large box cosmological simulations, see Section 1.4.

In this chapter, I leverage the sizeable sample of galaxy mergers available in large cosmological box hydrodynamical simulations to investigate the impact of mergers on galactic star formation during the post-merger stage (i.e., post-coalescence). Using numerical simulations mitigates the unconstrained merger timescales in observational studies, while the large simulation box provides a diverse and representative galaxy sample, therefore alleviating a major challenge for idealised and cosmological zoom-in simulations. I identify galaxy mergers in the IllustrisTNG simulation suite (Marinacci et al., 2018; Naiman et al., 2018; Nelson et al., 2018a; Pillepich et al., 2018b; Springel et al., 2018; Nelson et al., 2019a) and then analyse the post-merger galaxy sample by implementing a methodology akin to observations. By comparing the post-merger star formation rates to controls that have not undergone a merger, I am able to isolate the effects of the merger on star formation rates (e.g., Patton et al., 2020).

The chapter is structured as follows: I first introduce the methodology in Section 4.2. In Section 4.3 I present the results highlighting the role of galaxy mergers in inducing star formation and I investigate major drivers affecting the strength of the SFR enhancements. Section 4.4 discusses the effects of control matching and simulation resolution, and ties my results to observational studies. Finally, I summarise my conclusions in Section 4.5.

4.2 Methods

The work presented in this chapter investigates the signatures of galaxy mergers during the post-merger stage. I focus on post-merger galaxies thus complementing the work of Patton et al. (2020) who studied galaxy pairs in IllustrisTNG. I identify galaxy mergers in the IllustrisTNG simulation suite (Marinacci et al., 2018; Naiman et al., 2018; Nelson et al., 2018a; Pillepich et al., 2018b; Springel et al., 2018; Nelson et al., 2019a) and compare the properties of the mergers' descendants to galaxies that have not undergone a merger in their recent evolution. In this section, I describe the numerical simulations (i.e., IllustrisTNG simulations), the details of the merger-identification method, and the process of generating a statistical control galaxy sample

for comparison.

4.2.1 Numerical simulations: TNG100-1 & TNG300-1

The work presented here is primarily focused on quantifying the effects of galaxy mergers beyond coalescence (post-mergers). I employ the IllustrisTNG simulation suite (Marinacci et al., 2018; Naiman et al., 2018; Nelson et al., 2018a; Pillepich et al., 2018b; Springel et al., 2018; Nelson et al., 2019a), which consists of several large box cosmological magneto-hydrodynamical simulations. I focus my analysis on the highest resolution runs of the largest two volumes of the IllustrisTNG simulations – TNG100-1 and TNG300-1. Using such large volumes (110.7^3 Mpc^3 and 302.6^3 Mpc^3 for TNG100-1 and TNG300-1, respectively) ensures a substantial sample of galaxies ideal for a statistical study of galaxy mergers. The galaxy sample is simulated in a fully cosmological environment, and it has realistic evolutionary histories and galactic properties (e.g., Nelson et al., 2018a; Pillepich et al., 2018b; Springel et al., 2018; Donnari et al., 2019; Huertas-Company et al., 2019; Rodriguez-Gomez et al., 2019; Tacchella et al., 2019b; Torrey et al., 2019). While TNG300-1 provides larger galaxy and merger samples, TNG100-1 allows us to investigate the effects of galaxy mergers at higher mass and spatial resolutions. TNG100-1 (TNG300-1) has a dark matter mass resolution $m_{\rm dm} = 7.5 \times 10^6$ M$_\odot$ ($m_{\rm dm} = 5.9 \times 10^7$ M$_\odot$), and a baryonic mass resolution $m_{\rm b} \sim 10^6$ M$_\odot$ ($m_{\rm b} \sim 10^7$ M$_\odot$). I also use TNG100-2 to ensure model convergence and investigate resolution effects; TNG100-2 is a re-run of TNG100-1 at a roughly equal resolution to TNG300-1. All the simulations have a temporal resolution ~ 162 Myr.

For most of my analysis I will report results from TNG300-1 as my fiducial simulation because the large box size provides exquisite statistics. Nonetheless, the results are broadly consistent between TNG300-1 and TNG100-1. I refer the reader to Section 4.4.2 where I discuss the effects of varying the simulation resolution on my conclusions.

The IllustrisTNG galaxy formation model was introduced in Weinberger et al. (2017) and Pillepich et al. (2018a), and builds on its predecessor, the Illustris model (Vogelsberger et al., 2013; Torrey et al., 2014), with several additions and modifications to the numerical framework and physical model. The IllustrisTNG physical model includes:

1. Star formation: Star formation occurs in a pressurised interstellar medium

(ISM) for $n_{\rm H} \gtrsim 0.1$ cm^{-3} following the Springel & Hernquist (2003) formalism. Star particles represent stellar populations with a Chabrier (Chabrier, 2003) initial mass function.

2. Galactic winds: Stellar feedback is implemented using hydrodynamically decoupled winds that transport mass, momentum, metals, and thermal energy.

3. Metal enrichment: Metals are returned to the ISM via SN type Ia, SN type II, and AGB stars.

4. Gas cooling and heating: Gas can cool through primordial channels as well as metal-line cooling. Gas heating is calculated assuming a superposition of a redshift-dependent, spatially uniform UV background (Faucher-Giguère et al., 2009), and an AGN radiation field (Vogelsberger et al., 2013).

5. Growth and feedback of BHs: Accretion onto BH sink particles is described by Bondi-Hoyle accretion. The associated feedback from AGN employs kinetic feedback (low accretion rates), and thermal feedback (high accretion rates).

For a detailed description of the simulations and physical model, I refer the reader to the IllustrisTNG introduction and methods papers: Weinberger et al. (2017); Marinacci et al. (2018); Naiman et al. (2018); Nelson et al. (2018a); Pillepich et al. (2018a,b); Springel et al. (2018), and references therein.

4.2.2 Merger identification

I identify galaxy-galaxy mergers in IllustrisTNG from the publicly available merger trees created using SUBLINK (Rodriguez-Gomez et al., 2015). The SUBLINK merger trees link sub-haloes to their progenitors and descendants. Consequently, galaxy mergers are defined as nodes within a tree; viz. a merger occurs when a sub-halo has two distinct direct progenitors. Note that I use "post-merger" to refer to galaxies immediately after the merger (i.e., first snapshot after the merger) which corresponds to ≤ 162 Myr post-merger at the snapshot time resolution of IllustrisTNG. In Section 4.3.2, I follow the evolution of post-mergers and hence, in that section only, "post-merger" refers to galaxies that have undergone a merger in their recent past. Therefore, post-mergers (merger remnants) are parametrized by:

- z: The redshift of the post-merger. I include in my analysis post-mergers at $z \leq 1$, which allows us to study the redshift evolution (or lack thereof) of mergers and their descendants.

- $M_\star$: The stellar mass of the post-merger. Various studies have noted the spurious assignment of mass caused by sub-haloes in close proximity when using halo finders (i.e., numerical stripping). For example, the dark matter mass of satellites has been shown to correlate with the distance to their host galaxies (Sales et al., 2007; Wetzel et al., 2009). Numerical stripping has also been demonstrated to affect stellar mass estimates (i.e., Rodriguez-Gomez et al., 2015). I circumvent the subtleties of stellar mass calculations by adopting the maximum stellar mass over the past 0.5 Gyr ($M_\star^{\rm max}$) for all mass ratio calculations following Patton et al. (2020). This approach is similar to Rodriguez-Gomez et al. (2015), with an additional restriction on lookback time; i.e., I minimise the effects of numerical stripping yet I still account for physical stripping by limiting the lookback time. Driven by the simulation resolution, galaxies with stellar masses $\log(M_\star/{\rm M}_\odot) \geq 9$ are reliably resolved. Therefore, I limit my analysis to post-mergers with stellar mass $10^{10} \leq M_\star/{\rm M}_\odot \leq 10^{12}$ and progenitors with stellar mass $M_\star \geq 10^{10}{\rm M}_\odot$ (see the mass ratio description).

- μ: The stellar mass ratio of the progenitors. Note that I define the mass ratio to be $0 < \mu \leq 1$. In cases where more than two direct progenitors are found, I parametrize the merger remnant using only the most major merger. The masses used to calculate μ correspond to the stellar mass within twice the stellar half-mass radius. My analysis includes descendants of mergers with $\mu \geq 0.1$, which is a requisite for investigating the varying effects of mass ratio in galaxy mergers. The simulation's mass resolution limit, coupled with the mass ratio range, determines the stellar mass range of the post-merger sample and their progenitors: $10^{10} \leq M_\star/{\rm M}_\odot \leq 10^{12}$.

I am primarily interested in studying the effects of galaxy mergers on star formation during the post-merger stage, therefore I exclude from my sample post-mergers that are currently undergoing new close interactions but have not yet fully merged. Particularly, I ignore post-mergers that are overlapping with another galaxy, which would hinder my ability to separate the effects of the current interaction from those

of the merger. Following the methodology of Patton et al. (2020), I define:

$$r_{\rm sep} = \frac{r}{R_{1/2}^{\rm host} + R_{1/2}^{\rm comp}} \tag{4.1}$$

where r is the separation of the host (post-merger) from its nearest neighbour (companion), $R_{1/2}^{\rm host}$ is the stellar half-mass radius of the host (post-merger), and $R_{1/2}^{\rm comp}$ is the stellar half-mass radius of the nearest neighbour. I exclude post-mergers with $r_{\rm sep} \leq 2$ from my sample. In addition, I ignore galaxies with unresolved SFRs, viz. $SFR < 10^{-3}$ M$_\odot$ yr^{-1} and $SFR < 10^{-4}$ M$_\odot$ yr^{-1} in TNG100-1 and TNG300-1, respectively (see Donnari et al., 2019).

My post-merger sample consists of $1,855$ post-mergers in TNG100-1, and $25,836$ post-mergers in TNG300-1 with stellar masses $10^{10} \leq M_\star/{\rm M}_\odot \leq 10^{12}$, $z \leq 1$, and $\mu \geq 0.1$. The properties of the post-merger sample are summarised in Figure 4.1 which shows the distributions of $M_\star$, μ, and z for the post-merger sample in TNG300-1 and TNG100-1. The post-mergers in my sample are uniformly distributed across redshift $0 \leq z \leq 1$. While the merger sample in IllustrisTNG spans a large range of mass ratios, minor mergers ($\mu < 0.3$) dominate the population of mergers. I note that the dearth of post-mergers at $10^{10} < M_\star/{\rm M}_\odot \lesssim 10^{10.2}$ is driven by the stellar mass limits applied in the post-merger selection (i.e., progenitor stellar mass $M_\star \geq 10^{10}$ M$_\odot$). Figure 4.2 depicts selected examples of post-mergers from my sample. The post-mergers exhibit disturbed morphologies with evident low surface brightness features (e.g., shells, tidal tails).

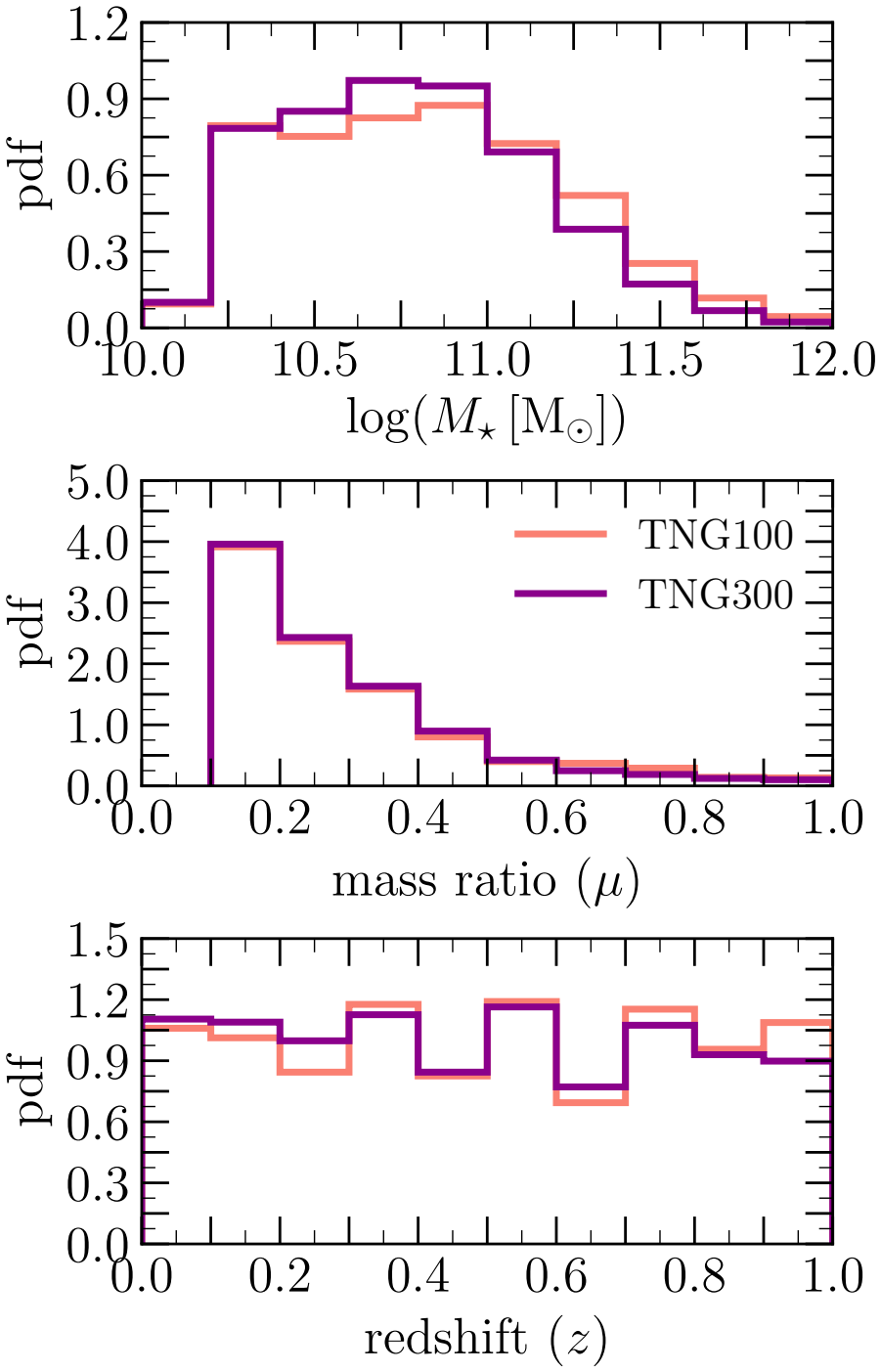

Figure 4.1: The stellar mass ($M_\star$), mass ratio (μ), and redshift (z) distributions of my post-merger samples selected from TNG100 (salmon histogram) and TNG300 (purple histogram). The sample spans a wide range in mass ratio ($\mu \geq 0.1$) and redshift ($z \leq 1$) which is key when studying the effects of galaxy mergers during the post-merger stage. In total, I selected $1,855$ post-mergers from TNG100 and $25,836$ from TNG300.

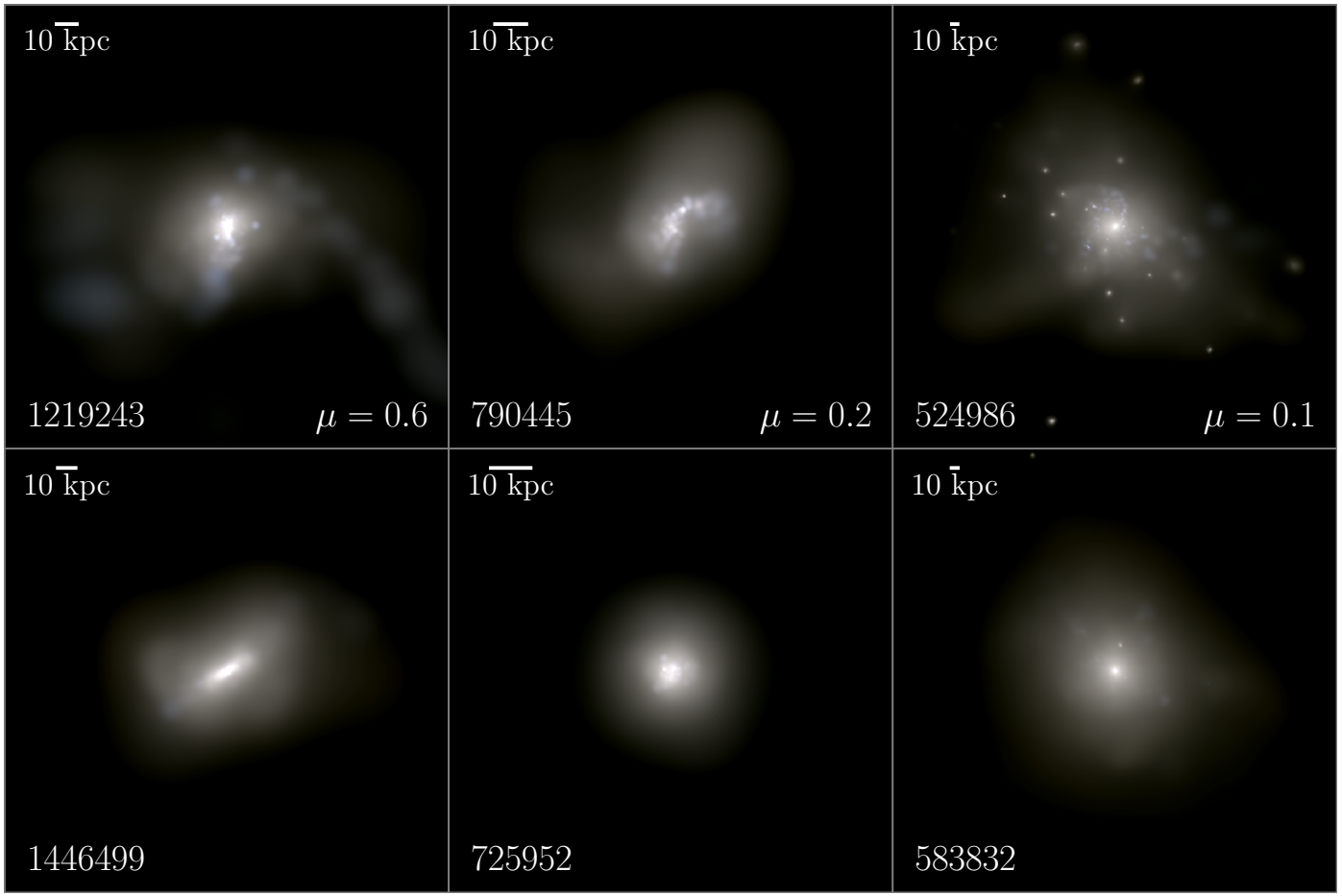

Figure 4.2: An example of three $z = 0$ post-mergers (top panels) with different mass ratios (μ) along with their respective control galaxies (bottom panels) selected from TNG300-1. The panels show synthetic stellar composite images using the `JWST_f200w, JWST_f115w` and `JWST_f070w` photometric filters; the images were generated using the IllustrisTNG image visualisation tool (Nelson et al., 2019a). The `SubfindID` is indicated in the lower left corner of each panel, and scale bar (top left) indicates a 10 kpc physical scale. The merger remnants exhibit evident low surface brightness features and disturbed morphologies.

4.2.3 Statistical controls

I quantify the effects of galaxy mergers by adopting a commonly used control matching approach in observational studies of galaxy interactions/mergers (e.g., Ellison et al., 2013b; Patton et al., 2013). For each post-merger, I identify a control galaxy to which I compare the properties of the post-merger. In this section, I describe the process of creating the control sample.

Large-box cosmological simulations provide a large and diverse population of galaxies that allows us to statistically study the changes in post-mergers compared to similar galaxies that have not undergone a merger. Comparing merger descendants to galaxies that have not undergone a recent merger allows us to isolate the effects of a merger whilst removing biases that may arise from known galaxy correlations (e.g., environment, stellar mass, redshift).

Following Patton et al. (2016) and Patton et al. (2020), I assign a single control galaxy to each post-merger in my sample. However, whereas Patton et al. (2020) studied the pair interaction phase I am interested in studying post-mergers. Therefore, I apply some modifications to my control matching process. I first create a galaxy pool that includes all galaxies at $z \leq 1$ with resolved[1] SFRs, $M_\star \geq 10^{10}$ $M_\odot$, and $r_{\rm sep} > 2$. I exclude galaxies that have undergone a merger ($\mu \geq 0.1$) within the past 2 Gyr, thus generating an initial pool that includes $3,934,409$ galaxies in TNG300-1 ($263,794$ galaxies in TNG100-1). I then quantify the environment of each galaxy (with stellar mass $M_{\star,\rm host}$) in the pool by calculating the number of neighbours within a 2 Mpc radius (hereafter N_2) and the distance to the nearest neighbour with $M_\star \geq 0.1 \times M_{\star,\rm host}$ (hereafter r_1). I also classify control galaxies and post-mergers as star-forming (SF) or passive. The classification is performed by applying a linear fit to the star forming main sequence (SFMS) at stellar masses between $10^9 - 10^{10.2}$ $M_\odot$ which is extrapolated to higher $M_\star$ following the methodology of Donnari et al. (2019). Galaxies that lie below $2\sigma_{\rm MS}$ from the SFMS are classified as passive[2]. Finally, for each post-merger I select the single *best* statistically matched control galaxy as follows: I first reduce the control pool to those galaxies that are in the same snapshot and have the same class (i.e., SF or passive) as the post-merger (i.e., matching in redshift and class). I stress the importance of the SF/passive class match: ignoring the class in the matching procedure would yield an unfair comparison where SF galaxies

[1] SFRs are not resolved below 10^{-3} $M_\odot$/yr in TNG300-1, and 10^{-4} $M_\odot$/yr in TNG100-1.

[2] $\sigma_{\rm MS}$ is the standard deviation of the SFMS residuals between $10^9 - 10^{10.2}$ $M_\odot$; for TNG300-1 $\sigma_{\rm MS} = 0.3$ dex

may have passive controls (and vice versa). Then, I search the snapshot-culled control pool for galaxies with $M_\star$ within a tolerance of 0.05 dex, and N_2 and r_1 within 10% of each post-merger. In most cases the initial tolerances yield at least one match. However, in some cases where no matches are found within the initial tolerances, I grow the tolerance range by 0.05 dex and 10% and repeat the search until at least one match is found. If more than one match is found, I select the *best* match in all three parameters $M_\star$, N_2, and r_1 following the weighting scheme of Patton et al. (2016). I exclude from my analysis post-mergers that require more than 4 iterations to identify a control; four iterations corresponds to unacceptably large matching tolerances (i.e., $\Delta \log M_\star = 0.2$, 40% in N_2, and 40% in r_1). Figure 4.3 compares the distributions of post-mergers and their controls (both selected from TNG300-1) in the three matching parameters: $M_\star$, r_1, and N_2. The post-mergers are excellently matched by the control population. The TNG100-1 post-merger sample is as closely matched as that of TNG300-1.

Once the controls have been identified, I statistically quantify the enhancement (or suppression) in star formation by comparing post-mergers to their controls as an ensemble using the following metric:

$$Q(sSFR) \equiv \frac{\langle sSFR_{\rm pm} \rangle}{\langle sSFR_{\rm control} \rangle} \tag{4.2}$$

where $\langle sSFR_{\rm pm} \rangle$ is the arithmetic mean of the post-mergers' specific star formation rates (sSFRs), and $\langle sSFR_{\rm control} \rangle$ is the arithmetic mean of the controls' sSFRs. The sSFR is calculated using the SFR within twice the stellar half mass radius and the associated stellar mass. The metric used in this work has been extensively used in the literature to study the effects of galaxy interactions on star formation (e.g., Patton et al., 2013, 2020).

4.3 Results

4.3.1 Effects of mergers

Star formation in post-mergers

I first investigate the effect of mergers on the SFR of the selected post-merger galaxy sample. Figure 4.4 shows the distribution of post-mergers in the SFR$-M_\star$ plane

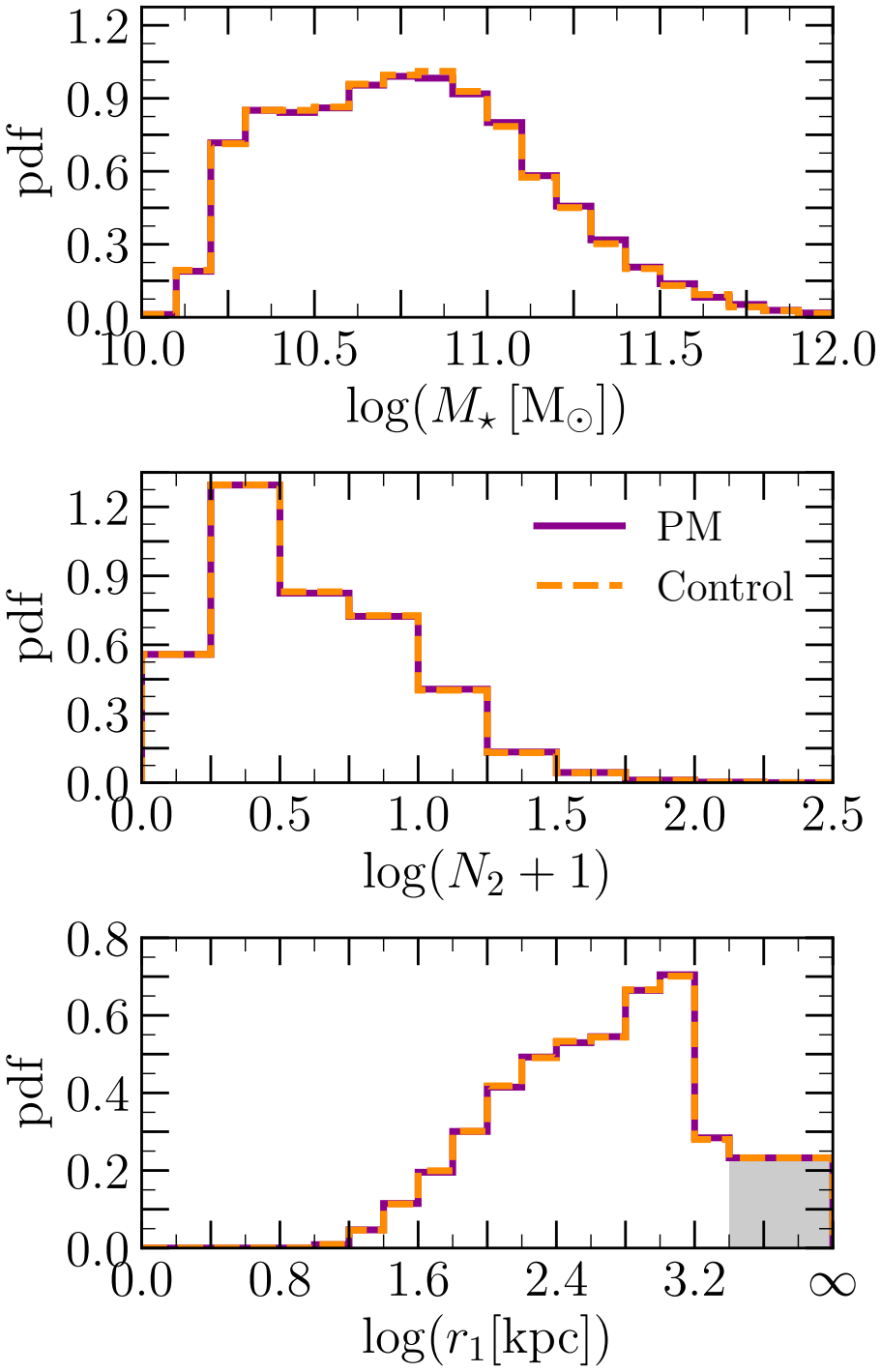

Figure 4.3: A comparison between the post-merger sample and their respective controls in TNG300-1. The grey shaded bin in the r_1 distribution includes all galaxies with $r_1 > 2$ Mpc. The figure only shows the quantities which are allowed to vary during the control matching (i.e., $M_\star$, N_2, and r_1). The control matching is equally excellent for the TNG100 sample (not shown).

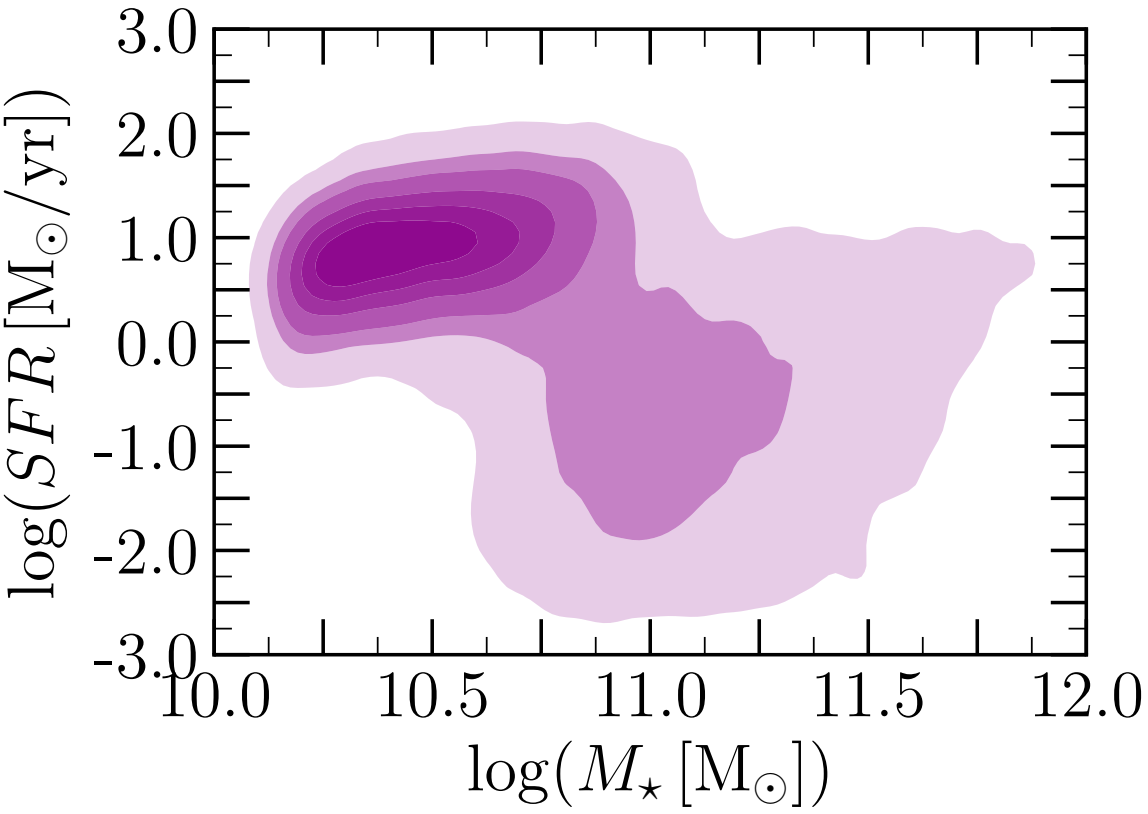

Figure 4.4: The distribution of post-mergers in TNG300-1 in SFR$-M_\star$ space. The post-mergers sample I present spans a large range in SFR and stellar mass including star-forming galaxies as well as passive galaxies.

in TNG300-1, my fiducial simulation. While most of the post-mergers populate the star-forming galaxy main sequence (67% of the post-merger sample in TNG300-1), my post-merger sample spans a wide range in stellar mass and SFR including passive galaxies (33% of the post-merger sample in TNG300-1). Therefore, the post-merger sample selected from IllustrisTNG is well-suited for a systematic and statistical study of the SFRs in post-merger systems.

To *fairly* investigate the effects of galaxy mergers on the post-mergers' SFR I compare the SFR of post-merger galaxies to their control counterparts. I remind the reader that the control galaxies are chosen to have not undergone a merger ($\mu \geq 0.1$) within the past 2 Gyr while being matched to the post-merger sample in N_2, r_1, redshift, and $M_\star$. Table 4.1 summarises the comparison of the average sSFRs of post-merger and their respective controls, $Q(sSFR)$ (defined in equation 4.2). In the full sample, post-mergers statistically have elevated SFRs with a mean enhancement of $Q(sSFR) = 2.057 \pm 0.024$.

	$Q(sSFR)$	$\sigma_{\mathrm{Q(sSFR)}}\sqrt{N}$
all	2.057	0.024
star-forming	2.073	0.020
passive	0.983	0.022

Table 4.1: A comparison of the sSFRs of post-mergers and their controls. The table reports $Q(sSFR)$ and the associated standard error on the mean for the full post-merger sample, and sub-samples therein. The post-merger sample generally has elevated $Q(sSFR)$ values. The signal is dominated by the star-forming post-mergers while the passive post-mergers exhibit sSFRs which are, on average, consistent with their controls.

The SFR enhancement (or lack thereof) is more pronounced for the star-forming and passive post-merger sub samples, respectively. The SFRs are enhanced in the star-forming sample with $Q(sSFR) = 2.073 \pm 0.020$. The enhancement reported in my SF post-merger sample is consistent with those reported in observational studies. For example Ellison et al. (2013b) measured a factor of 2.5 increase in the SFR of (star forming) post mergers in the SDSS, very similar to the factor of two found here. Conversely, the passive post-merger sample is statistically consistent with no SFR enhancement ($Q(sSFR) = 0.983 \pm 0.022$).

In summary, the post-merger sample in IllustrisTNG exhibits a statistical enhancement in SFR consistent with observations. The enhancements are more pronounced in star-forming post-mergers. In the following sections, I will dissect the dependence of the SFR enhancement/suppression on galaxy properties (e.g., redshift, stellar mass) and therefore gain insight on the physical mechanisms driving said enhancement/suppression.

Effect of redshift evolution

From the perspective of galaxy mergers, the Universe was much sprier at earlier times: several theoretical and observational studies report a decline of the galaxy merger rate with decreasing redshift (e.g., Lin et al., 2008; de Ravel et al., 2009; Lotz et al., 2011; López-Sanjuan et al., 2013; Rodriguez-Gomez et al., 2015). Whilst mergers can efficiently drive SFR enhancements at low redshifts, their contribution to the Universe's star formation rate density is thought to decrease with increasing

redshifts (e.g., Rodighiero et al., 2011; Kaviraj et al., 2013; Madau & Dickinson, 2014; Lofthouse et al., 2017; Wilson et al., 2019). The scenario in which the contribution of galaxy mergers to star formation decreases with increasing redshift is challenged by other studies which report that galaxy interactions continue to induce star formation at high redshift (e.g., Lin et al., 2007; Wong et al., 2011). Therefore, to properly quantify the contribution of mergers to the global star formation rate density, one must assess the effect of mergers on SFR enhancements across cosmic time. For example, Patton et al. (2020) examined the redshift dependence of SFR enhancement in galaxy pairs and reported smaller mean SFR enhancement with increasing redshift. Patton et al. (2020) demonstrate that the decrease in the mean SFR enhancements at higher redshift is offset by the increased fraction of galaxies undergoing merger-triggered SFR enhancements leading to higher net SFR enhancements (11% at $z < 0.2$ to 16% at $0.6 < z < 1$) in their sample.

Figure 4.5 shows the evolution in the mean sSFR across redshift for post-mergers and their controls (top panel), and the associated sSFR enhancement in post-mergers (middle and bottom panels). The mean sSFRs of both post-mergers and controls decline with decreasing redshift, a well-understood consequence of the decreasing accretion rate onto haloes (e.g., Dekel et al., 2009) and therefore the increasing quenched fraction (e.g., Donnari et al., 2019). Despite the evolution of the average sSFR across cosmic time, post-mergers exhibit a steady sSFR enhancement, $Q(sSFR) \sim 2$, at all redshifts $0 \leq z \leq 1$. By separating the sample by their SFRs, the lower panel of Figure 4.5 shows that star forming post-mergers drive the aforementioned enhancement, while passive post-mergers have sSFRs statistically consistent with their respective controls. The distinction between the star-forming and passive post-merger samples hints at galaxy mergers enhancing the pre-existing conditions for star formation rather than triggering new processes; possibly emphasising the role of the galactic gas content (see the discussion on the merger gas fraction later in this section).

Note that the sSFR enhancements driven by galaxy mergers persist consistently up to $z = 1$ in my sample. This is consistent with results by Rodríguez Montero et al. (2019), who analysed galaxy mergers with $\mu \geq 0.25$ in the SIMBA simulation (Davé et al., 2019) and found an enhancement of a factor of $\sim 2 - 3$ for $z \leq 2$. However, the absence of evolution in $Q(sSFR)$ with redshift in my sample is in contrast to recent work by Patton et al. (2020), who studied SFR enhancement during the pair phase using the same simulation suite and with similar methods as those used herein. Patton et al. (2020) report a mild evolution in $Q(sSFR)$ with redshift: a mean

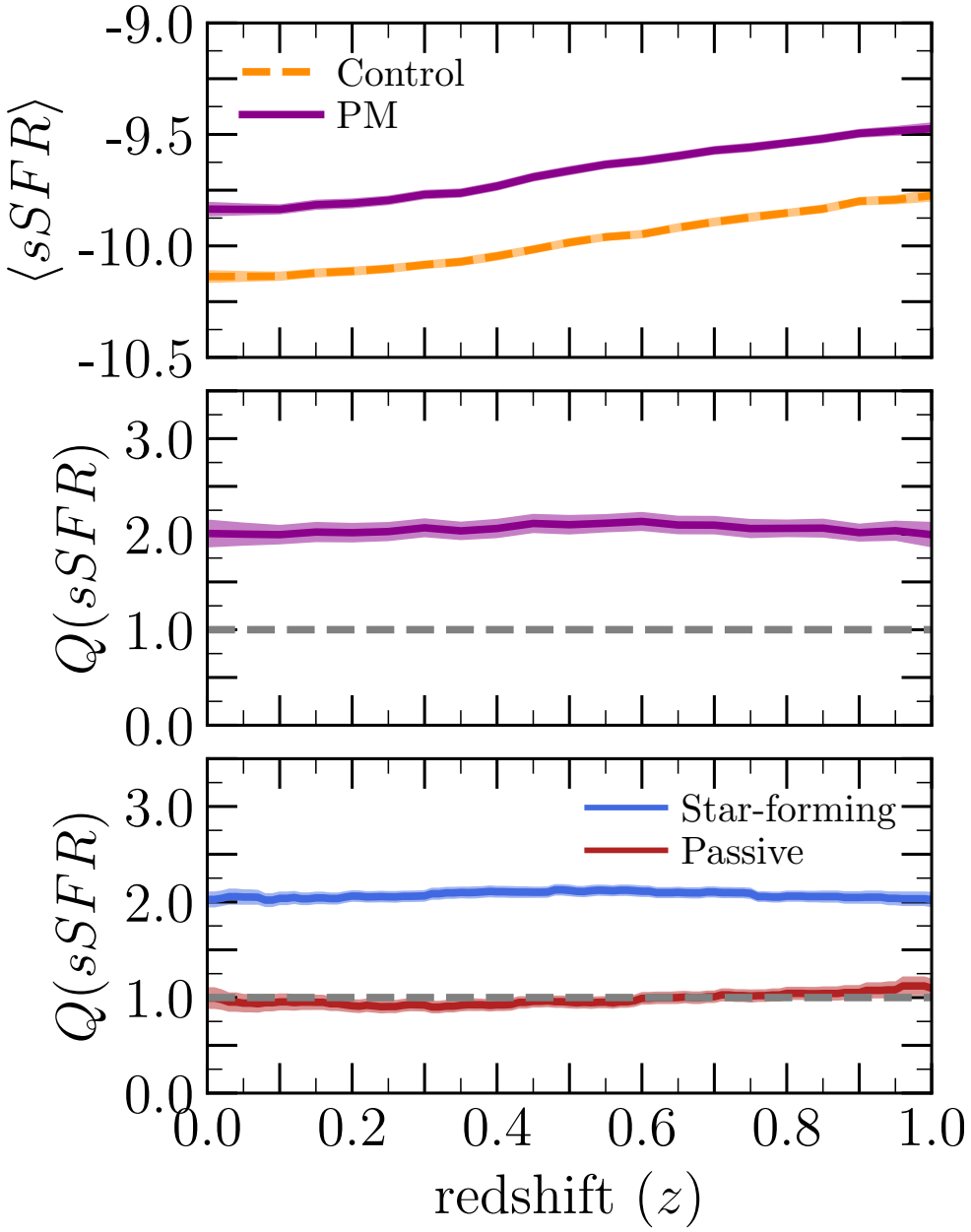

Figure 4.5: The redshift-evolution of the sSFR enhancement in post-mergers. The top panel shows the running average sSFR for post-mergers (dark-purple) and their associated controls (orange) with the shaded region representing twice the standard error on the mean in bins or redshift. The middle panel shows the dependence of $Q(sSFR)$ (and the associated uncertainty; see equation 4.2) on redshift for the full post-merger sample while the bottom panel shows $Q(sSFR)$ for star-forming (blue) and passive (red) post-mergers. Post-mergers exhibit enhanced sSFRs at all redshifts ($0 \leq z \leq 1$). The enhancement is dominated by the star-forming post-mergers (67% of the sample) while the sSFRs of passive post-mergers (33% of the sample) are consistent with those of the controls.

$Q(sSFR) \sim 1.7$ at $0.8 < z < 1$ increases, with decreasing redshift, to $Q(sSFR) \sim 2.4$ at $z < 0.2$. The different redshift evolution results between my study of post-mergers and Patton et al.'s pairs work may be due to differences in the galaxy properties of the two samples. Namely, the mass distribution of the post-merger sample presented here lacks post-mergers at $M_\star \sim 10^{10}$ $M_\odot$ while the pairs sample of Patton et al. (2020) includes galaxies to lower masses. Alternatively, the difference in my control matching strategy and that of Patton et al. (2020) may also contribute the aforementioned difference in redshift evolution.

In order to more fairly compare my work to that of Patton et al. (2020) I repeated my analysis using the exact matching strategy used in Patton et al. (2020). I find that the sSFR enhancement in the reconstructed post-merger sample evolves with redshift ($Q(sSFR) \sim 4$ at $z = 0$ to $Q(sSFR) = 2.7$ at $z = 1$). The redshift-evolution of the merger-induced SFR enhancement in the reconstructed star-forming post-mergers is even stronger, while the passive post-mergers now show suppressed SFRs (i.e., matched to star-forming control galaxies). Additionally, I tested the effects of the sample's mass distribution on the redshift evolution of $Q(sSFR)$. I repeated the analysis of Patton et al. (2020) using my control matching strategy which resulted in no redshift evolution in $Q(sSFR)$. Therefore, the redshift dependence of $Q(sSFR)$ is driven by the control matching strategy: i.e., star-forming galaxies being matched to the passive galaxies which are more abundant at lower redshift.

Effect of mass ratio

Hydrodynamical simulations provide a solid understanding of the importance of the merger mass ratio on the measured enhancements and timescale on which the effects of a merger are visible (e.g., Bournaud et al., 2005; Cox et al., 2008; Johansson et al., 2009; Lotz et al., 2010a). These previous works have found that minor mergers (small μ) induce weaker starbursts, and short-lived observable asymmetries. On the contrary, major, gas-rich mergers induce the most prominent starbursts and the most long-lived asymmetrical features. However, previous works have mostly focused on mergers in idealised settings (i.e., binary disc mergers) where one can perform well targeted experiments to isolate the effects of galaxy properties (e.g., mass ratio, gas fraction) on the merger outcome (e.g., starburst strength, asymmetry metrics).

In this sub-section, I investigate the relevance of the merger mass ratio (μ) on the induced sSFR enhancement in a large-box cosmological simulation. Figure 4.6 shows

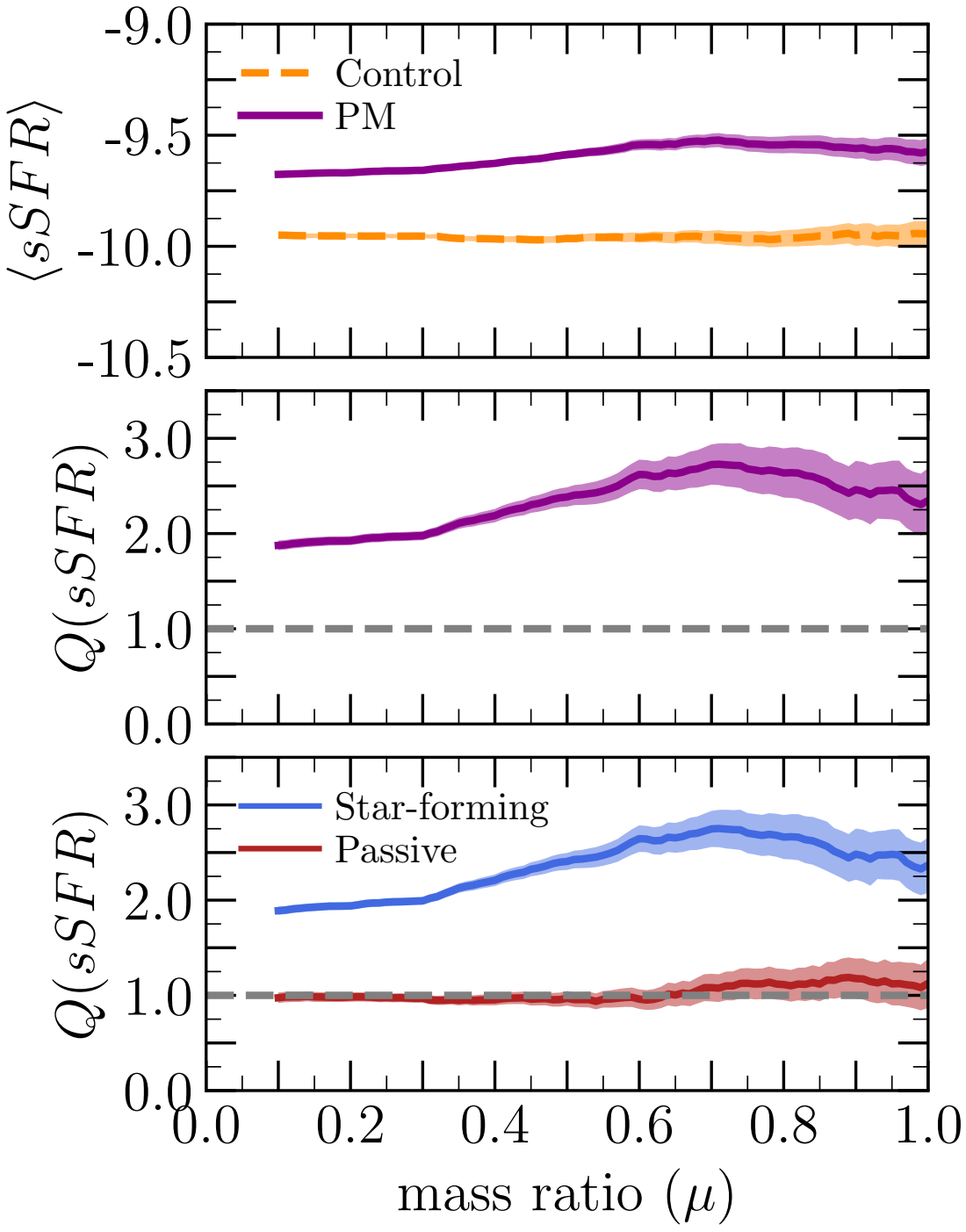

Figure 4.6: The dependence of the enhancement in the post-mergers' sSFR on the parents' merger mass ratio (μ). The shaded region represents twice the standard error on the mean in bins of μ. Post-mergers exhibit enhanced sSFR for all mass ratios with an increasing enhancement for major mergers. The enhancement is dominated by the star-forming post-mergers, while the passive post-mergers sSFR are consistent with their controls.

the mean sSFR at different mass ratios for post-mergers and their associated controls (top panel), and the dependence of the induced sSFR enhancement on the merger mass ratio (middle and bottom panels). Mergers with all mass ratios drive an enhancement in sSFR in my post-merger sample. The enhancement is more pronounced for major mergers ($\mu \geq 0.3$) with $Q(sSFR) \sim 2.5$, while minor mergers $\mu \sim 0.1$ show more modest (yet still significant) enhancements with $Q(sSFR) \sim 2$. My results are consistent with other works exploring mergers in cosmological numerical simulations (i.e., Rodríguez Montero et al., 2019). Passive post-mergers exhibit sSFRs which are consistent with their controls while star-forming post-mergers dominate the enhancements shown in the full post-merger sample.

The results of the work presented here are qualitatively consistent with previous simulations of idealised mergers (e.g., Cox et al., 2008; Johansson et al., 2009). Major mergers induce aggressive gravitational torques which drive dynamical instabilities in the ISM thus enhancing star formation. On the contrary, minor mergers induce more modest gravitational torques thus driving smaller enhancements. I note that the impact of minor mergers may be overestimated for galaxies that undergo multiple mergers; viz. if a galaxy undergoes a merger before the effects of a previous merger have decayed I would overestimate the boost in star formation. However, such a scenario is rare and the associated effects should be small. Moreover, smooth accretion onto the merging systems may lead to an over-estimated SFR enhancement. However, smooth accretion would affect the SFR enhancements at all mass ratios and therefore would not generate an artificial bias. In addition, the effects of smooth accretion correlate with the environmental density, yet my results are robust to changes in environment (i.e., different environments show a similar dependence of $Q(sSFR)$ on μ).

Comparisons to observational studies of post-merger galaxies are particularly complicated owing to the difficulty in assessing the mass ratio of a galaxy merger resulting in an observed post-merger galaxy. Nonetheless, one can qualitatively compare this work's results to the enhancements driven by galaxy mergers of varying mass ratios during the pair stage. For example, Scudder et al. (2012) studied galaxy pairs selected from the SDSS and concluded that modest enhancements in SFR ($\log(SFR_{\rm pm}) - \log(SFR_{\rm control}) \leq 0.45$ dex) can be achieved over a wide range of mass ratios ($0.1 \leq \mu \leq 1$), whereas the strongest SFR enhancements ($\log(SFR_{\rm pm}) - \log(SFR_{\rm control}) \geq 0.8$ dex) are preferentially driven by major mergers ($\mu \geq 0.3$). Figure 4.7 shows the fraction of star-forming descendants of major mergers

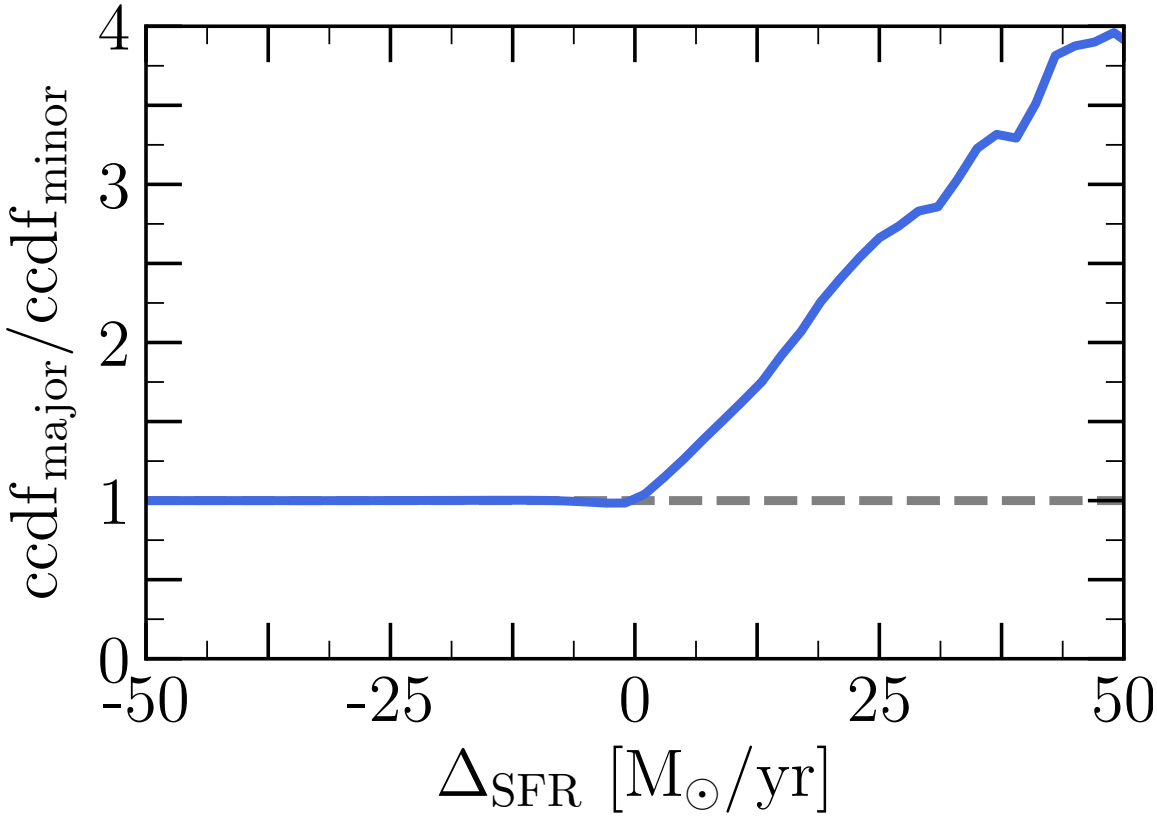

Figure 4.7: The fraction of star-forming descendants of major mergers ($\mu \geq 0.3$) with SFR enhancement greater than Δ_{SFR} (complementary cumulative distribution function; ccdf) relative to that of minor mergers ($0.1 \leq \mu < 0.3$). The definition of Δ_{SFR} is given in equation 4.3. Major mergers dominate the high tail of the Δ_{SFR} distribution.

($\mu \geq 0.3$) with enhancements greater than $\Delta_{\rm SFR}$ relative to that of minor mergers ($0.1 \leq \mu < 0.3$). I define the merger-induced star formation, $\Delta_{\rm SFR}$, for a star-forming post-merger as the vertical offset in SFR from the SFMS: i.e.,

$$\Delta_{\rm SFR} = SFR_{\rm pm} - SFR_{\rm SFMS}. \tag{4.3}$$

Post-mergers below the SFMS contribute a negative $\Delta_{\rm SFR}$. Figure 4.7 shows that strong enhancements of SFR are dominated by major mergers. For example, mergers that trigger an SFR that is 50 $M_{\odot}$/yr above the SFMS are approximately four times as likely to be major, rather than minor, mergers. My results are therefore qualitatively consistent with the conclusions of Scudder et al. (2012), namely that SFR enhancements are triggered by a wide range of mass ratios (Figure 4.6), but that the largest starbursts are preferentially produced by major mergers (Figure 4.7).

Although major mergers trigger the strongest starbursts, minor mergers are far more common (e.g. Figure 4.1). In Figure 4.8, I therefore quantify the fractional contribution to the total merger-induced star formation budget[3] (i.e., $\sum \Delta_{\rm SFR}$) as a function of mass ratio in the star-forming post-merger sample. The contribution to the total merger-induced SFR enhancement budget increases with decreasing mass ratio. Despite their lower average enhancement, the cumulative enhancement from minor mergers ($0.1 \leq \mu < 0.3$) accounts for $\sim 50\%$ of the merger-induced SFR budget. Hence, minor mergers are a significant contributor to the merger-induced SFR budget. These results are qualitatively consistent with earlier idealised merger simulations (e.g., Scudder et al., 2015). Since the contribution to the merger star formation budget continues to increase towards the smallest mass ratios in my samples (Figure 4.8), it would be of great interest to extend this study to even lower mass ratios. However, fully investigating the merger-induced SFR budget requires a much higher mass resolution. Such a study will be possible with the forthcoming IllustrisTNG50 simulation (Nelson et al., 2019b; Pillepich et al., 2019).

Effect of stellar mass

I have demonstrated that the enhancement in sSFR is more pronounced in the star-forming population of the post-merger sample while the passive post-mergers show statistically consistent sSFRs with their controls. The discrepancy in sSFR enhance-

[3]Note that I compute the total merger-induced SFR budget ($\sum \Delta_{\rm SFR}$) and *not* the total cosmic star formation budget.

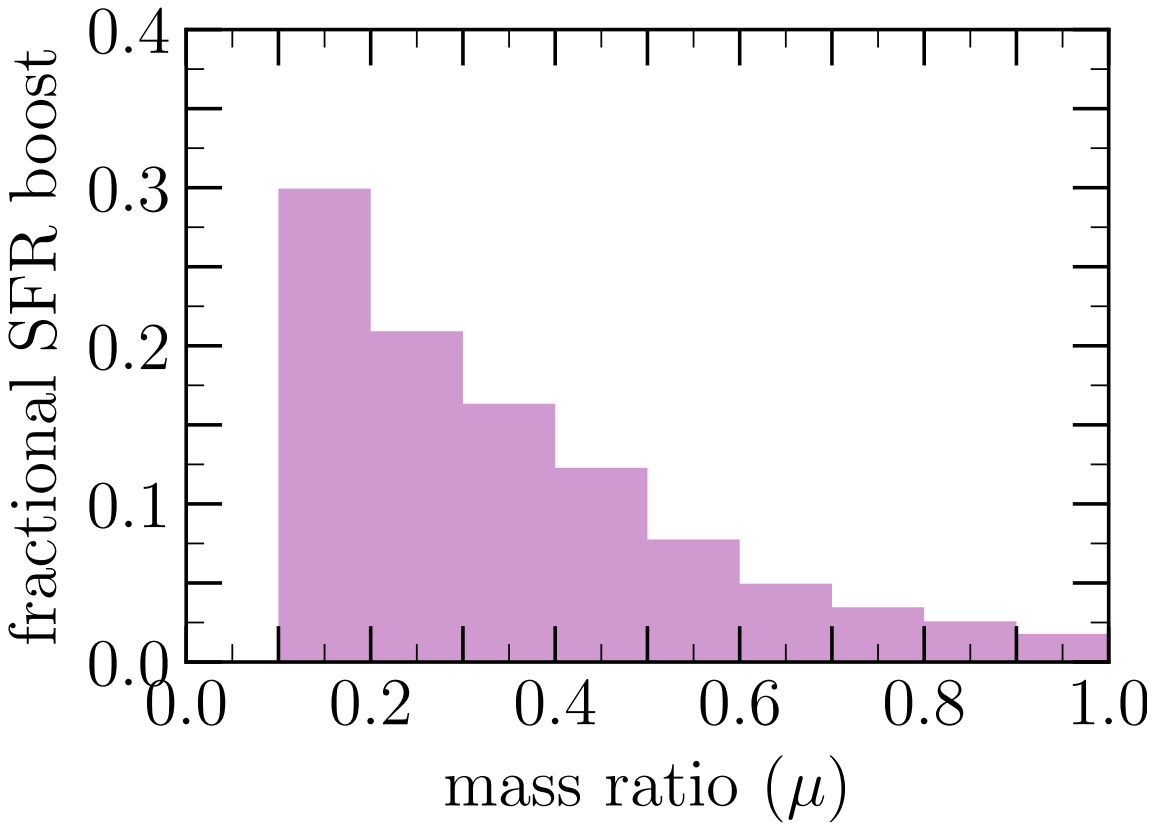

Figure 4.8: An accounting of the contribution to the total merger-driven SFR enhancement budget in the star-forming post-merger sample. The merger-induced star formation boost for a given post-merger is defined as the vertical offset from the SFMS (see equation 4.3). The contribution to the total merger-induced SFR enhancement increases with decreasing mass ratio thus indicating that minor mergers ($0.1 \leq \mu < 0.3$) are significant contributors to the global merger-induced SFR budget. Although major mergers ($\mu \geq 0.3$) induce the strongest bursts, the abundance of minor mergers compensates for their modest SFR enhancement when compared to major mergers.

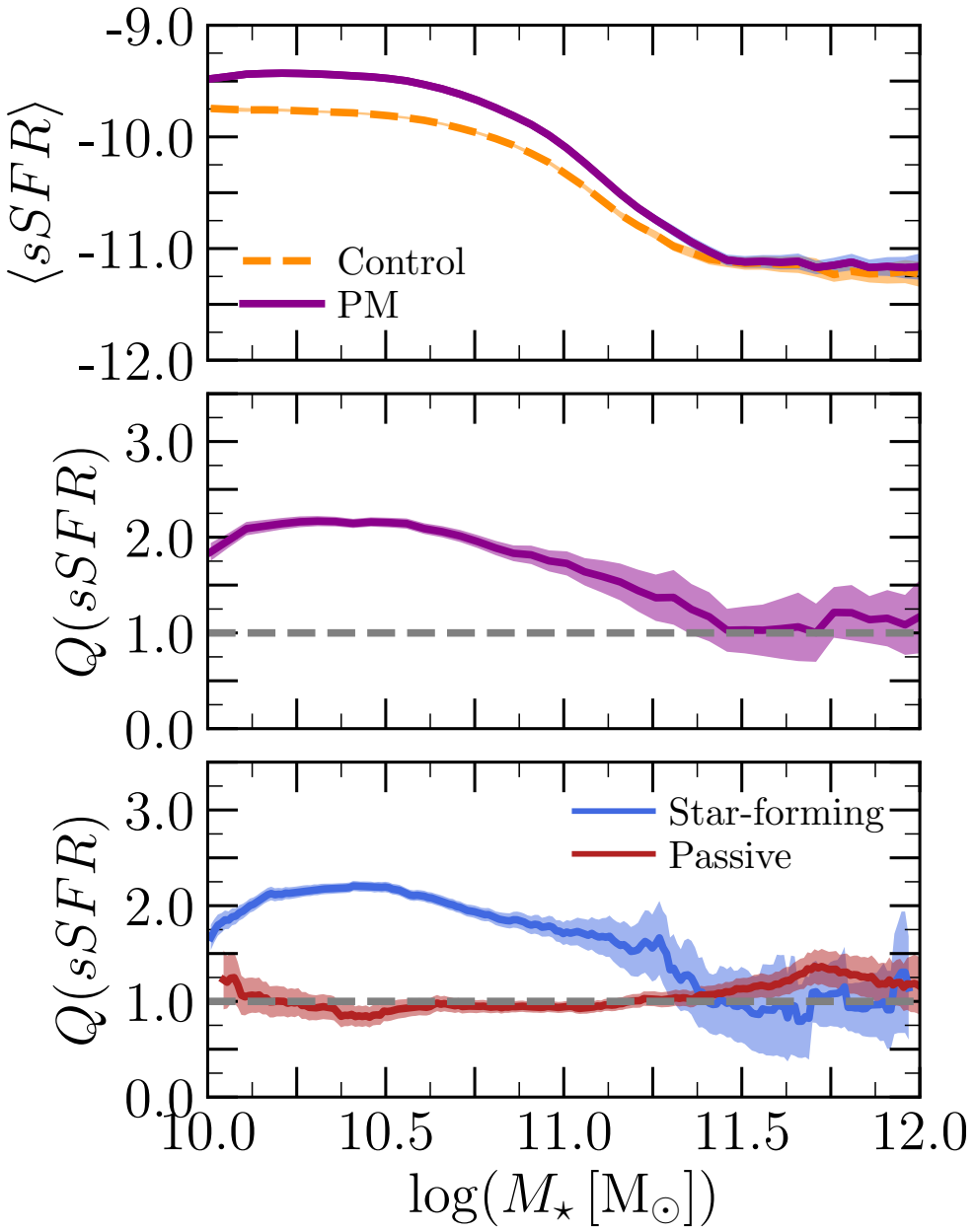

Figure 4.9: The dependence of the enhancement in the post-merger's sSFR on post-merger stellar mass. The shaded regions represent twice the standard error on the mean in bins of $\log(M_\star/\mathrm{M}_\odot)$. Star formation is most enhanced in post-mergers with $10.0 \leq \log(M_\star/\mathrm{M}_\odot) \leq 11.4$ with a declining enhancement for larger $M_\star$. For $\log(M_\star/\mathrm{M}_\odot) > 11.4$ post-mergers form stars at an average rate which is consistent with that of the control galaxies. The star-forming post-mergers show the same behaviour as the full post-merger sample while passive post-mergers are consistent with no enhancement for all post-merger $M_\star$ with a possible slight enhancement at the largest $M_\star$.

ment between star-forming and passive post-mergers holds at all redshifts (Figure 4.5) and mass ratios (Figure 4.6). Knowing that there is a correlation between the fraction of passive galaxies and stellar mass (see Figure 4.4), I investigate the dependence of the sSFR enhancement in post-mergers on stellar mass. I am interested in disentangling the source of the discrepancy in enhancement between star-forming and passive post-mergers.

Figure 4.9 shows the mean sSFR of post-mergers and their controls (top panel), and the associated enhancement (middle and bottom panels) as a function of post-merger stellar mass. The average sSFR of post-mergers and controls declines with stellar mass reconfirming that passive galaxies dominate the high-mass galaxy population (e.g., Bundy et al., 2010; Bluck et al., 2014). Unlike redshift and mass ratio, the stellar mass has a significant impact on the measured enhancement in sSFR. As the stellar mass increases, the sSFR enhancement diminishes to be consistent with the control sample and vanishes for $\log(M_\star/\mathrm{M}_\odot) > 11.4$. Post-mergers with stellar masses $\log(M_\star/\mathrm{M}_\odot) \leq 11.25$ exhibit an average enhancement in sSFR with $Q(sSFR) \sim 2$. On the contrary, the high stellar mass post-mergers, i.e. $\log(M_\star/\mathrm{M}_\odot) > 11.4$ are characterised by normal sSFRs (compared to their controls). The decline in $Q(sSFR)$ at $\log(M_\star/\mathrm{M}_\odot) < 10.25$ is caused by the minimum stellar mass limit I impose ($\log(M_\star/\mathrm{M}_\odot) \geq 10$) in order to reliably quantify the galaxies' recent merger histories: i.e., post-mergers with $\log(M_\star/\mathrm{M}_\odot) \sim 10$ will be paired with more massive controls which, on average, have higher SFRs thus leading to a decline in $Q(sSFR)$ at $\log(M_\star/\mathrm{M}_\odot) \sim 10$. The reported correlation of sSFR enhancement with stellar mass is consistent with the results of Rodríguez Montero et al. (2019) studying mergers in SIMBA, another cosmological hydrodynamical simulation (with a different physical model).

Dissecting the post-merger sample further is key to understanding the source of the dependence of sSFR enhancement on stellar mass. The lower panel of Figure 4.9 shows the enhancement at different stellar masses for the star-forming and passive post-merger sub-samples. While the star-forming post mergers follow the behaviour described above, the passive post-mergers exhibit typical sSFRs when compared to their controls at all stellar masses. Therefore, the stellar mass is not the fundamental driver of the differences between the star-forming and passive post-merger samples.[4] This is suggestive of a separate galaxy property, which correlates with

[4]Similar conclusions are supported by Figures 4.5, and 4.6: The redshift and mass ratio are not fundamental drivers of the differences between the star-forming and passive post-merger samples.

stellar mass and sSFR, driving the reported disparity between the passive and star-forming post-merger sub-samples (see the discussion on the merger gas fraction, next in this section).

Effect of merger gas fraction

So far, I have demonstrated that the redshift, mass ratio, and stellar mass may not be fundamental drivers of the discrepancy in the sSFR enhancement between passive and star-forming post-mergers. In fact, passive post-mergers show indistinguishable sSFRs from their controls at all redshifts, mass ratios, and stellar masses, while the star-forming post-mergers exhibit strong enhancements at all z, μ, and low $M_\star$. It is possible that the gas content, a fundamental contributor to star formation, is indeed driving the observed trends: gas content correlates with stellar mass, and drives star formation.

In this section, I explore the effect of the progenitor's gas content on the measured post-merger sSFR. I define

$$f_{\rm gas} \equiv \frac{\sum\limits_{\rm prog} M_{\rm gas}}{\sum\limits_{\rm prog} M_{\rm gas} + \sum\limits_{\rm prog} M_\star} \tag{4.4}$$

where $\sum_{\rm prog} M_{\rm gas}$ is the total gas mass (within $2 \times R_{\rm half,\star}$) of the progenitors and $\sum_{\rm prog} M_{\rm star}$ is the total stellar mass (within $2 \times R_{\rm half,\star}$) of the progenitors. Therefore, $f_{\rm gas}$ can be thought of as the total gas fraction available to form stars during the merger. Note that $f_{\rm gas}$ accounts for all gas phases and therefore should not be compared to the molecular and cold gas fractions reported by observational studies (e.g., Combes et al., 2013; Ellison et al., 2018b; Tacconi et al., 2018). Figure 4.10 shows the distribution of $f_{\rm gas}$ for the post-mergers in my sample. The gas fraction distribution is bi-modal. While the post-merger sample includes descendants of both gas-rich and gas-poor mergers, star-forming post-mergers are predominantly the descendants of gas-rich mergers. The gas fractions in Figure 4.10 are significantly higher than those reported in other studies using the IllustrisTNG simulations owing to differences in the definition of $f_{\rm gas}$. For example, Pillepich et al. (2019) report lower gas fractions for star-forming galaxies in the TNG50 box where they normalise the gas mass by the total dynamical mass within $2 \times R_{\rm half,\star}$ instead of the total baryonic mass as shown in Equation 4.4. I elect to normalise the gas mass by the baryonic mass following the

commonly employed formalism in observational studies.

Figure 4.11 shows the average sSFR for post-mergers and controls, and the associated enhancement as a function of $f_{\rm gas}$. As expected, both the sSFRs of post-mergers and controls correlate with $f_{\rm gas}$ (see the top panel of Figure 4.11). Additionally, the persistent enhancement reported in previous sections correlates strongly with $f_{\rm gas}$ with evident suppression in gas poor systems ($f_{\rm gas} < 0.1$), and elevated enhancements up to $Q(sSFR) \sim 3$ at the highest $f_{\rm gas}$. The correlation of $Q(sSFR)$ with $f_{\rm gas}$ also applies to the passive post-merger sub-sample, albeit to a lesser extent. Qualitatively, $Q(sSFR)$ for both passive and star-forming post-mergers show a consistent dependence on $f_{\rm gas}$: i.e., even passive post-mergers descending from gas rich mergers exhibit enhanced sSFRs when compared to their controls.

I note that the level of enhancement (i.e., $Q(sSFR)$) of star-forming and passive post-mergers, and the critical value of $f_{\rm gas}$ above which enhancements are measured remain inconsistent between the star-forming and passive post-merger sample. Even at fixed $f_{\rm gas}$, the passive post-mergers have lower $Q(sSFR)$ (for most values of $f_{\rm gas}$), thus suggesting that the gas fraction is not the sole driver, albeit a strong driver, of SFR enhancement in galaxy mergers. Such a discrepancy could be engendered by various, possibly competing, effects such as: (1) the efficiency of feedback at different stellar masses may require higher $f_{\rm gas}$ for high $M_\star$ galaxies in order to achieve an enhancement; and (2) the metric $f_{\rm gas}$ does not differentiate between hot, cold, and molecular gas which may affect the quantitative results. In fact, the IllustrisTNG physical model treats star-forming gas using an effective equation of state. The sub-grid multi-phase pressurised ISM treatment does not follow the detailed properties and physical state of the gas (i.e., atomic and molecular fractions) which poses a limitation to further analysis of the gas content of post-mergers in this work. Particularly, with the current model, one cannot reliably discern the cause of the measured enhancement – i.e., increased star formation efficiency or increased molecular gas content – without further modelling of the state of the gas (e.g., Lagos et al., 2011, 2014; Diemer et al., 2018, 2019) . Nonetheless, I will revisit the effect of the post-merger gas content in Section 4.4.1.

In addition to the possible effects of feedback efficiency and the sub-resolution properties of the gas reservoir, galaxy morphology could contribute to the aforementioned discrepancy between star-forming and passive galaxies. Mergers of bulge-dominated galaxies have been predicted (e.g., Cox et al., 2008) and observed (e.g., Saintonge et al., 2012) to have lower SFR enhancements. However, exploring the

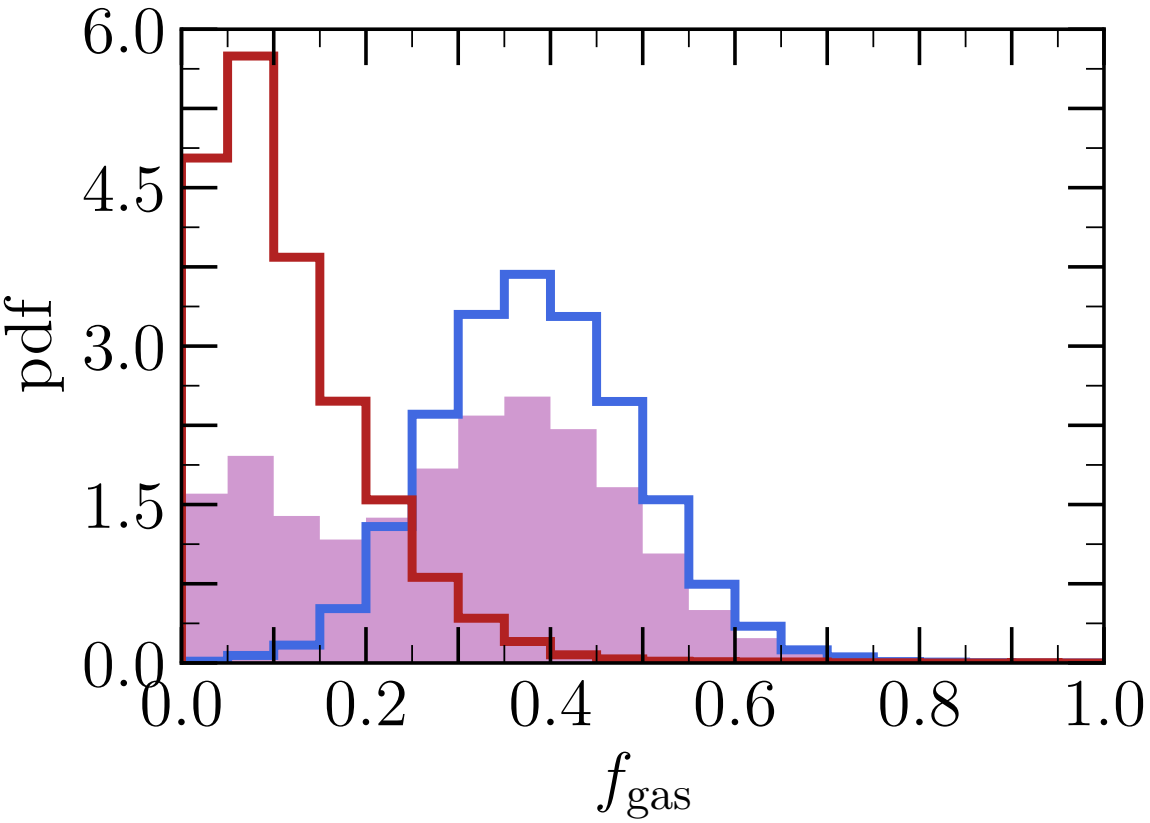

Figure 4.10: The gas fraction distribution of the post-merger sample in TNG300-1. The gas fraction is defined as the progenitors' gas mass normalised by the total baryonic mass within $2 \times R_{\rm half,\star}$ (see Equation 4.4). The filled purple histogram represents the full sample while the red and blue histograms represent the passive and star-forming post-mergers, respectively. The star-forming post-mergers are the descendants of gas-rich mergers when compared to their passive counterparts. Note that $f_{\rm gas}$ accounts for all gas phases and therefore should not be compared to the molecular and cold gas fractions reported by observational studies (e.g., Combes et al., 2013; Ellison et al., 2018b; Tacconi et al., 2018).

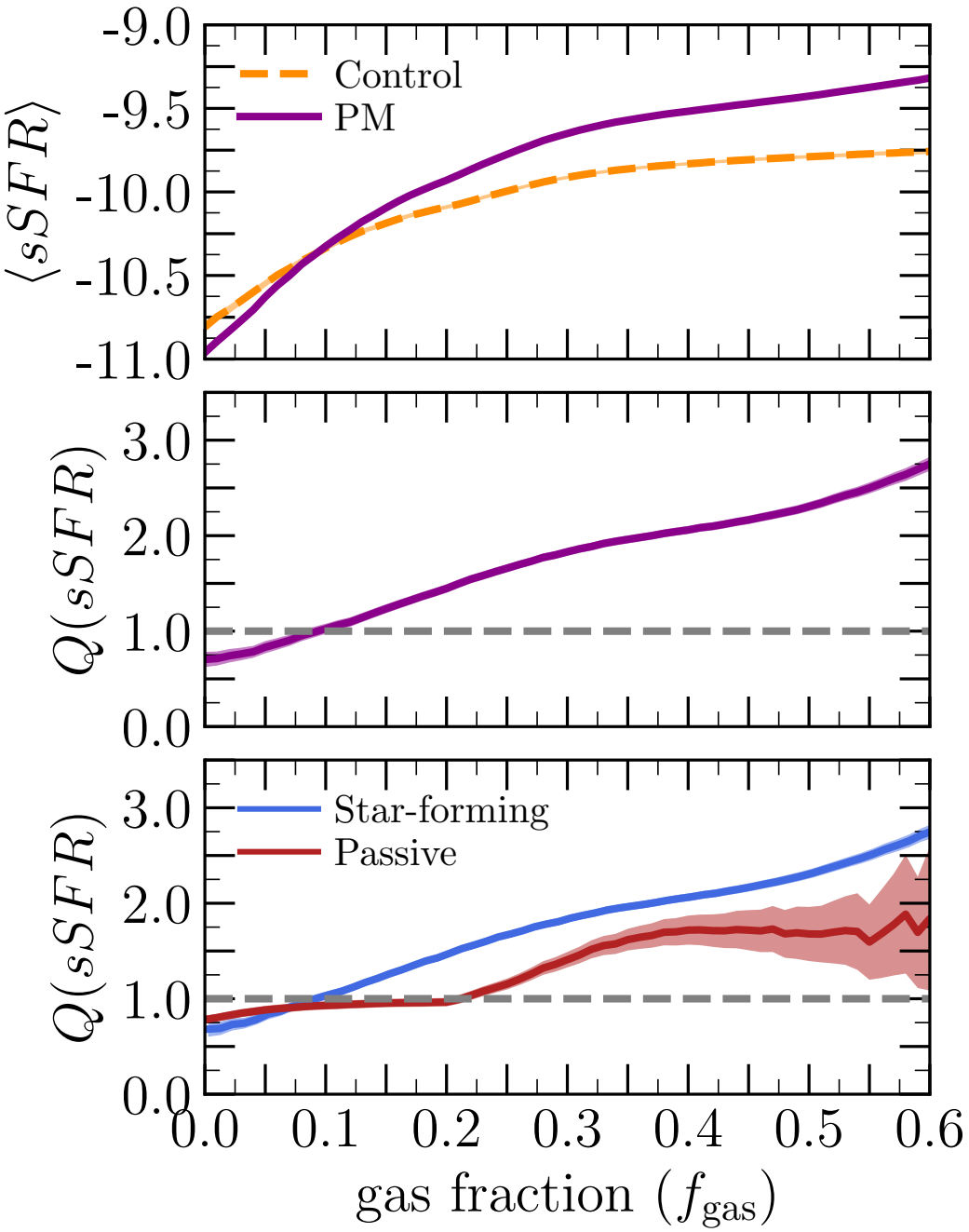

Figure 4.11: The effect of the progenitors' gas content on the observed enhancement in the post-merger phase. The shaded regions represent twice the error on the mean in bins of $f_{\rm gas}$. Gas rich mergers (i.e., high $f_{\rm gas}$) yield post-mergers with enhanced sSFRs. Alternatively, mergers between gas-poor galaxies (i.e., low $f_{\rm gas}$) develop into post-mergers with suppressed sSFR. The aforementioned correlation between $Q(sSFR)$ and the parents' gas content holds for both star-forming and passive galaxies with the effects being especially pronounced for the star-forming post-merger sample.

interplay between galaxy morphology and SFR enhancements in mergers within IllustrisTNG is beyond the scope of this work.

4.3.2 Evolution of post-mergers beyond coalescence

In Section 4.3.1 I demonstrated that post-mergers exhibit enhanced star formation rates compared to their controls, and tied the strength of the SFR enhancement to galaxy properties (e.g., z, μ, $M_\star$, $f_{\rm gas}$). All the results presented thus far treat the post-mergers *immediately* following the galaxy merger. In this section, I explore the forward evolution of the SFR enhancement (or suppression).

I trace the evolution of the post-mergers in two distinct ways.

i. **My first method** tracks every post-merger forward in time until another merger occurs ($\mu \geq 0.1$) or I reach $z = 0$. Then, at every snapshot, I identify control galaxies for the post-merger's descendants as described in Section 4.2.3. Regenerating the controls independently for each descendant is akin to observational studies where I have no prior knowledge of a post-merger's parents or their properties.

ii. In contrast, **my second method** traces both the post-merger and the associated control (identified immediately after the merger) forward in time (similar to numerical simulations of isolated binary galaxy mergers) until either the control or the post-merger undergoes a merger with $\mu \geq 0.1$.

I stress the subtle differences between the two methods. Calculating the controls at every snapshot independently compares the merger descendants to *similar* galaxies. Therefore, my first method is insensitive to some of the effects of galaxy mergers (i.e., transitioning between star-forming and passive, quenching). For example, in my first method post-mergers and their controls belong to the same class, hence the effects of post-mergers transitioning between classes are suppressed. Additionally, post-mergers with unresolved SFRs are removed from my sample, thus my first method does not include the effects of quenching. On the other hand, comparing the merger descendants to the associated control's descendants at the same redshift highlights the difference in the evolution of post-mergers and the controls which evolve secularly. Therefore, my second method is sensitive to post-mergers changing class or quenching.

Effects of the merger mass ratio

I first examine the evolution of the SFR enhancement and its dependence on the merger mass ratio. Figure 4.12 shows the evolution of sSFR and the sSFR enhancements over 2 Gyr following the merger; $T_{\rm merge}$ is a measure of the time since the most recent merger with $\mu \geq 0.1$. The left column of Figure 4.12 depicts the results of independently regenerating the galaxy controls at each snapshot (method i). The merger-induced sSFR enhancement decays following the merger; after ~ 0.5 Gyr the post-mergers' sSFRs are consistent with those of the controls (left middle panel). The bottom left panel shows the evolution of $Q(sSFR)$ for different mass ratios computed using method i. While there *is* a small dependence in the average $Q(sSFR)$ on μ, the μ-dependent enhancement only persists for $\lesssim 100$ Myr post-merger (~ 260 Myr given the time resolution of the simulation[5]). After ~ 100 Myr, the decay of $Q(sSFR)$ to normal values is identical for all mass ratios.

[5]The snapshot time resolution in IllustrisTNG is ~ 160 Myr. Therefore, the precision of merger-identification is ~ 160 Myr.

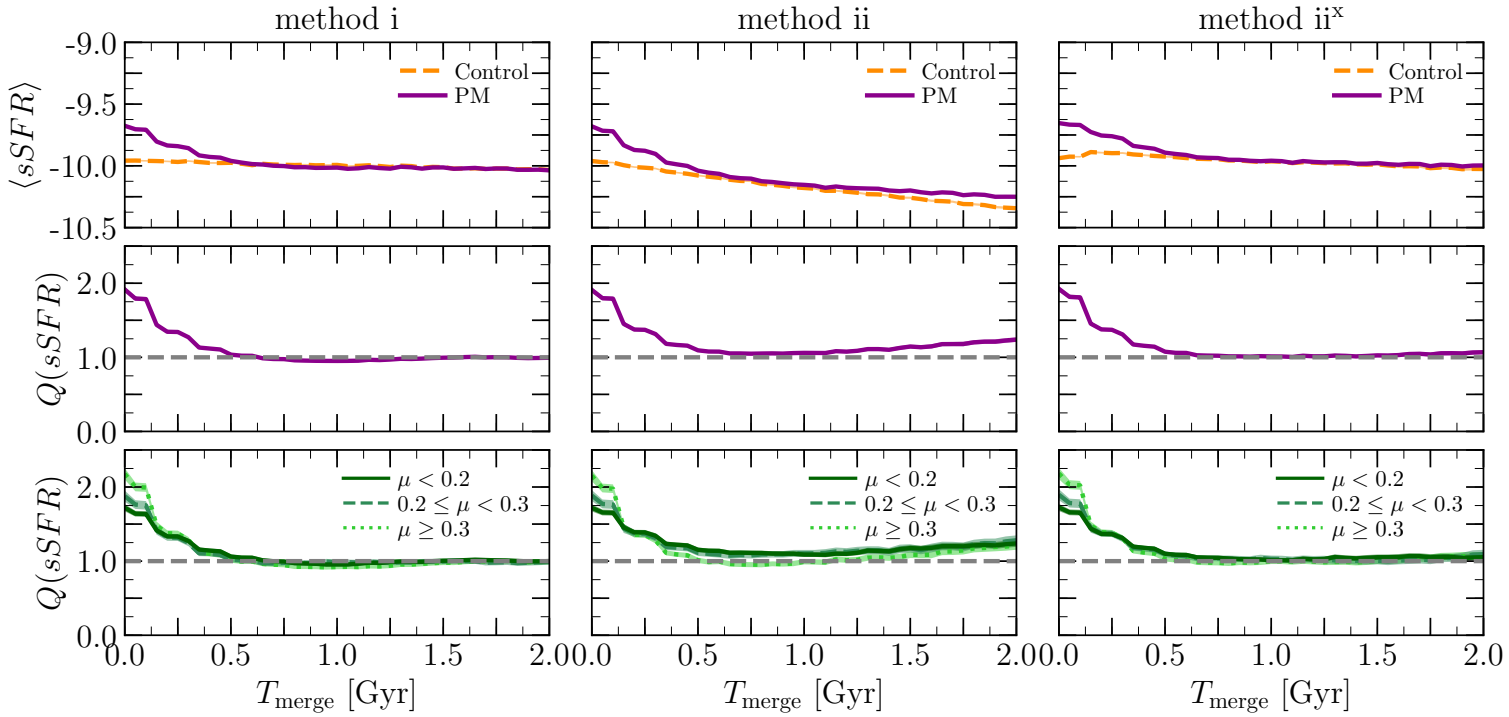

Figure 4.12: The evolution of star formation during the post-merger phase. The three columns (from left to right) show the results of the tracing/control matching methods: method i, method ii, and method ii^{x}, respectively. The top panels shows the running average sSFR for post-mergers (dark-purple) and their controls (orange) as a function of time after the merger. The middle panels show the evolution of $Q(sSFR)$ for the full post-merger sample, and the bottom panels show $Q(sSFR)$ for a sub-sample of post-mergers selected based on the parents' mass ratios. The shaded regions represent twice the standard error on the mean in bins of $T_{\rm merge}$. All methods show that the enhancement in sSFR decays following the merger and vanishes after $\sim$ 500 Myr. Although mergers with different mass ratios induce enhancements of varying strengths, all enhancements decay similarly after $\sim$ 100 Myr. The enhancement at later $T_{\rm merge}$ shown in method ii (middle column) is driven by the deviation in the post-merger and control properties (namely, different class for post-mergers and controls). Ensuring good control quality (method ii^{x}; right column) removes the spurious enhancements seen at large $T_{\rm merge}$ in method ii.

The middle column of Figure 4.12 encapsulates the results of my second method. The controls at $T_{\rm merge} = 0$ Gyr are traced forward in time and compared to the post-merger descendants at their respective redshift. Similar to method i, the SFR enhancement in post-mergers decays over $\sim$ 0.5 Gyr, and the dependence on the merger mass ratio is short lived. The upturn in $Q(sSFR)$ at large $T_{\rm merge}$ is caused by a deviation in the properties of the post-merger descendants and control's descendants which renders the control's descendants inadequate control matches for the post-merger descendants. Namely, the post-merger descendants and the control descendants do not belong to the same class (i.e., star-forming, passive) which leads to an unfair comparison of galaxies and their SFRs.

In order to mitigate the effects of the control quality on the results, I introduce a refined version of method ii, hereafter method ii$^{\rm x}$. I remove post-merger descendants (and their associated controls) if the control quality does not adhere to the conditions described in Section 4.2.3. Namely, I remove post-merger descendants (and their associated controls) in cases of unacceptably large matching tolerances (i.e., $\Delta \log(M_\star) >= 0.2$, 40% in N_2 and r_1), unresolved SFRs, and when the post-mergers and their associated controls do not belong to the same class (i.e., star-forming, passive). The results are shown in the right column of Figure 4.12. Constraining the quality of control matching (particularly the control and post-merger class) alleviates the spurious enhancement at $T_{\rm merge} > 1$ Gyr while maintaining similar results to method i (decay timescale of the SFR enhancement, and the short-lived dependence on μ).

All my methods show that the SFR enhancement decays following the merger and vanishes after $\sim$ 500 Myr, with little dependence on mass ratio. Although the mass ratio has been reported to have a significant impact[6] on the extent and time-scale of observed morphological disturbances of post-mergers (i.e., Lotz et al., 2010a), my post-merger sample indicates that the evolution of SFR enhancement beyond $\sim$ 100 Myr may be independent of mass ratio. I stress a possible caveat which may affect my results: Since $T_{\rm merge}$ measures the time since the most recent merger, it does not have any memory of a galaxy's previous history. Therefore, consecutive mergers (although rare) may hinder my ability to discern the effects of mergers with different mass ratios.

[6]Comparing the results presented in this work with idealised binary galaxy merger simulations is not wholly fair. Idealised simulations traditionally use gas-rich disc galaxies which do not reflect the nature of the post-mergers in IllustrisTNG.

Effects of the merger-induced starburst strength

I next investigate the effect of merger-induced starbursts on the evolution of post-merger galaxies. Figure 4.13 shows the evolution of $Q(sSFR)$ for post-mergers with different SFR strengths at $T_{\rm merge} = 0$ Gyr: starburst galaxies with $SFR > SFR_{\rm MS} + 2\sigma_{\rm MS}$, starburst galaxies with $SFR > SFR_{\rm MS} + 1\sigma_{\rm MS}$, and the rest of the star-forming post-mergers. The top, middle, and bottom panels show the results of method i, method ii, and method ii$^{\rm x}$, respectively. Independent of the method, the weakest starbursts (i.e., star-forming galaxies, or galaxies with $SFR > SFR_{\rm MS} + 1\sigma_{\rm MS}$) never lead to a statistical reduction in SFR following the merger. However, some mergers (with the strongest merger-induced SFRs) can evolve to have statistically suppressed star formation, although this is dependent on the control matching method. For example, method i (new controls generated at each snapshot) is insensitive to galaxy class transitions or quenching. Therefore, no SFR suppression is evident shortly after the merger. However, at ~ 1 Gyr, the strongest bursts evolve to have slightly suppressed SFRs. The suppression is caused by the systematically lower SFRs (compared to typical star-forming controls) of previously passive post-merger descendants evolving to be star-forming, an effect previously reported as 'rejuvenation' by Rodríguez Montero et al. (2019). The suppression vanishes after ~ 2 Gyr. In method ii (the same controls are traced in time alongside the post-mergers), the strongest merger-induced starbursts evolve to have statistically suppressed SFRs compared to their secularly evolving controls beyond ~ 0.5 Gyr. After ~ 2 Gyr, the merger descendants have SFRs that are consistent with their controls. I note that method ii provides an unfair comparison of star-forming galaxies to passive or quenched (unresolved SFRs) galaxies which causes the spurious enhancements at late $T_{\rm merge}$ (see Figure 4.12). Method ii$^{\rm x}$ alleviates the unfair comparison in method ii. Consequently, forcing the post-merger descendants and the control descendants to belong to the same class conceals the suppression evident in method ii. The dependence of the SFR suppression on class matching suggests that merger descendants exhibiting merger-induced starbursts evolve not only to have statistically suppressed SFRs but also become passive or quenched on faster timescales than their controls.

My sample shows that the descendants of galaxy mergers can evolve to have modestly suppressed SFRs that may persist for a Gyr or so. Some post-merger descendants can be rejuvenated after a period of SFR suppression. However, the level and existence of SFR suppression depends on the control matching method (unlike

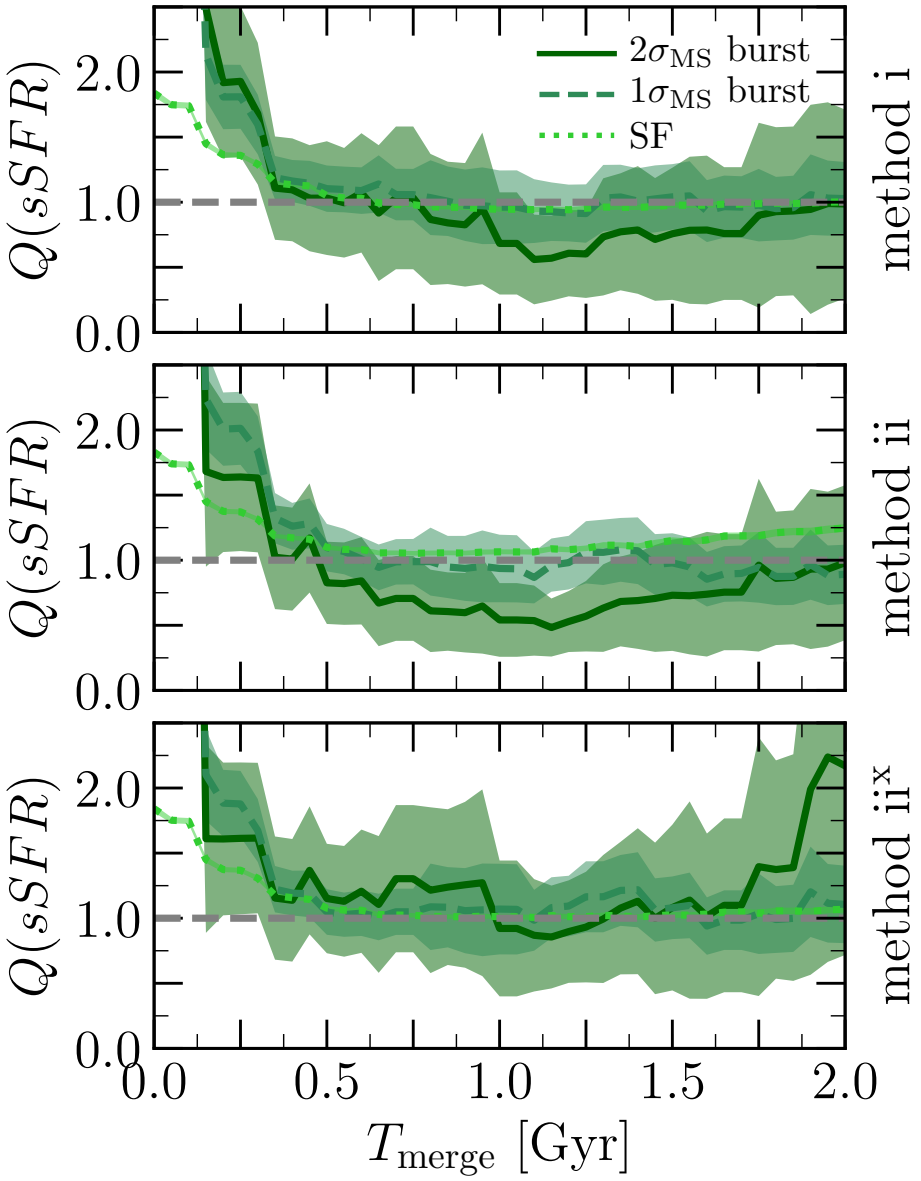

Figure 4.13: The evolution of star formation during the post-merger phase for post-mergers with different merger-induced star-burst strengths. From top to bottom, the panels show $Q(sSFR)$ for a sub-sample of post-mergers selected based on the strength of the SFR at $T_{\rm merge} = 0$ Gyr and traced using methods i, ii, and ii$^{\rm x}$, respectively. The shaded regions represent twice the standard error on the mean in bins of $T_{\rm merge}$. Independent of the method, the weakest starbursts (i.e., SF, $1\sigma_{\rm MS}$ burst) do not induce suppression in SFR. However, the strongest merger-induced SFRs can evolve to have statistically suppressed star formation. The level and existence of SFR suppression depend on the merger/control tracing method. Note: The $Q(sSFR)-$axis is truncated for visual purposes; 2σ bursts exhibit a peak $Q(sSFR) \simeq 12$ while 1σ bursts show an enhancement of $Q(sSFR) = 8.4$ at $T_{\rm merge} = 0$ Gyr.

the SFR enhancements which are very robust to method). The results presented here pertaining to merger-induced starbursts are consistent with the framework where galaxy mergers may drive SFR suppression (e.g., Hopkins et al., 2008). However, a detailed exploration of the connection between galaxy mergers and SFR suppression (i.e., timescales, physical processes, feedback) is beyond the scope of this work. By exploring the different methods presented here I have 1) shown that the largest starbursts can eventually suppress the SFR where the descendants become passive or quenched faster than their controls, but 2) the techniques used in observations (equivalent to method i and method ii[x]) would be largely insensitive to suppression in SFR.

4.4 Discussion

4.4.1 Controlling for gas fraction

In Section 4.3.1 I showed that the SFR enhancement correlates strongly with the progenitors' gas fraction ($f_{\rm gas}$). Yet, my results do not account for the post-merger's gas content when searching for a control galaxy. Understanding the effect of controlling for the gas content on the presented results is a vital test for observational studies, because the choice of matching parameters can significantly affect the conclusions. For example, Scudder et al. (2015) report different correlations between SFR and gas fraction depending whether they control for gas fraction; i.e., the merger-induced SFR enhancement correlates with the gas fraction *only* when the sample is *not* matched in gas fraction. In Figure 4.11 I already showed that, in agreement with Scudder et al. (2015), there is a correlation between SFR enhancement and gas fraction when gas fraction is not included in the control parameters. Now, I investigate whether the aforementioned result changes if gas fraction is controlled for.

The control sample is regenerated using the single best match in $M_{\rm gas}$, $M_\star$, z, N_2, and r_1 as described in Section 4.2.3. An initial tolerance of 0.05 dex is used for $M_{\rm gas}$; if no matches were found, I grow the tolerance by 0.05 dex. All the other parameters are treated as before (see §4.2.3).

Figure 4.14 shows a summary of the merger-driven SFR enhancements, initially reported in Section 4.3, re-calculated using the $M_{\rm gas}$-matched control sample. The results remain qualitatively unchanged although the strength of the enhancement (or

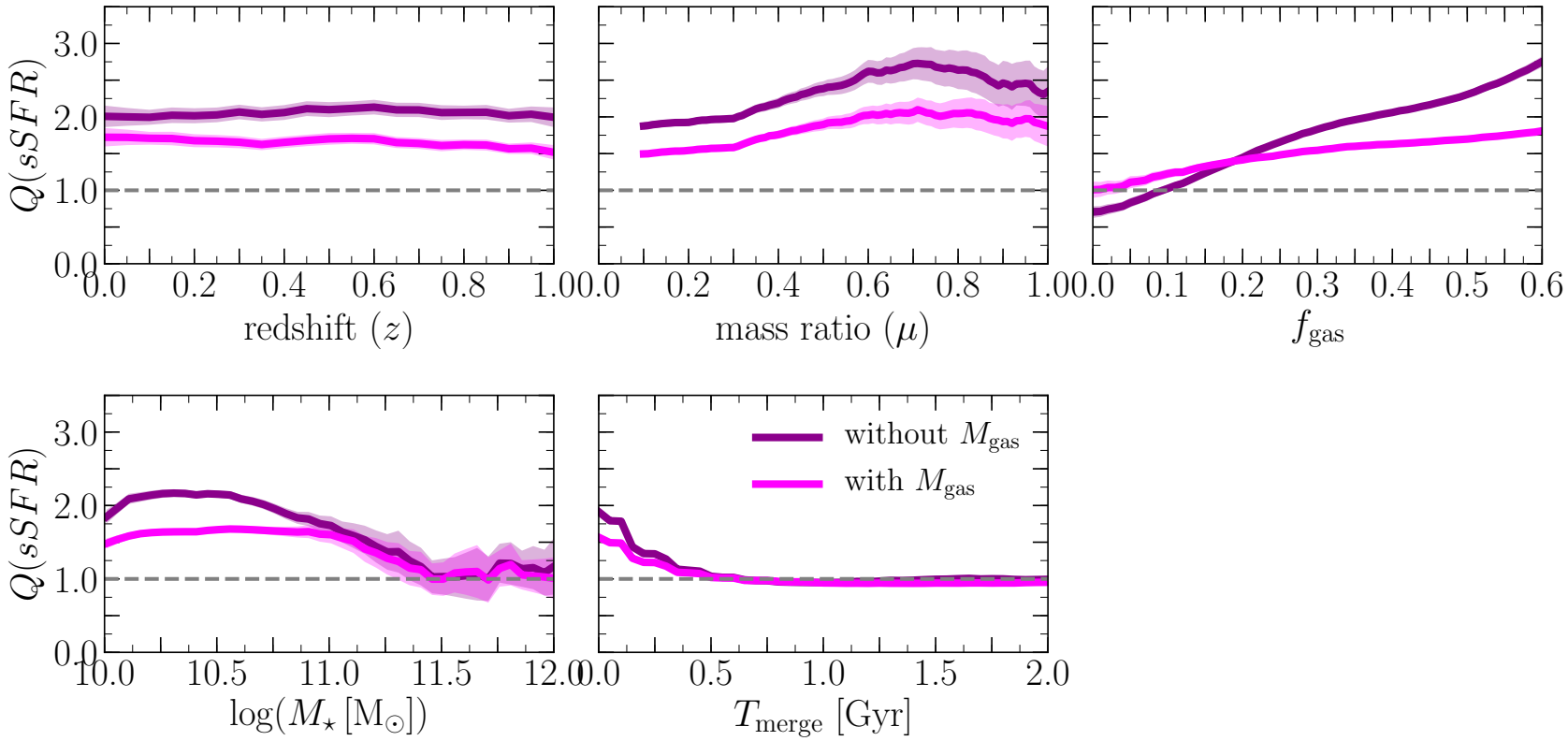

Figure 4.14: The effect of the controlling for gas mass (i.e., gas fraction) on the measured merger-driven SFR enhancement. The shaded regions represent twice the standard error on the mean. The results of TNG300-1 for two different types of matching, with and without matching on gas mass, are shown in magenta and dark-purple, respectively. Controlling for the gas mass reduces the strength of the measured SFR enhancement (or suppression). Nonetheless the results are consistent between the two control matching techniques.

suppression) is reduced when controlling for $M_{\rm gas}$. The results presented here are consistent with the results of Cao et al. (2016), who report enhanced SFRs in their star-forming spiral pairs compared to control galaxies with similar gas mass.

In terms of a direct comparison with observations, it is worth noting that the IllustrisTNG physical model does not explicitly track the atomic and molecular fractions in gas cells during the simulation. Therefore, I am unable to discern the sub-resolution physical state (i.e., atomic fraction, molecular fraction) of the gas reservoirs in the post-mergers and their controls. However, knowing that the IllustrisTNG physical model attributes star formation to gas cells which meet the sub-resolution star formation criterion ($SFR \propto \rho^{1.5}$), one can use the SFR as a proxy for the molecular gas content of galaxies (see Diemer et al., 2019). The measured SFR enhancement, which persists even when controlling for gas fraction, is suggestive of an enhanced *molecular gas* content in post-mergers. I will explore gas fraction evolution during galaxy mergers more extensively in the future. My results are qualitatively consistent with observational studies reporting that post-mergers are home to an enhanced molecular gas content (e.g., Pan et al., 2018; Violino et al., 2018). Additionally, my results are broadly consistent with the high resolution simulations of Moreno et al. (2019) who showed that the cold-dense gas content of galaxies is enhanced during the pair phase and immediately before the coalescence.

4.4.2 Effects of simulation resolution

A common effect of numerical resolution on star formation arises from the correlation of star formation with dense gas: i.e., stars are spawned from gas cells above a given density threshold (see §4.2). As the simulation's resolution (mass and spatial) increases, I am able to sample progressively denser gas. Therefore, more gas cells are eligible to form stars which increases the star formation rate. However, the effects of the increased star formation (and associated feedback) are overly complex. In this section, I perform a convergence test to determine how robust my results are to changes in the simulation's resolution. I direct the reader to Pillepich et al. (2018a) for a general discussion on the convergence of the IllustrisTNG physical model.

The results reported in Section 4.3 are for TNG300-1. Although TNG300-1 has a lower spatial resolution compared to TNG100-1, TNG300-1 provides a large number of post-mergers which allows for the statistical analysis of the post-merger suite that is necessary when exploring SFR enhancement as a function of other parame-

ters. I use three simulations to test the effects of numerical resolution: TNG100-1, TNG100-2, and TNG300-1. See Section 4.2 for a description of each of the three simulations. Figure 4.15 summarises the results of Section 4.3 for all three simulations. The simulations with similar resolution (i.e., TNG100-2, and TNG300-1) show the same results. However, TNG100-1 (the simulation with the higher mass and spatial resolutions), shows qualitatively similar, yet quantitatively different results. The enhancements reported in TNG100-1 are smaller than those of the lower resolution simulations. I note that the dependence on resolution is inconsistent with Patton et al. (2020) who showed a stronger enhancement in TNG100-1 compared to the lower resolution simulations which is possibly due to the differences in sample selection, control matching, and the SFR metric (SFR within the stellar half mass radius in Patton et al. (2020)) . Understanding the drivers of the differences between the two simulations (i.e., resolution levels) is beyond the scope of this work. However, I note that Donnari et al. (2019) report convergence between the two resolution levels (i.e., TNG100-1 and TNG300-1) when using SFRs averaged over timescales > 50 Myr for galaxies in the same mass range as the post-mergers studied here.

4.4.3 The evolution from the pair to post-merger phase

A particular strength of numerical simulations of galaxy mergers is the ability to track the evolution of galaxy mergers and quantify the strength and temporal extent of SFR enhancement and their dependence on galaxy properties. On the contrary, observational studies are unable to accurately follow the evolution of galaxy mergers beyond coalescence; therefore observational studies of post-mergers group the merger remnants together disregarding their evolution[7] (e.g., Ellison et al., 2015; Thorp et al., 2019). On the other hand, observational studies use the projected galaxy separation as a proxy for time evolution during the interaction/pair phase of galaxy mergers (e.g., Ellison et al., 2013b; Patton et al., 2016).

[7]Observational studies of post-mergers depend on morphological selection which are most sensitive to short timescales beyond coalescence (e.g., Lotz et al., 2008, 2010a,b)

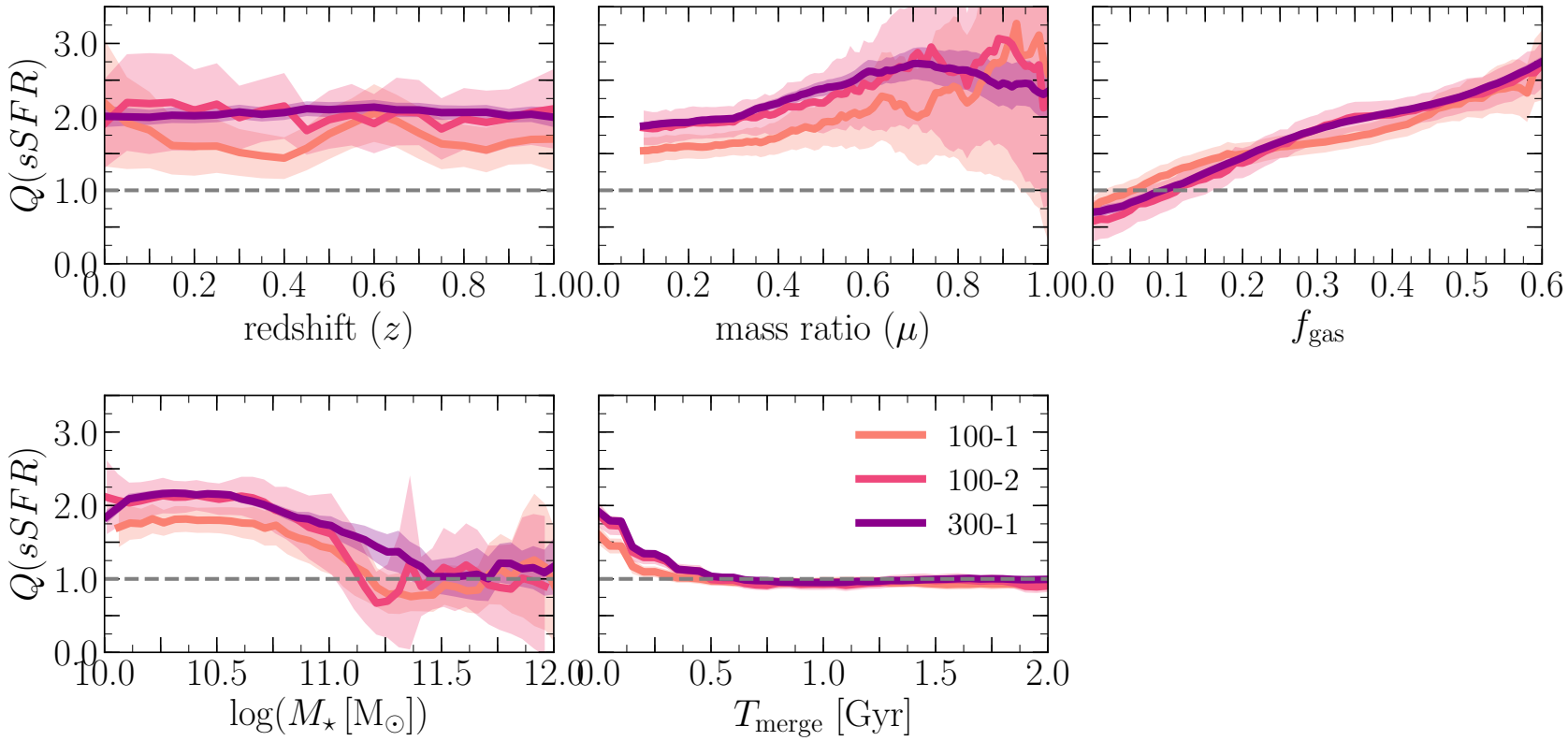

Figure 4.15: The effect of the simulation resolution on the results presented in this work. The shaded regions represent twice the standard error on the mean. The results of TNG100-1, TNG100-2, and TNG300-1 are broadly consistent. The effect of resolution are most prominent in the timescale on which the $Q(sSFR)$ decays in the post-merger phase. The enhancement in the lower resolution simulations (i.e., TNG100-2 and TNG300-1) wanes over $\sim$ 500 Myr vs. $\sim$ 300 Myr for the higher resolution simulation (i.e., TNG100-1).

Patton et al. (2020) studied galaxy pairs in Illustris-TNG applying a methodology akin to observations, and reported an enhancement in SFR for close pairs which is in qualitative agreement with observational galaxy pairs studies using SDSS. Knowing that my control matching strategy is different than that used in Patton et al. (2020), I reproduce the results of Patton et al. (2020) following the control matching methods used in this work (i.e., ignoring galaxies with unresolved SFRs, matching within the same class, limiting $r_{\rm sep} > 2$). Figure 4.16 combines the results of Patton et al. (2020) with my results to form a comprehensive picture of galaxy mergers and their evolution in Illustris-TNG. As the separation of galaxy pairs (r_1) decreases (pericentric passage), the galaxies experience an enhancement in their SFRs. The enhancement then decays as the galaxies move to their respective apocenters. Following coalescence, the SFR enhancement decays to be consistent with the controls within $\sim$ 500 Myr in TNG300-1. I note that the results of the pair phase are possibly underestimated (overestimated) at small (large) separations because, unlike the time domain, at a given separation (r_1) I would include the contribution from galaxies which haven not (have) undergone their first pericentric passage.

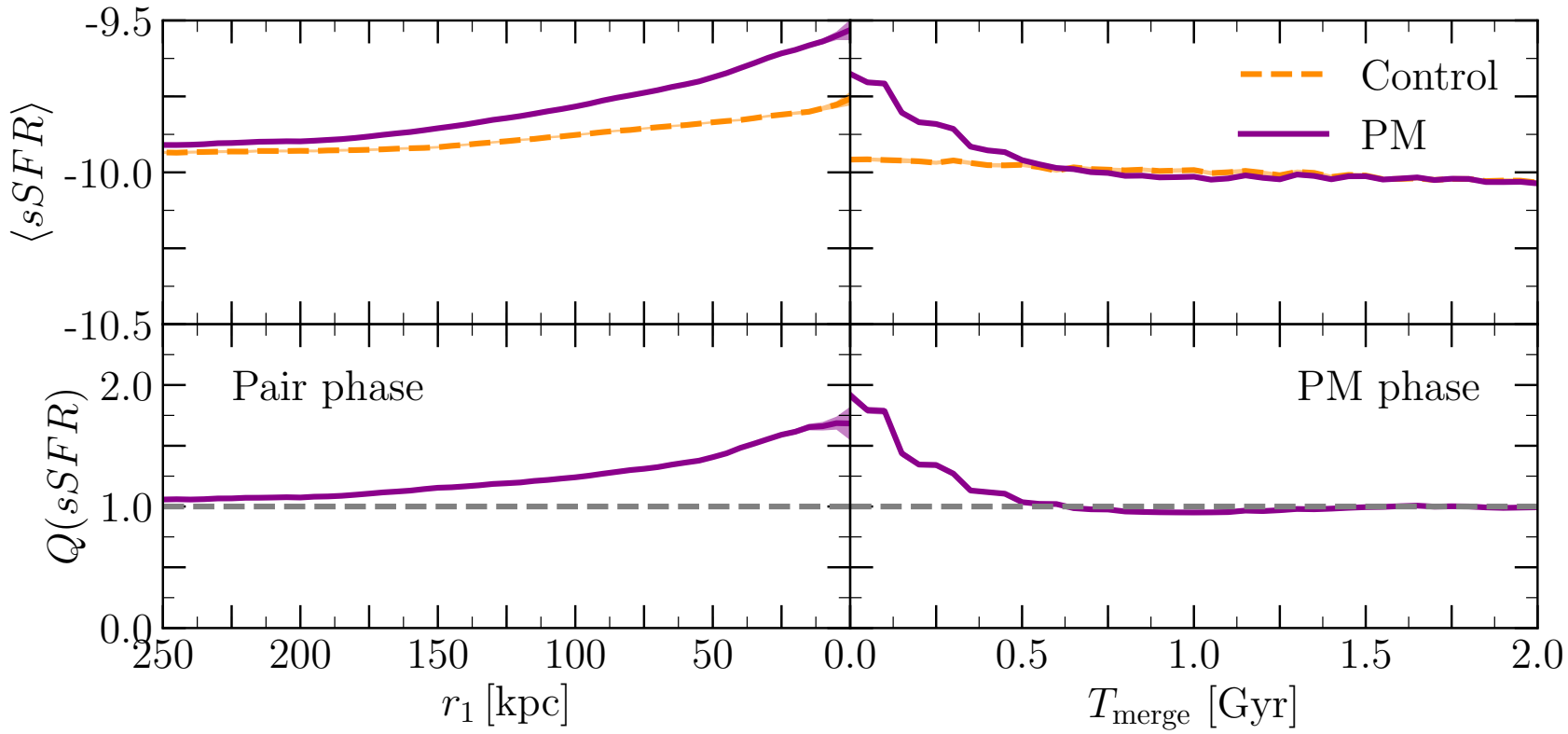

Figure 4.16: Reconciling the observable evolution of mergers during the galaxy pair phase (left panels; Patton et al., 2020) and the evolution of post-merger systems (right panels; see Figure 4.12) in TNG300-1. The controls are recalculated independently for each merger remnant as in the left column of Figure 4.12 (i.e. method i). The shaded regions (although remarkably small) represent twice the standard error on the mean. As the separation of galaxy pairs (r_1) decreases, the galaxies experience an enhancement in their SFRs. Following coalescence, the SFR enhancement decays to be consistent with the controls.

4.5 Conclusions

I present a large sample of post-mergers simulated in a cosmological environment (selected from the IllustrisTNG simulations) and analysed in an observationally motivated scheme (including the use of statistical controls) to demonstrate the effects of galaxy mergers on star formation. I quantify the strength and temporal extent of merger-driven SFR enhancements. Additionally, I tie the enhancement to various galactic properties and hence physical mechanisms. The large sample of post-mergers presented here provides a powerful tool to investigate the detailed evolution of galaxy mergers. I demonstrated that, for TNG300-1:

- **SFR enhancement:** The SFRs of post-merger galaxies, shortly following the merger (i.e., at the first snapshot following the merger), are enhanced by, on average, a factor of ~ 2 compared to their controls. The star-forming post-mergers dominate this enhancement, with a factor of ~ 2 higher SFRs than their controls. Passive post-mergers exhibit statistically consistent SFRs compared to their controls.

- **The redshift evolution of merger driven SFR enhancements:** My post-merger sample exhibits a robust enhancement in SFR (factor of ~ 2) for $0 \leq z \leq 1$, with no evident evolution with redshift. The global enhancement is driven by the star-forming post-merger galaxies, while the passive post-mergers have SFRs which are consistent with those of their controls.

- **The effect of the mass ratio:** The merger-driven SFR enhancement during the post-merger phase, on average, mildly depends on the mass ratio of the parent galaxies' merger. Minor mergers ($0.1 \leq \mu < 0.3$) drive modest enhancements (factor of ~ 2) while major mergers ($\mu \geq 0.3$) induce stronger SFR enhancements (factor of ~ 2.5).

- **The contribution of minor mergers to the merger-induced SFR budget:** Although major mergers ($\mu \geq 0.3$) drive stronger SFR bursts, they are vastly outnumbered by minor mergers ($0.1 \leq \mu < 0.3$) which, in spite of their weaker SFR enhancement, still contribute $\sim 50\%$ of the total merger-driven SFR enhancement in TNG300-1.

- **The dependence on stellar mass:** The SFR enhancements in post-merger galaxies show a strong dependence on the hosts' stellar masses. Post-mergers

with stellar mass $\log(M_\star/\mathrm{M}_\odot) \leq 11.5$ exhibit SFR enhancements of a factor of $\sim$ 2 with declining enhancements for larger stellar masses. For post-mergers with stellar masses above $\log(M_\star/\mathrm{M}_\odot) > 11.4$, the dependence on SFR enhancement disappears. The dependence of SFR enhancement on stellar mass is driven by the star-forming post-merger sample; passive post-mergers have SFRs which are, on average, consistent with the SFRs of the controls.

- **The effects of the merger gas content:** Merger induced star-formation in my post-merger sample (both star-forming and passive) correlates strongly with the merger gas fraction. The descendants of the mergers with the highest gas fractions exhibit the strongest enhancements ($\sim 1.75 - 2.5$) while the descendants of the lowest gas fraction mergers show suppression in SFR when compared to their controls.

- **The effect of controlling for gas fraction:** The SFR enhancements in star-forming post-mergers are stronger than their passive counterparts even at the same gas fraction. Moreover, even when constraining the post-merger gas fraction in the control-matching process, SFR enhancements persist, albeit to a weaker extent. The discrepancy in SFR enhancement between the star-forming and passive post-mergers, and the persistence of the SFR enhancement when controlling for the post-merger gas content, are suggestive of additional processes being at play in driving the SFR enhancement (e.g., gas phase, feedback, star-formation efficiency).

- **The evolution of post-mergers beyond coalescence:** The SFR enhancements in post-mergers decay on a timescale of ~ 0.5 Gyr. While the strength of the merger-driven SFR enhancement within $\sim 100 - 260$ Myr post-coalescence is dependent on the merger mass ratio, the decay in SFR enhancement is *independent of mass ratio* beyond this timescale.

- **The role of galaxy mergers in suppressing star formation:** Although galaxy mergers do not globally suppress star formation (i.e., quenching), the strongest merger-driven starburst galaxies evolve to be passive/quenched on faster timescales than their controls.

- **Effects of simulation resolution:** The results reported here are qualitatively consistent for the different IllustrisTNG simulation boxes (i.e., resolutions).

Chapter 5

Assessing the existence of the resolved star formation main sequence in numerical simulations

This chapter is published as Hani et al. (2020a).

Abstract

The correlation between galaxies' integrated stellar masses and star formation rates (the 'star formation main sequence'; SFMS) is a well-established scaling relation. Recently, surveys have found a relationship between the star formation rate and stellar mass surface densities on kpc and sub-kpc scales (the 'resolved SFMS'; rSFMS). In this chapter, I demonstrate that the rSFMS emerges naturally in FIRE-2 zoom-in simulations of Milky Way-mass galaxies. I make SFR and stellar mass maps of the simulated galaxies at a variety of spatial resolutions and star formation averaging time-scales and fit the rSFMS using multiple methods from the literature. While the absolute value of the SFMS slope ($\alpha_{\rm MS}$) depends on the fitting method, the slope is steeper for longer star formation time-scales and lower spatial resolutions regardless of the fitting method employed. I present a toy model that quantitatively captures the dependence of the simulated galaxies' $\alpha_{\rm MS}$ on spatial resolution and use it to illustrate how this dependence can be used to constrain the characteristic mass of star-forming clumps.

5.1 Introduction

In Chapter 4 I demonstrated the significant effect of galaxy mergers on *global* star formation in a large galaxy sample. Understanding how mergers affect the local properties of galaxies is key to our understanding of galaxy evolution; e.g., how do

post-merger galaxies evolve along local galaxy scaling relations? How is star formation boosted/suppressed in different regions within post-merger galaxies? However, before studying the effects of simulated mergers on the kpc-scale local galaxy properties, one must first demonstrate the existence and robustness of local scaling relations in numerical simulations of *normal* galaxies. In this chapter, I explore the existence of a simulated star formation main sequence (SFMS) on kpc-scales.

The SFMS (Brinchmann et al., 2004; Daddi et al., 2007; Noeske et al., 2007; Salim et al., 2007) is one of the most prominent scaling relations in galaxy evolution. The SFMS is a relatively tight (scatter of $\lesssim 0.3$ dex; Speagle et al., 2014; Whitaker et al., 2015), and roughly linear correlation between the integrated galactic stellar mass and star formation rates of actively star-forming galaxies. While the SFMS spans a wide range in stellar mass, and exists up to redshift $z \sim 5$ (e.g., Brinchmann et al., 2004; Daddi et al., 2007; Elbaz et al., 2007; Noeske et al., 2007; Pannella et al., 2009; Schreiber et al., 2015), its quantitative parameterization exhibits strong evolution leading to some debate in the literature (e.g., Speagle et al., 2014; Whitaker et al., 2015; Schreiber et al., 2015). Nonetheless, the SFMS is a principal scaling relation that is reproduced in all modern galaxy formation simulations (e.g., Torrey et al., 2014; Furlong et al., 2015; Sparre et al., 2015, 2017; Donnari et al., 2019) and semi-analytic models (e.g., Dutton et al., 2010; Hirschmann et al., 2016; Brennan et al., 2017).

The existence of the SFMS has been considered the smoking gun of self regulation within the galactic gas reservoir (flow of gas is modulated by feedback processes; Schaye et al., 2010; Davé et al., 2011; Lilly et al., 2013; Tacchella et al., 2016). Some works have interpreted the existence of the SFMS as evidence that star formation operates in a quasi-steady state (e.g., Noeske et al., 2007). Therefore, galaxies of a given halo mass have similar growth histories, with SFRs that vary little on short ($\lesssim 100$ Myr) time-scales (e.g., Peng et al., 2010; Behroozi et al., 2013; Lu et al., 2014; Abramson et al., 2015). Alternatively, other studies argue that the SFMS is a result of the central limit theorem (e.g., Gladders et al., 2013; Kelson, 2014). Cosmological zoom-in simulations that resolve the multiphase structure of the ISM and incorporate explicit stellar feedback (Hopkins et al., 2014, 2018) indicate that galaxies have bursty star formation histories (SFRs fluctuate by more than an order of magnitude over a $\lesssim 100$ Myr timescale). Nevertheless, although individual galaxies cross the SFMS many times and do not evolve along it (Orr et al., 2017), a tight SFMS consistent with that observed still emerges when considering a population of galaxies (Sparre

et al., 2017).

Recently, the correlation between stellar mass and star formation rate has been studied on kpc-scales using photometric and integral field unit (IFU) observations (e.g., Cano-Díaz et al., 2016; González Delgado et al., 2016; Abdurro'uf & Akiyama, 2017; Hsieh et al., 2017; Maragkoudakis et al., 2017; Ellison et al., 2018a; Liu et al., 2018; Erroz-Ferrer et al., 2019). The rise of IFU surveys – such as Mapping Nearby Galaxies at Apache Point Observatory (MaNGA; Bundy et al., 2015), Sydney-Australian Astronomical Observatory Multi-object IFU (SAMI; Bryant et al., 2015), and Calar Alto Legacy Integral Field Area Survey (CALIFA; Sánchez et al., 2012) – paved the way for a statistical exploration of the kpc-scale *resolved*[1] SFMS (rSFMS; e.g., Cano-Díaz et al., 2016; Hsieh et al., 2017; Ellison et al., 2018a). The rSFMS is the tight correlation between the stellar surface mass density ($\Sigma_\star$) and star formation rate surface density ($\Sigma_{\rm SFR}$). Lin et al. (2019b) suggests that the rSFMS is a manifestation of more fundamental correlations between (1) the molecular gas surface density ($\Sigma_{\rm H_2}$) and $\Sigma_{\rm SFR}$ (Kennicutt-Schmidt; Schmidt, 1959; Kennicutt, 1998; Kennicutt & Evans, 2012), and (2) $\Sigma_\star$ and $\Sigma_{\rm H_2}$ (molecular gas main sequence). Nonetheless, the emergence of the rSFMS suggests that the global relation is an integrated manifestation of the resolved relations.

While the observed rSFMS has been documented by recent observational surveys on ∼kpc and 100 pc scales, the $\Sigma_\star - \Sigma_{\rm SFR}$ correlation has not been explored in depth in numerical simulations. To date, Trayford & Schaye (2019) remains the only study to investigate the existence and redshift evolution of the rSFMS in numerical simulations, particularly the EAGLE cosmological simulation (Crain et al., 2015; Schaye et al., 2015). In this chapter, I present a study of the rSFMS in cosmological zoom-in simulations that resolve the dense ISM and include explicit stellar feedback. Specifically, I analyse a set of Milky Way-mass ($M_{\rm halo} \sim 10^{12} {\rm M}_\odot$ at $z \approx 0$) simulated galaxies from the Feedback in Realistic Environments (FIRE) Project[2] run using the FIRE-2 physics modules (Hopkins et al., 2018). The goal of this chapter is to examine the existence and robustness of the simulated rSFMS. The exquisite spatial resolution of the FIRE simulations makes them ideally suited for testing the robustness of the rSFMS, a task that is not feasible using IllustrisTNG.

The chapter is structured as follows: I first introduce the methodology in Section

[1]Note: I will refer to the local, kpc-scale, SFMS as *resolved* to be consistent with other studies; this does *not* imply that the physical processes driving the local SFMS are resolved at kpc-scales.

[2]http://www.fire.northwestern.edu

5.2. In Section 5.3 I present the results highlighting that the rSFMS emerges naturally in FIRE-2 zoom-in simulations although the rSFMS slope ($\alpha_{\rm MS}$) depends on the fitting method, SFR time-scale, and the observed spatial resolution. I then present a toy model that quantitatively captures the dependence of the simulated galaxies' $\alpha_{\rm MS}$ on spatial resolution and use it to illustrate how this dependence can be used to constrain the characteristic mass of star-forming clumps. Finally, I summarise my conclusions in Section 5.4.

5.2 Simulations and analysis methods

In this Chapter, I examine the existence and robustness (to observational resolution, SFR tracer time-scale, and fitting method) of the resolved $\Sigma_\star - \Sigma_{\rm SFR}$ correlation using simulations of Milky Way-mass galaxies from the FIRE project; all details of the methods are described in Section 2 of Hopkins et al. (2018). The simulations were run using GIZMO[3] (Hopkins, 2015) in its meshless finite-mass (MFM) configuration. Both hydrodynamic and gravitational (force-softening) spatial resolution are set in a fully adaptive Lagrangian manner; mass resolution is fixed. The simulations include cooling and heating from a meta-galactic background and local stellar sources from $T \sim 10 - 10^{10}$ K; star formation in locally self-gravitating, dense, self-shielding molecular, Jeans-unstable gas, assuming an instantaneous efficiency of 100 per cent per local free-fall time ($\rho_{\rm SFR} = \rho_{\rm mol}/t_{\rm ff}$); and stellar feedback from OB & AGB mass loss, SNe Ia & II, and multi-wavelength photo-heating and radiation pressure, with inputs taken directly from stellar evolution models. The FIRE physics, source code, and all numerical parameters are *exactly* identical to those in Hopkins et al. (2018).

The work presented here uses isolated Milky Way-mass FIRE-2 galaxies with $z = 0$ halo masses ranging between 1.08×10^{12} and 1.71×10^{12} $M_\odot$. In particular, I use the following FIRE-2 galaxies: `m12b`, `m12c`, `m12f`, `m12i`, `m12m`, `m12r`, and `m12w`. The halos were simulated with a baryon mass resolution $m_{\rm b} = 7,100$ $M_\odot$. I include all snapshots with $z \lesssim 0.1$ in my analysis (70 snapshots). For more details about the galaxies used, I refer the reader to Wetzel et al. (2016), Hopkins et al. (2018), and Samuel et al. (2020).

Star formation rate surface density, and stellar mass surface density maps were generated for the FIRE-2 galaxies with $z \lesssim 0.1$[4] following Orr et al. (2018). Only

[3] http://www.tapir.caltech.edu/~phopkins/Site/GIZMO.html

[4] The results presented in this work remain unchanged when using independent snapshots (every ~ 115 Myr $> t_{\rm dyn}$).

particles within 15 kpc above/below the galactic disc contribute to the surface density maps[5]. The galaxies are deposited, face-on (along the stellar angular momentum axis), onto 30×30 kpc^2 grids with resolutions ranging from 100 pc to 5 kpc. Note that I do not explore resolutions higher than 100 pc, where I expect my star formation rate tracers to be affected by Poisson statistics (i.e. only a few young star particles contributing to a pixel). The SFR is measured using three SFR tracers: (1) 'instantaneous' SFR, (2) 10 Myr-averaged SFR, and (3) 100 Myr-averaged SFR.[6] The time-averaged SFRs were calculated using the stellar particles' ages and correcting for mass-loss from stellar winds and stellar evolution. The instantaneous SFR refers to the SFR computed from the gas particles' densities and local free-fall timescales via the prescription stated above. Figure 5.1 shows a sample of the maps generated over a range of spatial resolutions and using different SFR time-scales.

Pixels within twice the stellar half-mass radius ($2 \times r_{\rm half}$) with non-zero $\Sigma_{\rm SFR}$ are extracted from the maps, and the $\Sigma_\star - \Sigma_{\rm SFR}$ distribution is fit to investigate the effect of resolution and SFR tracer on the slope of the rSFMS ($\alpha_{\rm MS}$). I implement two fitting methods that are commonly used to fit the SFMS: ordinary least squares (OLS; e.g. Liu et al., 2018), and orthogonal distance regression (ODR; e.g. Hsieh et al., 2017). While the absolute slope depends on the choice of fitting method (OLS, ODR, fitting medians, fitting modes), the qualitative trends shown in this work are robust to changes in the fitting method. Therefore, I adopt OLS to illustrate my results because it is more commonly used in the literature.

5.3 Results

5.3.1 The rSFMS in the FIRE-2 simulations

I first investigate the existence of the rSFMS in the simulations. Figure 5.2 shows the distribution of pixels from the simulated galaxies in $\Sigma_\star - \Sigma_{\rm SFR}$ space at three example resolutions: 100 pc, 500 pc, and 1 kpc.

[5]The particle selection is chosen to be consistent with Orr et al. (2018) who studies the Kennicutt-Schmidt relation in the same galaxy sample.

[6]Averaging time-scales of 10 and 100 Myr are often used to crudely proxy observational SFR tracers such as recombination lines and FIR emission (e.g. Sparre et al., 2017), but the time-scale probed by a specific tracer is sensitive to e.g. the detailed recent star formation history and how dust attenuation varies with age (see table 1 of Kennicutt & Evans, 2012, and the associated discussion). I adopt these specific time-scales because they are commonly used in the literature, but my conclusions are insensitive to these choices.

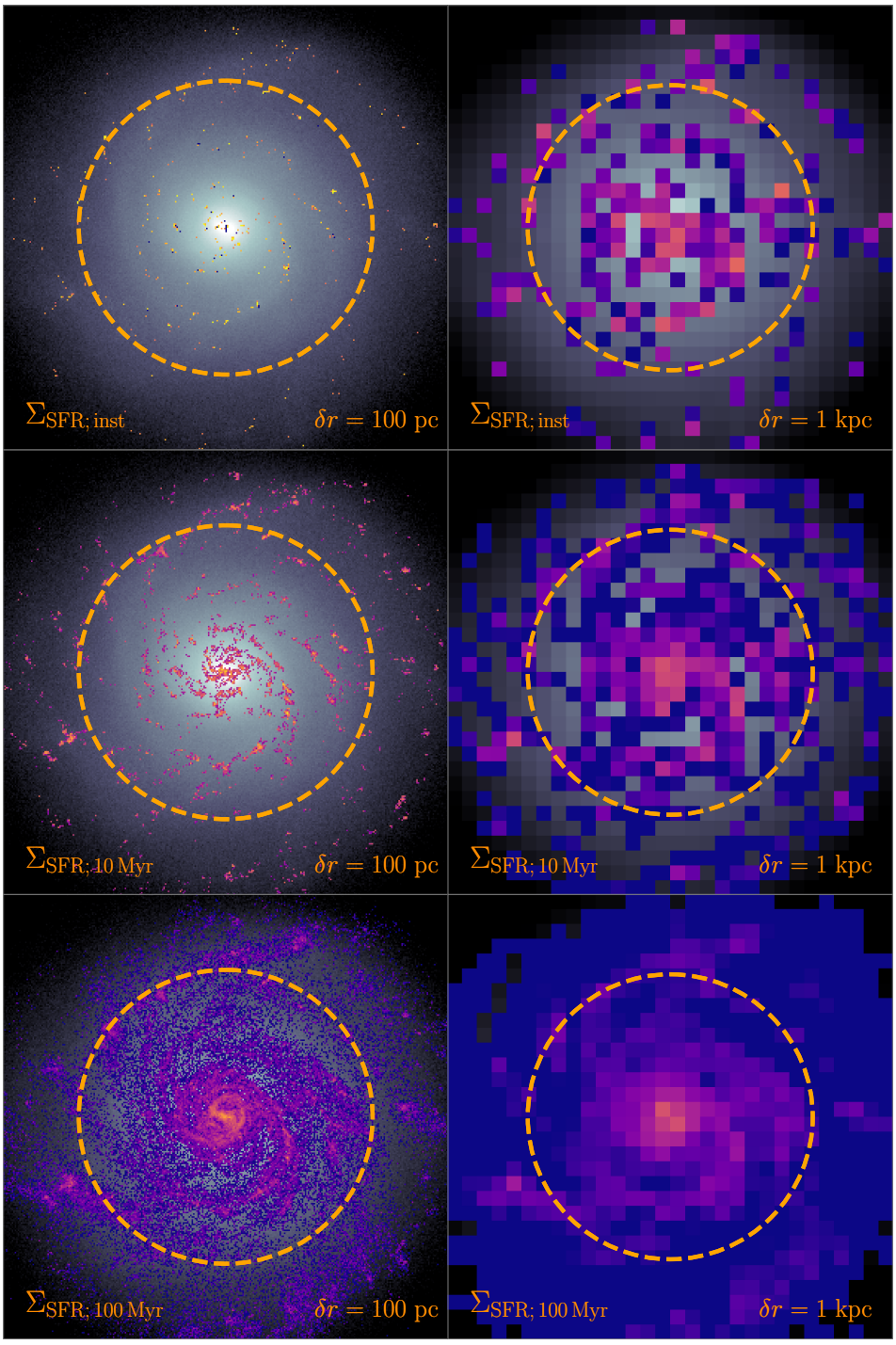

Figure 5.1: Stellar mass surface density ($\Sigma_\star$; greyscale) maps overlaid with SFR surface density ($\Sigma_{\rm SFR}$; coloured pixels) maps of a sample simulated galaxy (`m12m`) at 100 pc and 1 kpc pixel scales (left and right hand panels, respectively). Top to bottom, the panels show the instantaneous gas SFR, 10 Myr-averaged SFR, and 100 Myr-averaged SFR in a 30×30 kpc^2 field of view. The orange circle indicates $2 \times r_{\rm half}$.

The rSFMS emerges in the simulations even though it is not explicitly prescribed in the sub-grid physics model. A similar rSFMS is also seen in individual galaxies. At resolutions of $1-2$ kpc the slope of the rSFMS of the simulated galaxies is broadly consistent with observations ($\alpha_{\rm MS} \sim 0.62-1.09$ at $1-2$ kpc; Cano-Díaz et al., 2016; González Delgado et al., 2016; Abdurro'uf & Akiyama, 2017; Hsieh et al., 2017; Maragkoudakis et al., 2017; Liu et al., 2018).

Figure 5.3 shows the effect of pixel resolution on the measured rSFMS slope for my three SFR tracers (instantaneous, 10 Myr–average, 100 Myr–average). For reference, the open symbols show the measured $\alpha_{\rm MS}$ values from observational studies at low redshift (Cano-Díaz et al., 2016; González Delgado et al., 2016; Abdurro'uf & Akiyama, 2017; Hsieh et al., 2017; Maragkoudakis et al., 2017; Liu et al., 2018; Erroz-Ferrer et al., 2019). The different fitting methods and sample selections contribute to the scatter in the observed $\alpha_{\rm MS}$ (e.g. Hsieh et al., 2017; Lin et al., 2019b; Vulcani et al., 2019; Ellison et al., 2020). In the simulations, I find that as the spatial resolution increases, the rSFMS becomes shallower for all SFR tracers. The effect is more pronounced for the shorter-time-scale tracers. Additionally, at a given pixel scale, the slope depends on the SFR tracer. The shorter-time-scale tracers yield a shallower slope. I note that whilst the absolute value of the slope of the rSFMS and its dependence on resolution are sensitive to the details of the fitting method (such as choices of binning, weighting, SFR tracers), and the $\Sigma_\star - \Sigma_{\rm SFR}$ domain, the generic steepening of $\alpha_{\rm MS}$ with lower resolution (or longer timescale SFR tracers) is robust to such choices. The dependence of $\alpha_{\rm MS}$ on spatial resolution and the time-scale of the SFR tracer represents an important caveat for comparisons between observational studies.

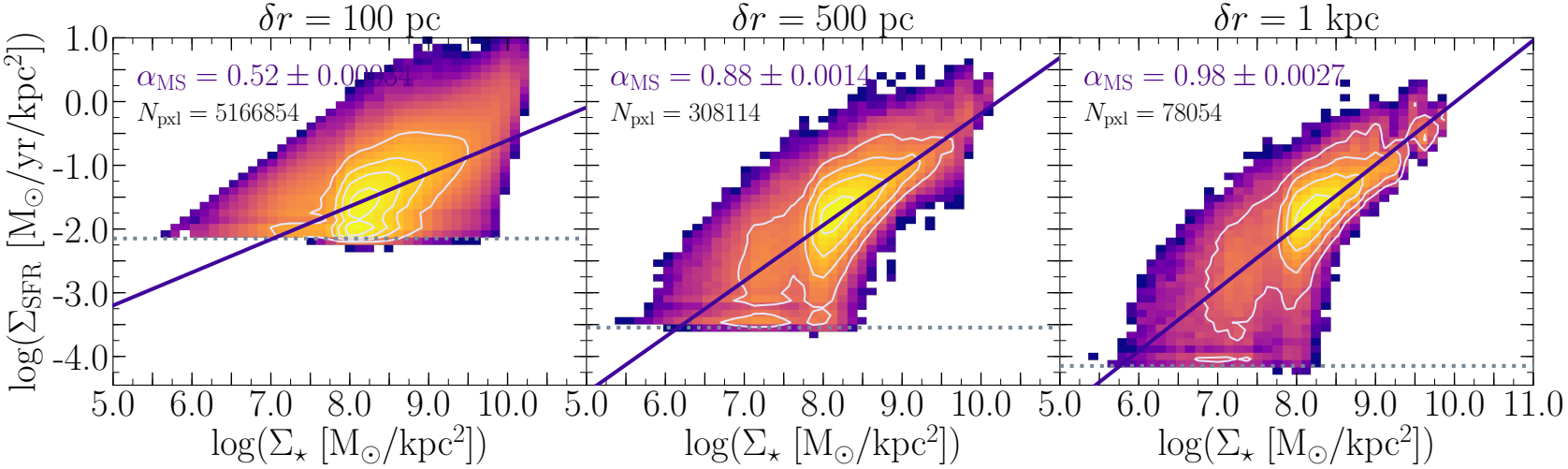

Figure 5.2: The 100 Myr-averaged rSFMS of the simulated galaxies using three pixel resolutions: 100 pc, 500 pc, and 1 kpc (left to right). The solid lines show the best fit to the pixel data in the $\Sigma_\star$-$\Sigma_{\rm SFR}$ space, with the slope ($\alpha_{\rm MS}$) annotated in the top left corner. The contours include 20%, 50%, 70%, and 90% of the pixels. The minimum resolved $\Sigma_{\rm SFR}$ is indicated by the horizontal dotted lines: $\log(\Sigma_{\rm SFR}/{\rm M}_\odot{\rm yr}^{-1}{\rm kpc}^{-2}) = -2.1$, -3.5, and -4.1 (left to right). An rSFMS is apparent at all spatial resolutions, and the relation flattens ($\alpha_{\rm MS}$ decreases) at higher spatial resolution.

5.3.2 The effect of clumpy star formation

I propose that the reason for the dependence of $\alpha_{\rm MS}$ on spatial resolution and SFR tracer time-scale is the contrast between the clumpy distribution of star-forming regions and the relatively smooth underlying stellar mass distribution. As the spatial resolution decreases, a pixel's $\Sigma_\star$ remains roughly unchanged, while the effective contribution of an *isolated* star-forming region decreases, thus causing a significant decrease in $\Sigma_{\rm SFR}$. This effect is less severe if there are more star-forming regions in a given pixel, since the higher filling factor mitigates the dilution effect of moving to lower resolution. The time-scale of the SFR tracer has a similar effect – as can be seen from Figure 5.1, if SFRs are averaged over a longer time, they have a larger filling factor. Since the gas profile decreases radially, star-forming regions are sparsely separated in the outer regions of a given galaxy (cf. Figure 5.1). Hence, the aforementioned effect of resolution and time-scales is more pronounced at lower $\Sigma_\star$ (which corresponds to larger radii, on average) thus causing a steeper $\Sigma_\star - \Sigma_{\rm SFR}$ correlation as the resolution decreases. The effect of resolution on the rSFMS slope is even more prominent for the shorter-time-scale SFR tracers, which trace smaller and 'patchier' regions (see Figure 5.1) and therefore are more severely affected by the change in pixel resolution.

In the scenario proposed above, the severity of the effect of pixel resolution (and SFR tracer time-scale) depends on the filling factor (and thus the total number, or equivalently the characteristic mass) of star-forming regions. The inset of Figure 5.3 shows the dependence of the rSFMS slope on the fraction of pixels (within $2 \times r_{\rm half}$) that host at least one star-forming region. The star formation filling factor correlates tightly with the rSFMS slope. As the star formation filling factor increases, the measured SFMS slope increases, thus supporting my hypothesis. Note that the SFMS slope exhibits a small dependence on the star formation time-scale at a given filling-factor, whereas $\alpha_{\rm MS}$ strongly depends on the filling factor.

I further investigate the dependence of $\alpha_{\rm MS}$ on spatial resolution (and filling factor) with a toy model of galactic star formation. The toy model includes two components: (1) smooth synthetic stellar profiles and (2) clumpy star formation. I generate 10^4 synthetic galaxies with a global 10 Myr–averaged SFR of 1 $M_\odot$/yr, appropriate for a $z \sim 0$ Milky Way-mass galaxy, and spawn them with star-forming regions as described below:

→ **Stellar profile:** The surface density profiles are described by an azimuthally

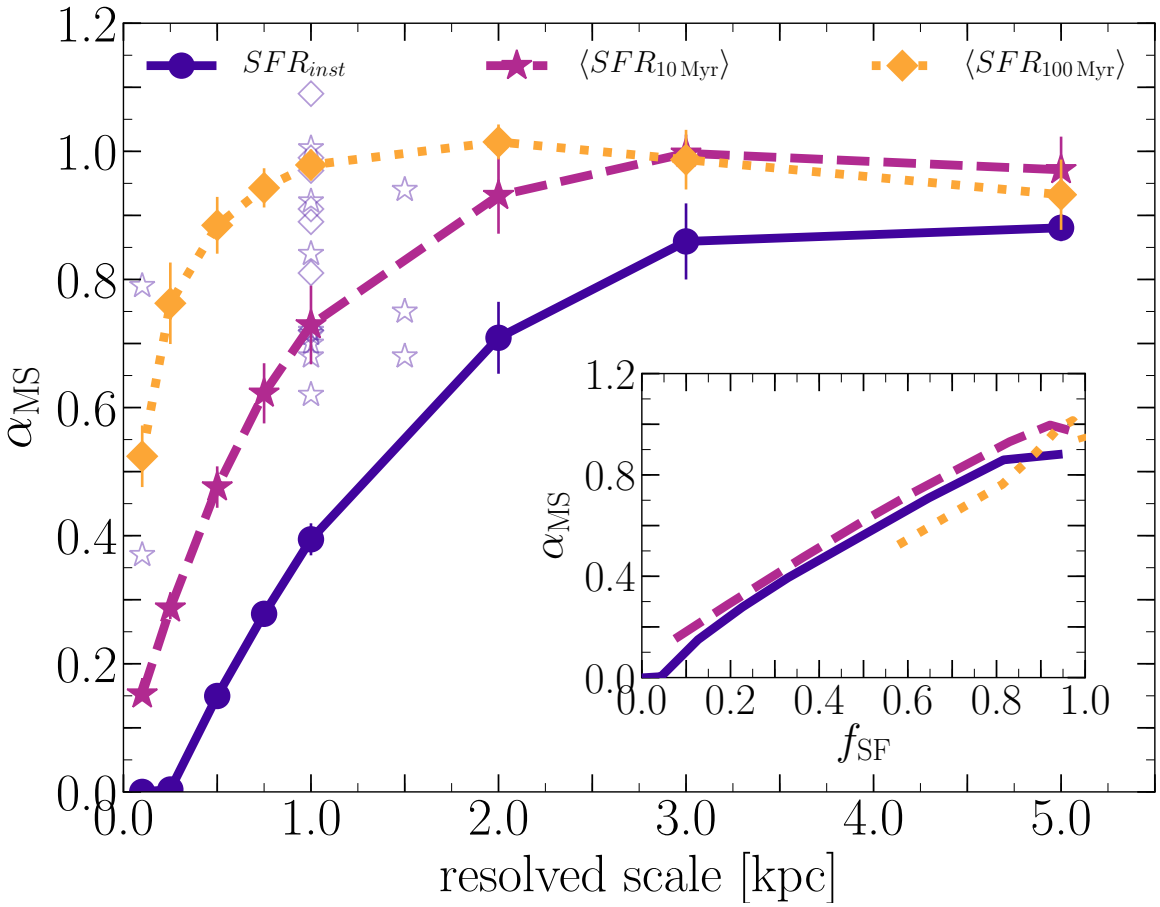

Figure 5.3: The dependence of the rSFMS slope (α_{MS}) of the simulated galaxies on pixel resolution. The colours and line styles indicate the slopes derived from different SFR tracers (instantaneous, 10 Myr, 100 Myr), and the error bars are jackknife errors highlighting the galaxy-to-galaxy variations in my sample. At coarser resolutions, the rSFMS becomes steeper. The dependence of the slope on resolution is more pronounced for SFR tracers with shorter time-scales. For reference the open symbols indicate the slopes measured by various observational studies at low redshift ($z \lesssim 0.1$; see text for details). The inset shows the dependence of α_{MS} on the filling factor of star-forming regions identified using the three SFR tracers. The slope depends strongly on the filling factor but is insensitive to the SFR tracer at a constant filling factor.

symmetric exponential disc profile:

$$\Sigma_\star(r) = \Sigma_0 e^{-(r-R_0)/R_\mathrm{d}},$$

where $\Sigma_0 = 6.1 \times 10^7$ $\mathrm{M}_\odot/\mathrm{kpc}^2$ is the stellar surface density at $R_0 = 8$ kpc, and the disc scale length is given by $R_\mathrm{d} = 2.9$ kpc (McGaugh, 2016).

→ **Star-forming regions:** I assume an exponential gas profile parameterized by a scale of 3.75 kpc (Kalberla & Dedes, 2008). I randomly spawn star-forming regions by sampling from a probability distribution following the gas surface density profile assuming a Kennicutt-Schmidt-like scaling (i.e. $P \propto \Sigma_\mathrm{gas}^{1.5}$; Kennicutt 1998) and deposit them onto a grid with a pixel scale of 20 pc. The masses of star-forming regions are drawn probabilistically from a Schechter distribution (e.g., Adamo et al., 2015): $P \propto M^\eta \exp\left(-M/M_\mathrm{cut}\right)$ where $\eta = -2$ and M_cut is allowed to vary. Therefore, the number of star-forming regions is dictated by the choice of M_cut and the total SFR. Each distribution is characterised by an average clump mass: M_SF.

Note that the toy model is *not* intended to be a *fit* to the FIRE galaxies presented in Section 5.3.1. Instead, the parametric stellar profile and star-forming region distribution are chosen to broadly represent a synthetic Milky-Way profile. I emphasise that the results of the toy model do not depend on the scaling parameters, the total SFR, η, or M_cut.

The synthetic galaxies are then degraded to lower resolutions, and the rSFMS is fitted following the method outlined above. Figure 5.4 demonstrates the effect of pixel resolution on the measured rSFMS slope for different M_SF. As the resolution decreases, the change in the rSFMS slope ($\Delta\alpha_\mathrm{MS} = \alpha_\mathrm{MS} - \alpha_{\mathrm{MS;\,100pc}}$) is more drastic. Different choices of M_SF exhibit a distinct behaviour with varying resolution. The galaxies with a small M_SF (large star formation filling factor since a high number of regions is required to accumulate the fixed total SFR) show a less severe dependence on resolution beyond a critical resolved scale due to the decreased sensitivity to dilution effects when the pixel filling factor is high. For a *large enough* pixel size, the underlying SFR field becomes statistically uniform, thus causing the rSFMS slope to exhibit a shallower dependence on resolution. The dependence of α_MS on resolution remains unchanged if the clump mass was fixed to M_SF.

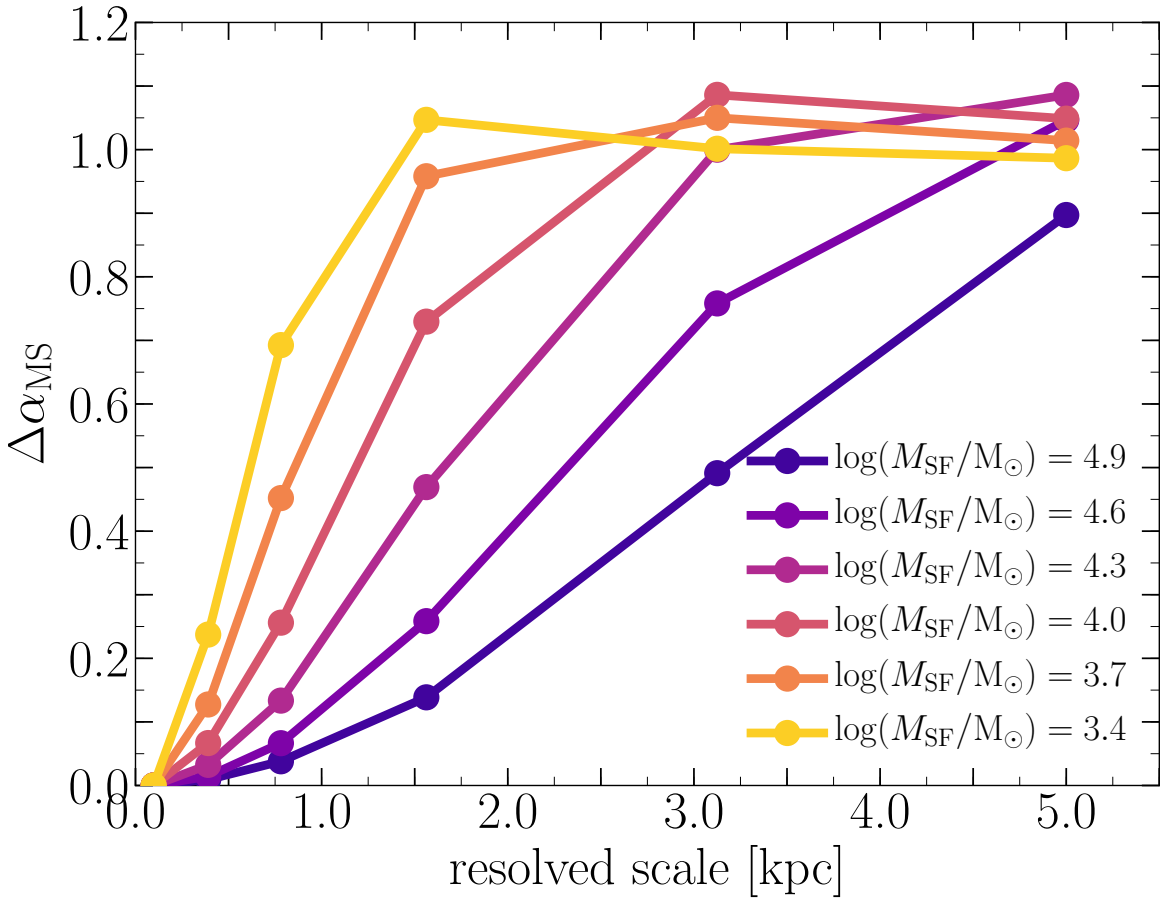

Figure 5.4: Results from the toy model demonstrating the effect of pixel resolution on the slope of the rSFMS in the presence of clumpy star formation. The colours indicate different choices of $M_{\rm cut}$ in the mass distribution of star-forming clumps spawned in the synthetic galaxy sample. The legend reports the average clump mass ($M_{\rm SF}$) of the distribution. The dependence of $\alpha_{\rm MS}$ on spatial resolution is highly sensitive to the characteristic mass of star-forming regions.

5.4 Summary & Discussion

In this Chapter, I presented the first analysis of the rSFMS of Milky Way-mass galaxies in the FIRE-2 simulations. I have demonstrated that the SFR tracer time-scales and pixel resolution can both have a significant impact on the derived slope of the rSFMS. I have shown that this effect is due to the clumpy nature of star formation; hence the measured slope of the rSFMS depends directly on the filling factor of star-forming regions, and the physical properties (i.e. mass) of star-forming clumps.

The dependence of the rSFMS slope on resolution and SFR tracer can be used to constrain properties (e.g. mass) of star-forming clumps (see Figure 5.4). Using a more *realistic* distribution of star-forming clump masses (e.g. a radially dependent Schechter function or power-law), the toy model presented in this work (§5.3.2) could potentially be used to infer observed average star-forming clump masses from the dependence of $\alpha_{\rm MS}$ on resolution. Additionally, the variation in the rSFMS slope may hint that the rSFMS may not be a fundamental diagnostic of star formation. Instead, understanding the scales at which the rSFMS deviates from the global and kpc-scale relations may shed more light on star formation on galactic scales.

Although the work presented here focuses on the rSFMS, the same slope dependence on resolution will be seen for other relationships that combine clumpy properties (here, $\Sigma_{\rm SFR}$) with more smoothly varying ones (here, $\Sigma_{\star}$). Conversely, relationships that use quantities that probe similar scales (such as the Kennicutt-Schmidt law) should not be strongly affected by resolution. Indeed, Orr et al. (2018) report that the Kennicutt-Schmidt law does not depend on resolution over a similar resolution range as studied in this work.

The work presented in this Chapter has notable implications for IFU surveys. Particularly, comparisons between surveys can be undermined by several effects, including (1) different pixel resolutions and (2) different SFR tracers, which are sensitive to different time-scales (and thus physical scales). Moreover, by progressively degrading high-resolution IFU data to coarser resolutions and analyzing the dependence of the rSFMS slope on spatial resolution, the characteristic mass of star-forming regions can be inferred using toy models similar to the one presented here.

Finally, this chapter demonstrates the existence and robustness of the rSFMS in numerical simulations. The existence of the simulated rSFMS allows galaxy comparisons and classification on resolved scales in simulations. For example, a pixel's

offset from the rSFMS can be used as a metric to compare and classify pixels. This approach is analogous to comparing galaxies and classifying them as star-forming or passive based on their offset from the global SFMS. In Chapter 6 I will leverage the existence of the rSFMS to quantify the effects of galaxy mergers on resolved scales.

Chapter 6

The resolved effects of galaxy interactions

Abstract

Galaxy scaling relations (e.g., mass metallicity relation, Kennicutt-Schmidt) have been key to our understanding of star formation and stellar feedback. In recent years, using statistical galaxy samples, IFU surveys have shown that these relations extend down to kpc and sub-kpc scales. Unlike observational studies, numerical simulations have not explored the emergence and evolution of resolved relations extensively; namely, the resolved SFMS and resolved mass metallicity relation. Moreover, our understanding of how galaxy mergers, a major evolutionary process, influence the resolved relations remains limited. In this chapter, I explore the effects of galaxy mergers on resolved scales. I present an analysis of the resolved properties of 1,927 post-merger galaxies selected from IllustrisTNG. I measure offsets of resolved regions from the resolved scaling relations to demonstrate how mergers impact galaxy properties. I demonstrate that merger-induced star formation enhancements ($\Delta \log(\Sigma_{\rm SFR}) \sim 0.4$ dex) are centrally peaked, and disappear at $r > 0.8$ $\rm r_{half}$. On the other hand, metallicities are diluted by as much as $\Delta \log(Z) \sim -0.08$ dex out $r = 4$ $\rm r_{half}$ in post-mergers. The extent and strength of the merger-induced effects depend on the merger and galaxy properties. Major mergers ($\mu \geq 0.3$) show the strongest central SFR enhancements ($\Delta \log(\Sigma_{\rm SFR}) \sim 0.6$ dex) and metallicity dilutions ($\Delta \log(Z) < -0.1$ dex). On the other hand, star formation is centrally boosted in star-forming post-mergers, while it is suppressed in the centres of passive post-mergers. The effects of mergers on star formation persist for ~ 0.5 Gyr for star-forming post-mergers. Within ~ 0.5 Gyr post-mergers show suppressed star formation in their outskirts ($r > 0.6$ $\rm r_{half}$). However, the effects of the merger on the gas metallicities persist for $1 - 2$ Gyr.

6.1 Introduction

In Chapter 4 I demonstrated that galaxy mergers can boost galactic star formation by a factor of ~ 2. However, the analysis in Chapter 4 focused on the *global* properties of galaxy mergers. In Chapter 5 I demonstrated the existence, and highlight the robustness, of the SFMS on kpc-scales (i.e., rSFMS) in simulations. In this chapter, I leverage the simulated rSFMS, and the kpc-scale MZR (rMZR) to investigate the resolved effects of galaxy mergers.

The effects of galaxy mergers on global galactic star formation and metallicities are well documented and founded by both observational and theoretical studies (see Section 1.3 and Chapter 4). Recently, the effects of galaxy interactions and mergers on star formation and metallicities have been also reported by observational studies on kpc-scales (Pan et al., 2019; Thorp et al., 2019). For example, Pan et al. (2019) used a morphologically classified sample to demonstrate that galaxy interactions can drive SFR enhancement throughout galaxies. Thorp et al. (2019), used a sample of post-mergers and reported a central boost in SFR by a factor of ~ 2.5. Despite their importance, galaxy mergers have not been *extensively* studied on *resolved* scales in numerical simulations. Numerical simulations studying the resolved effects of galaxy mergers use limited binary mergers suites and therefore do not include representative and diverse galaxy samples (e.g., Moreno et al., 2015; Rupke et al., 2010a; Sillero et al., 2017).

In this chapter I investigate the effects of galaxy mergers on kpc-scales using a large statistical sample of post-merger galaxies simulated in a fully cosmological environment. I (i) quantify the radial extent, and strength of SFR and metallicity enhancement and suppression during the post-merger phase, and (ii) constrain the evolution of the effects of the merger and their dependence on the merger properties (e.g., mass ratio, stellar mass, redshift). Additionally, I employ an observationally motivated methodology to facilitate comparisons to observational studies.

The chapter is structured as follows: In Section 6.2 I describe the simulations, the post-merger sample, and the methodology by which I "observe" the simulated galaxies. In Section 6.3 I present the preliminary results of this work, highlighting the effects of galaxy mergers on the star-formation and metallicity profiles in post-merger galaxies. I then discuss the results in Section 6.4. Finally, I present the conclusions of this work in Section 6.5, and discuss planned future work in Section 6.6.

6.2 Methods

I use the post-merger galaxy sample introduced in Chapter 4 (i.e., TNG100-1) to quantify the effects of galaxy mergers on the kpc-scale star formation and metallicity profiles of merger descendants. In this section, I provide an overview of the simulations, and the merger-identification methodology. I then describe how I "observe" the simulated galaxies and the process of generating a statistical control (non post-merger) sample to which I compare the properties of the merger descendants.

6.2.1 Numerical simulations: IllustrisTNG100-1

The work presented in this chapter utilises the IllustrisTNG simulations (Marinacci et al., 2018; Nelson et al., 2018a; Naiman et al., 2018; Pillepich et al., 2018b; Springel et al., 2018; Nelson et al., 2019a). I leverage the statistical power of the IllustrisTNG galaxy sample to investigate the effects of galaxy mergers in a large, diverse, and representative galaxy sample. The TNG galaxies have been evolved in a fully cosmological environment, thus yielding galaxies with *realistic* histories and observable properties (Naiman et al., 2018; Pillepich et al., 2018b; Springel et al., 2018; Donnari et al., 2019; Huertas-Company et al., 2019; Rodriguez-Gomez et al., 2019; Tacchella et al., 2019a).

I focus my analysis on TNG100-1, which is the highest resolution run of the intermediate volume box of the IllustrisTNG suite (110.7^3 Mpc^3). The large volume and spatial resolution of TNG100-1 render it ideal for comparison with current integral field spectroscopic surveys (e.g., MaNGA, SAMI, CALIFA). Although the larger, publicly available, TNG volume (i.e., TNG300-1) offers a substantial increase in the galaxy sample, its lower resolution ($\epsilon_{\rm dm} = 1.48$ kpc) is sub-optimal for comparisons to current observational surveys. The spatial resolution of TNG100-1 is characterised by a stellar and dark matter softening length $\epsilon_\star = \epsilon_{\rm dm} = 0.74$ kpc. Additionally, TNG100-1 has a dark matter mass resolution $m_{\rm dm} = 7.5 \times 10^6$ M$_\odot$, a baryonic mass resolution $m_{\rm b} = 1.4 \times 10^4$ M$_\odot$, and an average snapshot sampling every ~ 160 Myr.

The galaxy formation model implemented in IllustrisTNG (Weinberger et al., 2017; Pillepich et al., 2018a) is based on its precursor in the Illustris project (Vogelsberger et al., 2013; Torrey et al., 2014). For a description of IllustrisTNG and the TNG galaxy formation model see Section 4.2 or the IllustrisTNG introduction and methods papers: Weinberger et al. (2017); Marinacci et al. (2018); Nelson et al. (2018a); Naiman et al. (2018); Springel et al. (2018); Pillepich et al. (2018a,b), and

references therein.

6.2.2 Merger identification and the galaxy sample

I employ the post-merger galaxy sample introduced in Chapter 4. In this section, I present a synopsis of the merger-identification and sample selection method. I refer the reader to Chapter 4 for a detailed description of the merger-identification methodology.

Post-merger galaxies are identified using the merger trees which are constructed following the methodology of Rodriguez-Gomez et al. (2015). The merger trees assign a unique descendent to each simulated galaxy. Therefore, galaxy mergers are defined as nodes in the merger trees. Each post-merger galaxy is characterised by its (1) stellar mass[1] ($M_\star$), (2) redshift (z), and the (3) mass ratio[2] of the parents' merger (μ). Note that, unless otherwise noted, I refer to galaxies as post-mergers *only* in the first snapshot after the merger (within ~ 160 Myr).

I exclude galaxies with unresolved star formation rates ($SFR < 10^{-4}$ $\mathrm{M}_\odot$/yr) from my analysis. Moreover, I ignore subhalos with `SubhaloFlag` $= 0$, which are not thought to be of cosmological origin. I also exclude galaxies with nearby *overlapping* neighbours for two reasons: First, the fidelity in particle/gas cell association, and therefore mass and SFR calculations, declines drastically with decreasing separation. Second, because I am interested in the resolved profiles, overlapping neighbours contribute spurious high stellar, gas, and star formation rate density regions at large radii. To mitigate the effects of overlapping neighbouring galaxies, I exclude galaxies with $r_{\rm sep} \leq 4$ following the definition of Patton et al. (2020). Note that I use a larger $r_{\rm sep}$ threshold than that used in Chapter 4 because I am interested in the extended star formation and metallicity profiles rather than the *global* properties calculated within twice the stellar half mass radius ($r_{\rm half}$). Additionally, I exclude galaxies with a gas mass $\log(M_{\rm gas}/\mathrm{M}_\odot) < 10^8$, whose gas reservoirs are not well resolved at the mass resolution of TNG100-1.

My full galaxy sample consists of 177,737 galaxies with stellar masses $10 \leq \log(M_\star/\mathrm{M}_\odot) \leq 12$, and redshift $z \leq 1$. The post-merger sample contributes 1,919 galaxies with progenitor mass ratio $0.1 \leq \mu \leq 1$. The post-mergers, on average, exhibit enhanced global SFRs and disturbed morphologies with asymmetric low surface

[1] Following Patton et al. (2020), and Hani et al. (2020b) I use the maximum stellar mass within the past 500 Myr to mitigate the effects of numerical stripping.

[2] I define the mass ratio to be $0 < \mu \leq 1$.

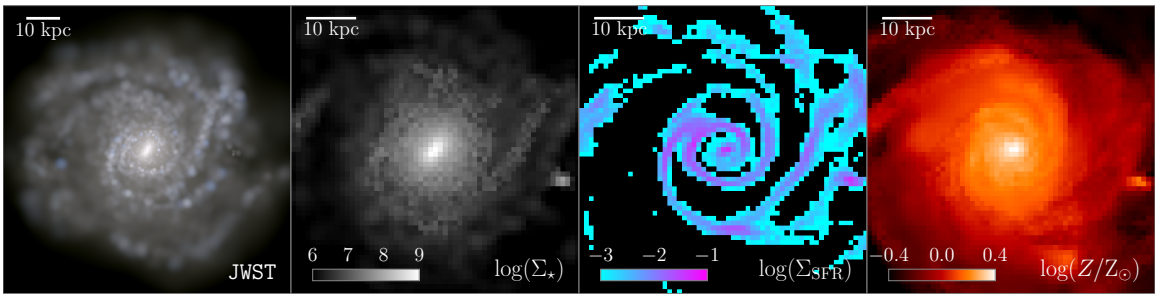

Figure 6.1: From left to right: An example synthetic JWST stellar composite image[3], and the associated $\Sigma_\star$, $\Sigma_{\rm SFR}$, and metallicity maps for the galaxy identified by `SubfindID` = 498854 at $z = 0$ in TNG100-1. The maps extend out to $5 \times r_{\rm half}$ from the host's centre with a resolution of ~ 1 kpc. The scale bar in the top left indicates a 10 kpc physical scale. Note that the synthetic `JWST` stellar composite image has a higher spatial resolution and a larger field-of-view ($15 \times r_{\rm half}$); the stellar composite image is not used in the analysis and is only included for illustration purposes.

brightness features (Chapter 4). The post-merger sample contributes 771,843 pixels (see Sections 6.2.3 and 6.2.4 for the details of the sample generation).

6.2.3 Resolved galaxy maps

I generate $\Sigma_\star$ maps, $\Sigma_{\rm SFR}$ maps, and SFR weighted metallicity (Z) maps for all the galaxies in my full galaxy sample. The maps represent the simulated analogue of the observational data products of integral field spectroscopic surveys; viz. I extract the physical quantities, measured from spectra in observational surveys, directly from the simulations. Figure 6.1 shows example maps of one simulated galaxy in TNG100-1.

The maps are generated by rendering the stellar particles and gas cells onto a Cartesian grid centred at the galactic potential minimum, and extending to $5 \times r_{\rm half}$ where $r_{\rm half}$ is the stellar half mass radius. I elect to render the galaxies at a spatial resolution of ~ 1 kpc (physical kpc) which is comparable to current surveys (i.e., MaNGA) and slightly coarser than the simulation's inherent spatial resolution. All galaxies are rendered along their stellar angular momentum axis (calculated using stellar particles within $2 \times r_{\rm half}$) thus yielding face-on maps. In order to alleviate the effects of interlopers along the line-of-sight (especially in dense environments), I ignore stellar particles and gas cells beyond $\pm 10 \times r_{\rm half}$ above/below the "galactic plane" as defined by the stellar angular momentum axis.

6.2.4 Statistical Controls

Understanding the effect of galaxy mergers on the SFR and metallicity profiles of galaxies requires a *fair* comparison of post-merger galaxies to a galaxy sample free of the effect of recent mergers. Removing known biases is a prerequisite of a fair comparison. For example, the galactic global SFR is known to correlate with stellar mass (e.g., Baldry et al., 2006; Peng et al., 2010, 2012), galactic environment (e.g., van den Bosch et al., 2007; Woo et al., 2013; Bluck et al., 2014, 2016), morphology (e.g., Wuyts et al., 2011; Mendel et al., 2013; Bluck et al., 2014), and a galaxy's distance to its nearest neighbour (e.g., Ellison et al., 2008a, 2013b; Patton et al., 2013, 2016). On the other hand, the SFR profile depends on the galaxy's global SFR and morphology (i.e., Ellison et al., 2018a). Therefore, in order to fairly compare post-merger galaxies to their merger-free counterparts I resort to statistical control matching, a commonly applied technique in observational studies (i.e., Ellison et al., 2018a; Thorp et al., 2019). In this section, I explain the details of the control matching method.

I first extract all the pixels with $\log(\Sigma_{\rm SFR}\,[{\rm M}_\odot/{\rm yr/kpc^2}]) \geq 3$ and $\log(\Sigma_\star\,[{\rm M}_\odot/{\rm kpc^2}]) \geq 6$. Note that I refer to spatial map elements as pixels because there is no spectral component in my analysis. Therefore, the pixels presented here are equivalent to *spaxels* in observational studies. Because I am interested in understanding the effects of galaxy mergers, I define a control pixel pool where the host galaxies have not undergone a merger with $\mu \geq 0.1$ within the past 2 Gyr (similar to control sample definition in Chapter 4.). The control pool contains 59,568,464 pixels extracted from 161,630 galaxies. Additionally, for each host galaxy I quantify the environment following Patton et al. (2020); I measure the distance to the nearest neighbour with $M_\star \geq 0.1 \times M_{\star,{\rm host}}$, and the number of neighbours with $M_\star \geq 10^9$ ${\rm M}_\odot$ within 2 Mpc. Finally, for each pixel in the full sample (i.e., post-mergers and controls) I select *at least* 5 control pixels: First, I reduce the control pool by only selecting control pixels with host galaxies at the same redshift (i.e., snapshot) as the pixel being controlled. Second, I search the redshift-culled control pixel pool for control pixels with (1) $\Sigma_\star$ within a tolerance of 0.1 dex, (2) radial distance from the centre of the host within $0.1r_{\rm half}$, (3) host $M_\star$ within 0.05 dex, (4) host r_1 within 10%, and (5) host N_2 within 10%. If more than five control pixels were found I consider the control matching complete. Otherwise, I grow the tolerances for $\Sigma_\star$, radial distance, $M_\star$, r_1, and N_2 by

[3]The synthetic JWST stellar composite image was generated using the image visualisation tool available at http://www.tng-project.org Nelson et al. (2019a).

0.05 dex, $0.1R_{\rm e}$, 0.05 dex, 10%, and 10%, respectively, and repeat the search up to three additional iterations. After four attempts the tolerances are considered to be too large for a satisfactory match. Therefore, I exclude pixels that require more than three iterations to identify an adequate control. The control-matched post-merger pixel sample includes 291,168 pixels. The median number of controls for each post-merger pixel is 25 with a median of 2 grows. Note that although only 38% of the post-merger pixels were assigned controls, I adopt the control matching methodology described above to allow for a fair and direct comparison with observations (i.e., Thorp et al., 2019). In future work, I will investigate different control matching tolerances and methodologies that would allow better matching, and increase the number of matched pixels. Figure 6.2 shows the distribution of the pixel and host properties in my control-matched post-merger sample.

With controls identified, pixels are statistically compared to their controls to quantify the effects of mergers on star formation and metallicity. I use comparative logarithmic metrics which have been extensively used in the literature (i.e., Ellison et al., 2018a; Thorp et al., 2019). The metrics compare a pixel's SFR and metallicity to its controls' median SFR and metallicity as follows:

$$\Delta \log\left(\Sigma_{\rm SFR}^{\rm pxl}\right) \equiv \log\left(\Sigma_{\rm SFR}^{\rm pxl}\right) - \log\left(\texttt{med}\left[\Sigma_{\rm SFR}^{\rm ctrl}\right]\right), \text{and} \tag{6.1}$$

$$\Delta \log\left(Z^{\rm pxl}\right) \equiv \log\left(Z^{\rm pxl}\right) - \log\left(\texttt{med}\left[Z^{\rm ctrl}\right]\right), \tag{6.2}$$

where the superscript "pxl" indicates pixel properties, the superscript "ctrl" indicates the controls' properties, and `med` represents the median. While I calculate the metrics in Equations 6.1 and 6.2 for all pixels (including the controls), I will only show the $\Delta \log(\Sigma_{\rm SFR})$ and $\Delta \log(Z)$ values for post-merger pixels in this chapter.

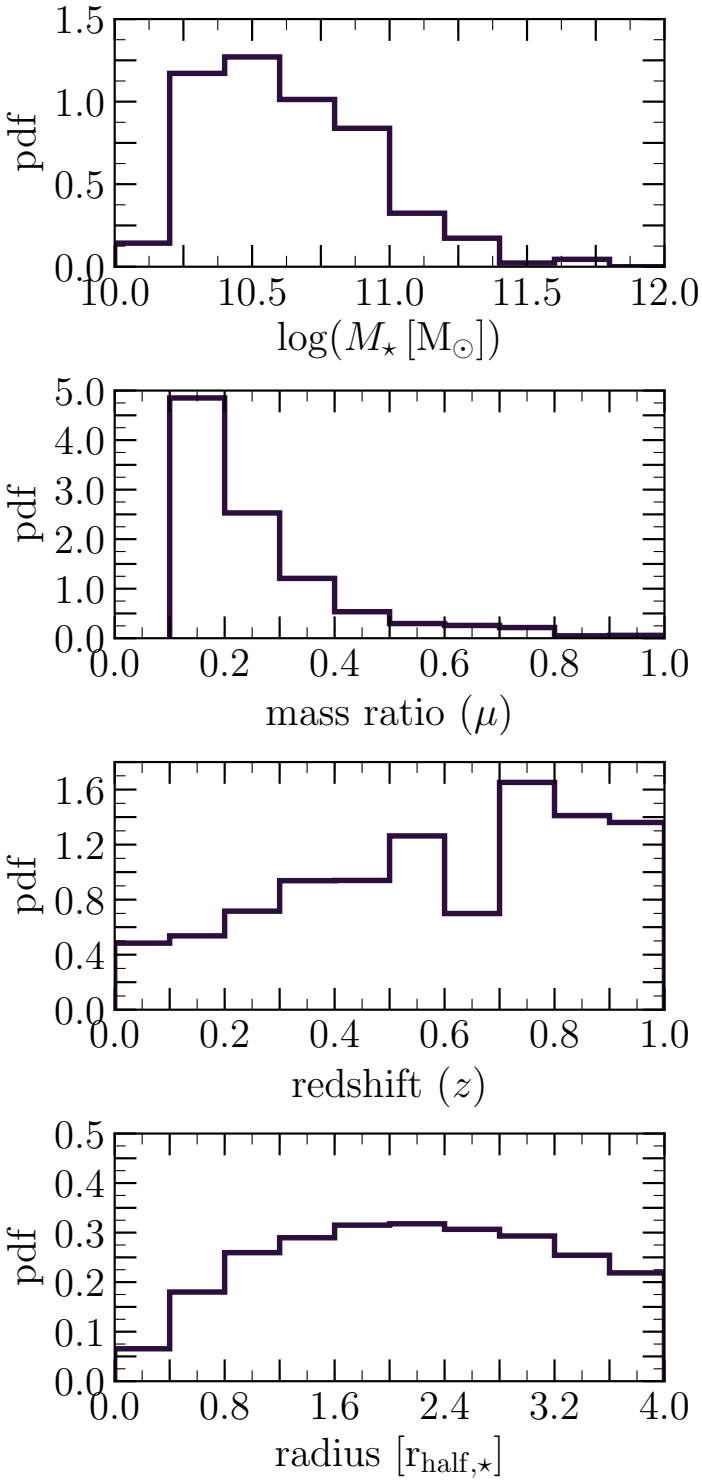

Figure 6.2: The distribution of pixel and host properties in my post-merger sample. The pixels span a wide range in radii, redshift, and merger mass ratio. Such diversity in pixel properties is key when studying the effects of mergers on the resolved properties of galaxies. The sample includes 291,168 pixels extracted from 1,927 post-mergers.

6.3 Results

In this chapter I am interested in studying the effects of galaxy mergers on resolved scales. I leverage known galaxy scaling relations that exist on "resolved" kpc-scales to investigate the impact of galaxy mergers. Several numerical studies have demonstrated the existence of kpc-scale resolved galaxy scaling relations (e.g., rSFMS, rMZR, Kennicutt-Schmidt; Orr et al., 2018; Trayford & Schaye, 2019, Qi et al. in prep., Chapter 5). For example, Qi et al. (in prep.) demonstrate the existence of observationally known scaling relations (i.e., rSFMS, rMZR) in the IllustrisTNG simulations with quantitatively consistent scalings. The authors also explore the physical origin of scaling relations on kpc-scales in IllustrisTNG. For example, they demonstrate that the rSFMS emerges in the IllustrisTNG simulations due to the star formation law (i.e., Kennicutt-Schmidt) and the equation of state implemented in the simulation.

The existence of the rMZR and rSFMS in IllustrisTNG provides a solid basis for studying the resolved properties of post-merger galaxies. In the following sections, I will demonstrate the effects of galaxy mergers on the star-formation and metallicity profiles of the mergers' descendants.

6.3.1 Resolved profiles of post-mergers

Effects of galaxy mergers

In Chapter 4 I demonstrated that post-mergers, on average, exhibit globally enhanced SFRs by factor of ~ 2 (see Table 4.1). In this section, I use the metrics outlined in Equations 6.1 and 6.2 to investigate how different regions within post-mergers contribute to the average global enhancement reported in Chapter 4.

Figure 6.3 shows the effects of mergers on the star formation and metallicity profiles of post-mergers. On average, star formation is enhanced within 0.8 $r_{\rm half}$ with a maximum enhancement $\Delta \log(\Sigma_{\rm SFR}) \sim 0.4$ dex at the centre. The SFR enhancement declines monotonically with increasing radius; post-mergers exhibit normal SFRs at $r > 0.8$ $r_{\rm half}$. On the other hand, metallicities are suppressed in post-mergers out to ~ 4 $r_{\rm half}$. Unlike the star formation enhancement, the metallicity suppression is not monotonic. The maximum suppression ($\Delta \log(Z) \sim -0.08$ dex) occurs at $r \sim r_{\rm half}$, while the metallicities exhibit minimal differences in the outskirts and in the centres of galaxies.

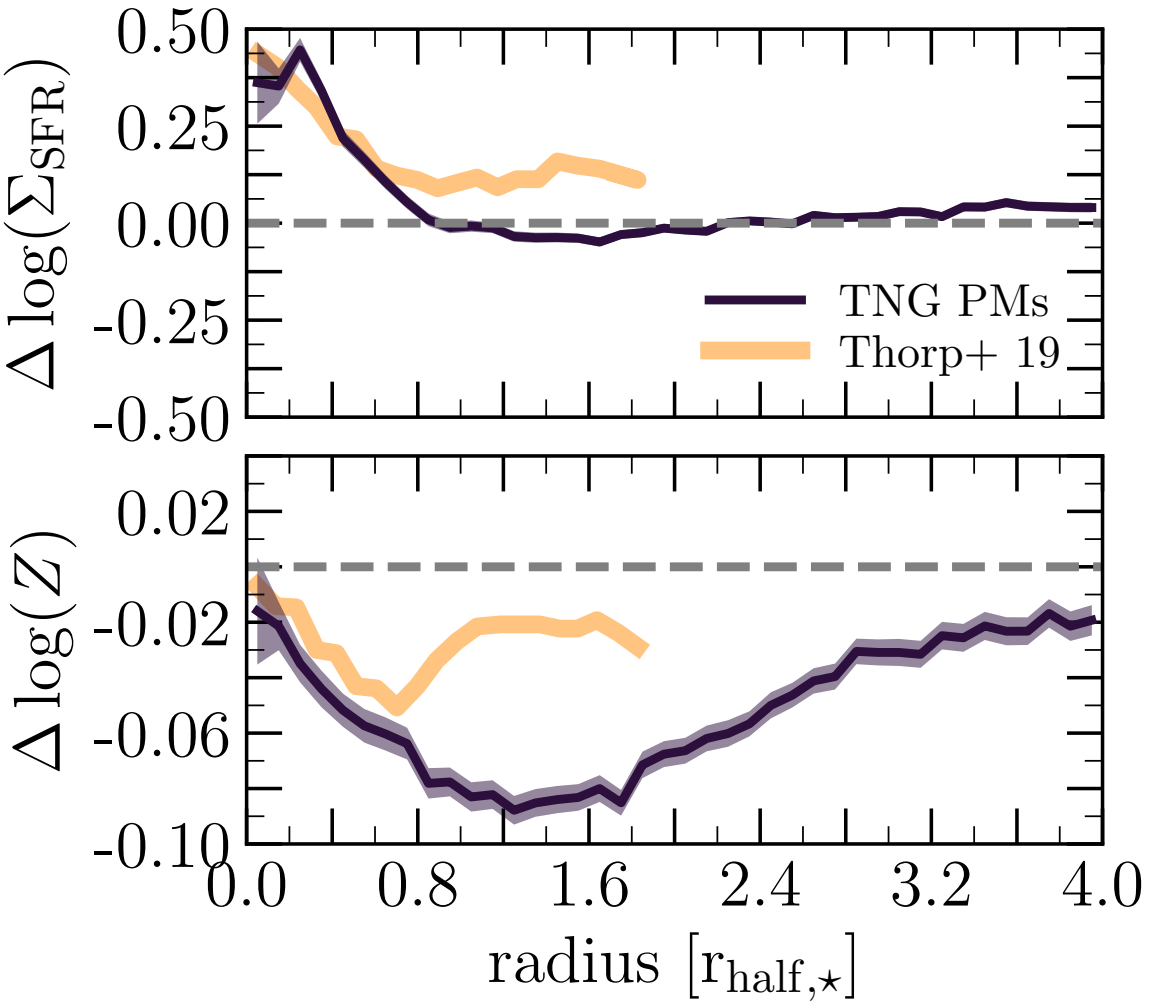

Figure 6.3: The comparative star formation and metallicity profiles of post-mergers in TNG100-1. The dark purple lines show median radial profiles of all pixels extracted from post-mergers. The shaded purple regions represent the standard error on the mean. The orange lines show the median profiles calculated by Thorp et al. (2019). Star formation is enhanced in the centre while the metallicity is suppressed globally in post-merger galaxies. While the TNG post-mergers show qualitatively similar results to observational data, there are noticeable differences in star formation and metallicity at $r > 0.8$ $r_{\rm half}$.

The centrally peaked and monotonically declining median star formation profile in my post-merger sample is qualitatively similar to those reported by observations (e.g., García-Marín et al., 2009; Barrera-Ballesteros et al., 2015; Cortijo-Ferrero et al., 2017b; Thorp et al., 2019) and simulations (e.g., Renaud et al., 2014; Moreno et al., 2015; Sparre & Springel, 2016; Moreno et al., 2019). Moreover, the suppression in

metallicity in my sample is consistent with predictions from high resolution numerical simulations (e.g., Torrey et al., 2012; Bustamante et al., 2018), and has been confirmed by observational studies (e.g., Thorp et al., 2019). For example, Figure 6.3 shows the results of Thorp et al. (2019) for comparison. While my results show qualitative similarities to those of Thorp et al. (2019), there are notable differences in both the star formation and metallicity profiles at $r > 0.8$ r_{half}. The media star formation profile in my post-merger sample is consistent with that of the controls at $r > 0.8$ r_{half}, while Thorp et al. (2019) reports enhancements even at larger radii. Moreover, the observed metallicity profile in Thorp et al. (2019) turns over at $r > 0.8$ r_{half}, while my post-merger sample shows a maximum metlallicity suppression at $r \sim 1.2$ r_{half}. One possible cause for these differences is the sample selection methodology; i.e., Thorp et al. (2019) analyses the properties in a morphologically selected sample of post-merger. Visual selection relies on morphological features which strongly depend on the merger properties (mass ratio, gas fraction; e.g., Lotz et al., 2010a,b), thus yielding a biased post-merger sample. I discuss my results, and compare them with other studies in Section 6.4.

I note that the individual galaxies show a stark diversity in their star formation and metallicity profiles. Figure 6.4 shows the star formation and metallicity profiles of three post-mergers selected from my sample. While the median profile of all post-mergers in my sample shows a monotonically declining star formation profile with no enhancement at $r > 0.8$ r_{half}, individual galaxies may differ significantly. For example, some post-mergers exhibit suppressed central star formation, while others show star formation enhancements that extend out to ~ 4 r_{half}. On the contrary, other post-mergers show no signs of the merger in their star formation profiles. Similarly, the metallicity profiles of individual post-mergers may differ significantly from the median profile of the entire sample. Some post-mergers exhibit enhanced central metallicities, while others show enhancements in the outskirts. In future work I will discuss possible drivers of such diversity by correlating the effect of the merger to other known merger or pixel properties.

Effects of mass ratio

The merger mass ratio is one of the key parameters defining a galaxy merger. Various hydrodynamical simulations demonstrate the correlation between the effects of the merger (their strengths, and timescales on which they are prominent) and the merger

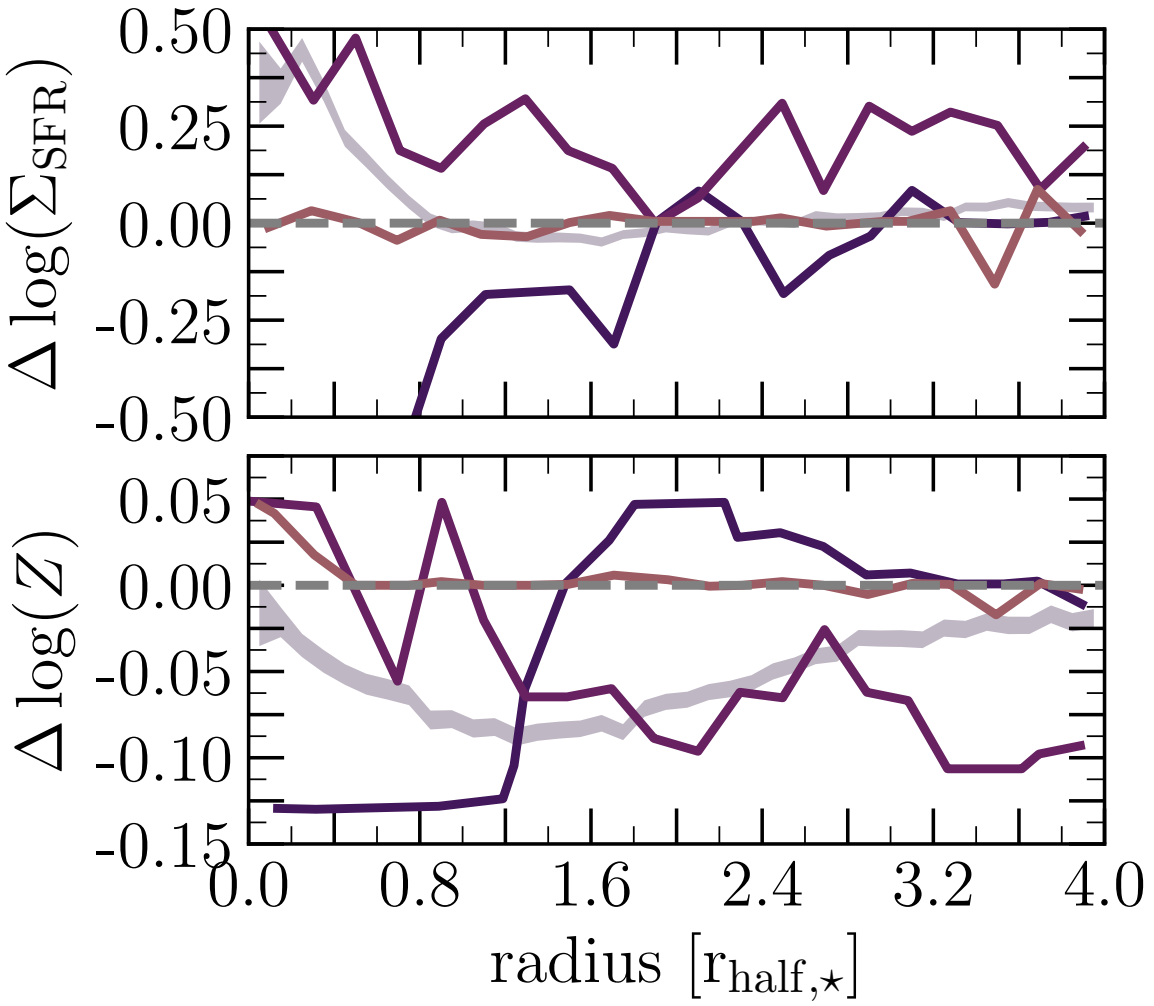

Figure 6.4: Example comparative star formation and metallicity profiles of three post-mergers in TNG100-1 (coloured lines). The shaded regions show the median radial profiles in Figure 6.3 for comparison. Post-mergers show remarkable diversity in their profiles.

mass ratio (e.g., Bournaud et al., 2005; Cox et al., 2008; Johansson et al., 2009; Lotz et al., 2010a). For example, the most prominent morphological disturbances, long-lived extended asymmetries, and the strengths of merger-induced starbursts correlate closely with the merger mass ratio (e.g., Bournaud et al., 2005; Cox et al., 2008; Lotz et al., 2010a; Scudder et al., 2012). In Section 4.3.1 I demonstrated the effect of the merger mass ratio (albeit weak) on the strength of the merger-induced global SFR enhancement. In this section, I explore the effects of the merger ratio on the resolved star formation and metallicity profiles of my post-merger sample.

Figure 6.5 shows the median comparative star formation and metallicity profiles

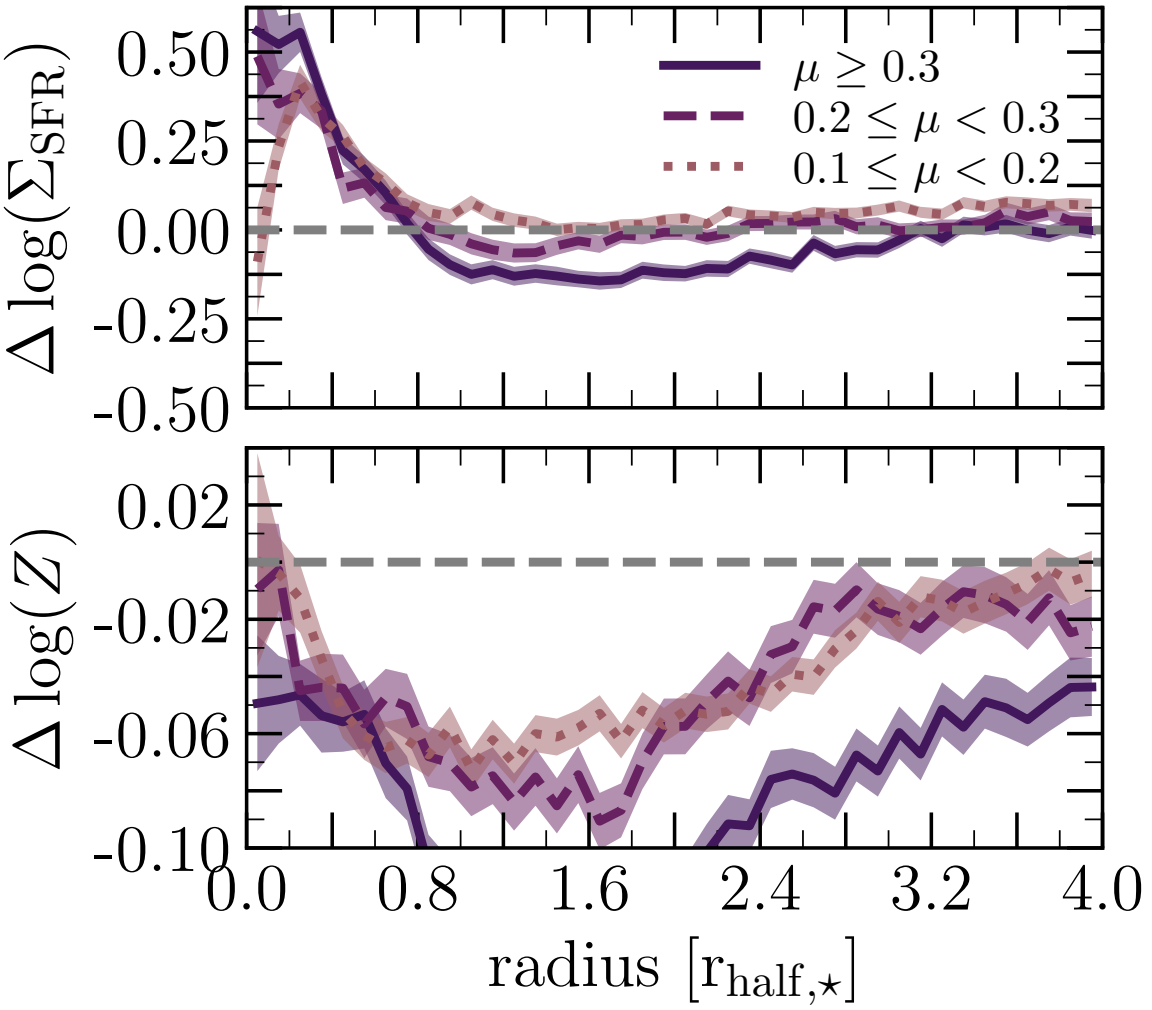

Figure 6.5: The dependence of the comparative star formation and metallicity profiles of post-mergers in TNG100-1 on the merger mass ratio. The lines show median radial profiles of all pixels extracted from post-mergers. The shaded regions represent the standard error on the mean. Major mergers exhibit the strongest central star formation enhancement, while they suffer from suppression in star formation in their outskirts. Similarly, the metallicity dilution are strongest for the most major mergers.

for the descendants of mergers with different mass ratios. The strength of the central boost in star formation depends on the merger mass ratio: Major mergers ($\mu \geq 0.3$) show the strongest central star formation enhancement $\Delta \log(\Sigma_{\rm SFR}) \sim 0.56$ dex. The strength of the central enhancement decreases with decreasing mass ratio. For all mass ratios, the SFR enhancement declines towards the outskirts of the post-merger galaxies. Major mergers yield suppressed star formation at $r \geq 0.8$ $r_{\rm half}$, while the rest of the post-mergers show normal star formation profiles for $r > 0.8$ $r_{\rm half}$. On the

other hand, the metallicity profiles of post-merger galaxies are suppressed regardless of mass ratio. However, the suppression is strongest ($\Delta \log(Z) < -0.1$ dex) for major mergers ($\mu \geq 0.3$).

My results are consistent with predictions from high resolution numerical simulations. Namely, Moreno et al. (2015) reported suppressed star formation in the outskirts of major mergers using a binary merger suite. Additionally, the dependence of the metallicity dilution on the merger mass ratio is consistent with the findings of Bustamante et al. (2018) who used cosmological zoom-in simulations and demonstrated similar central suppression in metallicity. However, in contrast with isolated binary merger simulation suites, and cosmological zoom-in simulations, the post-merger sample I present offers a large galaxy sample with statistically representative merger (e.g., mass ratio, orbital parameters) and galaxy properties (e.g.., gas content, morphology) thus allowing for (1) a realistic and fair comparison to observations, and (2) a detailed analysis of the physical mechanisms at play during galaxy mergers. My results support the scenario where merger-induced asymmetric torques give rise to gravitational instabilities that funnel gas into the centres of galaxies. I will explore the driver of the metallicity dilution and star formation enhancement in future work.

Effects of the galaxy's type

In Chapter 4 I showed that passive post-mergers, on average, show no enhancement in their global SFRs, while their star-forming counterparts exhibit SFRs that are enhanced by a factor of ~ 2 (see Table 4.1). In this section, I explore the effects of mergers on the resolved profiles of passive and star-forming galaxies as defined in Chapter 4.

Understanding the difference between passive and star-forming galaxies is a complex matter. A galaxy's star formation rate often correlates with internal and external properties such as morphology (e.g., Lang et al., 2014; Bluck et al., 2014), colour (e.g., Baldry et al., 2004), stellar mass (e.g., Baldry et al., 2006; Bluck et al., 2014), and environment (e.g., Woo et al., 2015; Bluck et al., 2016). Therefore, comparing passive and star-forming galaxies reflects the complex interplay of various physical processes. Nonetheless, there are valuable lessons to be learnt from such comparison.

Figure 6.6 shows comparative star formation and metallicity profiles of post-mergers in TNG100-1 split by galaxy type; star-forming post-mergers contribute to 79% of the post-merger pixels, while passive post-mergers contribute 21% of the to-

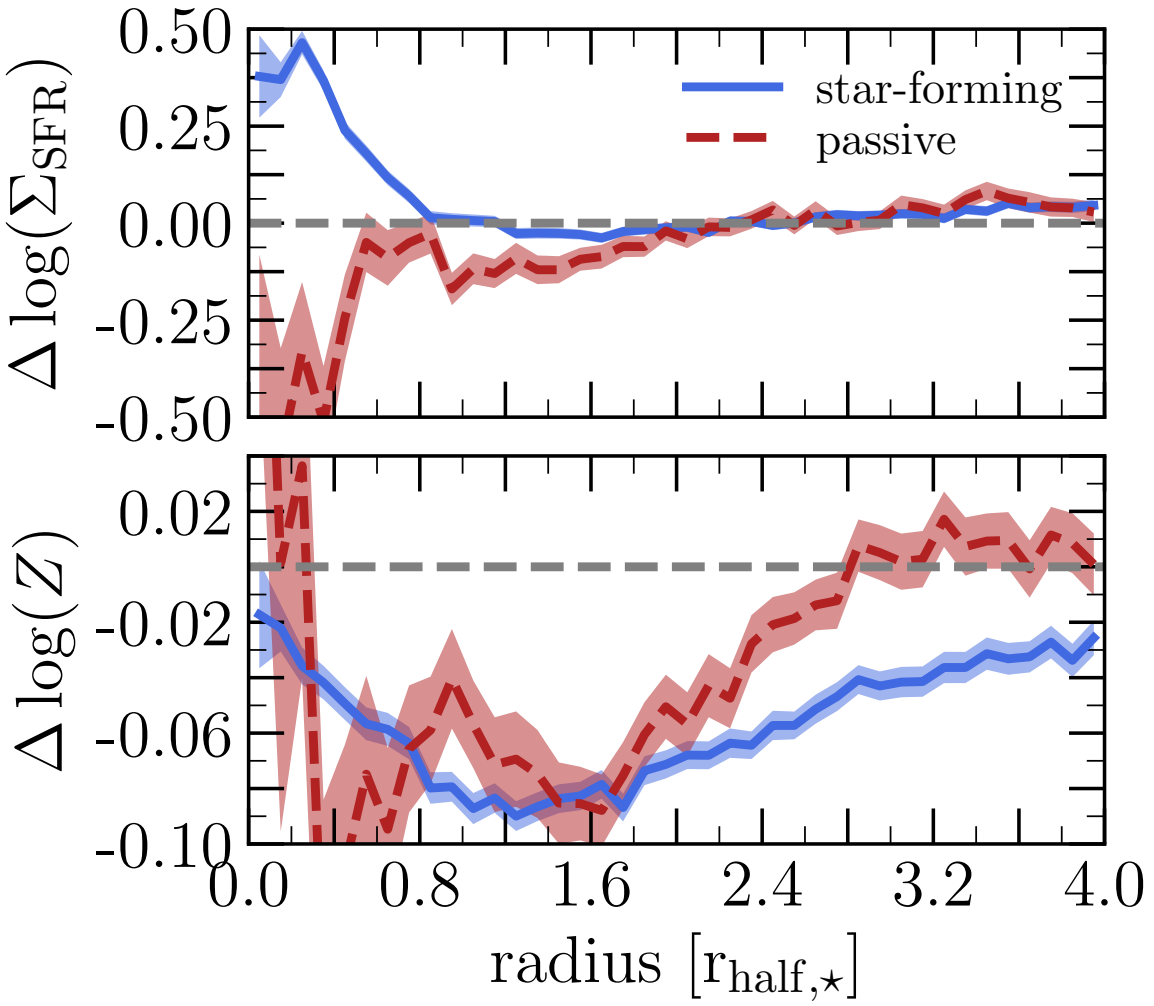

Figure 6.6: The dependence of the comparative star formation and metallicity profiles of post-mergers in TNG100-1 on galaxy type. The lines show median radial profiles of all pixels extracted from post-mergers. The shaded regions represent the standard error on the mean. Star-forming galaxies dominate the profiles shown in Figure 6.3, while passive galaxies exhibit little merger-induced effects in their SFR profiles except for the central 0.6 $r_{\rm half}$ where the SFR is suppressed. On the other hand, while passive and star-forming galaxies show suppressed metallicities, passive galaxies show metallicities consistent with their controls for $r > 2.8$ $r_{\rm half}$.

tal post-merger pixel sample. Star-forming galaxies show similar star formation and metallicity profiles to those of the total sample shown in Figure 6.3. However, passive galaxies exhibit SFRs consistent with their controls except at $r < 0.6$ $r_{\rm half}$ where there is a suppression in the SFR. The star formation profiles in star-forming and passive post-mergers in my sample are consistent with those reported in observational stud-

ies using non-merging galaxies (e.g., Ellison et al., 2018a; Tacchella et al., 2018; Lin et al., 2019a; Breda et al., 2020). On the other hand, the metallicity profiles for both star-forming and passive galaxies exhibit suppressed metallicities. However, passive galaxies show metallicities that are consistent with their controls in the outskirts ($r > 2.8$ r_{half}). The differences between the star-forming and passive samples could be because of differences in (1) the gas reservoir properties (e.g., metallicity, density), (2) the physical conditions (e.g., cooling/heating), or (3) the availability of gas (e.g., gas content, gas fraction). I will explore the source of the differences between the two galaxy types in future work.

6.3.2 Evolution of mergers beyond coalescence

In Section 6.3.1 I demonstrated the effects of galaxy mergers on the star formation and metallicity profiles in the first snapshot ($\sim$ 160 Myr) after the merger. I showed that galaxy mergers induce central enhancements in star formation, and diluted metallicity profiles. In this section, I explore how the resolved effects of the merger evolve during the post-merger phase.

As described in Section 6.2, I search for controls for each post-merger pixel independently. Therefore, the pixels extracted from the descendants of the post-mergers have their controls independently generated at each snapshot (i.e., I do not trace the control pixels in time). Pixels are then compared to their controls using the metrics in Equations 6.1 and 6.2 at every snapshot after the merger.

The evolution of the star formation profile

Figure 6.7 shows the evolution in the star formation profiles of post-mergers for 2 Gyr after the merger. The enhanced central star formation ($\Delta \log(\Sigma_{SFR}) \sim 0.25$ dex) persists during the first 0.5 Gyr after the merger within $r < 0.5$ r_{half}, while star formation is mildly suppressed ($\Delta \log(\Sigma_{SFR}) \sim -0.12$ dex) at $r > 0.5$ r_{half}. Note that the region of enhanced star formation shifts to smaller radii after $\sim$ 0.5 Gyr after the merger compared to immediately following the merger. In contrast, the suppression of star formation in passive post-mergers extends to all radii; the strength of the suppression increases with decreasing radius. The effects of the merger on star formation dissipate within $\sim 1 - 2$ Gyr in star-forming galaxies. However, passive post-merger galaxies continue to show suppressed star formation profiles even after $1 - 2$ Gyr. I note that the long-lasting suppression of star formation in passive galaxies does not necessarily

indicate that the galaxies are permanently passive. Passive galaxies that rejuvenate with a sufficient increase in their SFR would be considered star-forming galaxies, and therefore they do not contribute to the profiles of passive galaxies. Rodríguez Montero et al. (2019) reported post-merger rejuvenation in the SIMBA simulation. I also showed in Chapter 4 signatures of rejuvenation in my post-merger sample (see Figure 4.13). In future work, I will investigate the cause of the long-lasting suppression in passive galaxies and the properties of post-mergers that rejuvenate.

In Section 6.3.1, I demonstrated the effect of the merger mass ratio on the star formation and metallicity profiles of post-mergers. Figure 6.7 shows the evolution of the post-merger star formation profiles as a function of merger mass ratio. While all mergers drive a central enhancement in star formation, major mergers induce the strongest enhancement (Figure 6.5). However, star formation is suppressed in the outskirts of all post-mergers, and the strength of the suppression correlates with the merger mass ratio. Namely, major mergers ($\mu \geq 0.3$) induce the strongest central enhancements ($\Delta \log(\Sigma_{\rm SFR}) \sim 0.37$ dex) coupled with the highest suppressions ($\Delta \log(\Sigma_{\rm SFR}) \sim -0.2$ dex) in star formation in the outskirts. Nonetheless, regardless of the merger mass ratio, the star formation profiles evolve similarly and the effects of the merger on star formation are almost non-existent after $\sim 1-2$ Gyr.

The early evolution of the star formation profiles and the effects of the merger mass ratio are consistent with the scenario where galaxy mergers give rise to gas inflows. The inflows would increase star formation in the central regions and possibly drive a suppression in star formation in the outskirts (e.g., Moreno et al., 2015). In future work, I will explore the source of the global suppression in star formation in passive post-mergers, as well as the mild suppression in star formation at high radii in star-forming post-mergers, and its dependence on mass ratio.

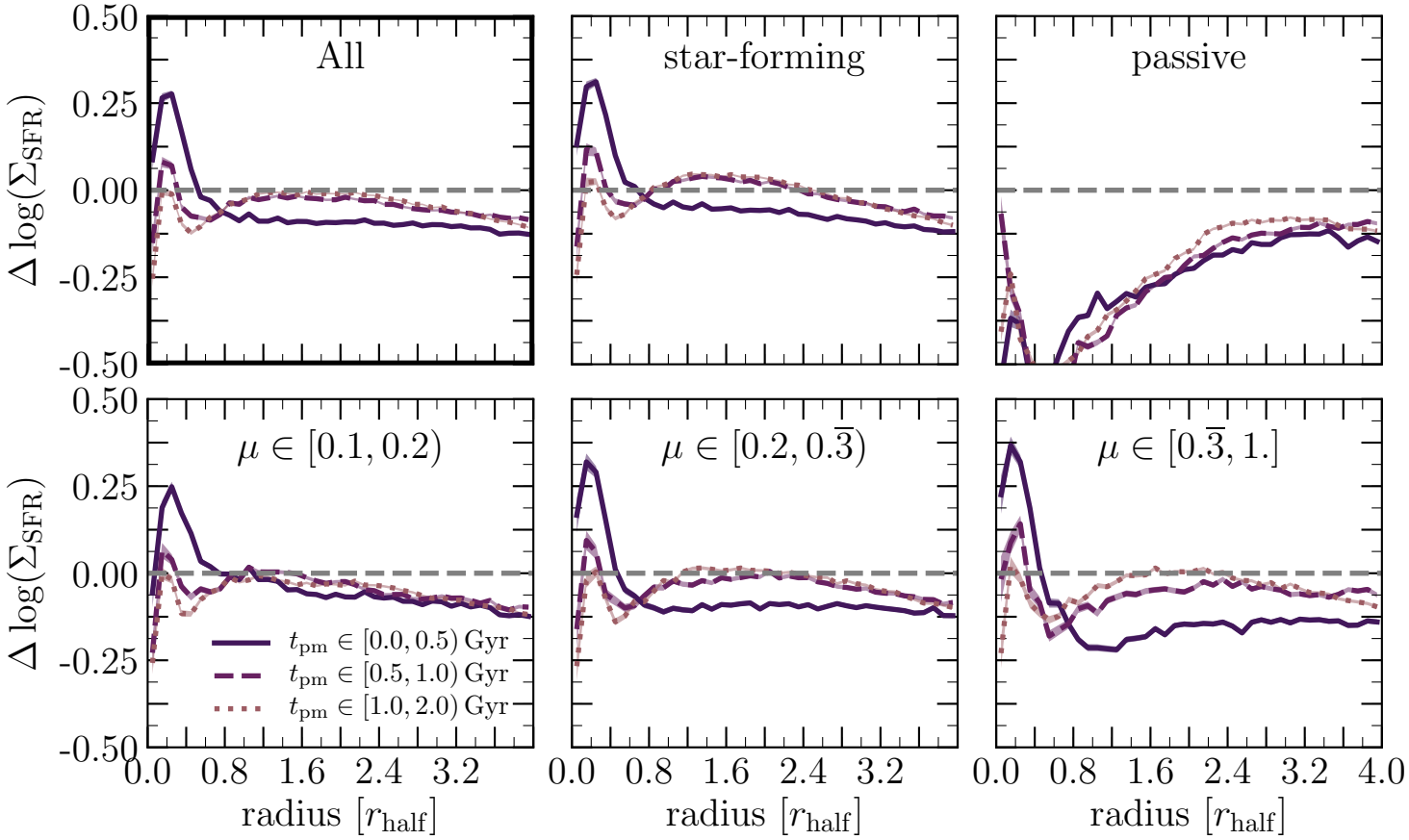

Figure 6.7: The evolution of the comparative star formation profile after the merger. The lines show three time bins after the merger. Left to right, the top panels show the evolution of the full sample, star-forming galaxies, and passive galaxies. The bottom panels show the evolution of the descendants of mergers with different mass ratios divided by increasing mass ratio from left to right. The effects of the merger on star formation in star-forming post-mergers dissipate after $\sim 1-2$ Gyr independent of mass ratio. However, passive post-mergers exhibit suppressed star formation at all radii after the merger. Major mergers show the strongest star formation enhancement in their centres paired with suppression in their outskirts.

The evolution of the metallicity profile

Figure 6.8 shows the evolution in the metallicity profiles of post-mergers for 2 Gyr after the merger. Although I showed that central metallicities are suppressed within $\sim$ 160 Myr after the merger (Figure 6.3), the centrally enhanced star formation enriches the gas reservoir driving an enhancement in central metallicities for both star-forming and passive post-mergers within 0.5 Gyr after the merger. The metallicity enhancement is centred within $r < 0.4$ r_{half} for all post-mergers. Outside of $r \sim 0.4$ r_{half} the gas phase metallicity is suppressed by as much as $\Delta \log(Z) \sim -0.08$ dex in star-forming galaxies, and $\Delta \log(Z) \sim -0.12$ dex in passive galaxies. The strength of the suppression in metallicity declines with increasing radius. In star-forming post-mergers metallicities remain suppressed even at $r \sim 4$ r_{half}, while the metallicity profiles of passive galaxies are consistent with their controls at $r \geq 3.2$ r_{half}. Following the merger, the metallicity profile of passive post-mergers shows little evolution. In contrast, the suppressed metallicity profiles of star-forming post-mergers evolve drastically; the suppression dwindles after the merger. After $\sim 1-2$ Gyr, the metallicity profiles of star-forming post-mergers are consistent with their controls within ± 0.02 dex.

Cosmological zoom-in simulations of galaxy mergers stress the effect of the merger mass ratio on the merger-induced metallicity dilution (e.g., Bustamante et al., 2018). Figure 6.7 shows the evolution of the post-merger metallicity profiles as a function of merger mass ratio. The strength of the metallicity dilution (at $r \geq 0.4$ r_{half}) within 0.5 Gyr after the merger depends on mass ratio. Major mergers ($\mu \geq 0.3$) drive the strongest metallicity dilutions with $\Delta \log(Z) < -0.1$ dex while minor mergers ($\mu < 0.2$) contribute a maximal dilution of $\Delta \log(Z) \sim -0.06$ dex. Within $1-2$ Gyr after the merger, the effects of minor mergers have mostly faded. In contrast, the merger-induced metallicity dilution in merger remnants with mass ratio $\mu \geq 0.2$ persists even after $1-2$ Gyr.

Post-mergers show an small enhancement ($\Delta \log(Z) \sim 0.02$ dex) in their metallicity profiles at $r > 2$ r_{half} within $1-2$ Gyr after the merger. The enhancement is surprising given that the star-formation profiles do not show any enhancement at such large radii. In fact, some star formation profiles are suppressed beyond 2 r_{half}. The cause of the metallicity enhancements in the outskirts of post-mergers remains unclear: i.e., (1) is the metallicity *truly* increasing in the outskirts (e.g., metallicity enhancement from a galactic fountain), or (2) is the enhancement an artefact of my

methodology? I will investigate the cause of the enhancement in future work.

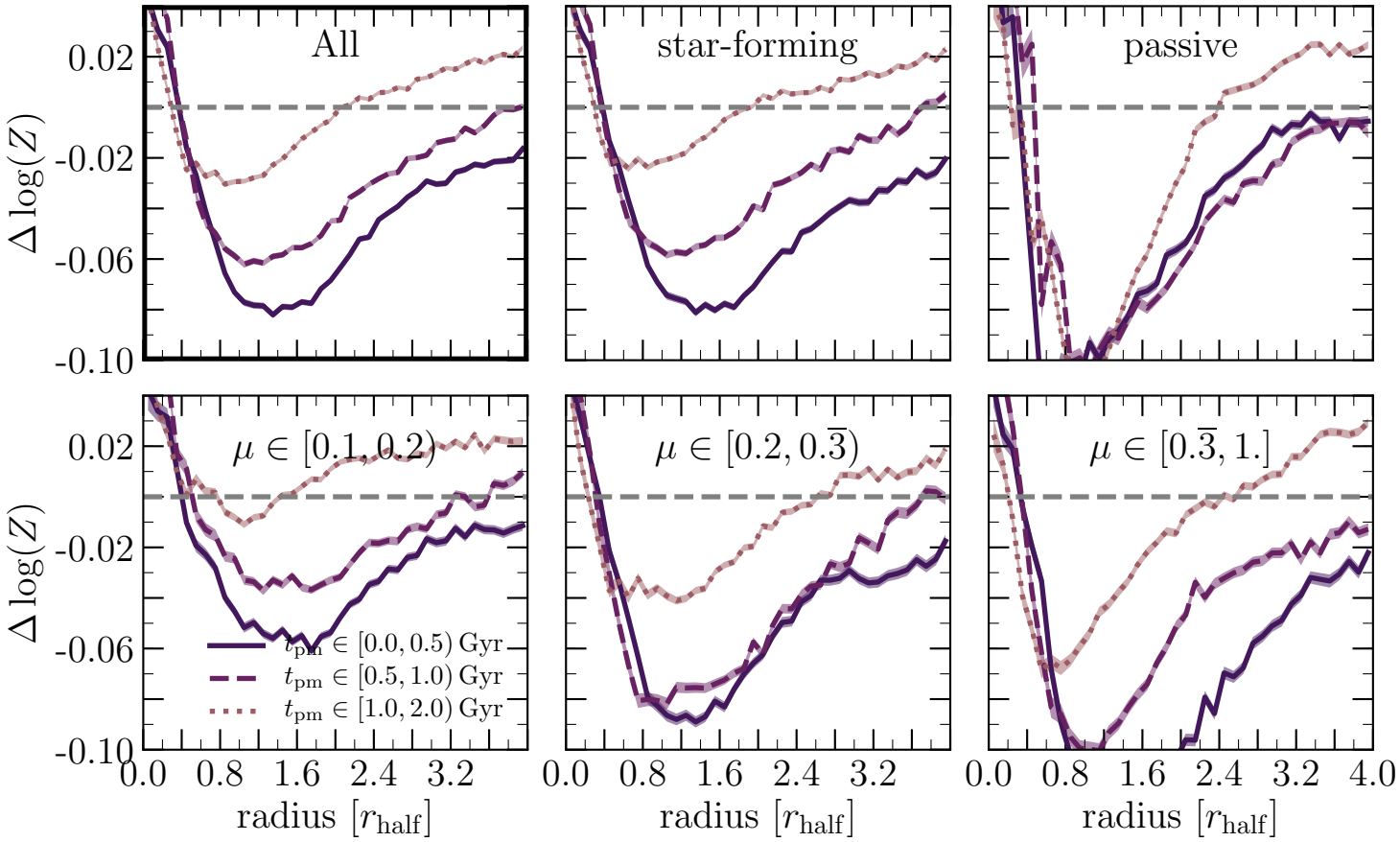

Figure 6.8: The evolution of the comparative metallicity profile after the merger. The lines show three time bins after the merger. Left to right, the top panels show the evolution of the full sample, star-forming galaxies, and passive galaxies. The bottom panels show the evolution of the descendants of mergers with different mass ratios divided by increasing mass ratio from left to right. The merger-induced metallicity dilution is replenished in the centres of post-mergers within ~ 0.5 Gyr after the merger. However, the dilution remains at $r > 0.4$ $r_{\rm half}$ for all post-mergers. The strength of the dilution depends on the merger mass ratio. Passive post-merger show minimal evolution in their metallicity profiles even after $1-2$ Gyr, while metallicities in star-forming post-mergers are consistent with their controls within ± 0.02 dex. The origin of the metallicity enhancements at large radii $1-2$ Gyr after the merger remains unclear.

6.4 Discussion

High resolution numerical simulations provide a unique perspective on the processes triggering star formation during mergers. Galaxy mergers can trigger compressive tides (Powell et al., 2013; Renaud et al., 2014) or strong inflows (Moreno et al., 2015) that drive an increase in star formation. However, while numerical models agree on the role of galaxy mergers in driving global and central SFR enhancements, the spatial extent of the enhanced star formation remains uncertain. For example, Moreno et al. (2015), using a suite of binary merger simulations, reports enhanced star formation in the centres of the galaxies accompanied with suppression in the outskirts. On the contrary, Renaud et al. (2014) demonstrates that galaxy mergers are prone to extended regions of compressive tides that can lead to elevated star formation on extended scales. The disagreement on the scales of the enhancement/suppression of star formation during galaxy mergers may be indicative of the complex and diverse physical processes affecting the gas reservoir, or the limitations of the various simulations (i.e, resolution, physical model). Therefore, a diverse merger sample (like the one used in this chapter) is ideal for testing and understanding the physical processes driving the elevated/suppressed SFRs in galaxy mergers. My results are in agreement with high resolution numerical simulations that stress that galaxy mergers can drive central SFR enhancements (e.g., Renaud et al., 2014; Moreno et al., 2015; Sparre & Springel, 2016; Moreno et al., 2019). Moreover, the remarkable diversity in the comparative profiles of individual TNG post-mergers may suggest that tidal compression and gas inflows are both at play in the TNG sample. I will revisit the diversity of galaxy profiles in future work.

Observational studies targeting galaxy interactions and post-mergers report qualitatively similar results: Star formation is boosted in the centre while the enhancement declines outwards (e.g., García-Marín et al., 2009; Barrera-Ballesteros et al., 2015; Cortijo-Ferrero et al., 2017b; Thorp et al., 2019). Some disagreement remains about the effect of galaxy mergers on extended galactic scales. For example, some studies report normal, and possibly suppressed, SFRs in the outskirts of interacting galaxies and post-mergers (e.g., Barrera-Ballesteros et al., 2015), while others report enhanced star formation at least out to 2 effective radii (e.g., Cortijo-Ferrero et al., 2017b; Thorp et al., 2019). Resolving the dispute over the extended effects of star formation has been a challenge for observational studies because of the differences in (1) sample selection, (2) sample size, (3) spatial coverage, and (4) methodology.

The diversity in the simulated post-merger profiles (Figure 6.4) suggest that the tension between observational studies may be driven by their different sample selection techniques. Nonetheless, my results (i.e., median profiles) qualitatively agree with observational studies where post-mergers exhibit monotonically declining $\Sigma_{\rm SFR}$ enhancement with a central peak (e.g., García-Marín et al., 2009; Barrera-Ballesteros et al., 2015; Cortijo-Ferrero et al., 2017b; Thorp et al., 2019). In future work, I will explore the star formation profile in the outskirts of post-mergers and investigate the differences between my results and other studies.

I now shift focus to the effect of galaxy mergers on the gas phase metallicity, a well studied effect by both observations and simulations. Observations of the central regions of interacting galaxies report centrally diluted metallicities (e.g., Ellison et al., 2008a; Stinson et al., 2012). The central metallicity dilution is supported by many numerical simulations (e.g., Torrey et al., 2012; Bustamante et al., 2018). Simulations also propose an extended flattening in metallicity gradients (Rupke et al., 2010a; Sillero et al., 2017). Recent IFU studies of post-mergers also report suppressed metallicities out to 1.9 effective radii with maximum dilution of $\Delta \log(Z) \sim -0.05$ (i.e., Thorp et al., 2019). The metallicity dilution in the TNG post-merger sample is qualitatively consistent with the prediction from high resolution numerical simulations as well as kpc-scale observational studies of post-mergers. Nonetheless, there are noticeable differences in the strength and extent of the dilution between observational studies and my results (e.g., see Figure 6.3). In future work, I will investigate the physical mechanisms driving the dilution and the shape of the metallicity profiles. The minimal levels of metallicity dilution at small radii are most likely due to the metal enrichment associated with the enhanced star formation.

6.5 Conclusions

I present a resolved analysis of star formation and metallicity in a large sample of post-mergers simulated in a cosmological environment. I employ an observationally motivated methodology to demonstrate the effects of galaxy mergers on star formation and metallicity profiles. Additionally, I quantify the strength, radial extent, and temporal evolution of the mergers' effects. I demonstrated that:

- **Post-merger profiles:** Galaxy mergers drive a central enhancement in star formation: $\Delta \log(\Sigma_{\rm SFR}) \sim 0.4$ dex. The enhancement dwindles with increasing radius and disappears for $r > 0.8$ $\rm r_{half}$.

- **Metallicity profiles:** Galaxy mergers induce a metallicity dilution out to $r = 4$ r_{half} with a maximal suppression of $\Delta \log(Z) \sim -0.08$ dex. The dilution is rapidly replenished in the central regions due to the increased star formation.

- **The dependence on mass ratio:** The strength of the merger-induced central boost in star formation depends on the merger mass ratio; major mergers ($\mu \geq 0.3$) drive the strongest boosts with $\Delta \log(\Sigma_{SFR}) \sim 0.6$ dex. The enhancement declines with increasing radius and disappears for $r > 0.8$ r_{half}. While minor mergers ($\mu < 0.3$) exhibit SFRs that are consistent with their controls for $r > 0.8$ r_{half}, major mergers ($\mu \geq 0.3$) show a mild suppression in star formation.

  All mergers exhibit diluted metallicities with major mergers ($\mu \geq 0.3$) showing the strongest dilutions ($\log(Z) < -0.1$ dex). Additionally, the radial extent of the dilution depends on mass ratio with major mergers ($\mu \geq 0.3$) showing diluted metallicities out to $r = 4$ r_{half} in contrast with minor mergers ($\mu < 0.3$) that show normal metallicities at $r > 2.8$ r_{half}.

  The dependence on mass ratio is possibly indicative of merger induced gravitational torques driving gas inflows thus boosting star formation in the centres and suppressing gas metallicities.

- **The dependence on galaxy type:** Star-forming post-mergers exhibit central enhancements in star formation that decline with increasing radius. On the contrary, passive post-mergers show suppressed central star formation for $r < 0.6$ r_{half}.

  Gas metallicities are suppressed in both star-forming, and passive post-mergers. While passive post-mergers show normal metallicities beyond $r > 2.8$ r_{half}, their star-forming counterparts exhibit suppressed metallicities out $r = 4$ r_{half}.

- **The evolution of star formation beyond coalescence:** Within 0.5 Gyr after the merger, star formation remains enhanced ($\Delta \log(\Sigma_{SFR}) \sim 0.25$ dex) in the central regions ($r < 0.6$ r_{half}) of star-forming galaxies, while the outskirts suffer a mild suppression ($\Delta \log(\Sigma_{SFR}) \sim -0.1$ dex). The strengths of the central enhancement and extended suppression in star formation depends on the merger mass ratio; major mergers ($\mu \geq 0.3$) show the strongest star formation enhancement ($\Delta \log(\Sigma_{SFR}) \sim 0.37$ dex) and suppression ($\Delta \log(\Sigma_{SFR}) \sim -0.18$ dex). On the other hand, passive post-mergers exhibit globally suppressed star formation within 0.5 Gyr after the merger.

The effects of the merger on star formation decay within $1-2$ Gyr after the merger independently of mass ratio. Although, passive galaxies continue to show globally suppressed star formation with little time evolution.

- **The evolution of metallicity beyond coalescence:** Although all post-mergers exhibit diluted metallicities within $\sim$ 160 Myr after the merger, all central metallicities are enriched ($\Delta \log(Z) > 0.04$ dex) within 0.5 Gyr. However, metallicities remain diluted in all post-mergers for $r > 0.4$ $r_{\rm half}$. The strength of the dilution depends on the merger mass ratio.

  Following the merger, the metallicity profile of passive post-mergers shows little evolution. In contrast, the metallicity suppression in star-forming post-mergers dwindles within $\sim 1-2$ Gyr to achieve metallicities that are consistent with their controls within ± 0.02 dex. However, the merger-induced effects on the metallicity profiles of merger remnants with mass ratio $\mu \geq 0.2$ persist even after $1-2$ Gyr.

6.6 Future work

The analysis presented in this chapter represents the preliminary results from the final paper that will come out of my thesis. In this section, I will highlight some of the ongoing and future investigations required to understand the mechanisms giving rise to the results reported in Section 6.3.

Are mergers special?

In Chapter 4 and the previous sections of the current chapter I demonstrated that galaxy mergers can have a strong effect on galactic star formation. Mergers can, on average, boost the global SFR by a factor of ~ 2 (Chapter 4) and drive central enhancements in star formation by a factor of $\sim 2-3$ (e.g., Figure 6.3). While mergers are an important mechanism through which galaxies can enhance their SFRs, other secular processes can also drive star formation enhancements (e.g., bars, disc instabilities). Therefore, although mergers show a significant impact on star formation and metallicity profiles, it is worth investigating whether the strength and radial extent of the merger-induced enhancement and suppression are unique to mergers. For example, do mergers with enhanced star formation differ in their resolved profiles from secular star-burst galaxies? Additionally, do passive galaxies show similar profiles to

passive post-mergers? For example, Figure 6.6 shows that the profiles of star-forming and passive post-mergers are qualitatively similar to the those of non-merging galaxies in observational studies (e.g., Ellison et al., 2018a; Tacchella et al., 2018; Lin et al., 2019a; Breda et al., 2020).

Understanding the effects of galaxy mergers requires a fair comparison between post-mergers and their controls. Particularly, one must control for the galaxies' SFR. Such a controlled comparison provides a fair ground to investigate whether the effects of galaxy mergers are unique for a given level of SFR enhancement. In future work, I will compare the star formation and metallicity profiles of post-mergers to those of an SFR-matched control sample to investigate the unique effects of galaxy mergers.

Towards a physical picture of the resolved effects of mergers

In Section 6.3 I demonstrated the significant impact of galaxy mergers on star formation and metallicity profiles. I also showed that the strength, radial extent, and temporal evolution of the merger's impact depends on other galaxy properties such as mass ratio, and galaxy type. While the effects of the mergers are evident, their cause remains unclear. For example, is the suppression in star formation in the outskirts of galaxies caused by (1) an insufficient amount of gas to sustain star formation, or (2) properties of the gas reservoir (density, temperature) which are sub-optimal for star formation. In case of sub-optimal gas reservoir properties, it is key to uncover the reason causing such sub-optimal properties; for example, are feedback processes hindering star formation, or are the timescales (e.g., cooling time) governing the evolution of the gas reservoir too long? On the other hand, what is the cause of the enhanced central star formation? While previous numerical simulations indicate that merger driven inflows can give rise to higher gas densities and therefore higher central $\Sigma_{\rm SFR}$, I have yet to confirm that in the TNG post-merger sample.

Understanding the physical mechanisms that drive the results of this chapter is key to our understanding of the effects of mergers. In future work, I will explore the properties and evolution of the gas profiles in my sample. Additionally, I will explore the flow of gas within the post-merger which will shed light on the reasons behind the measured effects on the star formation, and metallicity profiles.

Chapter 7

Future prospects for the CGM, star formation, and galaxy mergers

Galaxy evolution is a complex process with multiple culprits that have varying degrees of importance. The gas reservoir, star formation, AGN activity, and galaxy mergers are all considered corner stones of galaxy evolution (amongst others). Numerical simulations provide a valuable tool to investigate and dissect the complex interplay of various processes that may have a significant effect on a galaxy's evolution. In this thesis, I have presented a series of studies exploring the CGM, and galactic star formation. I have:

- quantified the diversity in the CGM of Milky Way-like galaxies, and identified key physical mechanisms that shape the CGM (Chapter 2),
- demonstrated the long-lasting significant effects of galaxy mergers on the size, gas content, metallicity, and ionisation of the CGM (Chapter 3),
- explored the effects of galaxy mergers on galactic star formation in a large simulated galaxy sample, and identified the dependence of SFR enhancement on merger properties (Chapter 4),
- demonstrated that the rSFMS emerges naturally in FIRE-2, a simulation suite that resolves the dense ISM and includes explicit stellar feedback, while the rSFMS slope's depends on spatial resolution, and can be used to constrain the characteristic mass of star-forming clumps (Chapter 5), and
- investigated the effects of galaxy mergers on star formation, and gas phase metallicities on resolved scales using a large and representative simulated post-merger galaxy sample (Chapter 6).

7.1 The effects of galaxy mergers on the CGM

In Chapter 3 I presented a case study conveying that mergers have a significant effect on the CGM. I demonstrated that merger-driven outflows can enhance the metallicity of the CGM by $\log([O/H]) \sim 0.2 - 0.4$ dex for more than 2 Gyrs, and increase the covering fractions of metals by factors of a few thus increasing the characteristic size of the CGM. Additionally, merger-driven AGN activity significantly alters the CGM's ionisation balance.

Knowing that galaxy mergers *can* have such a long-lasting and significant effect on the CGM of the descendant galaxies (Chapter 3), it is particularly interesting to quantify the effect of the merger properties (i.e., mass ratio, orbital parameters, gas fraction, morphology) on the CGM. Merger properties have been shown to have a notable effect on the duration, and strength of merger-induced starbursts, AGN activity, and morphological disturbances (e.g., Di Matteo et al., 2007; Lotz et al., 2008, 2010a,b). Therefore, owing to the associated feedback (i.e., outflows), one may expect the CGM properties to depend on the merger properties (see Figure 3.12).

The ideal experimental setup to test the effects of galaxy mergers on the CGM is a large and diverse statistical galaxy sample to account for the diversity in the CGM (Chapter 2). Studying the CGM of galaxy mergers in IllustrisTNG-50[1] (Nelson et al., 2019b; Pillepich et al., 2019) offers the large, realistic, and diverse galaxy samples available in large-box cosmological simulations, but simulated at the high resolution (spatial and mass resolutions) of cosmological zoom-in simulations. Mergers can be identified following the methodology developed in Chapter 4. The CGM properties of merging galaxies can then be compared to their non-interacting controls' CGMs using the metrics introduced in Chapters 2 and 3. Such a comparison will quantify the effect of galaxy mergers on the CGM's gas content, metallicity, ionisation, and structure. Additionally, by tracing the orbits of merging systems, one can examine the effects of gas stripping and feedback on the structure, and content of the CGM.

The statistical analysis of a large and diverse sample of galaxy mergers will provide unprecedented constraints on the effects of galaxy mergers on the CGM: viz.
(i) the contribution from merger-induced features to the enrichment in the CGM,
(ii) the effects of gas stripping, and merger-induced feedback on the composition and ionisation state of the extended CGM, and
(iii) the dependence of the merger's effects on merger properties: namely, mass ratio

[1]Note that the IllustrisTNG-50 data is not currently publically available.

and gas fraction.

7.2 Next generation CGM studies

Our understanding of the CGM's properties has been spearheaded by modern absorption line studies during the past decade (Section 1.2.2). However, many open questions continue to pose major challenges to our understanding of the CGM and galaxy evolution: How do the CGM's content and structure evolve? How do baryons flow through the CGM? What is the fate of the CGM? What are the details of the CGM's role in galaxy evolution?

Theoretical and numerical challenges

Massive extended gas halos exhibit complex and diverse structure (Chapter 2) and kinematics (e.g., Stern et al., 2016; Peeples et al., 2019). The complexity of the CGM structure poses a major challenge for numerical simulations: the scale problem (see Section 1.4). Simulations of the CGM must resolve the extended, hot, and diffuse gas as well as cool dense clumps. In addition to the complex structures within each phase of the CGM, simulations must resolve boundary layers on sub-pc scales in order to properly model hydrodynamic instabilities. Such a feat is beyond any of the state-of-the-art simulations targeting the CGM. Although impressive advancements have been undertaken introducing unprecedented spatial resolution to the CGM (e.g., Peeples et al., 2019; van de Voort et al., 2019). A possible remedy to the scale problem may emerge from pairing idealised models of dense clouds embedded in CGM-like environments (e.g., Armillotta et al., 2017; Fielding et al., 2017) with simulations that model the CGM in a cosmological context. However, it remains unclear whether modelling the unresolved interfaces between hot and cold gas using sub-grid processes would be a fruitful endeavour.

In recent years, numerical simulations of galaxy evolution took a step forward to remedy the scale problem when modelling the CGM. Various studies devised methods to increase the spatial resolution in the CGM (e.g., Hummels et al., 2019; Suresh et al., 2019; Peeples et al., 2019; van de Voort et al., 2019). However, with the increased spatial resolution, emerged a new challenge: model convergence. Moving forward, numerical models must reconcile their resolution dependence in order to converge at a reliable model of the CGM. Nonetheless, models with increased CGM resolution report an increase in the abundance of high-density, small-scale clumps

which is suggestive of a possible mist-like cool CGM (i.e., Hummels et al., 2019; Suresh et al., 2019; van de Voort et al., 2019). The presence of high-density, small-scale clumps is supported by absorption-line-studies that (i) report the abundance of multi-phase absorbers, and (ii) reproduce the spectral line profiles of absorbers in the CGM by invoking a patchy CGM (e.g., Stern et al., 2016; Werk et al., 2016).

Observational challenges

Although numerical simulations of the CGM face many challenges, they have been instrumental in understanding the flow of gas in to, out of, and within the CGM (e.g., Ford et al., 2014; Hafen et al., 2020). For example, simulations demonstrate that a significant fraction of CGM metals are carried by galactic outflows (e.g., Fumagalli et al., 2011; Muratov et al., 2017), while some of the metals flow between galaxies through the CGM (e.g., Anglés-Alcázar et al., 2017; Hafen et al., 2020). Constraining the gas flow in the CGM requires an observationally well-constrained and characterised gas mass budget. Observations characterising the CGM baryon budget must span a variety of galaxy properties such as stellar mass (e.g., Tumlinson et al., 2011; Bordoloi et al., 2014b) and star formation rate (e.g., Tumlinson et al., 2011; Borthakur et al., 2013; Heckman et al., 2017; Prochaska et al., 2017), as well as the rarer evolutionary episodes such as AGN (e.g., Berg et al., 2018), and mergers. Although some observational studies have explored the CGM of rare stages of galaxy evolution (e.g., Heckman et al., 2017; Berg et al., 2018) more work is required to constrain and properly characterise the CGM's baryon budget.

In addition to constraining the CGM's baryon budget, observational studies using QALs suffer from some limitations. Most notable of which are (i) the assumptions associated with ionisation corrections, (ii) modelling the physical structures that contribute to observed absorption lines, and (iii) capturing the diversity of the CGM's structure. Numerical simulations (i.e., Stern et al., 2016; Peeples et al., 2019) demonstrate the complexity of CGM structures that contribute to absorption with "simple" observed kinematic profiles. While it is possible that we are unable to extract *additional* information about individual absorbers from spectra, high resolution spectroscopy may offer an unprecedented view on the kinematics and properties of small-scale CGM absorbers. On the other hand, ionisation corrections are plagued with assumptions (ionising field, ionisation equilibrium) that render them uncertain. The uncertainty of ionisation corrections has a direct impact on the inferred CGM

properties (i.e., gas mass, metal mass).

The future of CGM studies

While many groups are developing simulations with exquisite resolution to resolve the CGM sub-structure and hydrodynamical properties (e.g., Hummels et al., 2019; Suresh et al., 2019; Peeples et al., 2019; van de Voort et al., 2019), the next generation of observations is key to answer the questions related to the CGM's properties, and role in galaxy evolution. With the HST being decommissioned in the mid 2020s, we must look for alternative observational approaches to study the CGM. Current imaging campaigns have proven successful in using sensitive IFUs such as MUSE and KCWI to target the CGM in emission at intermediate to high redshift (Martin et al., 2019; Rupke et al., 2019). In addition, high resolution spectroscopy will pave the way for a more detailed understanding of the kinematics of CGM absorbers (e.g., the Echelle SPectrograph for Rocky Exoplanet and Stable Spectroscopic Observations: ESPRESSO). Looking to the future, large radio arrays such as the Square Kilometre Array would provide additional constraints on the H I content of the CGM of low to intermediate redshift galaxies. Moreover, the hot gas in the CGM will be accessible in the X-ray with the Advanced Telescope for High ENergy Astrophysics (ATHENA) at increased sensitivity and spatial resolution. Additionally, proposed instruments such as the Large Ultraviolet/Optical/Near Infrared Surveyor (LUVOIR) would provide unprecedented metal mapping thought the CGM with significant improvements over HST. However, for the time being, the available absorption line surveys targeting the low-redshift CGM using HST-COS (e.g., Tumlinson et al., 2011; Bordoloi et al., 2014b; Heckman et al., 2017; Berg et al., 2018) will continue to lead the way on the observational front as they provide the largest samples of low-redshift CGM observations. The high redshift CGM continues to be accessible using current instrumentation such as ESPRESSO, and the VIsible Multi-Object Spectrograph (VIMOS).

7.3 Next generation studies of galactic star formation

Star formation is one of the key physical mechanisms in galaxy evolution. It is at the heart of galaxy growth, and the regulation of the gas reservoir. However, the details of star formation remain hazy. For example, what regulates star formation? How does star formation evolve within galaxies? How does stellar feedback affect galaxy evolution?

Star formation is often modelled using phenomenological sub-grid models due to the inadequately low resolution in simulations. Models of star formation are often motivated by the observational imprints of star formation on larger scales (e.g., winds, fountains) or galaxy scaling relations (i.e., SFMS). However, the physical mechanism by which stars produce such signatures remain unclear from a theoretical perspective. For example, how does stellar feedback couple to the gas reservoir to launch the observed winds? And, why does the star formation rate of galaxies scale with their stellar mass? Moving toward simulations that explicitly resolve the ISM and stellar feedback (e.g., Hopkins et al., 2018) will provide a better understanding of the physical processes driving star formation. Such an undertaking requires new models of the ISM, and exquisite spatial resolution.

In recent years, the emergence of the rSFMS provided a more substantial constraint for our understanding of star formation. However, theoretical studies have yet to explore the kpc-scale rSFMS in detail (Trayford & Schaye, 2019; Hani et al., 2020a). Studying the rSFMS in numerical simulations will help answer some of the major open questions: e.g., what gives rise to the rSFMS? What drives the scatter in the rSFMS? High resolution observational studies (e.g., PHANGS; Leroy et al., 2016) provide a complementary approach to unveiling the origins of the rSFMS. Moreover, combining studies of star formation with multi-phase gas measurements is a fruitful approach to understanding the rich interplay between star formation and the gas reservoir (e.g., Bigiel et al., 2011; Bolatto et al., 2017; Ellison et al., 2020). Multi-band studies of star formation will allow us to track all phases of star formation from birth (molecular gas) to feedback (ionised gas). The combination of physically motivated high-resolution numerical models, and milti-band high-resolution observational constraints will put our understanding of galactic star formation on a more solid footing.

7.4 Concluding remarks

The work I present in this thesis provides a stepping stone towards a better understanding of galaxy evolution. Ultimately, understanding galaxy evolution requires an intricate understanding of the interplay between various physical processes (star formation, AGN activity), their associated feedback, hydrodynamical processes, and the gas reservoir within and outside galaxies. A future combination of state-of-the-art numerical models, and observations will paint a complete picture of how galaxies evolve, and the role the gas reservoirs play in their evolution.

Bibliography

Abadi M. G., Navarro J. F., Steinmetz M., Eke V. R., 2003, ApJ, 591, 499

Abdurro'uf Akiyama M., 2017, MNRAS, 469, 2806

Abramson L. E., Gladders M. D., Dressler A., Oemler Augustus J., Poggianti B., Vulcani B., 2015, ApJ, 801, L12

Adamo A., Kruijssen J. M. D., Bastian N., Silva-Villa E., Ryon J., 2015, Monthly Notices of the Royal Astronomical Society, 452, 246

Adelberger K. L., Steidel C. C., Shapley A. E., Pettini M., 2003, ApJ, 584, 45

Adelberger K. L., Shapley A. E., Steidel C. C., Pettini M., Erb D. K., Reddy N. A., 2005, ApJ, 629, 636

Agertz O., Kravtsov A. V., 2016, ApJ, 824, 79

Aller M. C., Richstone D. O., 2007, ApJ, 665, 120

Anglés-Alcázar D., Davé R., Özel F., Oppenheimer B. D., 2014, ApJ, 782, 84

Anglés-Alcázar D., Faucher-Giguère C.-A., Kereš D., Hopkins P. F., Quataert E., Murray N., 2017, MNRAS, 470, 4698

Armillotta L., Fraternali F., Werk J. K., Prochaska J. X., Marinacci F., 2017, MNRAS, 470, 114

Bahcall J. N., Spitzer Lyman J., 1969, ApJ, 156, L63

Baldry I. K., Glazebrook K., Brinkmann J., Ivezić Ž., Lupton R. H., Nichol R. C., Szalay A. S., 2004, ApJ, 600, 681

Baldry I. K., Balogh M. L., Bower R. G., Glazebrook K., Nichol R. C., Bamford S. P., Budavari T., 2006, MNRAS, 373, 469

Baldry I. K., Glazebrook K., Driver S. P., 2008, MNRAS, 388, 945

Barnes J. E., Hernquist L. E., 1991, ApJ, 370, L65

Barnes J. E., Hernquist L., 1996, ApJ, 471, 115

Barnes J., Hut P., 1986, Nature, 324, 446

Barrera-Ballesteros J. K., et al., 2015, A&A, 579, A45

Barrera-Ballesteros J. K., Sánchez S. F., Heckman T., Blanc G. A., The MaNGA Team 2017, ApJ, 844, 80

Behroozi P. S., Conroy C., Wechsler R. H., 2010, ApJ, 717, 379

Behroozi P. S., Wechsler R. H., Conroy C., 2013, ApJ, 770, 57

Berg T. A. M., et al., 2016, MNRAS, 463, 3021

Berg T. A. M., Ellison S. L., Tumlinson J., Oppenheimer B. D., Horton R., Bordoloi R., Schaye J., 2018, MNRAS, 478, 3890

Bergeron J., 1986, A&A, 155, L8

Bergeron J., Boissé P., 1991, A&A, 243, 344

Bernardi M., Shankar F., Hyde J. B., Mei S., Marulli F., Sheth R. K., 2010, MNRAS, 404, 2087

Bessiere P. S., Tadhunter C. N., Ramos Almeida C., Villar Martín M., 2012, MNRAS, 426, 276

Best P. N., Kauffmann G., Heckman T. M., Brinchmann J., Charlot S., Ivezić Ž., White S. D. M., 2005, MNRAS, 362, 25

Bigiel F., et al., 2011, ApJ, 730, L13

Bird S., Haehnelt M., Neeleman M., Genel S., Vogelsberger M., Hernquist L., 2015, MNRAS, 447, 1834

Bird S., Rubin K. H. R., Suresh J., Hernquist L., 2016, MNRAS, 462, 307

Blanton M. R., et al., 2003, ApJ, 594, 186

Bluck A. F. L., Mendel J. T., Ellison S. L., Moreno J., Simard L., Patton D. R., Starkenburg E., 2014, MNRAS, 441, 599

Bluck A. F. L., et al., 2016, MNRAS, 462, 2559

Blumenthal K. A., Barnes J. E., 2018, MNRAS, 479, 3952

Blumenthal K. A., et al., 2019, MNRAS, p. 3093

Bogdán Á., et al., 2015, ApJ, 804, 72

Bolatto A. D., et al., 2017, ApJ, 846, 159

Bordoloi R., et al., 2011, ApJ, 743, 10

Bordoloi R., Lilly S. J., Kacprzak G. G., Churchill C. W., 2014a, ApJ, 784, 108

Bordoloi R., et al., 2014b, ApJ, 796, 136

Bordoloi R., Wagner A. Y., Heckman T. M., Norman C. A., 2017, ApJ, 848, 122

Bordoloi R., Prochaska J. X., Tumlinson J., Werk J. K., Tripp T. M., Burchett J. N., 2018, ApJ, 864, 132

Borthakur S., Heckman T., Strickland D., Wild V., Schiminovich D., 2013, ApJ, 768, 18

Borthakur S., et al., 2015, ApJ, 813, 46

Borthakur S., et al., 2016, ApJ, 833, 259

Bothwell M. S., Maiolino R., Cicone C., Peng Y., Wagg J., 2016, A&A, 595, A48

Bournaud F., Jog C. J., Combes F., 2005, A&A, 437, 69

Bowen D. V., Chelouche D., Jenkins E. B., Tripp T. M., Pettini M., York D. G., Frye B. L., 2016, ApJ, 826, 50

Bower R. G., Benson A. J., Malbon R., Helly J. C., Frenk C. S., Baugh C. M., Cole S., Lacey C. G., 2006, MNRAS, 370, 645

Breda I., et al., 2020, A&A, 635, A177

Brennan R., et al., 2017, MNRAS, 465, 619

Brinchmann J., Charlot S., White S. D. M., Tremonti C., Kauffmann G., Heckman T., Brinkmann J., 2004, MNRAS, 351, 1151

Bryan G. L., et al., 2014, ApJS, 211, 19

Bryant J. J., et al., 2015, MNRAS, 447, 2857

Buff J., McCray R., 1974, ApJ, 189, 147

Bundy K., et al., 2010, ApJ, 719, 1969

Bundy K., et al., 2015, ApJ, 798, 7

Burchett J. N., et al., 2016, ApJ, 832, 124

Bustamante S., Sparre M., Springel V., Grand R. J. J., 2018, MNRAS, 479, 3381

Cano-Díaz M., et al., 2016, ApJ, 821, L26

Cantalupo S., et al., 2019, MNRAS, 483, 5188

Cao C., et al., 2016, ApJS, 222, 16

Casteels K. R. V., et al., 2014, MNRAS, 445, 1157

Castor J. I., Abbott D. C., Klein R. I., 1975, ApJ, 195, 157

Ceverino D., Klypin A., Klimek E. S., Trujillo-Gomez S., Churchill C. W., Primack J., Dekel A., 2014, MNRAS, 442, 1545

Chabrier G., 2003, PASP, 115, 763

Chen H.-W., Lanzetta K. M., Webb J. K., 2001, ApJ, 556, 158

Chen H.-W., Helsby J. E., Gauthier J.-R., Shectman S. A., Thompson I. B., Tinker J. L., 2010, ApJ, 714, 1521

Chen H.-W., Gauthier J.-R., Sharon K., Johnson S. D., Nair P., Liang C. J., 2014, MNRAS, 438, 1435

Chisholm J., Tremonti C., Leitherer C., 2018, MNRAS, 481, 1690

Christensen C. R., Davé R., Governato F., Pontzen A., Brooks A., Munshi F., Quinn T., Wadsley J., 2016, ApJ, 824, 57

Ciotti L., Ostriker J. P., 2001, ApJ, 551, 131

Combes F., García-Burillo S., Braine J., Schinnerer E., Walter F., Colina L., 2013, A&A, 550, A41

Conselice C. J., 2003, ApJS, 147, 1

Cooke J., O'Meara J. M., 2015, ApJ, 812, L27

Cooksey K. L., Thom C., Prochaska J. X., Chen H.-W., 2010, ApJ, 708, 868

Corlies L., Schiminovich D., 2016, ApJ, 827, 148

Corlies L., Peeples M. S., Tumlinson J., O'Shea B. W., Lehner N., Howk J. C., O'Meara J. M., 2018, preprint, (arXiv:1811.05060)

Cortijo-Ferrero C., et al., 2017a, MNRAS, 467, 3898

Cortijo-Ferrero C., et al., 2017b, A&A, 607, A70

Cowie L. L., Ostriker J. P., Stark A. A., 1978, ApJ, 226, 1041

Cox T. J., Primack J., Jonsson P., Somerville R. S., 2004, ApJ, 607, L87

Cox T. J., Jonsson P., Primack J. R., Somerville R. S., 2006a, MNRAS, 373, 1013

Cox T. J., Di Matteo T., Hernquist L., Hopkins P. F., Robertson B., Springel V., 2006b, ApJ, 643, 692

Cox T. J., Jonsson P., Somerville R. S., Primack J. R., Dekel A., 2008, MNRAS, 384, 386

Crain R. A., et al., 2015, MNRAS, 450, 1937

Daddi E., et al., 2007, ApJ, 670, 156

Davé R., Katz N., Weinberg D. H., 2002, ApJ, 579, 23

Davé R., Finlator K., Oppenheimer B. D., 2011, MNRAS, 416, 1354

Davé R., Thompson R., Hopkins P. F., 2016, MNRAS, 462, 3265

Davé R., Anglés-Alcázar D., Narayanan D., Li Q., Rafieferantsoa M. H., Appleby S., 2019, MNRAS, 486, 2827

Dekel A., Sari R., Ceverino D., 2009, ApJ, 703, 785

Di Matteo T., Springel V., Hernquist L., 2005, Nature, 433, 604

Di Matteo P., Combes F., Melchior A. L., Semelin B., 2007, A&A, 468, 61

Di Matteo P., Bournaud F., Martig M., Combes F., Melchior A.-L., Semelin B., 2008, A&A, 492, 31

Diemer B., et al., 2018, ApJS, 238, 33

Diemer B., et al., 2019, MNRAS, 487, 1529

Donnari M., et al., 2019, MNRAS, 485, 4817

Dutta R., Srianand R., Gupta N., 2018, MNRAS, 480, 947

Dutta R., Srianand R., Gupta N., 2019, MNRAS, 489, 1099

Dutton A. A., van den Bosch F. C., Dekel A., 2010, MNRAS, 405, 1690

Edwards D., Heath D., 1976, Ap&SS, 41, 183

Elbaz D., et al., 2007, A&A, 468, 33

Ellison S. L., Ibata R., Pettini M., Lewis G. F., Aracil B., Petitjean P., Srianand R., 2004, A&A, 414, 79

Ellison S. L., Patton D. R., Simard L., McConnachie A. W., 2008a, AJ, 135, 1877

Ellison S. L., Patton D. R., Simard L., McConnachie A. W., 2008b, ApJ, 672, L107

Ellison S. L., Patton D. R., Mendel J. T., Scudder J. M., 2011, MNRAS, 418, 2043

Ellison S. L., Mendel J. T., Scudder J. M., Patton D. R., Palmer M. J. D., 2013a, MNRAS, 430, 3128

Ellison S. L., Mendel J. T., Patton D. R., Scudder J. M., 2013b, MNRAS, 435, 3627

Ellison S. L., Fertig D., Rosenberg J. L., Nair P., Simard L., Torrey P., Patton D. R., 2015, MNRAS, 448, 221

Ellison S. L., Sánchez S. F., Ibarra-Medel H., Antonio B., Mendel J. T., Barrera-Ballesteros J., 2018a, MNRAS, 474, 2039

Ellison S. L., Catinella B., Cortese L., 2018b, MNRAS, 478, 3447

Ellison S. L., Viswanathan A., Patton D. R., Bottrell C., McConnachie A. W., Gwyn S., Cuillandre J.-C., 2019, MNRAS, 487, 2491

Ellison S. L., et al., 2020, MNRAS, 493, L39

Erroz-Ferrer S., et al., 2019, MNRAS, 484, 5009

Fabian A. C., 2012, ARA&A, 50, 455

Farina E. P., Falomo R., Decarli R., Treves A., Kotilainen J. K., 2013, MNRAS, 429, 1267

Farina E. P., Falomo R., Scarpa R., Decarli R., Treves A., Kotilainen J. K., 2014, MNRAS, 441, 886

Farouki R. T., Shapiro S. L., 1982, ApJ, 259, 103

Fattahi A., et al., 2016, MNRAS, 457, 844

Faucher-Giguère C.-A., Lidz A., Zaldarriaga M., Hernquist L., 2009, ApJ, 703, 1416

Feltre A., et al., 2018, A&A, 617, A62

Ferland G., et al., 2013a, Rev. Mex. Astron. Astrofis., 49, 137

Ferland G. J., et al., 2013b, Rev. Mex. Astron. Astrofis., 49, 137

Fielding D., Quataert E., McCourt M., Thompson T. A., 2017, MNRAS, 466, 3810

Forbes J. C., Lin D. N. C., 2018, preprint, (arXiv:1810.12925)

Ford A. B., Oppenheimer B. D., Davé R., Katz N., Kollmeier J. A., Weinberg D. H., 2013, MNRAS, 432, 89

Ford A. B., Davé R., Oppenheimer B. D., Katz N., Kollmeier J. A., Thompson R., Weinberg D. H., 2014, MNRAS, 444, 1260

Fox A. J., et al., 2015, ApJ, 799, L7

Fumagalli M., Prochaska J. X., Kasen D., Dekel A., Ceverino D., Primack J. R., 2011, MNRAS, 418, 1796

Furlong M., et al., 2015, MNRAS, 450, 4486

García-Marín M., Colina L., Arribas S., Monreal-Ibero A., 2009, A&A, 505, 1319

Genel S., et al., 2014, MNRAS, 445, 175

Gerke B. F., et al., 2007, MNRAS, 376, 1425

Gladders M. D., Oemler A., Dressler A., Poggianti B., Vulcani B., Abramson L., 2013, ApJ, 770, 64

Gómez F. A., et al., 2017, MNRAS, 472, 3722

González Delgado R. M., et al., 2016, A&A, 590, A44

Goulding A. D., et al., 2018, PASJ, 70, S37

Governato F., et al., 2009, MNRAS, 398, 312

Grand R. J. J., Springel V., Gómez F. A., Marinacci F., Pakmor R., Campbell D. J. R., Jenkins A., 2016, MNRAS, 459, 199

Grand R. J. J., et al., 2017, MNRAS, 467, 179

Grisdale K., Agertz O., Romeo A. B., Renaud F., Read J. I., 2017, MNRAS, 466, 1093

Gupta A., Mathur S., Krongold Y., Nicastro F., Galeazzi M., 2012, ApJ, 756, L8

Hafen Z., et al., 2020, MNRAS, 494, 3581

Hani M. H., Sparre M., Ellison S. L., Torrey P., Vogelsberger M., 2018, MNRAS, 475, 1160

Hani M. H., Ellison S. L., Sparre M., Grand R. J. J., Pakmor R., Gomez F. A., Springel V., 2019, MNRAS, 488, 135

Hani M. H., Hayward C. C., Orr M. E., Ellison S. L., Torrey P., Murray N., Wetzel A., Faucher-Giguère C.-A., 2020a, MNRAS, 493, L87

Hani M. H., Gosain H., Ellison S. L., Patton D. R., Torrey P., 2020b, MNRAS, 493, 3716

Hayward C. C., Hopkins P. F., 2017, MNRAS, 465, 1682

Heckman T. M., Borthakur S., 2016, ApJ, 822, 9

Heckman T., Borthakur S., Wild V., Schiminovich D., Bordoloi R., 2017, ApJ, 846, 151

Heitsch F., Putman M. E., 2009, ApJ, 698, 1485

Hernández-Toledo H. M., Avila-Reese V., Conselice C. J., Puerari I., 2005, AJ, 129, 682

Hernández-Toledo H. M., Avila-Reese V., Salazar-Contreras J. R., Conselice C. J., 2006, AJ, 132, 71

Hernquist L., 1987, ApJS, 64, 715

Hernquist L., 1989, Nature, 340, 687

Hernquist L., Quinn P. J., 1987, ApJ, 312, 1

Hickox R. C., Mullaney J. R., Alexander D. M., Chen C.-T. J., Civano F. M., Goulding A. D., Hainline K. N., 2014, ApJ, 782, 9

Hirschmann M., De Lucia G., Fontanot F., 2016, MNRAS, 461, 1760

Hopkins P. F., 2014, GIZMO: Multi-method magneto-hydrodynamics+gravity code, Astrophysics Source Code Library (ascl:1410.003)

Hopkins P. F., 2015, MNRAS, 450, 53

Hopkins P. F., Quataert E., 2010, MNRAS, 407, 1529

Hopkins P. F., Hernquist L., Cox T. J., Robertson B., Krause E., 2007a, ApJ, 669, 45

Hopkins P. F., Hernquist L., Cox T. J., Robertson B., Krause E., 2007b, ApJ, 669, 67

Hopkins P. F., Hernquist L., Cox T. J., Kereš D., 2008, ApJS, 175, 356

Hopkins P. F., Kereš D., Oñorbe J., Faucher-Giguère C.-A., Quataert E., Murray N., Bullock J. S., 2014, MNRAS, 445, 581

Hopkins P. F., et al., 2018, MNRAS, 480, 800

Hsieh B. C., et al., 2017, ApJ, 851, L24

Huertas-Company M., et al., 2013, MNRAS, 428, 1715

Huertas-Company M., et al., 2019, MNRAS, 489, 1859

Hummels C. B., Bryan G. L., Smith B. D., Turk M. J., 2013, MNRAS, 430, 1548

Hummels C. B., et al., 2019, ApJ, 882, 156

Johansson P. H., Naab T., Burkert A., 2009, ApJ, 690, 802

Johnson S. D., Chen H.-W., Mulchaey J. S., Tripp T. M., Prochaska J. X., Werk J. K., 2014, MNRAS, 438, 3039

Johnson S. D., Chen H.-W., Mulchaey J. S., 2015a, MNRAS, 449, 3263

Johnson S. D., Chen H.-W., Mulchaey J. S., 2015b, MNRAS, 452, 2553

Kacprzak G. G., Churchill C. W., Nielsen N. M., 2012, ApJ, 760, L7

Kacprzak G. G., Muzahid S., Churchill C. W., Nielsen N. M., Charlton J. C., 2015, ApJ, 815, 22

Kalberla P. M. W., Dedes L., 2008, A&A, 487, 951

Kauffmann G., et al., 2003, MNRAS, 346, 1055

Kaviraj S., et al., 2013, MNRAS, 429, L40

Keeney B. A., Danforth C. W., Stocke J. T., Penton S. V., Shull J. M., Sembach K. R., 2006, ApJ, 646, 951

Keeney B. A., Stocke J. T., Danforth C. W., Carilli C. L., 2011, AJ, 141, 66

Keller B. W., Wadsley J., Benincasa S. M., Couchman H. M. P., 2014, MNRAS, 442, 3013

Kelson D. D., 2014, arXiv e-prints, p. arXiv:1406.5191

Kennicutt Robert C. J., 1998, ApJ, 498, 541

Kennicutt R. C., Evans N. J., 2012, ARA&A, 50, 531

Kewley L. J., Ellison S. L., 2008, ApJ, 681, 1183

Kewley L. J., Geller M. J., Barton E. J., 2006, AJ, 131, 2004

Kewley L. J., Rupke D., Zahid H. J., Geller M. J., Barton E. J., 2010, ApJ, 721, L48

Knapen J. H., Cisternas M., Querejeta M., 2015, MNRAS, 454, 1742

Kormendy J., Ho L. C., 2013, ARA&A, 51, 511

Koyamada S., Misawa T., Inada N., Oguri M., Kashikawa N., Okoshi K., 2017, ApJ, 851, 88

Lacey C., Cole S., 1993, MNRAS, 262, 627

Lagos C. D. P., Baugh C. M., Lacey C. G., Benson A. J., Kim H.-S., Power C., 2011, MNRAS, 418, 1649

Lagos C. D. P., Baugh C. M., Zwaan M. A., Lacey C. G., Gonzalez-Perez V., Power C., Swinbank A. M., van Kampen E., 2014, MNRAS, 440, 920

Lang P., et al., 2014, ApJ, 788, 11

Lanzetta K. M., Bowen D., 1990, ApJ, 357, 321

Lanzetta K. M., Bowen D. V., Tytler D., Webb J. K., 1995, ApJ, 442, 538

Lee H., Skillman E. D., Cannon J. M., Jackson D. C., Gehrz R. D., Polomski E. F., Woodward C. E., 2006, ApJ, 647, 970

Lehner N., O'Meara J. M., Fox A. J., Howk J. C., Prochaska J. X., Burns V., Armstrong A. A., 2014, ApJ, 788, 119

Lehner N., Howk J. C., Wakker B. P., 2015, ApJ, 804, 79

Lelli F., Verheijen M., Fraternali F., 2014a, MNRAS, 445, 1694

Lelli F., Verheijen M., Fraternali F., 2014b, A&A, 566, A71

Leroy A. K., et al., 2016, ApJ, 831, 16

Li C., White S. D. M., 2009, MNRAS, 398, 2177

Liang C. J., Chen H.-W., 2014, MNRAS, 445, 2061

Lilly S. J., Carollo C. M., Pipino A., Renzini A., Peng Y., 2013, ApJ, 772, 119

Lin L., et al., 2007, ApJ, 660, L51

Lin L., et al., 2008, ApJ, 681, 232

Lin L., et al., 2019a, ApJ, 872, 50

Lin L., et al., 2019b, ApJ, 884, L33

Liu Q., Wang E., Lin Z., Gao Y., Liu H., Berhane Teklu B., Kong X., 2018, ApJ, 857, 17

Lofthouse E. K., Kaviraj S., Conselice C. J., Mortlock A., Hartley W., 2017, MNRAS, 465, 2895

López-Sanjuan C., et al., 2013, A&A, 553, A78

Lopez S., Ellison S., D'Odorico S., Kim T.-S., 2007, A&A, 469, 61

Lopez S., et al., 2018, Nature, 554, 493

Lotz J. M., Jonsson P., Cox T. J., Primack J. R., 2008, MNRAS, 391, 1137

Lotz J. M., Jonsson P., Cox T. J., Primack J. R., 2010a, MNRAS, 404, 575

Lotz J. M., Jonsson P., Cox T. J., Primack J. R., 2010b, MNRAS, 404, 590

Lotz J. M., Jonsson P., Cox T. J., Croton D., Primack J. R., Somerville R. S., Stewart K., 2011, ApJ, 742, 103

Lu Z., Mo H. J., Lu Y., Katz N., Weinberg M. D., van den Bosch F. C., Yang X., 2014, MNRAS, 439, 1294

Ly C., Malkan M. A., Rigby J. R., Nagao T., 2016, ApJ, 828, 67

Machado R. E. G., Tissera P. B., Lima Neto G. B., Sodré L., 2018, A&A, 609, A66

Madau P., Dickinson M., 2014, ARA&A, 52, 415

Maiolino R., et al., 2017, Nature, 544, 202

Maragkoudakis A., Zezas A., Ashby M. L. N., Willner S. P., 2017, MNRAS, 466, 1192

Marinacci F., Pakmor R., Springel V., 2014a, MNRAS, 437, 1750

Marinacci F., Pakmor R., Springel V., Simpson C. M., 2014b, MNRAS, 442, 3745

Marinacci F., Grand R. J. J., Pakmor R., Springel V., Gómez F. A., Frenk C. S., White S. D. M., 2017, MNRAS, 466, 3859

Marinacci F., et al., 2018, MNRAS, 480, 5113

Marinacci F., Sales L. V., Vogelsberger M., Torrey P., Springel V., 2019, MNRAS, 489, 4233

Martin C. L., 2005, ApJ, 621, 227

Martin D. C., et al., 2019, Nature Astronomy, 3, 822

McConnell N. J., Ma C.-P., 2013, ApJ, 764, 184

McCourt M., Oh S. P., O'Leary R., Madigan A.-M., 2018, MNRAS, 473, 5407

McElroy R., Croom S. M., Pracy M., Sharp R., Ho I. T., Medling A. M., 2015, MNRAS, 446, 2186

McGaugh S. S., 2016, ApJ, 816, 42

McLure R. J., Dunlop J. S., 2002, MNRAS, 331, 795

Mendel J. T., Simard L., Ellison S. L., Patton D. R., 2013, MNRAS, 429, 2212

Mihos J. C., Hernquist L., 1996, ApJ, 464, 641

Moffett A. J., Kannappan S. J., Berlind A. A., Eckert K. D., Stark D. V., Hendel D., Norris M. A., Grogin N. A., 2015, ApJ, 812, 89

Monachesi A., et al., 2019, MNRAS, 485, 2589

Monaghan J. J., 1992, ARA&A, 30, 543

Montuori M., Di Matteo P., Lehnert M. D., Combes F., Semelin B., 2010, A&A, 518, A56

Moreno J., Torrey P., Ellison S. L., Patton D. R., Bluck A. F. L., Bansal G., Hernquist L., 2015, MNRAS, 448, 1107

Moreno J., et al., 2019, MNRAS, 485, 1320

Moss V. A., Lockman F. J., McClure-Griffiths N. M., 2017, ApJ, 834, 155

Muratov A. L., Kereš D., Faucher-Giguère C.-A., Hopkins P. F., Quataert E., Murray N., 2015, MNRAS, 454, 2691

Muratov A. L., et al., 2017, MNRAS, 468, 4170

Murray N., Quataert E., Thompson T. A., 2005, ApJ, 618, 569

Naiman J. P., et al., 2018, MNRAS, 477, 1206

Narayan R., Yi I., 1994, ApJ, 428, L13

Nelson D., Genel S., Pillepich A., Vogelsberger M., Springel V., Hernquist L., 2016, MNRAS, 460, 2881

Nelson D., et al., 2018a, MNRAS, 475, 624

Nelson D., et al., 2018b, MNRAS, 477, 450

Nelson D., et al., 2019a, Computational Astrophysics and Cosmology, 6, 2

Nelson D., et al., 2019b, MNRAS, 490, 3234

Nielsen N. M., Kacprzak G. G., Muzahid S., Churchill C. W., Murphy M. T., Charlton J. C., 2017, ApJ, 834, 148

Nielsen N. M., Kacprzak G. G., Pointon S. K., Churchill C. W., Murphy M. T., 2018, ApJ, 869, 153

Noeske K. G., et al., 2007, ApJ, 660, L43

Nulsen P. E. J., Fabian A. C., 2000, MNRAS, 311, 346

Oppenheimer B. D., Davé R., 2006, MNRAS, 373, 1265

Oppenheimer B. D., Schaye J., 2013, MNRAS, 434, 1063

Oppenheimer B. D., et al., 2016, MNRAS, 460, 2157

Oppenheimer B. D., Segers M., Schaye J., Richings A. J., Crain R. A., 2018a, MNRAS, 474, 4740

Oppenheimer B. D., Schaye J., Crain R. A., Werk J. K., Richings A. J., 2018b, MNRAS, 481, 835

Orr M. E., et al., 2017, ApJ, 849, L2

Orr M. E., et al., 2018, MNRAS, 478, 3653

Pakmor R., Springel V., 2013, MNRAS, 432, 176

Pakmor R., Marinacci F., Springel V., 2014, ApJ, 783, L20

Pakmor R., Springel V., Bauer A., Mocz P., Munoz D. J., Ohlmann S. T., Schaal K., Zhu C., 2016, MNRAS, 455, 1134

Pan H.-A., et al., 2018, ApJ, 868, 132

Pan H.-A., et al., 2019, ApJ, 881, 119

Pannella M., et al., 2009, ApJ, 698, L116

Patton D. R., Ellison S. L., Simard L., McConnachie A. W., Mendel J. T., 2011, MNRAS, 412, 591

Patton D. R., Torrey P., Ellison S. L., Mendel J. T., Scudder J. M., 2013, MNRAS, 433, L59

Patton D. R., Qamar F. D., Ellison S. L., Bluck A. F. L., Simard L., Mendel J. T., Moreno J., Torrey P., 2016, MNRAS, 461, 2589

Patton D. R., et al., 2020, MNRAS, 494, 4969

Peeples M. S., Werk J. K., Tumlinson J., Oppenheimer B. D., Prochaska J. X., Katz N., Weinberg D. H., 2014, ApJ, 786, 54

Peeples M. S., et al., 2019, ApJ, 873, 129

Peng Y.-j., et al., 2010, ApJ, 721, 193

Peng Y.-j., Lilly S. J., Renzini A., Carollo M., 2012, ApJ, 757, 4

Perez M. J., Tissera P. B., Scannapieco C., Lambas D. G., de Rossi M. E., 2006, A&A, 459, 361

Perez J., Michel-Dansac L., Tissera P. B., 2011, MNRAS, 417, 580

Péroux C., Rahmani H., Arrigoni Battaia F., Augustin R., 2018, MNRAS, 479, L50

Pettini M., Rix S. A., Steidel C. C., Adelberger K. L., Hunt M. P., Shapley A. E., 2002, ApJ, 569, 742

Pillepich A., et al., 2018a, MNRAS, 473, 4077

Pillepich A., et al., 2018b, MNRAS, 475, 648

Pillepich A., et al., 2019, MNRAS, 490, 3196

Pimbblet K. A., Shabala S. S., Haines C. P., Fraser-McKelvie A., Floyd D. J. E., 2013, MNRAS, 429, 1827

Pointon S. K., Nielsen N. M., Kacprzak G. G., Muzahid S., Churchill C. W., Charlton J. C., 2017, ApJ, 844, 23

Pop A.-R., Pillepich A., Amorisco N. C., Hernquist L., 2018, MNRAS, 480, 1715

Powell L. C., Bournaud F., Chapon D., Teyssier R., 2013, MNRAS, 434, 1028

Prochaska J. X., Gawiser E., Wolfe A. M., Castro S., Djorgovski S. G., 2003, ApJ, 595, L9

Prochaska J. X., Weiner B., Chen H.-W., Mulchaey J., Cooksey K., 2011, ApJ, 740, 91

Prochaska J. X., et al., 2017, ApJ, 837, 169

Puchwein E., Springel V., 2013, MNRAS, 428, 2966

Putman M. E., Peek J. E. G., Joung M. R., 2012, ARA&A, 50, 491

Rahmati A., Pawlik A. H., Raičevic M., Schaye J., 2013, MNRAS, 430, 2427

Renaud F., Bournaud F., Kraljic K., Duc P. A., 2014, MNRAS, 442, L33

Rhodin N. H. P., Agertz O., Christensen L., Renaud F., Fynbo J. P. U., 2019, MNRAS, 488, 3634

Richter P., et al., 2017, A&A, 607, A48

Rodighiero G., et al., 2011, ApJ, 739, L40

Rodriguez-Gomez V., et al., 2015, MNRAS, 449, 49

Rodriguez-Gomez V., et al., 2017, MNRAS, 467, 3083

Rodriguez-Gomez V., et al., 2019, MNRAS, 483, 4140

Rodríguez Montero F., Davé R., Wild V., Anglés-Alcázar D., Narayanan D., 2019, MNRAS, 490, 2139

Rudie G. C., Steidel C. C., Pettini M., Trainor R. F., Strom A. L., Hummels C. B., Reddy N. A., Shapley A. E., 2019, ApJ, 885, 61

Rupke D. S., Veilleux S., Sanders D. B., 2005a, ApJS, 160, 115

Rupke D. S., Veilleux S., Sanders D. B., 2005b, ApJ, 632, 751

Rupke D. S. N., Kewley L. J., Barnes J. E., 2010a, ApJ, 710, L156

Rupke D. S. N., Kewley L. J., Chien L. H., 2010b, ApJ, 723, 1255

Rupke D. S. N., et al., 2019, Nature, 574, 643

Saintonge A., et al., 2012, ApJ, 758, 73

Sales L. V., Navarro J. F., Abadi M. G., Steinmetz M., 2007, MNRAS, 379, 1464

Salim S., et al., 2007, ApJS, 173, 267

Samuel J., et al., 2020, MNRAS, 491, 1471

Sánchez S. F., et al., 2012, A&A, 538, A8

Sánchez S. F., et al., 2013, A&A, 554, A58

Sánchez S. F., et al., 2017, MNRAS, 469, 2121

Sanders R. L., et al., 2015, ApJ, 799, 138

Sargent W. L. W., Steidel C. C., Boksenberg A., 1988, ApJ, 334, 22

Satyapal S., Ellison S. L., McAlpine W., Hickox R. C., Patton D. R., Mendel J. T., 2014, MNRAS, 441, 1297

Scannapieco E., Brüggen M., 2015, ApJ, 805, 158

Scannapieco C., Tissera P. B., White S. D. M., Springel V., 2006, MNRAS, 371, 1125

Schawinski K., Thomas D., Sarzi M., Maraston C., Kaviraj S., Joo S.-J., Yi S. K., Silk J., 2007, MNRAS, 382, 1415

Schaye J., et al., 2010, MNRAS, 402, 1536

Schaye J., et al., 2015, MNRAS, 446, 521

Schmidt M., 1959, ApJ, 129, 243

Schneider E. E., Robertson B. E., Thompson T. A., 2018, ApJ, 862, 56

Schreiber C., et al., 2015, A&A, 575, A74

Scott T. C., et al., 2014, A&A, 567, A56

Scudder J. M., Ellison S. L., Torrey P., Patton D. R., Mendel J. T., 2012, MNRAS, 426, 549

Scudder J. M., Ellison S. L., Momjian E., Rosenberg J. L., Torrey P., Patton D. R., Fertig D., Mendel J. T., 2015, MNRAS, 449, 3719

Segers M. C., Oppenheimer B. D., Schaye J., Richings A. J., 2017, MNRAS, 471, 1026

Shen S., Madau P., Aguirre A., Guedes J., Mayer L., Wadsley J., 2012, ApJ, 760, 50

Shen S., Madau P., Guedes J., Mayer L., Prochaska J. X., Wadsley J., 2013, ApJ, 765, 89

Shimizu I., Todoroki K., Yajima H., Nagamine K., 2019, MNRAS, 484, 2632

Sijacki D., Vogelsberger M., Genel S., Springel V., Torrey P., Snyder G. F., Nelson D., Hernquist L., 2015, MNRAS, 452, 575

Silk J., Rees M. J., 1998, A&A, 331, L1

Sillero E., Tissera P. B., Lambas D. G., Michel-Dansac L., 2017, MNRAS, 472, 4404

Simard L., Mendel J. T., Patton D. R., Ellison S. L., McConnachie A. W., 2011, ApJS, 196, 11

Sinha M., Holley-Bockelmann K., 2009, MNRAS, 397, 190

Snyder G. F., Hopkins P. F., Hernquist L., 2011, ApJ, 728, L24

Sparre M., Springel V., 2016, MNRAS, 462, 2418

Sparre M., Springel V., 2017, MNRAS, 470, 3946

Sparre M., et al., 2015, MNRAS, 447, 3548

Sparre M., Hayward C. C., Feldmann R., Faucher-Giguère C.-A., Muratov A. L., Kereš D., Hopkins P. F., 2017, MNRAS, 466, 88

Sparre M., Pfrommer C., Vogelsberger M., 2019, MNRAS, 482, 5401

Speagle J. S., Steinhardt C. L., Capak P. L., Silverman J. D., 2014, ApJS, 214, 15

Spitzer Lyman J., 1956, ApJ, 124, 20

Springel V., 2000, MNRAS, 312, 859

Springel V., 2010, MNRAS, 401, 791

Springel V., 2011, in Alves J., Elmegreen B. G., Girart J. M., Trimble V., eds, IAU Symposium Vol. 270, Computational Star Formation. pp 203–206, doi:10.1017/S1743921311000378

Springel V., Hernquist L., 2003, MNRAS, 339, 289

Springel V., Hernquist L., 2005, ApJ, 622, L9

Springel V., White S. D. M., Tormen G., Kauffmann G., 2001, MNRAS, 328, 726

Springel V., Di Matteo T., Hernquist L., 2005a, MNRAS, 361, 776

Springel V., et al., 2005b, Nature, 435, 629

Springel V., et al., 2018, MNRAS, 475, 676

Stark D. P., et al., 2015, MNRAS, 450, 1846

Steidel C. C., Erb D. K., Shapley A. E., Pettini M., Reddy N., Bogosavljević M., Rudie G. C., Rakic O., 2010, ApJ, 717, 289

Steidel C. C., et al., 2014, ApJ, 795, 165

Stern J., Hennawi J. F., Prochaska J. X., Werk J. K., 2016, ApJ, 830, 87

Stinson G., Seth A., Katz N., Wadsley J., Governato F., Quinn T., 2006, MNRAS, 373, 1074

Stinson G. S., et al., 2012, MNRAS, 425, 1270

Stone J. M., Gardiner T. A., Teuben P., Hawley J. F., Simon J. B., 2008, ApJS, 178, 137

Strickland D. K., Heckman T. M., 2009, ApJ, 697, 2030

Su M., Slatyer T. R., Finkbeiner D. P., 2010, ApJ, 724, 1044

Suresh J., Bird S., Vogelsberger M., Genel S., Torrey P., Sijacki D., Springel V., Hernquist L., 2015, MNRAS, 448, 895

Suresh J., Rubin K. H. R., Kannan R., Werk J. K., Hernquist L., Vogelsberger M., 2017, MNRAS, 465, 2966

Suresh J., Nelson D., Genel S., Rubin K. H. R., Hernquist L., 2019, MNRAS, 483, 4040

Tacchella S., Dekel A., Carollo C. M., Ceverino D., DeGraf C., Lapiner S., Mand elker N., Primack Joel R., 2016, MNRAS, 457, 2790

Tacchella S., et al., 2018, ApJ, 859, 56

Tacchella S., et al., 2019a, MNRAS, p. 1573

Tacchella S., et al., 2019b, MNRAS, 487, 5416

Tacconi L. J., et al., 2018, ApJ, 853, 179

Taylor P., Kobayashi C., 2014, MNRAS, 442, 2751

Thom C., et al., 2012, ApJ, 758, L41

Thorp M. D., Ellison S. L., Simard L., Sánchez S. F., Antonio B., 2019, MNRAS, 482, L55

Timmes F. X., Woosley S. E., Weaver T. A., 1995, ApJS, 98, 617

Tissera P. B., Lambas D. G., Abadi M. G., 1997, MNRAS, 286, 384

Torrey P., Cox T. J., Kewley L., Hernquist L., 2012, ApJ, 746, 108

Torrey P., Vogelsberger M., Genel S., Sijacki D., Springel V., Hernquist L., 2014, MNRAS, 438, 1985

Torrey P., et al., 2018, MNRAS, 477, L16

Torrey P., et al., 2019, MNRAS, 484, 5587

Trayford J. W., Schaye J., 2019, MNRAS, 485, 5715

Tremonti C. A., et al., 2004, ApJ, 613, 898

Tripp T. M., Savage B. D., Jenkins E. B., 2000, ApJ, 534, L1

Trump J. R., et al., 2011, ApJ, 733, 60

Tumlinson J., et al., 2011, Science, 334, 948

Tumlinson J., et al., 2013, ApJ, 777, 59

Tumlinson J., Peeples M. S., Werk J. K., 2017, ARA&A, 55, 389

Turk M. J., Smith B. D., Oishi J. S., Skory S., Skillman S. W., Abel T., Norman M. L., 2011, The Astrophysical Journal Supplement Series, 192, 9

Umemura M., 1993, ApJ, 406, 361

Vanzella E., et al., 2017, MNRAS, 465, 3803

Veilleux S., Cecil G., Bland-Hawthorn J., 2005, ARA&A, 43, 769

Veilleux S., et al., 2013, ApJ, 776, 27

Violino G., Ellison S. L., Sargent M., Coppin K. E. K., Scudder J. M., Mendel T. J., Saintonge A., 2018, MNRAS, 476, 2591

Vogelsberger M., Genel S., Sijacki D., Torrey P., Springel V., Hernquist L., 2013, MNRAS, 436, 3031

Vogelsberger M., et al., 2014a, MNRAS, 444, 1518

Vogelsberger M., et al., 2014b, Nature, 509, 177

Vulcani B., et al., 2019, MNRAS, 488, 1597

Wang L., Dutton A. A., Stinson G. S., Macciò A. V., Penzo C., Kang X., Keller B. W., Wadsley J., 2015, MNRAS, 454, 83

Weinberger R., et al., 2017, MNRAS, 465, 3291

Werk J. K., Prochaska J. X., Thom C., Tumlinson J., Tripp T. M., O'Meara J. M., Meiring J. D., 2012, ApJS, 198, 3

Werk J. K., Prochaska J. X., Thom C., Tumlinson J., Tripp T. M., O'Meara J. M., Peeples M. S., 2013, ApJS, 204, 17

Werk J. K., et al., 2014, ApJ, 792, 8

Werk J. K., et al., 2016, ApJ, 833, 54

Werk J. K., et al., 2019, ApJ, 887, 89

Wetzel A. R., Cohn J. D., White M., 2009, MNRAS, 395, 1376

Wetzel A. R., Tinker J. L., Conroy C., 2012, MNRAS, 424, 232

Wetzel A. R., Hopkins P. F., Kim J.-h., Faucher-Giguère C.-A., Kereš D., Quataert E., 2016, ApJ, 827, L23

Whitaker K. E., et al., 2015, ApJ, 811, L12

White S. D. M., 1978, MNRAS, 184, 185

White S. D. M., Rees M. J., 1978, MNRAS, 183, 341

Wiersma R. P. C., Schaye J., Theuns T., Dalla Vecchia C., Tornatore L., 2009, MNRAS, 399, 574

Wilson T. J., et al., 2019, ApJ, 874, 18

Wisotzki L., et al., 2016, A&A, 587, A98

Wolfe A. M., 1986, Philosophical Transactions of the Royal Society of London Series A, 320, 503

Wolfe A. M., Lanzetta K. M., Foltz C. B., Chaffee F. H., 1995, ApJ, 454, 698

Wong K. C., et al., 2011, ApJ, 728, 119

Woo J., et al., 2013, MNRAS, 428, 3306

Woo J., Dekel A., Faber S. M., Koo D. C., 2015, MNRAS, 448, 237

Woo J.-H., Son D., Bae H.-J., 2017, ApJ, 839, 120

Wuyts S., et al., 2011, ApJ, 742, 96

Zahid H. J., Kewley L. J., Bresolin F., 2011, ApJ, 730, 137

Zahid H. J., Bresolin F., Kewley L. J., Coil A. L., Davé R., 2012, ApJ, 750, 120

Zahid H. J., Torrey P., Vogelsberger M., Hernquist L., Kewley L., Davé R., 2014, Ap&SS, 349, 873

Zech W. F., Lehner N., Howk J. C., Dixon W. V. D., Brown T. M., 2008, ApJ, 679, 460

Zheng Y., Peek J. E. G., Putman M. E., Werk J. K., 2019, ApJ, 871, 35

Zschaechner L. K., et al., 2016, ApJ, 832, 142

Zubovas K., Nayakshin S., 2012, MNRAS, 424, 666

de Ravel L., et al., 2009, A&A, 498, 379

van de Voort F., Schaye J., Altay G., Theuns T., 2012, MNRAS, 421, 2809

van de Voort F., Springel V., Mandelker N., van den Bosch F. C., Pakmor R., 2019, MNRAS, 482, L85

van den Bosch F. C., et al., 2007, MNRAS, 376, 841